EXPERIMENTAL AND COMPUTATIONAL VIBRATIONAL SUM FREQUENCY SPECTROSCOPY STUDIES OF ATMOSPHERIC ORGANICS AND THEIR SURFACE-ACTIVE HYDRATION AND OLIGOMER PRODUCTS AT THE AIR-WATER INTERFACE

by

BRITTANY PIERCE GORDON

A DISSERTATION

Presented to the Department of Chemistry and Biochemistry
and the Graduate School of the University of Oregon
in partial fulfillment of the requirements
for the degree of
Doctor of Philosophy

December 2019

DISSERTATION APPROVAL PAGE

Student: Brittany Pierce Gordon

Title: Experimental and Computational Vibrational Sum Frequency Spectroscopy Studies of Atmospheric Organics and Their Surface-Active Hydration and Oligomer Products at the Air-Water Interface

This dissertation has been accepted and approved in partial fulfillment of the requirements for the Doctor of Philosophy degree in the Department of Chemistry and Biochemistry by:

Marina G. Guenza	Chairperson
Geraldine L. Richmond	Advisor
George V. Nazin	Core Member
Emilie E.E. Hooft	Institutional Representative

and

Kate Mondloch Interim Vice Provost and Dean of the Graduate School

Original approval signatures are on file with the University of Oregon Graduate School.

Degree awarded December 2019

DISSERTATION ABSTRACT

Brittany Pierce Gordon

Doctor of Philosophy

Department of Chemistry and Biochemistry

December 2019

Title: Experimental and Computational Vibrational Sum Frequency Spectroscopy Studies of Atmospheric Organics and Their Surface-Active Hydration and Oligomer Products at the Air-Water Interface

Organics at aerosol interfaces greatly affect aerosol properties in turn affecting the climate. However, many aspects about the formation and atmospheric processing of aerosols, in particular secondary organic aerosol (SOA), remain poorly understood. The traditional mechanism of SOA formation does not adequately predict experimental observations in the atmosphere. It is increasingly being recognized that aqueous phase processing of atmospheric organics is another important pathway to SOA formation. A better picture of the surface behavior of these organics and their reaction products will aid in further understanding the role these organics play in the formation potential of aqueous secondary organic aerosol. The work within details studies on the adsorption, orientation, and hydration state of select atmospheric carbonyls (glyoxal, hydroxyacetone, methylglyoxal, and pyruvic acid) and their aqueous reaction products at the air-water interface. Data are gathered using a combination of experimental and theoretical techniques, including vibrational sum frequency (VSF) spectroscopy, surface tensiometry measurements, classical molecular dynamics (MD) simulations, and density functional theory (DFT) calculations.

This dissertation includes previously published and unpublished co-authored material.

CURRICULUM VITAE

NAME OF AUTHOR: Brittany Pierce Gordon

GRADUATE AND UNDERGRADUATE SCHOOLS ATTENDED:

University of Oregon, Eugene
New College of Florida, Sarasota
Santa Fe College, Gainesville

DEGREES AWARDED:

Doctor of Philosophy, Chemistry, 2019, University of Oregon
Masters of Science, Chemistry, 2019, University of Oregon
Bachelors of Arts, Chemistry, 2013, New College of Florida, Sarasota
Associates of Arts, Biology, 2010, Santa Fe College, Gainesville

AREAS OF SPECIAL INTEREST:

- Spectroscopy
  - Chirped Pulse Fourier Transform Microwave (CP-FTMW) Spectroscopy
  - Vibrational Sum Frequency (VSF) Spectroscopy
- Computational Chemistry
  - Atomistic Density Functional Theory (DFT)
  - Atomistic Molecular Dynamics (MD)
- Atmospheric Chemistry
  - Secondary Organic Aerosol (SOA) Formation

PROFESSIONAL EXPERIENCE:

1st place Physical Chemistry Division Poster Session, American Chemical Society, 2017
Graduate Teaching Fellow –Presidential Undergraduate Research (PURS) Program, University of Oregon, 2014-2017
Graduate Teaching Fellow – Physical Chemistry Lab, University of Oregon, 2013-2015
Graduate Research Fellow - Richmond Lab, University of Oregon, 2014-2019

GRANTS, AWARDS, AND HONORS:

Teaching Award for Physical Chemistry Lab, University of Oregon, 2015
1st place Physical Chemistry Division Poster Session, American Chemical Society, 2017

PUBLICATIONS:

Gordon, B. P. Waveguide Chirped-Pulse Fourier Transform Microwave Spectra of Small Alkylthiols. *Undergraduate Thesis (B.A.)* - New College of Florida, **2013**.

L. Kolesniková, L., Tercero, B., Cernicharo, J., Alonso, J. L., Daly, A. M., Gordon, B. P., Shipman, S. T. Spectroscopic Characterization and Detection of Ethyl Mercaptan in Orion. *Astrophys. J. Lett.,* **2014,** *784 (L7),* 8pp.

Wren, S. N., Gordon, B. P., Valley, N. A., McWilliams, L. E., Richmond, G. L. Hydration, Orientation, and Conformation of Methylglyoxal at the Air-Water Interface. *J. Phys. Chem. A* **2015** *119* (24), 6391-6403.

Gordon, B. P., Moore, F. G., Scatena, L. F., Valley, N. A., Wren, S. N., Richmond, G. L. Model Behavior: Characterization of Hydroxyacetone at the Air-Water Interface Using Experimental and Computational Vibrational Sum Frequency Spectroscopy. *J. Phys. Chem. A* **2018** *122* (15), 3837-3849.

Ciszewski, R. K., Gordon, B. P., Muller, B. N., Richmond, G. L. Takes Two to Tango: The Choreography of the Co-Adsorption of CTAB and Hexanol at the Oil-Water Interface. *J. Phys. Chem. B* **2019** *123* (40), 8519-8531.

Gordon, B. P., Moore, F. G., Scatena, L. F., Richmond, G. L. On the Rise: Experimental and Computational VSFS Studies of Pyruvic Acid and its Surface Active Oligomer Species at the Air-Water Interface. *J. Phys. Chem. A* **2019***, 123 (49), 10609-10619*

Gordon, B. P., Moore, F. G., Scatena, L. F., Richmond, G. L. Diol It Up: The Influence of NaCl on Methylglyoxal Surface Adsorption and Hydration State at the Air-Water Interface. **To be submitted to Journal of Physical Chemistry A in December 2019*

Gordon, B. P., Moore, F. G., Scatena, L. F., Richmond, G. L. Mix and Match: VSF studies of Glyoxal and its Surface Active Oligomers at the Air-Water Interface. **In Preparation*

Gordon, B. P., Moore, F. G., Valley, N. A., Richmond, G. L. Level Up: Methodology Improvements for Calculation of VSF Spectra of Aqueous Organic Interfaces Using Gas-Phase Water Microclusters. **In Preparation*

ACKNOWLEDGMENTS

Thank you to the entire Richmond Lab. I have loved my time here and will always treasure it. In particular, I would like to give thanks to Dr. Clive Kittredge, my mentor during my REU and first friend in the lab. To my mentors after joining the lab, Dr. Sumi Wren and Nick Valley, who provided me with an incredible foundation for my future work. Dr. Jenny Hensel, for always being a friend and mentor. Dr. Regina Ciszewski, my friend and office mate who put up with my eccentricities with just a smile and a laugh. Andrew Carpenter, who I could always count on for good scientific discussion. Evan Christoffersen, who is keeping Frankenstein alive. To Grace Lindquist and Michael Crawford, my former minions, for all your help and support and just being awesome to work with! Priscilla Lewis, our Lab Mom, who keeps it all from going off the rails. And my advisor, Dr. Geraldine Richmond, not only for your role as my mentor, but also for all the work you do to inspire and further the cause of women in science.

I especially want to thank Dr. Larry Scatena and Dr. Fred Moore for your mentorship, patience, thoughtfulness, friendship, and utterly invaluable support. And of course, Frankenstein, my laser that just keeps on keeping on through thick and thin since 1994. We have been through the trenches together, but old Frankenstein always pulled through and has never run better!

Thank you to the UO Chemistry department for all their help and support during my six years here. I also want to thank Dr. John Hardwick for being the best professor anyone could ever hope to be a teaching assistant for. It was genuinely a pleasure and privilege to work with you. The skills I learned in my two years teaching Physical Chemistry lab with you proved to be instrumental in my own research. Every time I write anything, I think of your favorite quote: “I wanted to write you a short note but I didn’t have time, so I wrote you a long one.” So, so true. Also thank you to Dr. Shannon Boettcher, my research advisor and mentor during my 2012 REU at UO. While my time in your group might have been brief, the wisdom you offered me stuck and helped me on my way ever since.

I would also like to express my sincere gratitude for my amazing thesis committee, Dr. Marina Guenza, Dr. George Nazin, and Dr. Emilie Hooft. You have

always been supportive and offered insightful feedback. Not every grad student looks forward to annual reviews, but thanks to my great committee, I always did.

And finally, I would give thanks to my family for their everlasting support and confidence in me, even when (especially when!) I doubted myself. To my aunt, Sharon Potts, and my dad, Dr. Michael Gordon, who I know are proud of me even if they are no longer with us. My uncle, Dr. Phillip Gordon, who was always sure I would be next Dr. Gordon. To Taylor Potts-Gordon, my itty-bitty baby cousin (who is somehow actually in her in 20s with a degree of her own and also taller than me) for always inspiring me and also making me laugh. And my amazing Aunt Carol, who always gets me.

To my sister and her amazing family. My brother-in-law Eddie Fraiman for his unwavering faith in me and laughing at the thought of me not getting into college, grad school, whatever. My amazing, incredible, brilliant niece and nephews, Maayan, Zev, and Alon (the Science Kiddos!) You guys never cease to astound me with how brilliant you are! Seriously, what other kids know about Rayleigh scattering, wave-particle duality, and black holes? You are all amazing and I can't wait to do science with you! And to my sister, and best friend Paule. Thank you for your support and help and guidance and advice, but also being the one I can always count on to talk about science and books and thought experiments with.

To my parents, Debra Gordon and Franklin Lampp, for always being my rock and personal cheerleaders. Thank you for always being the ones I could be cranky at when I was stressed and then still driving down to see me and bring me homemade soup. Thank you for the countless practice talks I made you sit through and all the papers you looked over for me (even though you couldn't understand half the words) just to put my mind at ease. You guys are the best and I couldn't have done it without you!

And finally, thank you to Gremlin, Loki, Thor and Fenrir, the best pets anybody could ever ask for. You little dudes got me through a lot of hard times and I will be forever grateful for that.

This material is based upon work supported by the National Science Foundation under Grant No. CHE 1051215 and Grant No. CHE 1505891 awarded to Dr. Geraldine Richmond at the University of Oregon.

For my brilliant niece and nephews (the science kiddos!) Maayan, Zev, and Alon.
May this work inspire you even a fraction as much as you all have inspired me.

TABLE OF CONTENTS

Chapter Page

Chapter Page

Chapter Page

Chapter Page

LIST OF FIGURES

Figure Page

Figure Page

LIST OF TABLES

Table Page

CHAPTER I

INTRODUCTION

Atmospheric aerosols are solid or liquid suspensions in the gas phase. They are of great importance and can affect both the climate and human health. Aerosols influence the climate directly by scattering and absorbing light and indirectly by acting as nucleation sites in cloud formation.[1-2] Aerosol composition is complex and varied, and consists of both inorganic and organic constituents.[3-6] Many of the organics found in aerosols are formed by gas phase reactions of primary organic precursors and are thus considered secondary organics. Aerosols containing secondary organics are known as secondary organic aerosol (SOA).

Due to the high surface area to volume ratio of aerosols, molecules at aerosol surfaces play a particularly large role in their atmospheric chemistry.[7-8] Additionally, the presence of organics and salts can significantly affect SOA properties.[1-8] However, because of the complexity of SOA, little is currently known about how these components individually or in concert affect aerosol behavior. The dearth of knowledge makes predicting formation and aging of SOA in the atmosphere very challenging and has necessitated oversimplifications in atmospheric models.[1-10] The "standard" or "gas phase" mechanism of SOA formation considers only gas phase oxidation of volatile organic precursors. These oxidized organic products are less volatile, and form SOA by reversibly coalescing into molecular clusters or by condensing onto preexisting particles. However, the "gas phase" mechanism cannot adequately account for the quantity or variety of observed SOA.[1-3,5-7,9,10]

These discrepancies have prompted the notion that aqueous phase processing of atmospheric organics also contributes significantly to SOA formation. The proposed mechanism accounts for reactions occurring in the particle phase which lead to the formation of SOA mass (hereafter aqSOA). Semi-volatile organics, in particular carbonyls, which can partition from the gas phase into aerosol, fog, and cloud water, are the primary candidates for this kind of aqSOA processing.[1-6,9-10] Atmospheric organics with carbonyl moieties favor this kind of chemistry because once in the aqueous phase, the carbonyls readily hydrate to form less volatile geminal diols. Aqueous phase oxidation and oligomerization reactions[1-6] (e.g., aldol condensation, acetal formation) of the hydrated species can lead to the formation of additional high molecular weight oligomers and/or highly oxygenated products.[x] Due to their low-volatility, these products generally remain in the particle phase and thereby increase SOA mass.

This sort of aqSOA formation mechanism could account for observed particle phase concentrations of atmospheric carbonyls, which are significantly higher than predicted based on physical solubility alone.[1,9,10] However, the chemical processes responsible for the uptake and enhanced partitioning of these species are still not fully understood.[1-6,9-10] Moreover, the presence of these organics and their unique products from aqueous phase processing has the ability to alter climate-relevant aerosol characteristics in significant ways. For example, the addition of hygroscopic mass leads to an increase in particle size that affects light scattering and cloud nucleation activity.[3,6,10] To be able to predict the impact of aqSOA, it is important to fully characterize not only the identity and interfacial behavior of the individual organic constituents, but also the perturbations in behavior that arise from their interactions with other aerosol components, especially inorganic salts and other organics.

Alone, atmospheric salts can affect water structure[7-8] and organic number density at the air-water interface (i.e., the aerosol surface), in turn altering aerosol hygroscopicity and surface tension.[3-6] Some salts are thought to catalyze the oligomerization reactions responsible for the formation of additional higher molecular weight species.[3-6] The presence of salts can also shift the hydration equilibrium of organics with multiple hydration states.[11-12] More work is required to understand the formation of these species.

Furthermore, it has been observed that aerosol with multiple organic species can have unpredicted synergistic effects on aerosol surface tension and hygroscopicity, particularly in the presence of salt. These effects have been ascribed to the adsorption of mixed organics to the particle interface and exceed what would be expected based on predictions from bulk properties.[6,13,14] Changes in the surface tension and hygroscopicity of aerosols have important atmospheric consequences, such as enhancing aerosol cloud nucleation activity.[1-3,5,6,13,14] Complete characterization of SOA surfaces and prediction of their behavior requires understanding of the identity, behavior, and orientation of the species present at the interface. Bulk-to-surface partitioning can also increase the uptake of gaseous organics because the gas-to-particle partitioning of organics is governed by bulk concentrations. Surface partitioning to aerosol interfaces effectively lowers bulks concentrations, which allows for increased gas-to-particle phase uptake. This can lead to significantly higher concentrations of organics in the particle phase.[15-17] As mentioned previously, surface tension depression in aerosol due to surface active species and bulk-to-surface partitioning have been shown to affect aerosol cloud nucleation activity.[3,15] It is also known that SOA can form organic surface films, which may impede gas-aerosol mass transport by acting as a kinetic barrier.[3,6,13] Finally, it has been suggested that reactions could occur on particle surfaces and contribute to aqueous phase processing.[1,2]

To improve our understanding of SOA interfaces, we must first characterize the organics that are thought to play an important role in aqSOA formation. To decouple the interactions of the many constituents of SOA, a firm foundation needs to be established for how a given organic component behaves at and impacts the interface. This research will investigate the adsorption of atmospheric carbonyls to aqueous surfaces, which includes determination of the orientations, conformations, hydration states, and reaction products of the studied carbonyls at the interface. With that information, investigations will progress to studying how the addition of non-reactive salts or other organic species influences the system further.

Aqueous systems of glyoxal (GL), hydroxyacetone (HA), methylglyoxal (MG), and pyruvic acid (PA) have been studied with a focus on elucidating their surface orientations, hydration states, and conformations at the air-water interface. Understanding these properties will help to lower the uncertainties associated with atmospheric aerosol formation by providing insight into the behaviors of these complex systems. This information will aid in further understanding the ultimate fate of these organics within aqueous aerosol and their SOA forming potential. The work described within utilizes a combined approach consisting of experimental vibrational sum frequency (VSF) spectroscopy and Wilhelmy plate surface tensiometry with computational molecular dynamics (MD) simulations and density functional theory (DFT) calculations to investigate organic adsorption to the air-water interface as a model for aqueous SOA.

CHAPTER II

METHODS

The methods and techniques utilized in this work have been thoroughly covered in previous publications and dissertations. For this reason, only a brief discussion is included here.

Theory of Vibrational Sum Frequency (VSF) Spectroscopy

A powerful experimental technique used for studying interfacial behavior is vibrational sum frequency (VSF) spectroscopy. VSF spectroscopy is a nonlinear technique that is inherently surface-selective and provides a convolution of orientation and population information for anisotropically ordered, surface-active, noncentrosymmetric molecules. A sum frequency signal is generated by overlapping a visible beam and an IR beam in time and space (Figure 2.1). The intensity of the VSF signal is proportional to the square of the nonlinear second-order macroscopic susceptibility, χ^2, and the intensities of the IR and visible beams (Eq. 2.1).

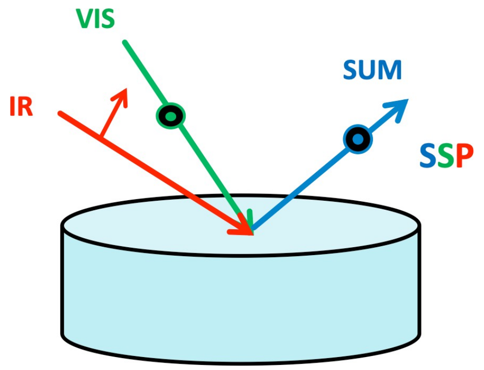

Figure 2.1: VSF generation at the air-water interface.

$$! \propto \left| !^{!}_{(\;)} \right|^{!} !_{!"\#} \; !_{!"} \qquad (2.1)$$

The susceptibility depends on the number density of molecules at the interface, *N,* and on the orientation of those molecules, which is accounted for in the tensor, $<\beta_v>$, the macroscopic average of the molecular hyperpolarizabilities (Eq. 2.2).

$$\chi_v^{(2)} = \frac{N}{\varepsilon_0}\langle \beta_v \rangle \tag{2.2}$$

The second-order susceptibility has both resonant ($\chi_{Rv}{}^{(2)}$) and non-resonant, ($\chi_{NR}{}^{(2)}$) components. The resonant portion of the VSF response contains information about both the *population* and *orientation* of species adsorbed at an interface. To deconvolve these numerous contributions, VSF spectra are fit using equation 1:[1-2]

$$\chi^{(2)} = \chi_{NR}^{(2)} e^{i\psi} + \sum_v \int_{-\infty}^{\infty} \frac{A_v e^{i\varphi_v} e^{-[(\omega_L-\omega_v)/\Gamma_v]^2}}{\omega_L - \omega_{IR} + i\Gamma_L}\, d\omega_L \tag{2.3}$$

The first term in Equation 2.3 is the nonresonant susceptibility, described by an amplitude and phase, ψ. The second term defines contributions from the resonant second-order susceptibility ($\chi_{Rv}{}^{(2)}$) as the summation over all VSF active resonant vibrational modes. Included in this resonant second-order susceptibility are the transition strength (A_v), phases (φ_v), and terms describing the homogeneous line widths of the individual molecular transitions (Γ_L) as well as inhomogeneous broadening (Γ_v). The Lorentzian, resonant modes and IR frequencies are defined as ω_L, ω_v, and $\omega_{IR,}$ respectively. Equation 1 is utilized for the fitting equation and spectral analysis of the VSF data, using mode specific fixed Lorentzian widths modes (based on reported vibrational lifetimes of the specific transition)[3-7] for the CH (2 cm^{-1}), coordinated OH and C=O (5 cm^{-1}), and 'free' OH (12 cm^{-1}).

VSF spectra can be acquired in different polarization schemes which allow different aspects of the molecular orientations to be probed. Spectra discussed in this proposal are obtained using either the *ssp* or *sps* polarization scheme, where the three letters denote the polarizations of the sum frequency, visible and IR beams respectively. The *ssp* scheme probes molecular dipole components perpendicular to the air-water interface while the *sps* scheme probes components parallel to the interface.

Laser System

VSF spectra were obtained using a newly-assembled picosecond system.[8,11-12] The system consists of a modelocked Ti:Sapphire laser which seeds an ultrafast regenerative amplifier to produce a ~2000 μJ pulsed (~2.6 ps) visible beam centered at 800 nm with a 7 nm bandwidth at a repetition rate of 1 kHz. The amplified beam is split with ~ 500 μJ directed to the visible line. The remaining ~ 1500 μJ is sent to an optical parametric amplifier (OPA) in tandem with difference frequency generator (DFG) for mixing and variable IR generation, producing IR light from 4000 cm^{-1} (~ 25 μJ) to 800 cm^{-1} (~2μJ). The visible and IR beams are overlapped in time and space at the air-water interface. The resultant sum frequency beam is detected using a thermoelectrically cooled CCD camera. The aqueous samples are held in meticulously clean, shallow glass dishes on a vertically translatable stage.

The picosecond laser system used to obtain the VSF results discussed here has been described,[8-16] such that only a brief description is necessary for this work. A sum frequency (SF) beam is generated by overlapping a fixed visible beam (12500 cm^{-1}) with a tunable IR beam at the air-water interface in a copropagating geometry at 45° and 60°

(Figure 2.1), respectively, relative to the surface normal. The SF beam leaving the interface is collected using a curved mirror set at its focal length and directed into a thermoelectrically cooled CCD camera (Pixas, Princeton Instruments). A LabView program measures the CCD intensity while scanning (3 cm^{-1} wavelength step) over the tunable IR range between 4000 cm^{-1} to 1200 cm^{-1}. The nonresonant SF response of an uncoated gold substrate was measured daily for each data set, and used to normalize the experimental spectra for VSF power. Daily calibration of the tunable IR beam was performed by measuring the absorption of a polystyrene standard and fitting to the known assignments. Spectra presented here are averages of ~6 or more spectra taken over multiple days. The resolution of the VSF system used herein is ≅10 - 18 cm^{-1}.

Shallow glass dishes (≥ 8mm depth) are utilized as sample cells and are cleaned according to the rigorous protocol described in previous works.[8-16] The dishes are placed on a vertically translatable stage. The stage is adjusted between each scan to account for any evaporation. Care was taken to ensure that evaporation did not alter the solution concentration. All VSF measurements were acquired at room temperature (~20 °C) under ambient conditions.

Surface Tensiometry: The Wilhelmy Plate Method

Contributions to the VSF signal from number density and molecular orientation are decoupled experimentally through the use of Wilhelmy Plate surface tensiometry measurements. This method measures surface tension (mN m^{-1}) as a function of time (s) by lowering a platinum plate into a solution in a clean glass dish at the air-water interface (Figure 2.2). The force exerted on the plate by the solution is measured using a force balance (KSV Instruments). Surface tensions (γ) are converted to surface pressures (π) by subtracting the daily-measured surface tension of neat water.

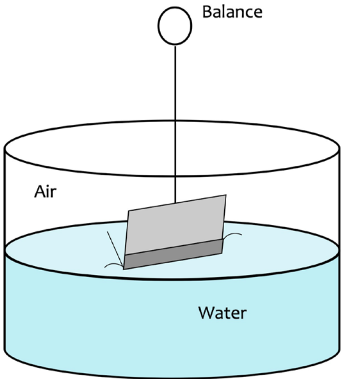

Figure 2.2: Diagram of Wilhelmy Plate surface tensiometry set up at the air-water interface.

Contributions to the VSF signal from number density and molecular orientation are decoupled experimentally through the use of Wilhelmy plate[17] surface tensiometry measurements. The force exerted on the plate by the solution is measured using a force balance (KSV). Surface tensions (γ) are converted to surface pressures (π) by subtracting the daily-measured surface tension of neat water. The platinum plate was cleaned and rinsed repeatedly in 18.2 MΩ-cm nanopure water and then dried under flame between measurements. All measurements were recorded under ambient conditions at room temperature (~20 °C).

It is worth noting that the surface tension versus time measurements reveal an extremely slow adsorption of HA to the interface. Equilibrium values occur after > 5 hours with a slowed increase over the next 24 hrs. This slow equilibration time is not unexpected as it has been observed in similar systems such as aqueous methylglyoxal.[8-16]Further note that VSF itself is an extremely sensitive probe of interfacial contaminants and that no evidence of contamination was observed. For this reason, VSF spectra were obtained after each sample had equilibrated (for at least two hours) confirmed by the invariance of VSF results over time.

Surface pressure data, *π*, was collected as a function time for neat water and organic solutions between 0.01 M and 2M. For each organic in solution, the equilibrated surface pressure value (> 2 hours) is plotted as a function of the natural log of bulk organic concentration, [OR]. From this surface pressure isotherm, the maximum surface excess can be calculated according to the Gibbs adsorption equation:[18]

$$\Gamma_{OR} = (1/RT)(d\pi/d\ln a_{OR})_T \tag{2.4}$$

where Γ_{OR} is the maximum surface excess, π is the surface pressure in mN m^{-1}, and a_{OR} is the activity. For those organics that lack experimental activity data, concentrations not corrected for activity were used instead (a_{OR} = [OR]). The slope of a linear fit of the surface pressure versus the natural log of the activity (here, [OR]) is equivalent to the maximum surface excess. The minimum area per molecule can then be found by inverting the surface excess.

Computational Methodology

VSF spectra can be very difficult to interpret because of the multiple contributions to the observed intensity. Additional techniques, in particular computational calculations, are extremely valuable to help decouple these contributions. A combination of molecular dynamics (MD) and density functional theory (DFT) calculations allow us to obtain information about the orientational, depth specific behavior of molecules in order to decouple the contributions to the experimentally observed signal.

A combination of computational techniques are used to generate calculated VSF spectra. In addition to simulating spectra, the analysis also extracts structural details about the system, such as density profiles, as well as depth-resolved orientation and conformation information, which are vital in helping to understand the behavior of the

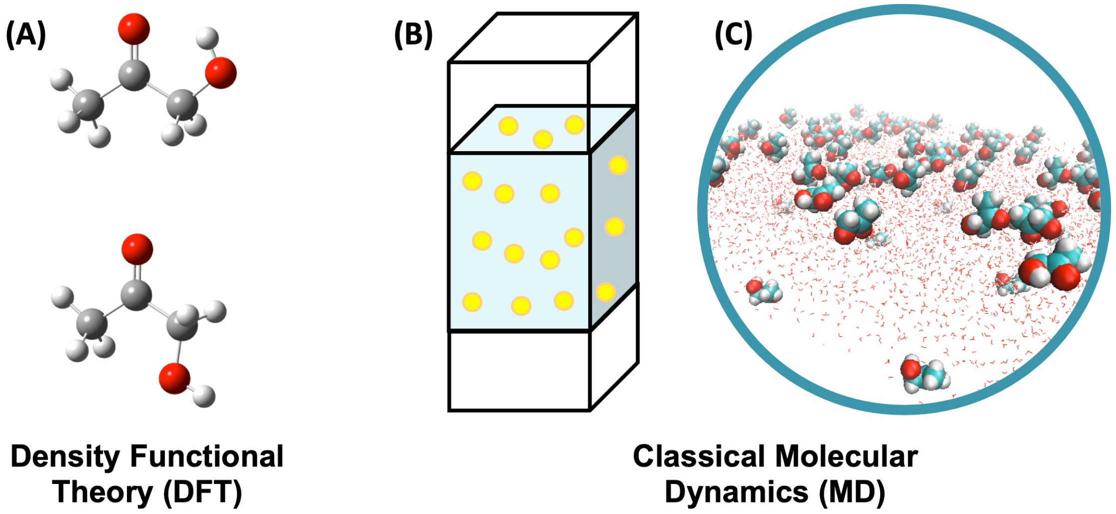

Figure 2.3. Computational Methods: (A) DFT point structures for two conformations of hydroxyacetone. (B) Depiction of MD simulation box consisting of organics (yellow spheres) dissolved in a water slab with two air-water interfaces. representing organics. (C) Graphical representation of MD Simulation coordinates for 16 Hydroxyacetone (~1M HA) in a 30 Å × 30 Å × 30 Å box with 900 H_2O (at 300 K.)

system. This methodology is ideal because it is both computational efficient for the systems of interest and highly adaptable. This approach has been shown to be robust for numerous and varied chemical systems when compared with experimental spectra.[8-16]

Classical Methods: DFT

Classical MD calculations are performed with the Amber 12 suite[19] of programs on systems of small organic molecules at varying concentrations. Water was simulated using the POL3 model.[20] The organics are parameterized using values from the Amber FF02EP polarizable force field[21] and charges are scaled using RESP fitting.[22]

Starting configurations are created using the PACKMOL program.[23] Generally, boxes are 30 x 30 x 30 Å and contain 900 water molecules in addition to the organics. An air-water interface is simulated by extending one of the box dimensions to 120 Å and applying periodic boundary conditions, creating a water slab with two surfaces.

Energy minimization is performed using conjugate gradient and steepest descent methods at 0 K followed by a 2 ns equilibration to bring the system to 298 K. The minimized systems are furthered evolved for 50 ns at 298 K with a 1 fs time step. Atomic coordinates are recorded every 100 fs, resulting in 500,000 data points.

Quantum Mechanical Methods: DFT

Density functional theory (DFT) calculations are performed using the B3LYP exchange-correlation functional and a 6-311++G(2d,2p) basis set in the NWchem[24] and Gaussian 09[25] program packages. Full geometry optimization and frequency calculations, as well as polarizabilities and dipole moments at displaced geometries along each normal mode, are performed for all reasonable gas phase conformers. Second-order vibrational perturbation theory is used to calculate anharmonic corrections to vibrational frequencies.

Generating VSF spectra requires the second-order susceptibility tensor for all major conformations and orientations sampled in a dynamical interfacial system. Thus, for each normal mode of each HA conformer, the polarizabilities and dipole moment derivatives were calculated using three-point finite differentiation and combined according to Equation (2.5) to approximate the second-order linear susceptibility response tensor.

$$!^{(!)}_{!"\#} \propto \sum_{!,!,!} !_{!"\#} \frac{!!_{!"}}{!!_{!}} \frac{!!_{!}}{!!_{!}} \qquad (2.5)$$

Here, α is the molecular polarizability, μ is the dipole moment, Q_q, is the normal coordinate of the mode q, and C is a geometrical factor relating the molecular and laboratory reference frames.

Using an in-house code,[97] VSF intensities and phases were then calculated by inspecting the second-order susceptibility tensor and assigning the static gas phase DFT structures with the molecular orientations and conformations populated in the MD simulations. The calculated intensities were empirically broadened using Lorentzian and Gaussian widths informed by the experimental VSF spectral fits.

Computational Analysis: In-House Full Analysis (FAS) Code

Generally speaking, there are three primary methods for calculating the second-order susceptibility tensor which differ in the approximations made that make the calculations feasible.[26-29] The methodology used by the Richmond lab involves assigning conformers found in the MD simulations to gas phase DFT structures and using an in-house code developed by Dr. Nick Valley[29] to calculate the tensor. In addition to simulating spectra, the analysis also extrapolates structural details about the system, such as density profiles, as well as depth-resolved orientation and conformation information, which are vital in helping to understand the behavior of the system. This methodology is ideal because it is both computational efficient for the systems of interest and highly adaptable. This approach has been shown to be robust for numerous and varied chemical systems when compared with experimental spectra.[29-31]

CHAPTER III

NEAT WATER AT THE AIR-WATER INTERFACE

The contents of this chapter have been or are intended to be published in whole or in part. The text presented here has been modified from the publication below:

Gordon, B. P., Wren, S. N., Moore, F. G., Scatena, L. F., Richmond, G. L. Diol it up: The Influence of NaCl on Methylglyoxal Surface Adsorption and Hydration State at the Air-Water Interface. **To be submitted to Journal of Physical Chemistry A in December 2019*

The VSF spectrum of neat water has been extensively studies in the previous decades, in the literature.[1-9] While a few outstanding questions remain,[8, 10-12] these efforts have yielded a general consensus on the resonances giving rise to the OH stretching region of neat water. Ranging from 3200 - 3700 cm^{-1}, contributions from more- and less-coordinated water at occur at the low to high frequency ranges of this region, respectively. At the air-water interface, modes from non-hydrogen bonded “free” OH oscillators occur at ~3700 cm^{-1}. This is most apparent in the *ssp* polarization scheme, where a sharp, well-defined peak creates a characteristic spectrum (Fig. 3.1B). Resonances arising from OH stretching modes in a continuum of hydrogen bonded states and environments occur at lower frequencies, producing a very broad feature from
~3200-3600 cm^{-1}.

VSF studies of the bending region of water are still relatively young in the *ssp* polarization [13-15] and has yet to be reported in the *sps* polarization (Figures 3.1A and C, respectively). As such, this region is less well understood and is an active area of research in the community. While the overall line shape of *ssp* polarized water-bending region has been well established, [16-17] the specific underlying contributions and interference that contribute intensity in this region are complex and still being determined.

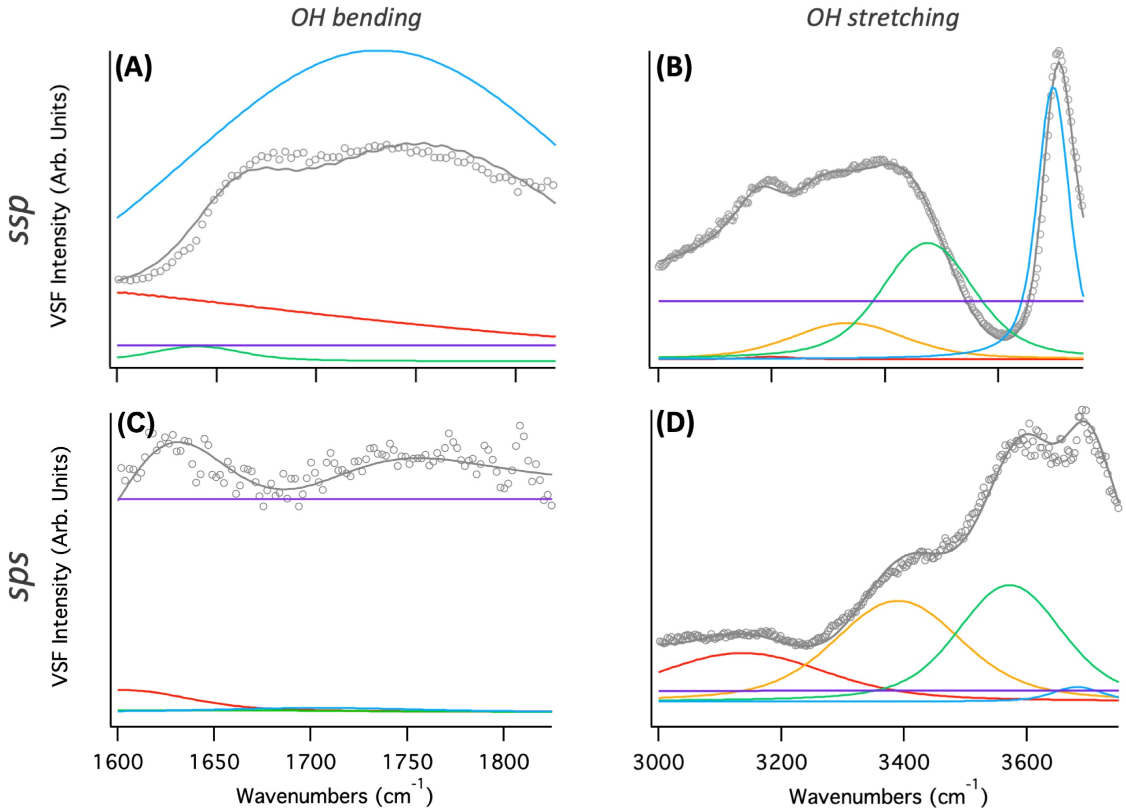

Figure 3.1. VSF spectra of neat water: VSF Experimental data (open circles) and corresponding fits (solid lines) for neat water in the *ssp* (A,B) and *sps* (C,D) polarization schemes for the HOH bending region (left) and the OH stretching region (right). Colored traces correspond to fit contributions from individual resonances.

In brief, spectral contributions are thought to be composed of contributions from HOH bending modes at ~1640 cm^{-1} (from water in a continuum of solvation environments) interfering with an underlying low intensity broad librational overtone centered around ~1440 cm^{-1}.[15, 18] Persistent intensity is observed above > 1700 cm^{-1} where the background fails to return to zero. Though this has been attributed the bending modes of more coordinated water, is currently thought to be an interference effect. [16]

The *ssp* results obtained here show excellent agreement with reported spectra, [13-17] facilitating identification of oriented water at the air-water interface. Notably, our *sps* bending spectrum of water does show apparent features, which were fit to plausible frequency positions. However, due to the low signal-to-noise ratio and lack of literature precedent, these fits of the *sps* bending spectrum remain highly tentative. Data tables of VSF fits are supplied in Appendix A Tables A1 and A2.

CHAPTER IV

METHYLGLYOXAL AT THE AIR-WATER INTERFACE

The contents of this chapter have been previously published in whole or in part. The text presented here has been modified from the publication below:

Wren, S. N., Gordon, B. P., Valley, N. A., McWilliams, L. E., Richmond, G. L. Hydration, Orientation, and Conformation of Methylglyoxal at the Air-Water Interface. *J. Phys. Chem. A* **2015** *119* (24), 6391-6403

Bridge

Aqueous-phase processing of methylglyoxal (MG) has been suggested to constitute an important source of secondary organic aerosol (SOA). The uptake of MG to aqueous particles is higher than expected due to the fact that its carbonyl moieties can hydrate to form geminal diols, as well as the fact that MG and its hydration products can undergo aldol condensation reactions to form larger oligomers in solution. MG is known to be surface active but an improved description of its surface behavior is crucial to understanding MG-SOA formation. These studies investigate MG adsorption, focusing on its hydration state at the air-water interface, using a combined experimental and theoretical approach that involves vibrational sum frequency (VSF) spectroscopy, molecular dynamics simulations, and density functional theory calculations. Together, the experimental and theoretical data show that MG exists predominantly in a singly hydrated state (diol) at the interface, with a higher diol-tetrol ratio at the surface than that for the bulk. In addition to exhibiting a strong surface activity, we find that MG significantly perturbs the water structure at the interface. The results have implications for understanding the atmospheric fate of methylglyoxal.

Methylglyoxal at the neat air-water interface was the first system studied in this project. The complexities revealed in the coarse of this work determined the direction of going forward. Additionally, significant improvements were made to the picosecond laser system after the publication of this work. The vast improvements in spectral signal revealed features previously buried in the noise and later prompted retreatment and reinterpretation, as will be discussed further in Chapter VIII. Nonetheless, this initial treatment of neat-MG in its published form has been included to provide context about the state of affairs that necessitated the subsequent work.

Introduction

Atmospheric aerosols play an important role in influencing climate (both directly, by scattering incident radiation and indirectly, by influencing cloud properties), human health, and air quality. Understanding of the formation and subsequent processing of atmospheric aerosol, particularly secondary organic aerosol (SOA) remains relatively poor. The 'traditional' SOA mechanism based on the reversible gas-particle partitioning of non- and semi-volatile species[1-3] tends to grossly underestimate the magnitude and variability of SOA in the atmosphere.[4-8] Increasingly it is being recognized that aqueous phase processing of water soluble atmospheric organics – particularly the α-dicarbonyl compounds glyoxal and methylglyoxal – could constitute a hitherto 'missing' SOA source.[9-12] In fact recent modeling studies[11-12] suggest that aqueous phase processing of glyoxal and methylglyoxal could contribute an additional global SOA source similar in magnitude to that obtained by the ‘traditional’ SOA mechanism. However, a better description of the interfacial behavior of these species is required in order to accurately predict and model their atmospheric fate and SOA-forming potential. In this study, we investigate the surface adsorption of methylglyoxal, focusing on its hydration state at the interface.

Glyoxal (GL) and methylglyoxal (MG) –gas phase oxidation products of both biogenic and anthropogenic precursors[11] – are semi-volatile and hence can be taken up by aerosol, fog, and cloud water.[13-14] In the aqueous phase, subsequent oxidation[15-18] and oligomerization[19-37] (e.g., aldol condensation, acetal formation) leads to the formation of low-volatility, high molecular weight and/or highly oxygenated products, thereby increasing SOA mass. Several studies indicate that these oligomeric products remain in the particle phase even after water evaporation.[33-34, 37-38] Self- and/or cross-oligomerization has been shown to be accelerated by drying[34-35, 37, 39] and catalyzed by strong acids,[28, 40-42] amines,[8, 22, 25, 31-32, 34-35] ammonium sulfate,[22-23, 26-27, 43-44] and carbonate salts.[26, 45]

Aqueous phase processing of organics significantly perturbs climate-relevant aerosol properties. The addition of hygroscopic mass results in an increase in particle size and thus influences both the direct and indirect climate effect of aerosols.[12] Moreover, studies[19-21, 26-28, 39, 46-48] have shown that oligomerization reactions involving glyoxal and methylglyoxal lead to the formation of light-absorbing species (e.g., C-N containing compounds such as imidazoles), depending on the identity and presence of a surrounding organic matrix.[49] This formation of ‘brown carbon’ has important climate consequences since it perturbs aerosol radiative properties.[47] Despite the importance of aqueous phase processing of glyoxal and methylglyoxal, many aspects of this chemistry remain uncertain. In particular, measured concentrations of glyoxal and methylglyoxal in inorganic aerosol are higher than those estimated based on bulk Henry's law coefficients and the reasons for this enhanced uptake are not fully understood.[12, 31, 50-51]

The focus of the current study is methylglyoxal, since both the parent compound and its oligomerization products have been found[19] to be surface active. This surface activity has significant implications for aerosol processing and properties. For instance, Romakkaniemi et al.[52] have shown that the uptake of methylglyoxal to submicron-sized particles is enhanced by more than an order of magnitude when surface partitioning is taken into account. This is due to the fact that gas-to-particle partitioning based on Henry's law uptake is governed by bulk concentrations, which are effectively lowered by surface partitioning. In addition, surface tension depression due to surface active species, as well as bulk-to-surface partitioning, may influence a particle's ability to act as cloud condensation nuclei (CCN). [53-56] Although model calculations indicate that particle concentrations of methylglyoxal and its reaction products may be too low for surface tension depression to influence cloud droplet activation,[46, 52] Sareen et al.[57] have observed that methylglyoxal uptake to ammonium sulfate seed aerosols results in enhanced CCN activity. The authors suggest that the surface-adsorbed organic species induce changes to the CCN activity, primarily by altering the properties (e.g., hygroscopicity) of the particle's surface. In addition, organic surface films may act as a kinetic barrier to gas- aerosol mass transport and thereby influence particle equilibration and water/gas uptake.[58] The possibility of surface reactions contributing to aqueous SOA formation has also been suggested.[9, 12] Consequently, there has been a recent demand[9] for laboratory studies that address (a) the relative role of surface and bulk processes and (b) the role of surfactants in aqueous SOA formation. Therefore, in this study, we endeavour to develop a fundamental understanding of methylglyoxal adsorption to the air-water interface. Results will serve as a foundation for future investigations into methylglyoxal surface behavior in more complex matrices.

Methylglyoxal Hydration

Critical to both the particle uptake and subsequent processing of methylglyoxal is its multi-step hydration to form gem-diols. Unhydrated methylglyoxal (MGM = methylglyoxal monomer) hydrates favorably at the aldehydic carbonyl (i.e., the α- carbon) to form the monohydrate (MGD = methylglyoxal diol) with a reported barrier ($\Delta G^{\ddagger}$) of +20.3 kcal mol^{-1} and an overall free energy change (ΔG) of -1.4 kcal mol^{-1} (note, the $\Delta G^{\ddagger}$ and ΔG are +24.1 and +2.5 kcal mol^{-1} respectively for hydration at the ketonic group)[59] The monohydrate undergoes a second hydration at the ketonic group (i.e., the β-carbon) to form the dihydrate (MGT = methylglyoxal tetrol) with a reported barrier ($\Delta G^{\ddagger}$) of +25.9 kcal mol^{-1} and an overall free energy change (ΔG) of +2.7 kcal mol^{-1} (or +1.3 kcal mol^{-1} relative to the unhydrated species).[59]

The substantial reaction barriers of these hydrolysis reactions can be overcome by acid catalysis,[60] with the acids facilitating the intermolecular hydrogen transfer. Hazra et al. have recently shown that atmospheric acids can catalyze gem-diol formation even under water restricted environments.[61]

Since the hydrated forms of GL and MG have lower vapor pressures, hydrate formation enhances their effective Henry's law coefficients; however, this effect on its own cannot account for their higher than expected particle concentrations.[12, 23] Chemical environments that shift the hydration equilibria toward more hydrated forms have the potential to further enhance the effective Henry's law coefficients. For example, in the case of glyoxal, it has been suggested that enhanced partitioning of glyoxal to ammonium sulfate aerosol can be attributed, in part, to a shift towards more hydrated structures (due to stabilization of hydrated glyoxal by sulfate ions).[23] Furthermore, the hydration equilibria of methylglyoxal are critical to its reactive pathways since it is the singly hydrated form (MGD) that contains a reactive carbonyl moiety.[37] MGD can react via self- aldol condensation via two routes, depending on the location of enol formation.[19] The two-step dehydration is also key to methylglyoxal's fate when cloud droplets evaporate: dehydration to the monohydrate is thought to trigger oligomerization, thereby trapping a large fraction of MG in the particle phase.[33, 37]

In bulk aqueous solution, methylglyoxal has been found experimentally to exist predominantly in its diol form with the ratio MGD/MGT ~ 1.5,[33, 62] consistent with thermodynamic calculations.[59] However, since methylglyoxal is surface active, knowledge of its hydration state at the *surface* is required in order to understand its fate and therefore its potential to form SOA. This study investigates methylglyoxal at the air- aqueous interface, with a particular focus on elucidating its hydration state there. A combination of surface-selective vibrational sum frequency spectroscopy, surface tensiometry, and computational methods provides a molecular-level picture of methylglyoxal behavior at the air-aqueous interface.

Experimental and Theoretical Methods

Vibrational Sum Frequency Theory

Vibrational sum frequency (VSF) spectroscopy has been used extensively for the study of water surfaces.[63-68] A brief description of the theory behind VSF spectroscopy is provided as it pertains to the experiments presented herein.[69] A fixed-frequency visible beam (800 nm) and tunable-frequency IR beam are overlapped in time and space at an aqueous surface, producing a third beam at the sum of the incident frequencies. The intensity of the sum frequency (SF) signal is proportional to the absolute square of the second-order susceptibility, $\chi^{(2)}$, which has both resonant and non-resonant components:

$$!^{(!)} = !^{(!)}_{!''} + \sum\nolimits_{!} !^{(!)}_{!,!} \tag{4.1}$$

Both components are proportional to the number of molecules, *N*, contributing to the sum frequency response and the orientational average of the molecular susceptibility, ⟨*β*⟩:

$$!^{(!)}_{!} = \frac{!}{!_{!}}\langle !_{!} \rangle \tag{4.2}$$

Hence via Eq. 4.2 the VSF response yields information about the *population* and *orientation* of surface-adsorbed species. VSF spectra are fit to deconvolve the nonresonant background and the individual resonant vibrational modes using:

$$!^{(!)} = !^{(!)}_{!''} !^{!!} + \sum\nolimits_{!} \int_{!!}^{!} \frac{!_{!}! \, !^{!''!\ !(!\ !!!/!^{!})^{!}}}{!_{!}!!_{!''}!!!_{!}} \, !!_{!} \tag{4.3}$$

The first term is the nonresonant susceptibility (described by an amplitude and phase, ψ). The second term is the sum over all VSF active resonant vibrational modes. The resonant susceptibility is fit as a convolution of homogeneous line widths of the individual molecular transitions (Γ_L) and inhomogeneous broadening (Γ_v).[70] The transition strength, Av, is proportional to the orientational average of the IR and Raman transition probabilities as well as the number of contributing molecules. The frequencies of the Lorentzian, resonant modes, and IR are ω_L, ω_v, and $\omega_{IR,}$ respectively. The phase of each resonant mode is φ_v. In this work, fixed Lorentzian widths of 2 cm^{-1}, 5 cm^{-1} and 12 cm^{-1} are used for the CH, both coordinated OH and C=O, and 'free' OH modes respectively.

Laser System

A schematic of the laser system is shown in Supporting Figure S1. Results obtained using this newly-assembled picosecond system are published here for the first time. Briefly, the system consists of a modelocked Ti:Sapphire laser in tandem with an ultrafast regenerative amplifier to produce a fixed visible (800 nm) beam. A portion of the visible beam is sent to an optical parametric amplifier (OPA) in tandem with a difference frequency generator (DFG) for mixing and IR generation.

The visible and IR beams are directed to the air-water interface in a copropagating geometry at 63° and 55° relative to the surface normal respectively for the CH/OH stretching region experiments, and at 45˚ and 60˚ respectively for the C=O stretching region experiments. The SF beam leaving the interface is detected using a thermoelectrically cooled CCD camera. The aqueous samples are held in scrupulously clean, shallow glass dishes on a vertically translatable stage. Full details of the experimental set-up can be found in the Appendix B.

Spectral Analysis

VSF spectra were acquired by measuring the intensity of the SF light as the IR frequency was scanned in 3 cm^{-1} increments over the relevant spectral range (~2700 – 4000 cm^{-1} for the CH/OH stretching region, ~ 1650 – 1900 cm^{-1} for the C=O stretching region). The spectra presented here were obtained using either the *ssp* or *sps* polarization schemes in which the three letters denote the polarizations of the SF, visible, and IR beams respectively. Changing the polarization scheme from *ssp* to *sps* allows us to compare vibrational contributions resulting from dipole components that are perpendicular or parallel to the interface, respectively. Sum frequency intensities were normalized to account for the frequency dependence of (a) the spatial overlap of the visible and IR beams; (b) the timing and energy of the IR pulses reaching the sample (which are influenced by the tuning curve of the OPA/DFG as well as interactions with ambient water vapor); and (c) the detection line optics used to collect the SF light. In these experiments, VSF spectra were normalized to the nonresonant response from an uncoated gold surface. IR frequencies were calibrated daily against a polystyrene standard. All measurements were made at ambient temperature ~ 20°C. Presented spectra are averages of 3 – 10 spectra acquired over a minimum of three days to ensure reproducibility and to reduce the signal-to-noise ratio. Daily spectra of the neat air-water interface were taken to ensure that the VSF response was comparable for each sample.

Surface Tension

Surface tension measurements were performed using the Wilhelmy plate method. Solutions were placed in a clean glass dish and a Pt plate was subsequently lowered to the air-water interface; great care was taken to ensure that the plate was correctly oriented with respect to the solution surface. A force balance (KSV Instruments) measuring the force acting on the Pt plate was used to measure surface tension (mN/m) as a function of time (s). Surface tensions (γ) were converted to surface pressures (π) by subtracting the daily-measured surface tension of neat water. The Pt pate was cleaned under flame until glowing orange and then rinsed repeatedly in 18.2 MΩ water between measurements.

Sample Preparation

Aqueous MG solutions (0 – 2M) were prepared volumetrically by diluting MG stock solution (40 wt% in H_2O, Sigma Aldrich) in nanopure water. Solutions were stored in Pyrex flasks and not further protected since photochemical degradation was not a concern for these experiments.[19] Solutions were prepared ≥ 24h before use unless otherwise stated. MG stock solution is known to contain trace pyruvic acid and hydroxyacetone impurities.[33] The prepared MG solutions were therefore acidic due to the fact that pyruvic acid is a strong acid (pKa ~ 2.5).[19] The bulk pH of an aqueous 0.50 M MG solution was measured with a commercial pH electrode to be ~ 2.6. This corresponds to a pyruvic acid concentration of less than 5×10^{-3} M (or < 1%). Since a low pH is consistent with the low pH of atmospheric SOA, the bulk pH of the aqueous MG solutions was not further adjusted. The possible, but unobserved, impact of acidity on the VSF spectra is discussed in the Supporting Information.

Computational Methods

Classical Molecular Dynamics

Classical molecular dynamics (MD) simulations of various MG species were performed to (a) gain insight into their surface behavior and (b) provide orientational and conformational information required to calculate VSF spectra. Simulations were performed using the Amber 12 suite of programs[71] using parameters and force fields derived in the same manner as in previous studies.[72-75] The MD simulations contained 1, 6, 10, 16 or 20 molecules of the target MG species along with 900 water molecules in a 30 Å cube, corresponding to total concentrations of roughly 0.06, 0.4, 0.6, 1.0 and 1.2 M respectively. A water slab with two surfaces was created by expanding one of the box dimensions to 120 Å and applying periodic boundary conditions. The interface is defined here by the Gibbs dividing surface; distances are reported relative to the interface. Data were collected for both water-vacuum interfaces, and bond angles are reported relative to the surface normal pointing into the vacuum phase. Starting configurations were created using PACKMOL.[76]

Simulations were performed on 'pure' systems, which contained exclusively MGM, MGD, or MGT in water. In this study, MGD represents the energetically favorable diol formed via hydration at the aldehydic carbon. The diol formed via hydration at the ketone was not considered due to the fact that this reaction has been calculated[59] to have a $\Delta G^\circ$of +2.5 kcal mol^{-1} and should contribute <1%. One 'mixed' system containing 10 MGD molecules and 6 MGT molecules (total of 16 molecules or ~1 M, with MGD/MGT ~1.7) was also simulated in order to (a) mimic the literature bulk composition (MGD/MGT ~1.5) and (b) test for possible interactions between MG species. It should be emphasized that these systems were not reactive.

Energy minimization of the initial system at 0 K was performed using a combination of steepest-descent and conjugate-gradients methods. Minimized structures were equilibrated by evolution through 2 ns of simulation from 0 K to 298 K. Each system was further evolved at 298 K in 1 fs time steps for a total of 50 ns, with atomic coordinates for analysis recorded every 100 fs. Results from the MD simulations (density profiles, angle distributions, conformer distributions etc.) were found to be independent of concentration and hence the remaining discussion focuses on simulations which contained a total of 16 molecules (~ 1 M). As well, the overall behaviors of MGD and MGT in the mixed system were not found to differ from their behaviors in the pure systems.

Quantum Mechanical Calculations

The calculations presented in this work were performed employing the NWChem[77] and Gaussian 09[78] program packages using the B3LYP exchange-correlation functional and a 6-311++G(2d,2p) basis set. Full geometry optimization and harmonic vibrational frequency calculations were performed for isolated gas phase MG species. Anharmonic corrections to vibrational frequencies were obtained by second-order vibrational perturbation theory. Energies and important dihedral angles for all structures can be found in Appendix B Table B1. Polarizabilities and dipole moment derivatives were calculated using three-point finite differentiation and combined to generate the second-order susceptibility according to:

$$!^{(!)}_{!''\#} \propto \sum_{!,!,!} !_{!''\#} \frac{!\,!_{!''}\;!\,!_{!}}{!\,!_{!}!\,!\;_{!}} \tag{4.4}$$

Where α is the molecular polarizability, μ is the dipole moment, Q_q, is the normal coordinate of the mode q, and C is a geometrical factor relating the molecular and laboratory reference frames. In-house code[72] was used to calculate vibrational sum frequency intensities by inspecting the second-order susceptibility tensor, accounting for orientations and conformations from the MD calculations as well as rotational averaging parallel to the interfacial plane. Calculated spectra were broadened using the same predetermined Lorentzian widths as the experimental spectra. Gaussian widths obtained from the fits to the experimental spectra were used to inform the broadening of the calculated spectra. Gaussian widths based on experimental fits of 40 cm^{-1} for C=O, 30 cm^{-1} for α-CH, 15 cm^{-1} for CH_3, and 80 cm^{-1} for methylglyoxal OH groups (MG-OH) were ultimately applied to the calculations.

Computational Results

Density Profiles

The bulk-to-surface partitioning of methylglyoxal is relevant to its particle uptake, as discussed in the Introduction. Understanding methylglyoxal surface activity is also required to interpret the VSF spectra. Density profiles from molecular dynamics simulations of the pure and mixed systems are displayed in Figure 4.1. The density profiles clearly show that unhydrated MG (MGM) is very surface active; methylglyoxal diol (MGD) is surface active but to a lesser degree, and methylglyoxal tetrol (MGT)

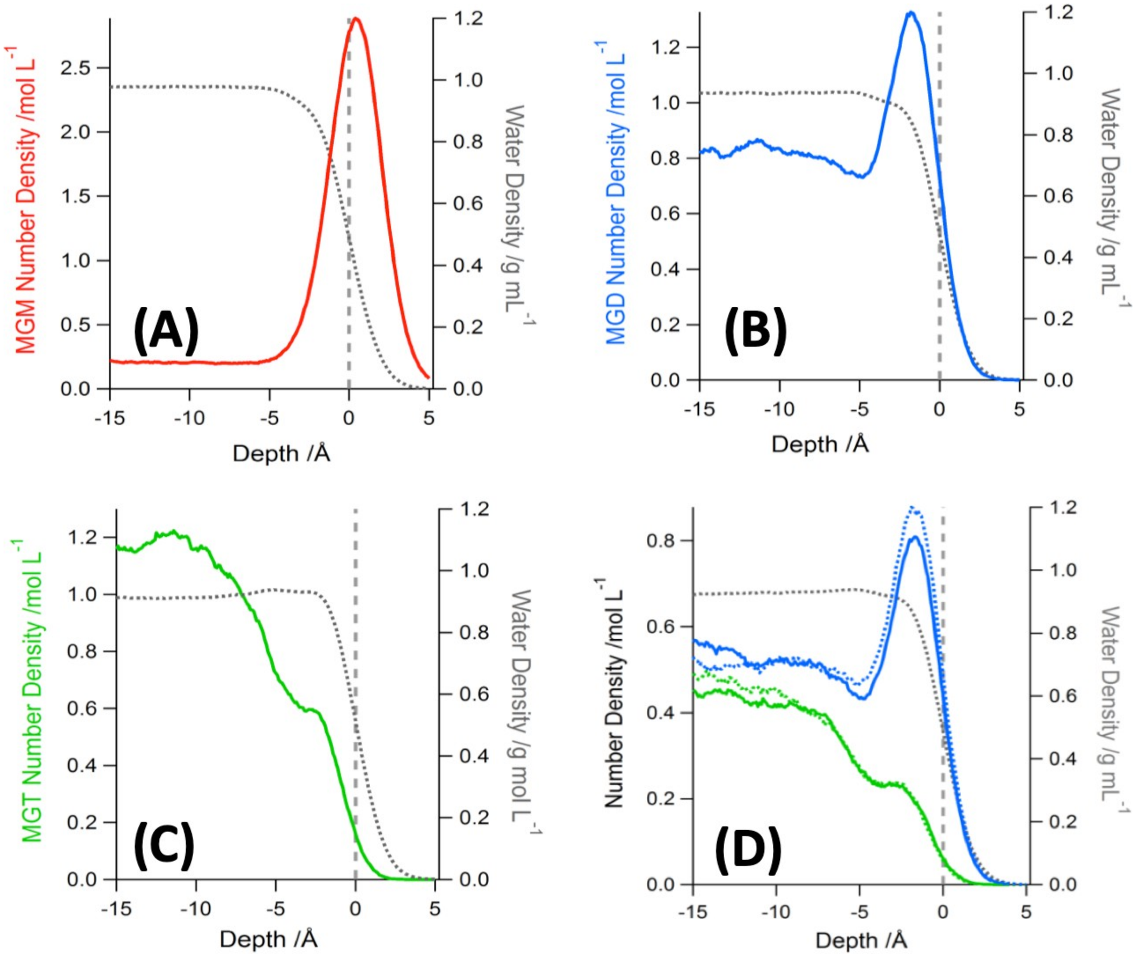

Figure 4.1. Surface partitioning of water and MG: Density profiles of water (grey, dotted line) and MG species (solid, colored line) obtained from the MD simulations with (A) 16 MGM (red), (B) 16 MGD (blue), (C) 16 MGT (green)) and (D) mixed (solid) and simulations with 10 MGD (blue) and 6 MGT (green), with pure (dashed) simulations of 10 MGD (blue) or 6 MGT (green).

prefers bulk solvation. Hence, as the degree of hydration increases, the surface activity of the MG species decreases. This result indicates that if MGM is present in the experimental systems, it should be present at the air-water interface, and perhaps detectable by VSF spectroscopy. Density profiles from the mixed system (solid traces, Figure 4.1D) illustrate that the different surface propensities of MGD and MGT lead to an enhanced MGD:MGT ratio at the air-water interface. Integration over a ±3 Å slice around the interface leads to a surface MGD/MGT ratio of 4.5, significantly higher than the accompanying bulk MGD/MGT ratio of 1.3 (note that the literature bulk ratio obtained in theoretical[59] and experimental[62] studies is 1.5).

Conformational Distributions

Calculated DFT structures for the various MG species are shown in Figure 4.2; they are denoted by a number following the species (e.g., MGM1). Conformers in the MD simulations were assigned to DFT structures based on a prescribed range of dihedral angles (Table B1 in dix B). DFT calculations show that the most energetically favorable MGM conformer has its carbonyl moieties oriented in a *trans* configuration (MGM1), consistent with previous theoretical calculations.[79-81] The *trans* to *cis* transformation was found to be effectively barrierless, but the *cis* configuration lies at much higher energies. Consequently, MGM was found to exist exclusively as MGM1 in the MD simulations.

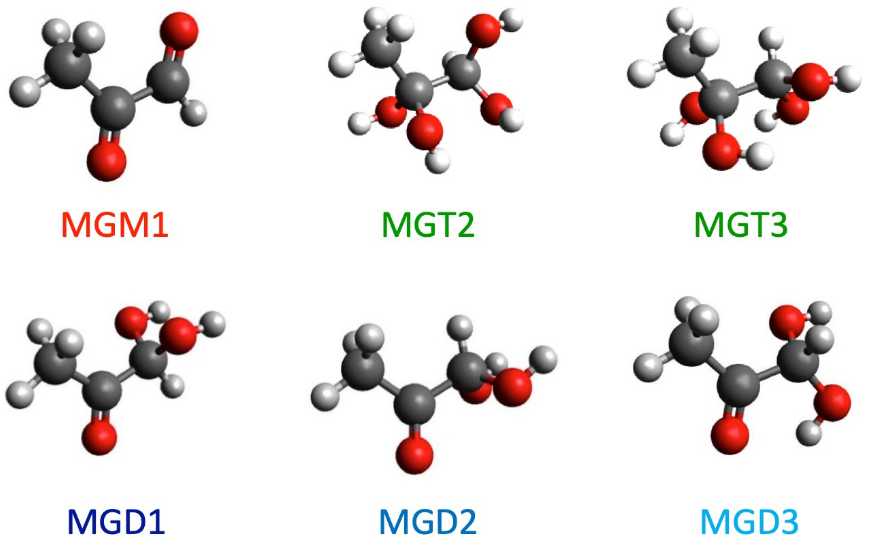

Figure 4.2. Gas phase DFT structures of MG species.

Three gas phase DFT structures were obtained for MGD. The MGD1 (α-CH bond *cis* to the C=O bond) and MGD2 (α-CH bond *trans* to the C=O bond) structures were found to be excellent matches to dominant conformers in the MD simulations. The MGD3 structure found in the DFT calculations appears to have an internal H-bond between one of the MG-OH groups and the carbonyl moiety, evidenced by the existence of a significantly red-shifted OH stretching frequency. This structure does not appear as a unique conformer in the MD simulations. Rather, conformers in transition between MGD1 and MGD2 are 'counted' as MGD3 (based on the relevant dihedrals). The overall bulk distribution of the three conformers in both the pure and mixed MD simulations is roughly 24% MGD1, 39% MGD2 and 26% MGD3 (with an additional 11% of molecules not represented by a stable DFT structure, and binned as MGD4).

The relative abundance of the three conformers varies as a function of depth from the interface as illustrated in Figure 4.3. The relative abundance of MGD2 falls off approaching the interface and is replaced by MGD1, with 34% MGD1 and 24% MGD2 at 0 Å. This is consistent with the fact that the DFT calculations show that the MGD2 structure is at a saddle-point on the gas phase potential energy surface and hence does not represent a favorable conformer in the gas phase. The larger bulk abundance of MGD2 in the MD simulations indicates more favorable solvation of MGD2 by water than the other conformers experience. Figure 4.3 clearly illustrates that the weaker solvation environment of the air-water interface impacts the relative populations of conformers. Similar impacts have previously been observed by our group via a combination of VSF spectroscopy and computational methods.[72, 74-75]

Finally, two gas phase DFT structures (MGT2, MGT3) were obtained for MGT, of roughly equal energy. In the MD simulations for both the pure and mixed systems, the dihedral between the α-CH and methyl group was found to be centered at 60˚, indicating a single minimum on the solvated energy landscape. This structure lies roughly between MGT2 and MGT3, and is represented by 52% MGT2 and 47% MGT3. Unlike with MGD, the conformation of MGT was not found to be impacted by its depth from the interface.

Surface Orientation of MGD

MD simulations containing 16 MGD (~ 1 M) were analyzed to determine the average surface orientation of MGD. MGD was selected for orientation analysis on the basis of its surface abundance, as inferred from the experimental and calculated VSF results (described below). Normalized distributions of characteristic MGD bond angles (with respect to the surface normal) are shown in Appendix B Figure B2 for bulk (-10 Å) and the surface (0 Å) species. The three bond angles analyzed are (a) the methyl group; (b) the C=O group; and (c) the βC-αC bond. The distributions show that at bulk depths, there is an isotropic distribution for all angles (i.e., no preferred orientation). At the

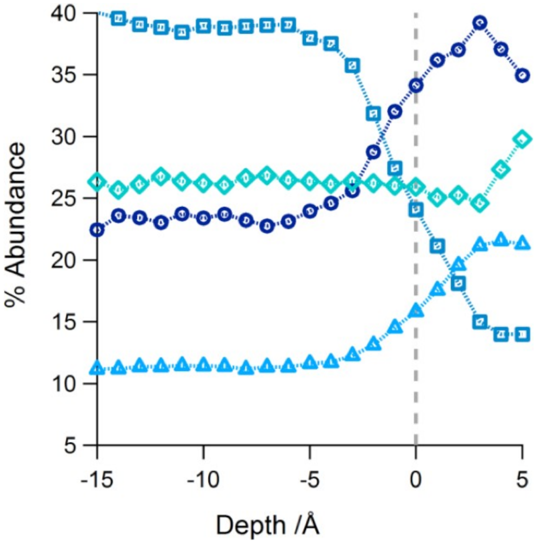

Figure 4.3. Percent abundance of the MGD conformers as a function of depth from the interface (Pure simulation with 16 MG molecules). MGD1 (circles), MGD2 (squares), MGD3 (diamonds) and MGD4 (triangles).

interface, the distributions narrow significantly, indicating a strong orientation preference with the methyl group sticking out of the interface at ~45˚, the C=O group parallel to the interface at ~90˚, and the βC-αC bond pointing toward the bulk at ~ 135˚. All MGD conformers were found to align at the interface with this orientation of the C-C-C backbone. This orientation allows for greater solvation of the geminal OH groups while permitting the hydrophobic methyl group to point away from the bulk. The αC-OH bonds show a broad angle distribution, giving rise to the various MGD conformers. MGD1 has its αC-OH groups pointing more towards the bulk, allowing for more favorable solvation than MGD2, possibly explaining its enhanced surface abundance.

Experimental Results

Surface Tensiometry

Equilibrium surface pressure data for MG in water are plotted as a function of MG concentration in Appendix B Figure B3. The surface pressure isotherm shows that methylglyoxal strongly adsorbs to the air-water interface (with a maximum surface pressure ~ 22 mN m^{-1}). Surface pressure values reported here are only slightly larger than those reported by Sareen et al.,[19] who measured methylglyoxal surface tension using pendant drop tensiometry. Maximum surface excess was calculated from the surface pressure data according to the Gibbs adsorption equation as described in Appendix B. The calculated surface excess was inverted to obtain an estimate for the minimum average area per molecule of ~73 $Å^2$ per molecule. This small molecular area corresponds to moderate packing of methylglyoxal species at the air-water interface. Surface tension measurements revealed a very slow adsorption of MG to the air water interface, with equilibrium solution values being reached after > 1 hr. VSF spectra presented below were therefore only obtained after samples had equilibrated as confirmed by invariance of spectra over time.

VSF Spectra: C=O Stretching Region

VSF spectra acquired in the C=O stretching region in the *ssp* polarization scheme are shown as a function of methylglyoxal concentration (0.10, 0.25, 0.50 M) in Figure 4.4 (#) with experimental data plotted as open symbols and the corresponding fits plotted as solid lines. The neat water spectrum is also shown in grey. Overall, the weak IR energies in this frequency region result in a much poorer signal-to-noise ratio relative to the CH/OH stretching region. VSF *sps* spectra were also acquired, but the signal-to-noise ratio was even lower for this polarization scheme. Consistent with literature[82], the water bending feature ~1660 cm^{-1} was fit to two peaks of opposite phase: a strong peak at 1642 cm^{-1} and a much weaker peak at 1753 cm^{-1}. For solutions containing MG, a broad feature appears indicating *oriented* surface adsorption of MG. This feature was fit to a strong peak at 1742 cm^{-1} and a weaker peak at 1663 cm^{-1}. The amplitude of the dominant peak at 1742 cm^{-1} increases with increasing MG concentration and is assigned to a carbonyl mode.

Only a few groups have reported C=O stretching frequencies for MG, although the techniques used have not been as surface-selective as VSF spectroscopy. Loeffler et al.[37] report the carbonyl band for singly-hydrated methylglyoxal (MGD) from ATR-FTIR experiments at 1724 cm^{-1}. Axson et al.[81] observe FTIR frequencies for gas phase MGM at

1723 cm^{-1} and 1741 cm^{-1}; they observe a new peak under higher RH% at 1780 cm^{-1} which they attribute to MGD. Unfortunately we cannot conclusively identify the species (MGM or MGD) contributing to the carbonyl peak in our spectra; however the presence of a carbonyl peak at the frequency observed here shows that methylglyoxal is not fully hydrated at the surface. The relatively high frequency of 1742 cm^{-1} is indicative of a very weakly solvated carbonyl mode.[74]

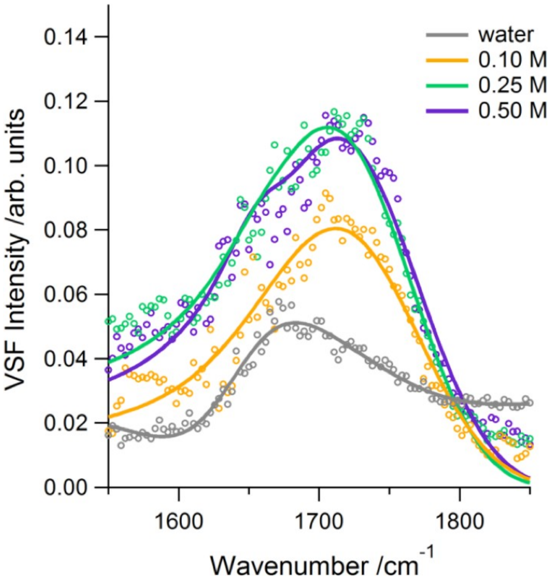

Figure 4.4. VSF ssp spectra of aqueous MG solutions in the C=O stretching region. Experimental data (open circles) and corresponding fits (solid lines) for neat water (grey) and 0.10 M (yellow), 0.25 M (green), 0.50 M (blue) and 1.00 M (purple) methylglyoxal.

The much weaker peak at 1663 cm^{-1} also increases in intensity with increasing MG concentration, appearing as a distinct shoulder in the 0.50 M spectrum. The peak at 1663 cm^{-1} is attributed to the water bend based on (a) it's similarity to the water bending frequency and (b) its absence in spectra acquired of 0.50 M methylglyoxal in D_2O (not shown). The enhancement of the water peak is also consistent with MG adsorption inducing strong orientation of the water structure, as observed for the CH/OH stretching region (see below). The blue shift in the water bending mode in the presence of MG is indicative of stronger hydrogen bonding.[82]

VSF Spectra: CH/OH Stretching Region

VSF spectra acquired in the CH/OH stretching region are shown as a function of methylglyoxal concentration (0.05, 0.10, 0.25, 0.50 M) in Figures 4.5a (*ssp* polarization scheme) and 4.5b (*sps* polarization scheme). Experimental data are plotted as open symbols and the corresponding fits are plotted as solid lines. VSF spectra of the neat air- water interface are shown in grey for each polarization scheme. Vibrational frequencies for MG obtained from global fitting to the experimental spectra are listed in Table 4.1. The uncertainty in the reported peak positions is ± 10 cm^{-1}.

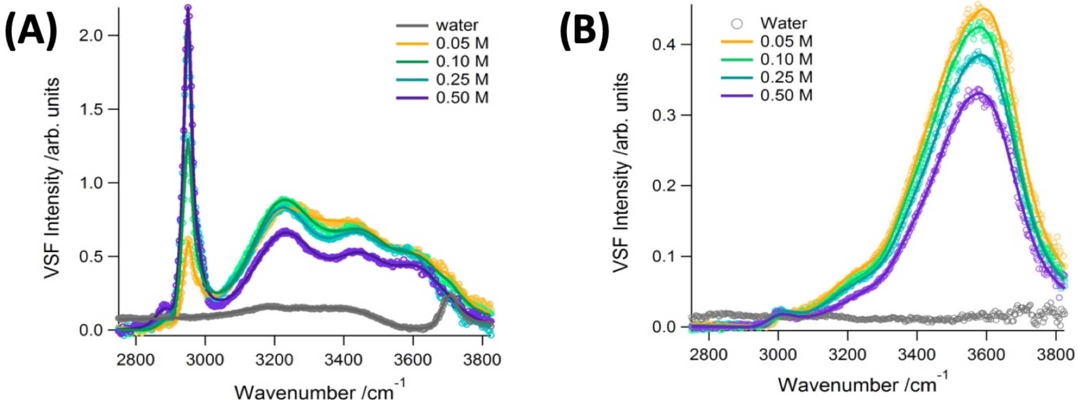

Figure 4.5 VSF ssp and sps spectra of MG in the CH/OH stretching region: VSF *ssp* (A) and *sps* (B) spectra of aqueous methylglyoxal solutions in the CH/OH stretching region. Experimental data (open circles) and corresponding fits (solid lines) for neat water (grey) and 0.05 M (yellow), 0.10 M (green), 0.25 M (blue) and 0.50 M (purple) methylglyoxal.

The VSF response from neat water has been studied extensively and the spectra presented here agree with previously reported spectra.[63-64, 67] The neat water spectrum shown in Figure 4.5A xhibits a broad feature between 3000 – 3600 cm^{-1} which is fit to peaks centered at 3205 cm^{-1}, 3320 cm^{-1} and 3560 cm^{-1} (simplistically, these modes are associated with coordinated OH oscillators in a hydrogen bonding continuum).[63] The sharp feature at ~3700 cm^{-1} corresponds to ‘free’ OH oscillators in the topmost molecular layer. The weak VSF response from neat water in the *sps* polarization scheme is as expected.[83]

Spectra of methylglyoxal solutions exhibit new features in the CH stretching region at 2800 – 3000 cm^{-1}. Global fitting over the concentration series revealed a minimum of four distinct peaks at 2891 cm^{-1}, 2936 cm^{-1}, 2949 cm^{-1} and 2972 cm^{-1} in the *ssp* polarization scheme (Figure 4.5A) and a single peak fit at 2988 cm^{-1} in the *sps* polarization scheme (Figure 4.5B). The peak at 2891 cm^{-1} is assigned to the α-CH mode of MGD; the remainder are assigned to methyl CH modes of MGD and MGT conformers. Additionally, in both *ssp* and *sps*, a very strong, broad feature appears at ~3550 cm^{-1}. This new feature can be fit to broad peaks of opposite phase: at 3544 cm^{-1} and 3540 cm^{-1} for *ssp* and at 3538 cm^{-1} and 3517 cm^{-1} for *sps*. These nascent peaks are attributed to geminal OH groups of hydrated MG species. All peak assignments are described in greater detail with the calculated VSF spectra, as discussed below.

In addition, spectra of methylglyoxal solutions exhibit increased intensity in the coordinated water region ~3200 – 3400 cm^{-1} relative to neat water. Due to the presence of water modes in this spectral region, it is difficult to decouple changes here due to water modes or MG modes. VSF *ssp* spectra obtained by Johnson et al. of aqueous acetaldehyde solutions also show enhanced intensity at ~3250 cm^{-1} relative to that of pure acetaldehyde (although reduced relative to neat water). [84] Acetaldehyde undergoes a single hydration in solution to form a gem-diol with a monohydrate fraction of ~0.7. The authors suggest that the observed broad band at ~3250 cm^{-1} could be due either to the OH stretch of the hydrogen-bonded gem-diol or to coordinated water. The influence of methylglyoxal surface adsorption on the interfacial water structure is discussed in further detail below.

Table 4.1: Fit assignments for MG. Frequencies (cm^{-1}) and assignments for peaks contributing intensity to experimental and calculated *sps* spectra. Reported experimental frequencies obtained from global fitting of the experimental spectra. The strongest peaks are shown in bold. Experimental uncertainty = ± 10 cm^{-1}

ssp Expt. Freq.	Calc. Freq.	Assignment (mode, species)	*sps* Expt. Freq.	Calc. Freq.	Assignment (mode, species)
1742	1738 1751 1752 1768 1781	αC=O, MGM1 βC=O, MGD1 βC=O, MGD3 βC=O, MGM1 βC=O, MGD2	-	-	-
2891	2777 **2860** **2870**	ald-CH, MGM1 α-CH, MGD2 α-CH, MGD3	*	2777 2834 2860 2870	ald-CH, MGM α-CH, MGT3 α-CH, MGD2 α-CH, MGD3
2936, 2949	2929 **2932** **2938** 2941	CH_3-SS, MGD2 **CH_3-SS, MGD1** **CH_3-SS, MGD2** α-CH, MGT2	*	2940 2942 2969 2970 2973	CH_3-AS, MGD2 CH_3-AS, MGM1 CH_3-AS, MGT2 CH_3-SS, MGT2 CH_3-AS, MGT3
2972	2969 **2970** 2981	CH_3-AS, MGT2 **CH_3-SS, MGT2** CH_3-SS, MGT3	2988	2998 2997 **3000** 3000	CH_3-OOP, MGM1 CH_3-OOP, MGD3 **CH_3-OOP, MGD1** CH_3-OOP, MGD2
3540, 3544	3460 3633 **3646** 3667	MG-OH, MGD3 MG-OH, MGD3 **MG-OH, MGD1** MG-OH, MGD2	3517, 3538	3633 **3647** 3667	MG-OH, MGD3 **MG-OH, MGD1** MG-OH, MGD2

* Not Observed

Experimental Versus Calculated VSF Spectra

VSF spectra were calculated in order to assist in interpreting the experimental spectra and to determine the hydration state of MG at the air-water interface. The calculated spectra for the pure systems are shown in Figure 4.6a and 4.6b for the CH

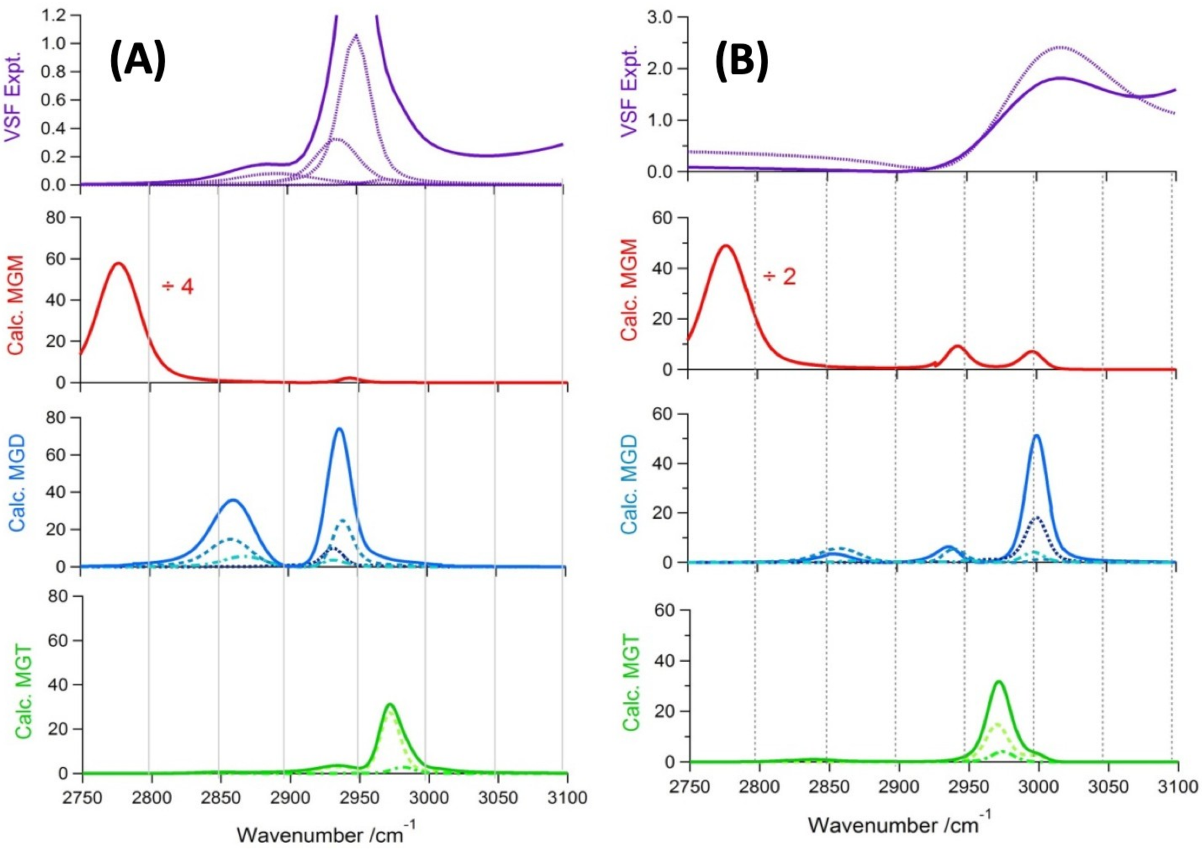

Figure 4.6. Experimental vs. calculated VSF MG spectra Comparison of experimental vs. calculated VSF *ssp* (A) and *sps* (B) spectra. Overall fit (solid) and contributing peaks (dashed) to the 0.5 M experimental spectrum (purple, 1st row). Overall (solid) and individual conformer (dashed) calculated spectra for MGM (red, 2nd row), MGD (blue, 3rd row) and MGT (green, 4th row) from pure simulations with 16 MG molecules. Calculated MGM spectra have been scaled as shown for ease of comparison.

stretching region in the *ssp* and *sps* polarization combinations respectively. For each, the top panel shows the overall fit and the contributing peaks to the experimental data (0.50 M MG). The calculated anharmonic frequencies (ω_v) and assignments for modes that contribute substantial intensity to the calculated spectra are listed in Table 4.1. In comparing the calculated and experimental spectra, note that contributions from water are not included in the calculated spectra. Intensities of CH peaks may be affected by neglecting intensity contributions from nearby water modes, and vibrational frequencies do not account for effects of solvation. The analysis here focuses on the CH stretching region, where calculated spectra have shown[72] good agreement with experimental spectra for methyl and methylene modes, since these modes are negligibly influenced by water solvation. Additionally, the fits to the experimental spectra include the minimum number of phenomenologically appropriate peaks that are necessary to obtain a reasonable fit.

The experimental *ssp* spectrum is dominated by a main peak which is a convolution of peaks at 2936 cm^{-1} and 2949 cm^{-1} and the *sps* spectrum is dominated by a single peak at 2988 cm^{-1}. By comparison, the calculated MGM *ssp* and *sps* spectra are in very poor agreement with the experimental result, both dominated by a strong peak at 2777 cm^{-1} corresponding to the aldehydic CH stretch (ald-CH). Previously measured[79-81] or calculated[79, 81] frequencies for the ald-CH stretch of MGM are also significantly lower than the experimentally observed peak, lying in the range 2811 – 2850 cm^{-1}. From, the gross mismatch between the experimental and calculated spectra, we conclude that MGM has a negligible presence at the interface.

Here, we argue that the chief interfacial species is, in fact, MGD. The agreement between the calculated MGD *ssp* spectrum and the experimental *ssp* spectrum is significantly better than for MGM (or MGT): the dominant experimental peak is very well matched by the higher frequency peak in the calculated MGD *ssp* spectrum, which has strong contributions from the methyl symmetric stretch (CH_3-SS). All three MGD conformers contribute to its overall intensity, with similar contributions from MGD2 (2938 cm^{-1}) and MGD1 (2932 cm^{-1}) and a weaker contribution from MGD3 (2929 cm^{-1}). The lower frequency peak in the calculated spectrum is attributed to the α-CH stretch, with contributions from both MGD2 (2860 cm^{-1}) and MGD3 (2870 cm^{-1}). These frequencies are only slightly lower than the experimental shoulder, which is fit at 2891

cm^{-1}. Axson et al.[81] measured (via FTIR) and calculated (B3LYP/6-31+G(d,p)) the α-CH stretch of MGD to be 2895 cm^{-1} and 2838 cm^{-1} respectively, with both values in good agreement with this study. Similarly, the calculated MGD *sps* spectrum is the best match to the experimental *sps* spectrum. Weak signals from α-CH and methyl asymmetric stretch (CH_3-AS) modes, likely below experimental limits of detection, are predicted at lower frequencies. The dominating feature in the calculated MGD *sps* spectrum is due to the symmetric out-of-plane methyl stretch (CH_3-OOP) of MGD1 (3000 cm^{-1}) and is in good agreement with the experimental fit.

We find that the calculated MGT *ssp* spectrum is a poorer match to the experiment and calculated intensities are relatively weak due to its low surface affinity. However, the high frequency peak in the calculated MGT *ssp* spectrum at ~2970 cm^{-1} (primarily due to the CH_3-SS of MGT2) could account for the very weak shoulder in the experimental spectrum at 2972 cm^{-1}. The calculated MGT *sps* spectrum is dominated by a peak at ~2970 cm^{-1} with contributions from the CH_3-AS of MGT2 (2969 cm^{-1}) and MGT3 (2973 cm^{-1}). To our knowledge, no calculated or experimental frequencies for MGT exist in the literature.

Taking solvation into account, we would expect the α-CH stretch to shift to higher frequencies. In fact Mucha and Mielke[80] calculated (MP2/6-311++G(2d,2p)) vibrational frequencies for MGM/H_2O/Ar complexes and found that the ald-CH stretch shifts to higher frequencies relative to the monomer due to shortening of the CH bond (experimentally they observed a shift of approx. +30 cm^{-1}). A shift of similar magnitude is not sufficient to bring the calculated MGM *ssp* spectrum into agreement with the experimental spectrum but could improve the agreement in the case of the calculated

MGD *ssp* spectrum. In the same study the authors found that the bond lengths of the methyl CH are unchanged for the various water complexes, further supporting our conclusion that methyl modes are less influenced by solvation, validating our focus on these modes.

Simulations of Mixed MGD and MGT

The calculated spectra for the mixed system containing 10 MGD and 6 MGT (overall MGD/MGT ~1.7) are shown in Figures 4.7A and 4.7B with the experimental spectra for the CH stretching region in the *ssp* and *sps* polarization combinations respectively. The composite spectrum is shown in black and the overall contributions from MGD and MGT (i.e., from all conformers) are shown in blue and green respectively. This approach gave similar results to spectra calculated by combining results from 'pure' systems of 10 MGD and 6 MGT molecules. The composite spectra for the 'mixed' system provide the closest match to the experimental spectra. For the *ssp* spectra, the small contribution from MGT results in an increase in intensity of the dominant peak ~2940 cm^{-1}, bringing it further into agreement with experiment. The composite spectrum also better captures the high frequency shoulder at ~2970 cm^{-1} due to the CH_3-SS of MGT2 (2970 cm^{-1}). For the *sps* spectra, the presence of MGT adds a peak at ~ 2969 cm^{-1} due to contributions from the CH_3-AS of MGT2 (2969 cm^{-1}) and MGT3 (2973 cm^{-1}). The single peak in our fit appears at 2988 cm^{-1} but is rather broad for a CH stretching peak (Gaussian width ~ 45 cm^{-1}).

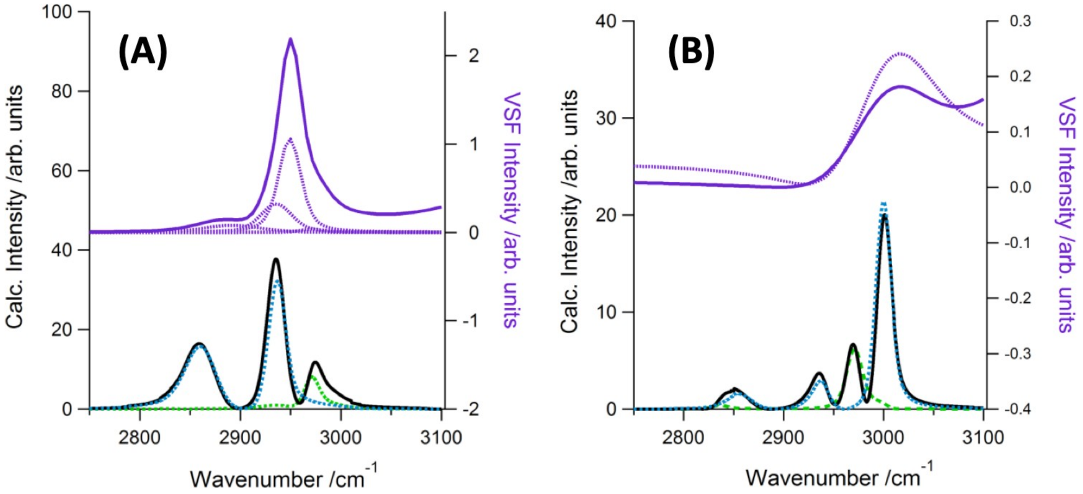

Figure 4.7. Experimental vs. calculated VSF spectra from mixed MG: Comparison of experimental vs. calculated VSF *ssp* (a) and *sps* (b) spectra . Top trace: overall fit (solid) and contributing peaks (dashed) to 0.5 M experimental spectrum. Bottom trace: composite spectrum (black, solid) and overall MGD (blue, dashed) and MGT (green dashed) spectra from the mixed simulation with MGD:MGT 10:6.

The composite spectra containing the cluster of peaks from both MGT and MGD could help explain this breadth. In both the *ssp* and *sps* calculated spectra, the dominant contribution is ultimately from MGD, due to the poor interfacial presence of MGT. Considering this agreement between the calculated and experimental spectra, we conclude that the dominant species present at the air-water interface of the experimental systems is MGD.

MG-OH Stretching Region

Although comparison of calculated and experimental spectra in the OH stretching region is difficult for the reasons mentioned above (i.e., interference with water modes, solvation effects), it is worth emphasizing that the calculated MGD spectra do predict strong signals from non-hydrogen-bonded MG-OH stretches (3630 – 3670 cm^{-1}). These are shown with the experimental spectra in Figures 4.8A and 4.8B in the *ssp* and *sps* polarization combinations respectively. The MGD3 conformer is calculated to have an (internal) hydrogen-bonded OH stretch at a lower frequency of 3460 cm^{-1} but this mode does not contribute significantly to the calculated VSF spectra. As well, the relative contribution from MGT OH modes is small, due to its weaker surface presence.

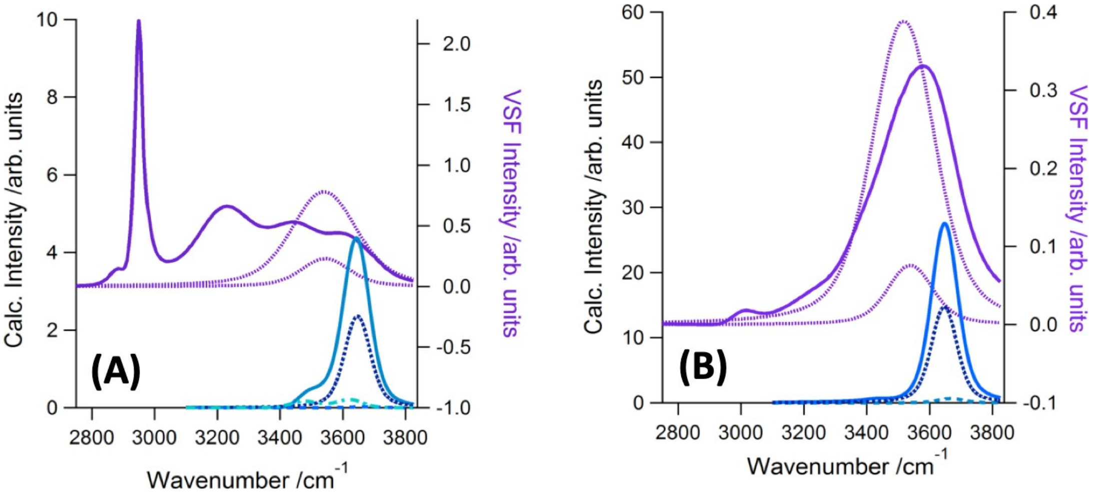

Figure 4.8. Experimental vs. calculated VSF MG spectra in the CH/OH stretching region: Comparison of experimental vs. calculated VSF *ssp* (A) and *sps* (B) spectra. Overall fit (solid) and contributing peaks (dashed) to 0.5 M experimental spectrum (top panel, purple). Overall (solid) and individual conformer (dashed) calculated spectra for MGD (bottom

The calculated frequencies for the MG-OH vibrations are in good agreement with previously calculated[81] frequencies but lie to the blue-side of the experimental frequencies obtained in this study (~ 3550 cm^{-1}) and by a previous FTIR study (~3505 cm^{-1}, 3585 cm^{-1}). However, the frequencies of non-hydrogen-bonded gas phase MG-OH modes would be expected to red-shift with solvation, bringing them into closer agreement with the fitted peak frequencies. The broad Gaussian widths obtained from the experimental fits (> 70 cm^{-1}) are indicative of a wide range of solvation environments, and probably also reflect the fact that multiple MG-OH modes contribute to this signal (i.e., from MGD and MGT and their various conformers, which contain two or four OH groups respectively).

Methylglyoxal Surface Adsorption and Interfacial Structure

Due to the large number of overlapping peaks and the coherent interference from nearby water modes, it is difficult to conclusively decouple MG and water contributions. The following discussion on changes to the interfacial structure is not meant to be highly quantitative but rather provide a qualitative picture of MG surface adsorption. Trends in VSF intensities are obtained from the fitted amplitudes, but are generally clear from visual inspection of the spectra; interpretation of the trends (to the extent provided here) is not particularly sensitive to exact peak frequencies or assignments.

The appearance of MG features in the VSF spectra is indicative of oriented surface adsorption of MG species, with the VSF intensities reflecting both surface population and orientation. The VSF fitted amplitudes of the dominant CH_3-SS peak (~2949 cm^{-1} in *ssp* and ~2988 cm^{-1} in *sps*) are observed to concomitantly increase with increasing bulk MG concentration, at least in part due to enhanced surface population of MG, consistent with surface tensiometry measurements and calculated density profiles. Increased surface packing of MG would also be expected to more strongly restrict the orientation of the methyl group, giving rise to increased intensity. A restricted orientation is reflected by its narrow angle distribution in the MD simulations.

The VSF fitted amplitudes of the MG-OH peaks follow a more complicated trend; this is visually quite striking in the *sps* spectra where the intensity of the nascent MG-OH peak at ~3550 cm^{-1} decreases with increasing bulk MG concentration. Given that the surface pressure isotherm shows increased surface population over the full concentration range studied, a decrease in VSF intensity is suggestive of a disordering of these modes at higher surface coverages. In contrast to the increased alignment of the methyl groups, the MG-OH groups exhibit increased disorder at higher MG surface coverages. The small size of the OH moieties, the rotational freedom of the O-H bonds, and the greater rotational freedom for the αC-βC bond to which the OH groups are attached, means solvation considerations will dominate the orientational behavior. In this case, increased surface packing appears to result in a solvation environment at the interface favoring increased disorder of the MG-OH oscillators.

Influence on Water Structure

The free OH feature is greatly diminished for solutions containing methylglyoxal (*ssp* spectra), although it is also obscured by the nearby MG-OH peaks. The reduction in the free OH signal is consistent with methylglyoxal's strong surface affinity and moderate surface packing, as these oscillators are particularly sensitive to perturbations at the air-water interface. Dramatic spectral changes in the coordinated water region between 3200 – 3400 cm^{-1} are also observed upon addition of methylglyoxal; these changes are most evident at the lowest MG surface coverages. VSF experiments involving deuterated solvents and/or solutes are often employed in order to decouple solvent and solute modes. Unfortunately this approach is not applicable in this case, due to the fast exchange between water and geminal OH groups of methylglyoxal. In *ssp*, the fitted amplitude of the coordinated water peaks at ~3200 cm^{-1} and ~3320 cm^{-1} are greatly enhanced for 0.05 M solutions relative to neat water; the fitted amplitudes for all coordinated water peaks are enhanced in *sps* (since they are essentially in the noise for neat water). However, at higher bulk MG concentrations, the intensities of the coordinated water peaks begin to decrease.

We conclude that a small amount of methylglyoxal induces enhanced ordering of interfacial water molecules. Several factors could be contributing to this effect including (a) an enhancement in the weak local electric field by surface-adsorbed MG and/or (b) favorable H-bonding of interfacial water molecules with geminal OH groups of hydrated MG species. The water peak at ~3200 cm^{-1}, which is typically assigned to strongly H-bound OH oscillators residing deeper in the interfacial region[85] is more strongly enhanced by small additions of MG than the other water peaks. This could indicate that MG strengthens the H-bonding network of water. In both cases, increased ordering of methylglyoxal would lead to increased ordering of interfacial water molecules while decreased ordering would cause the opposite effect. The strong and narrow (Gaussian width ~ 15 cm^{-1}) CH_3-SS peak observed in the *ssp* spectrum suggests that MG is, in fact, strongly oriented at the surface; the analysis of angle distributions in the MD simulations also supports this picture. The decrease in intensity of the water modes at higher bulk MG concentrations is consistent with the aforementioned disordering of MG-OH groups at higher MG surface coverages, which would weaken the local electric field and/or disrupt the H-bonding network. However, even at the highest MG concentration studied (0.50 M), the intensity of the water peak at ~3200 cm^{-1} is enhanced relative to neat water. Regardless of the underlying reason for the change (electric field effect and/or H-bonding between MG and water), the spectra clearly show that MG adsorption has a strong influence on the interfacial water structure. A change in water structure is also inferred from changes in the C=O spectral region.

Conclusions

We have used a combined experimental and computational approach to investigate methylglyoxal at the air-water interface. Together, surface tension, vibrational sum frequency and classical molecular dynamics simulations show that methylglyoxal exhibits an oriented adsorption to the air-water interface. Comparison of calculated and experimental VSF spectra in the CH stretching region indicates that unhydrated methylglyoxal monomer (MGM) is absent from the interface and that the dominant surface species is singly hydrated methylglyoxal diol (MGD). The presence of both C=O modes and strong geminal OH modes in the VSF spectra also point to MGD as the dominant surface species. Furthermore, these observations show that methylglyoxal is neither completely hydrated nor completely dehydrated at the interface. Moreover, MD simulations reveal that the preferred MGD conformer is different at the surface than in the bulk, with MGD1 (α-CH bond *cis* to the C=O bond) preferred at the surface. Density profiles extracted from the mixed molecular dynamics simulation containing MGD and MGT close to their bulk literature ratio of 1.5 indicate that the MGD/MGT ratio is significantly enhanced at the air-water interface, with a surface MGD/MGT ratio ~4.5. VSF spectra calculated from this mixed simulation are thus dominated by MGD features and are a good match to experimental spectra. Focusing on the MGD species, the picture that emerges is of a highly oriented interface with the hydrophobic methyl group pointing out into the vapor phase and the geminal OH groups pointing down into the bulk. The VSF spectra in the CH/OH stretching region and the C=O region indicate that this oriented adsorption of methylglyoxal has a dramatic influence on the water structure at the interface.

CHAPTER V

HYDROXYACETONE AT THE AIR-WATER INTERFACE

The contents of this chapter have been previously published in whole or in part. The text presented here has been modified from the publication below:

Gordon, B. P., Moore, F. G., Scatena, L. F., Valley, N. A., Wren, S. N., Richmond, G. L. Model Behavior: Characterization of Hydroxyacetone at the Air-Water Interface Using Experimental and Computational Vibrational Sum Frequency Spectroscopy. *J. Phys. Chem. A* **2018** *122* (15), 3837-3849.

Bridge

Small atmospheric aldehydes and ketones are known to play a significant role in the formation of secondary organic aerosols (SOA). However, many of them are difficult to experimentally isolate, as they tend to form hydration and oligomer species. Hydroxyacetone (HA) is unusual in this class as it contributes to SOA while existing predominantly in its unhydrated monomeric form. This allows HA to serve as a valuable model system for similar secondary organic carbonyls. In this paper the surface behavior of HA at the air–water interface has been investigated using vibrational sum frequency (VSF) spectroscopy and Wilhelmy plate surface tensiometry in combination with computational molecular dynamics simulations and density functional theory calculations. The experimental results demonstrate that HA has a high degree of surface activity and is ordered at the interface. Furthermore, oriented water is observed at the interface, even at high HA concentrations. Spectral features also reveal the presence of both *cis* and *trans* HA conformers at the interface, in differing orientations. Molecular dynamics results indicate conformer dependent shifts in HA orientation between the subsurface (~5 Å deep) and surface. Together, these results provide a picture of a highly dynamic, but statistically ordered interface composed of multiple HA conformers with solvated water. These results have implications for HA's behavior in aqueous particles, which may affect its role in the atmosphere and SOA formation.

It is important to note that this data was collected following significant improvements of the picosecond laser system. This resulted in superior signal-to-noise in the VSF spectra compared with that of the previous chapter

Introduction

Small oxygenated volatile organic compounds (OVOCs) are ubiquitous in the atmosphere and of great importance in secondary organic aerosol (SOA) formation.[1-13] Yet, there still exist many uncertainties in the specific roles these small organics play in the formation and consequent fate of SOA.[13-17] Water-soluble aldehydes and ketones have been of particular interest, due in part to their tendency to hydrate and oligomerize upon partitioning into the aqueous phase.[13, 18-35] Indeed, some of these organics (e.g. glyoxal,[24] methylglyoxal,[18, 36] pyruvic acid[31, 37]) are unusual in that their most stable forms in the aqueous phase are geminal diols, which are generally less stable than unhydrated carbonyls. This tendency to form higher molecular weight species leads to higher concentrations within aqueous aerosols than is predicted from Henry's Law, alone.[1, 11, 16-17, 19, 38-39] Once in the particle phase, these species participate in further oligomerization and oxidation reactions, thereby contributing to increased SOA mass, referred to as aqueous phase processing.[8, 18, 20-24, 27, 30-31, 34, 39-45]

Since aerosols have a large surface area to volume ratio, the surface chemistry of these particles can greatly influence their behavior and have far reaching effects on the environment.[1, 46-51] For example, it has been shown that surface interactions can strongly effect the adsorptions of atmospheric gases to aqueous surfaces.[47] Gaining a better understanding of the aerosol air-water interface is an on-going area of research.[13, 36, 45, 52-55] However, experiments with carbonyl species are often complicated because subsequent to purification (often, a challenge itself), exposure to water results in an equilibrium shift into a continuum of hydration species, effectively generating a mixed organic system.[18] Temperature, pH, and salinity can drive the hydration to favor one species, but each of these perturbations also has its own effect on the system and particularly on surface behavior.[18, 26, 31, 52, 56] Furthermore, the ratio of different hydration species can be depth dependent.[36] Thus, a small carbonyl that is surface active, atmospherically relevant, and unfavorable for either hydration or dimerization would serve as an invaluable model system for studying how these organics behave at aerosol interfaces.

Hydroxyacetone (HA) is just such a system. HA has been the focus of work in many fields due to its physiological, industrial, and astrochemical significance.[1, 57-68] This work focuses on HA's role as a prevalent semi-volatile atmospheric hydroxycarbonyl. HA has been observed experimentally in situ with other secondary organics known to contribute to SOA formation.[1] Some studies have identified HA as the most abundant carbonyl species in aqueous SOA.[1] HA is rather unique among these types of secondary organics because while HA can also hydrate to form a geminal diol, this hydration has been shown to be unfavorable. Glushonok et al. demonstrated that in the aqueous phase, 96-98% of HA exists in the unhydrated, monomeric carbonyl form with no covalently bonded dimeric or polymeric species detected. [68]

Although HA has been thoroughly examined in the gas, condensed (aqueous), and solid phases using multiple spectroscopic techniques,[1, 57-68] little to no work has been done on the surface chemistry of HA at liquid interfaces. To elucidate the behavior and conformational distribution of HA at the air-water interface, this study uses vibrational sum frequency (VSF) spectroscopy, a surface specific technique, in combination with surface tensiometry and computational methodologies. Of particular focus is the conformer distribution and hydrogen-bonding environment of HA at the air-water interface, as these properties have been shown to be phase dependent.[59, 61-63, 65-67] By characterizing the HA-neat water system, this work lays the groundwork for future studies on more complicated mixed organic systems.

Experimental Methods

Vibrational Sum Frequency Spectroscopy

Vibrational sum frequency (VSF) spectroscopy is a nonlinear technique that is inherently surface-selective and provides a convolution of orientation and population information for anisotropically ordered, surface-active, noncentrosymmetric molecules. This technique has been used extensively for the study of liquid interfaces.[69-81] A sum frequency signal is generated by overlapping a visible beam and a tunable-frequency IR beam in time and space, producing a third beam at the sum of the incident frequencies. The intensity of the VSF signal is proportional to the absolute square of the nonlinear second-order macroscopic susceptibility ($\chi^{(2)}$). The second-order susceptibility has both resonant ($\chi_{Rv}^{(2)}$) and non-resonant, ($\chi_{NR}^{(2)}$) components. The resonant portion of the VSF response contains information about both the *population* and *orientation* of species adsorbed at an interface. To deconvolve these numerous contributions, VSF spectra are fit using equation 1:[82-83]

$$!^{(!)} = !_{!''}^{(!)} !^{!!} + \sum_{!} \int_{!!}^{!} \frac{!_{!} !^{!''!} ! \, !^{(!!!!/!!)^{!}}}{!_{!} - !_{!''} + !!_{!}} !!_{!} \qquad (5.1)$$

The first term in Equation 1 is the nonresonant susceptibility, described by an amplitude and phase, ψ. The second term defines contributions from the resonant second- order susceptibility ($\chi_{Rv}^{(2)}$) as the summation over all VSF active resonant vibrational modes. Included in this resonant second-order susceptibility are the transition strength (A_v), phases (φ_v), and terms describing the homogeneous line widths of the individual molecular transitions (Γ_L) as well as inhomogeneous broadening (Γ_v). The Lorentzian, resonant modes and IR frequencies are defined as ω_L, ω_v, and ω_{IR}, respectively. Equation 1 is utilized for the fitting equation and spectral analysis of the VSF data, using mode specific fixed Lorentzian widths modes (based on reported vibrational lifetimes of the specific transition)[84-88] for the CH (2 cm^{-1}), coordinated OH and C=O (5 cm^{-1}), and 'free' OH (12 cm^{-1}).

VSF spectra discussed within are obtained using either the *ssp* or *sps* polarization scheme, where the three letters denote the polarizations of the sum frequency, visible and IR beams respectively. The *ssp* scheme probes molecular dipole components perpendicular to the air-water interface while the *sps* scheme probes components parallel to the interface.

Laser System

The picosecond laser system used to obtain the VSF results discussed here has been described.[36, 89-90] such that only a brief description is necessary for this work. A sum frequency (SF) beam is generated by overlapping a fixed visible beam (12500 cm^{-1}) with a tunable IR beam at the air-water interface in a copropagating geometry at 45° and 60°, respectively, relative to the surface normal. The SF beam leaving the interface is collected using a curved mirror set at its focal length and directed into a thermoelectrically cooled CCD camera (Pixas, Princeton Instruments). A LabView program measures the CCD intensity while scanning (3 cm^{-1} wavelength step) over the tunable IR range between 4000 cm^{-1} to 1200 cm^{-1}. The nonresonant SF response of an uncoated gold substrate was measured daily for each data set, and used to normalize the experimental spectra for VSF power. Daily calibration of the tunable IR beam was performed by measuring the absorption of a polystyrene standard and fitting to the known assignments. Spectra presented here are averages of ~6 or more spectra taken over multiple days. The resolution of the VSF system used herein is $\cong$10 cm^{-1}.

Shallow glass dishes ($\geq$ 8mm depth) are utilized as sample cells and are cleaned according to the rigorous protocol described in previous works.[36, 89-90] The dishes are placed on a vertically translatable stage. The stage is adjusted between each scan to account for any evaporation. Care was taken to ensure that evaporation did not alter the solution concentration. All VSF measurements were acquired at room temperature (~20 °C) under ambient conditions.

Surface Tensiometry

Contributions to the VSF signal from number density and molecular orientation are decoupled experimentally through the use of Wilhelmy plate[91] surface tensiometry measurements. The force exerted on the plate by the solution is measured using a force balance (KSV). Surface tensions (γ) are converted to surface pressures (π) by subtracting the daily-measured surface tension of neat water. The platinum plate was cleaned and rinsed repeatedly in 18.2 MΩ nanopure water and then dried under flame between measurements. All measurements were recorded under ambient conditions at room temperature (~20 °C).

It is worth noting that the surface tension versus time measurements reveal an extremely slow adsorption of HA to the interface. Equilibrium values occur after > 5 hours with a slowed increase over the next 24 hrs. This slow equilibration time is not unexpected as it has been observed in similar systems such as aqueous methylglyoxal.[36, 39] Further note that VSF itself is an extremely sensitive probe of interfacial contaminants and that no evidence of contamination was observed. For this reason, VSF spectra were obtained after each sample had equilibrated (for at least two hours) confirmed by the invariance of VSF results over time.

Sample Preparation

Aqueous HA solutions (0.1 – 5M) were prepared volumetrically by diluting HA stock solution (90 wt% in H_2O, Sigma Aldrich) in nanopure (18.2 MΩ) water. Since HA is extremely hydroscopic, the impurities contributing to the other 10% are attributed to solvated water.[62-63, 65] Solutions were prepared ≥ 24h before use and stored in Pyrex flasks.

Computational Methods

A combination of computational techniques are used to generate calculated VSF spectra. In addition to simulating spectra, the analysis also extracts structural details about the system, such as density profiles, as well as depth-resolved orientation and conformation information, which are vital in helping to understand the behavior of the system. This methodology is ideal because it is both computational efficient for the systems of interest and highly adaptable. This approach has been shown to be robust for numerous and varied chemical systems when compared with experimental spectra.[36, 89-97]

Classical Molecular Dynamics

Classical molecular dynamics (MD) simulations were performed using the Amber 12 suite of programs,[98] using parameters and force fields derived in the same manner as in previous studies.[92-93] PACKMOL[99] was used to create starting configurations. In each simulation, a specific number of HA and water molecules were arranged to form a 30 Å cube within a 30 Å x 120 Å x 30 Å simulation box, with periodic boundary conditions, forming a water slab with two surfaces. To preserve the volume of the system within the larger simulation box, as the number of HA molecules increased the number of water molecules was decreased, maintaining a total of ~2700 atoms. Simulations were performed for configurations of 1, 2, 4, 8, 16, 32, 80, and 160 HA molecules, corresponding to concentrations of ~0.05, 0.1, 0.25, 0.5, 1, 2, 5, and 10 M HA, respectively. In each configuration, the system was energy minimized at 0 K and equilibrated (by evolution through 2 ns of simulation from 0 K to 298 K), before being further evolved at 298 K in 1 fs time steps for a total of 50 ns, according to the methodology outlined in previous studies.[92-93]

Quantum Mechanical Calculations

Density functional theory (DFT) calculations are performed using the B3LYP exchange-correlation functional and a 6-311++G(2d,2p) basis set within the Gaussian 09[100] program package. Geometry optimizations, dihedral potential energy scans, and harmonic vibrational frequency calculations, as well as polarizabilities and dipole moments at displaced geometries along each normal mode, are performed for all reasonable gas phase conformers. Second-order vibrational perturbation theory is used to calculate anharmonic corrections to vibrational frequencies. Specifics of the resulting DFT structures are provided in the Appendix C.

Generating VSF spectra requires the second-order susceptibility tensor for all major conformations and orientations sampled in a dynamical interfacial system. Thus, for each normal mode of each HA conformer, the polarizabilities and dipole moment derivatives were calculated using three-point finite differentiation and combined according to Equation (2) to approximate the second-order linear susceptibility response tensor.

$$!^{(!)}_{!"\#} \propto \sum_{!,!,!} !_{!"\#} \frac{!!_{!"}}{!!_{!}} \frac{!!_{!}}{!!_{!}} \tag{5.2}$$

Here, α is the molecular polarizability, μ is the dipole moment, Q_q, is the normal coordinate of the mode q, and C is a geometrical factor relating the molecular and laboratory reference frames.

Using an in-house code,[97] VSF intensities and phases were then calculated by inspecting the second-order susceptibility tensor and assigning the static gas phase DFT structures with the molecular orientations and conformations populated in the MD simulations. The calculated intensities were empirically broadened using Lorentzian and Gaussian widths informed by the experimental VSF spectral fits.

Experimental VSF Spectra

VSF spectra were acquired for neat water and a series of HA concentrations (0.1, 0.25, 0.50, 1, and 2 M) in the *ssp* and *sps* polarizations for the COH/CH bending, C=O stretching, and CH/OH stretching regions. For clarity, a subset of these solutions (0.25, 0.5 and 2M, along with neat water) is shown in Figure 5.1. Spectra of the full concentration series are provided in the Appendix C, along with a description of the neat water VSF spectra. The strong VSF response in each spectral region confirms that HA has a high degree of surface activity and is oriented at the interface. As shown in Figure 5.1, features associated with CH and C=O modes grow in above the neat water spectra with increasing HA concentration, [HA]. The spectra shown in Figure 5.1 also contain contributions from oriented water at the interface, complicating their interpretation. Spectra of HA in D_2O were acquired in the COH/CH bending and C=O stretching regions (Figure 5.2) to help isolate and confirm the assignment of water and COH modes.

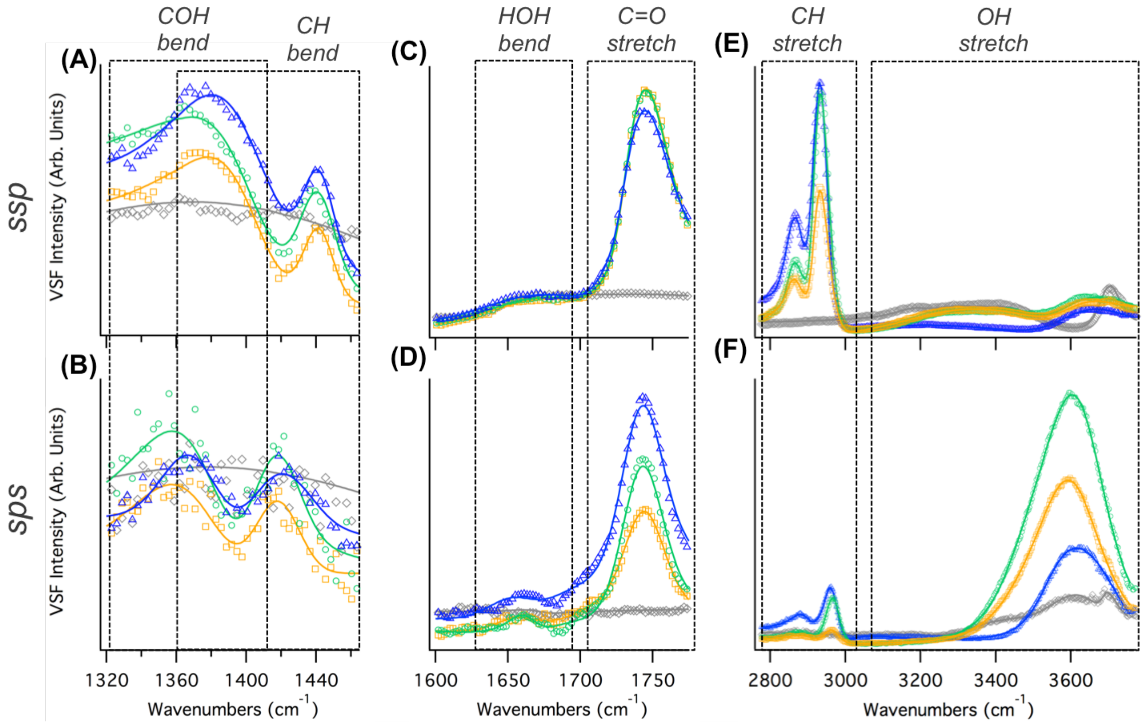

Figure 5.1. VSF Experimental data and corresponding fits for water and HA: VSF Experimental data (open circles) and corresponding fits (solid lines) for water and aqueous HA solutions in the COH/CH bending region (A,B), C=O stretching region (C,D), and the CH/OH stretching region (E,F) in the *ssp* polarization (top) and *sps* polarization (bottom). Water (gray, diamonds), 0.25M HA (orange, squares), 0.5M HA (green, circles), and 2M HA (dark blue, triangles). Dotted boxes are for visual reference of approximate spectral regions.

Overall, there is a transition point in the spectral trends of all three regions around 0.5 M HA, where intensity associated with CH modes generally continues to increase while intensity associated with OH and COH modes decreases and/or shifts in frequency. The COH/CH bending region (Fig 5.1 A,B) contains two broad features at ~1370 cm^{-1} (coupled COH and CH deformations) and 1420 cm^{-1} (CH deformations) that increase in intensity with [HA] until 0.5 M. At higher [HA], the 1420 cm^{-1} feature increases in the *ssp* spectra but decreases in the *sps* polarization scheme. Within each polarization, the lower frequency feature shows greater variation. Since the COH bending mode contributes more to the intensity in this part of the spectra (demonstrated by the decreased intensity when solvating HA in D_2O, Fig 5.2 A,B), these trends are consistent with a change in hydroxyl solvation environment. This is supported by spectra in the OH stretching region (Fig. 5.1 E,F), where the maximum OH intensity occurs at 0.5 M, before decreasing and slightly blue-shifting at higher [HA]. This blueshift is likely indicative of a less-solvated OH stretching mode but from this region alone one cannot distinguish between an HA associated OH mode and one associated with water.

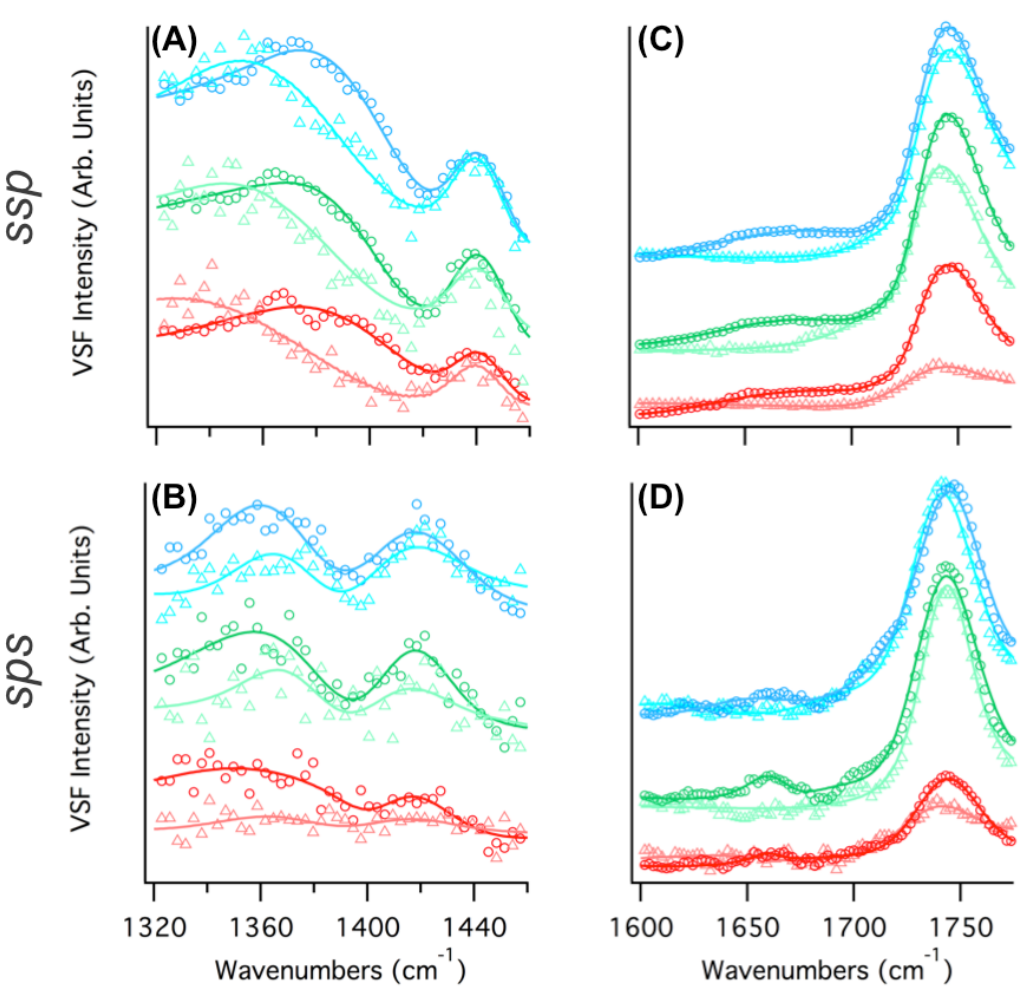

Figure 5.2. VSF Experimental spectra for HA in H_2O and D_2O: VSF Experimental spectra for HA in H_2O (open circles) and D_2O (open triangles) and corresponding fits (solid lines) in the COH/CH (A,B) bending and C=O stretching (C,D) regions in the *ssp* (top) and *sps* (bottom) polarization schemes for 0.1M HA (red), 0.5M HA (green), 1M HA (blue). Spectra are vertically offset for clarity.

In the CH stretching region (Fig. 5.1E,F), there are two dominant bands of intensity present in both ssp and sps polarizations. These features are around ~2900 cm^{-1} and ~2950 cm^{-1} respectively. Their likely origins are discussed later in this paper. They increase in amplitude with increasing [HA] until 0.5 M. Above that concentration, the ~2900 cm^{-1} feature continues to rise with [HA], but the ~2950 cm^{-1} feature plateaus. In the C=O stretching region (Fig. 5.1C,D), the carbonyl mode at ~1745 cm^{-1} increases with [HA] above 0.5 M in the *sps* polarization, while decreasing in the *ssp* polarization.

Some of these changes can be simply explained by a loss of water from the interface with increasing HA surface coverage. Yet, it is interesting to note that water is not completely excluded above 0.5 M HA, as evidenced by the continued presence of interfacial water modes. In Figures 5.1 C and D, in addition to the intense C=O stretching mode (~1745 cm^{-1}), there is also a low intensity feature centered around ~1650 cm^{-1}, which is attributed the bending mode of water.[69, 101-103] This assignment is confirmed by the loss of the feature when solvating HA in D_2O (Fig. 5.2 A,B). The persistence of some interfacial water at higher [HA] is not unexpected given the well-known hygroscopicity of HA.[62-63, 65]

This interfacial water can have significant spectral implications, as shown by further analysis of the C=O stretching mode (Fig. 5.2 C,D). Initial fitting of the main feature to a single carbonyl mode yielded peak positions of ~1742 and ~1752 cm^{-1} for the *ssp* and *sps* polarizations respectively. These assignments are somewhat implausible, since they are higher frequencies than any of the gas phase IR or Raman literature assignments.[62-63, 65] However allowing a second feature of opposite phase resulted in more plausible frequency positions at ~1725 cm^{-1} (negative phase, more H-bonded) and

~1737 cm^{-1} (positive phase, less H-bonded). These fits also suggest that the apparent frequency shift between polarization schemes is due to differing relative intensities of the two C=O stretching modes. If correct, such fits imply the existence of either carbonyl moieties in more than one solvation environment and/or more than one conformation. To investigate this further computational studies were pursued. (discussed further below).

However, variations in water content, alone, cannot explain why spectral features arising from relatively solvation-insensitive CH stretching and bending modes do not increase concomitantly with increasing [HA]. The complexity of the system is further highlighted by attempts to fit the two main features in the CH stretching region, which are shown in greater detail in Figure 5.3. Comparing the VSF spectra of the same [HA] in each polarization scheme reveals a shift in peak position of both features. Following the typical fitting protocol of using the minimum number of peaks, it is possible to fit these features to only two modes, but the fit does not converge to the same frequency positions between polarizations and yields implausibly high Gaussian broadenings. In fact, the full- width-half-max (FWHM) of these features are > 45 cm^{-1}, significantly higher than would be expected from singular a CH stretching mode, which are generally more on the order of ~10 cm^{-1}. [80] The shift in peak position, combined with the broad FWHM, signifies spectral congestion arising from the overlap of multiple CH stretching modes and/or environments that contribute to each of the two observed features.

The spectral congestion in this region could potentially be due to the presence of more than one HA conformer at the interface, and as previously mentioned, additional HA conformers could also explain the pair of carbonyls modes found in the C=O stretching region. The conformational distribution of HA has been the focus of many of

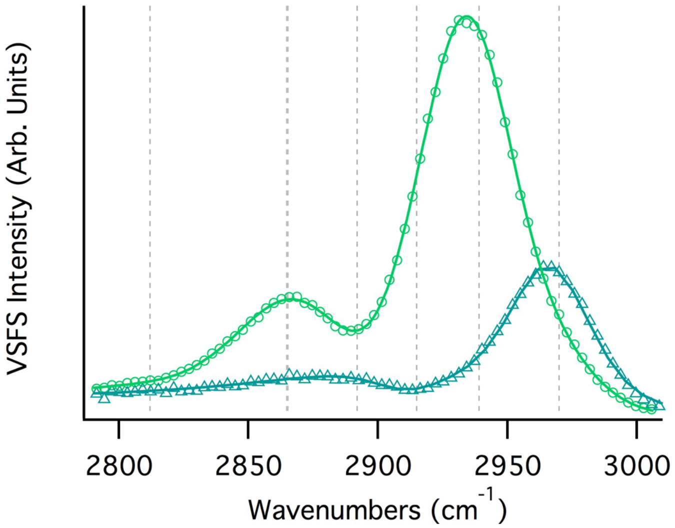

Figure 5.3: HA Experimental *ssp* and *sps* VSF CH stretching data: Experimental *ssp* (green, circles) and *sps* (teal, diamonds) VSF CH stretching data and corresponding fits (solid lines) for 0.5M HA. The dotted gray lines denote the position of HA peaks.

the spectroscopic studies on HA to date.[59, 61-63, 65-67] Briefly, the primary form of HA in the gas phase is the closed form *cis* conformation (Cc), which forms a five membered ring stabilized by an intramolecular hydrogen bond. Compared to the open form *trans* configuration (Tt), the gas phase Cc:Tt ratio was calculated to be 99:1.[66] However, condensed phase experiments have indicated additional conformers might be present in the aqueous solutions, specifically open form species that facilitate intermolecular hydrogen bonding and aggregation.[59, 62-63, 65] Computational studies by Sharma, et al., calculated populations of open form *cis* and *trans* configurations (Ct and Tt, respectively) in the solution phase to be in a Cc:Tt:Ct ratio of 83:11:6.[65] Sharma, et al.[67] also found that upon crystallization into the solid phase, HA takes on the Ct form, which was later confirmed by the work of Lasne, et al.[61] Low temperature studies also discovered that in this open configuration, HA can form H-bonded dimers and trimers via dual intermolecular hydrogen bonds with both the carbonyl and hydroxyl oxygen of other HA molecules.[67] This implies the potential for multiple solvation environments per conformer.

Examining each vibrational mode in both polarization schemes and D_2O uncovered some of the complexities of HA at the air-water interface. In particular, the systematic shift in the spectral behavior above 0.5 M HA and the presence of multiple HA conformations. Nonetheless, uncertainty in the assignments of the underlying modes precludes using the experimental fits for further spectral analysis without more information. To address outstanding concerns about the interfacial conformations and orientations of HA, complementary experimental and computational techniques are employed. The information gained from these techniques provides the context necessary to understand the interfacial trends giving rise to the experimental VSF spectra.

Experimental Surface Tensiometry

Equilibrium surface pressure data for aqueous solutions (0.1 to 5 M) are plotted in Figure 5.4A. The surface pressure data follow a Langmuir isotherm indicating adsorption of HA at the air-water interface: at lower [HA], the surface pressure increases linearly until ~0.5M, when it begins to plateau at ~21 mN m^{-1} as the maximum surface excess of is approached. Surface pressure values reported here are similar to the ~ 22 mN m^{-1} value observed for methylglyoxal,[36] whose dominant diol form has a structure quite similar to HA. Maximum surface excess was calculated from the surface pressure data according to the Gibbs adsorption equation, as previously described.[36, 90, 104] An estimate for the minimum average area per molecule of HA was found to be ~80 Å^2 mol^{-1} (again, comparable to the 73 Å^2 per molecule calculated for methylglyoxal). For a molecule the size of HA, this corresponds to moderate to low surface packing. Thus the surface pressure data support the main VSF findings of a) HA populating the air-water interface and b) water at the interface, even at the highest [HA] loadings. However, surface tensiometry cannot provide insight into the identity and orientation of HA conformers at the surface.

Computational Results

Despite the exquisite surface sensitivity of VSF and the assistance of surface tensiometry, aspects of HA's surface behavior still remain undetermined. In order to further deconvolve the contributions of surface population and orientation that give rise to the experimental VSF spectra, MD simulations of HA were analyzed to determine the depth dependent behavior of HA.

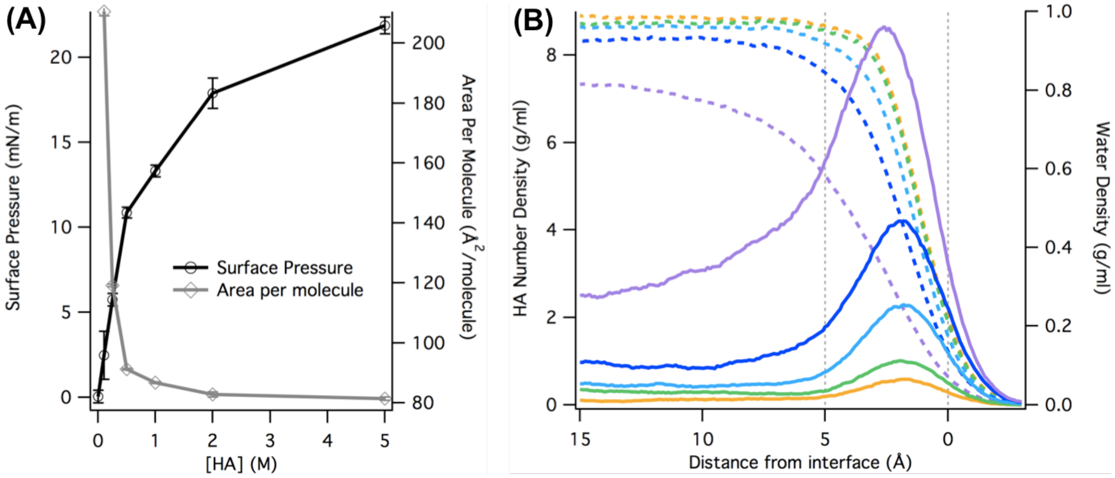

Figure 5.4. HA experimental surface pressure and calculated density profiles: (A) Hydroxyacetone surface pressure (left axis, black) and surface area per molecule (right axis, gray) as a function of bulk HA concentration, [HA]. Each point represents the average of 3-7 individual samples and the vertical error bars represent the standard deviation. (B) Density profiles of water (dotted lines) and HA (solid lines) obtained from the HA simulations with 4 HA (~0.25M, orange), 8 HA (~0.5M, green), 16 HA (~1M, blue), 32 HA (~1M, dark blue), 80 HA(~5M, purple). The dotted gray lines denote the approximate boundary between the surface (0 Å) and subsurface (5 Å).

The density profiles of HA and water obtained from each simulation are shown in Figure 5.4B. Since the amount of water in each simulation was scaled to preserve the volume of the box, the location of the interface is defined as being where the density of HA is at 50% of its peak value. This point was found to be within ±1 Å for all HA simulations, and defined as 0 Å. In each simulation, HA shows an affinity for the interface and show increasing surface coverage with [HA]. This agrees with the experimental surface tensiometry results and adds an additional level of detail. A sub- surface enhancement begins at ~5 Å and peaks at ~2 Å. At first glance, the HA interface appears to precede the water interface with increasing [HA], signifying some degree of water exclusion and increased HA surface coverage at the interface. However, the water profile actually becomes more gradual, indicating a broader boundary where the water is solvating an amorphous HA layer rather than forming a delineated interface with HA.

To appreciate what implications this has for the VSF results, the depth dependence of HA's condensed phase conformational space was examined. Calculated DFT structures for HA are shown in Figure 5.5A. Four gas phase minima were found by examining the dihedral potential energy surface. These are in agreement with previous findings in the literature.[65]

As previously mentioned, the conformational population distributions of HA has been a subject of much interest.[59, 61-63, 65-67] To briefly expand on this, the HA1-Cc conformer is the dominant structure in the gas phase, with only minimal contributions from any trans configuration.[62, 65] Mohacěk-Grosěv analyzed HA in the solution phase and assigned the contributions to a general *cis* conformer, but noted the presence of unassigned modes that were likely due to a *trans* configuration.[63] Later simulations by

Sharma, et al.[65] established that a *cis* conformer with a *gauche* hydroxyl group was the most abundant conformer in the solution phase-though not favorable in the gas phase. In this work, the MD simulations also yielded this additional structure, denoted HA5-Cg, which accounts for ~50% of bulk HA. The favorability of HA5-Cg in the solution phase is because the gauche orientation of hydroxyl group allows for greater intermolecular hydrogen bonding. Experimental support of this is provided by Jetzki et al.,[59] whose work proposes that the gas and particle phase HA spectra might have differing dominant conformers. The authors posited the existence of HA5-Cg in the condensed phase, arguing that the freedom to take part in intermolecular hydrogen bonding and the formation of aggregates might supersede the favorability of the intermolecular hydrogen bond of HA1-Cc.

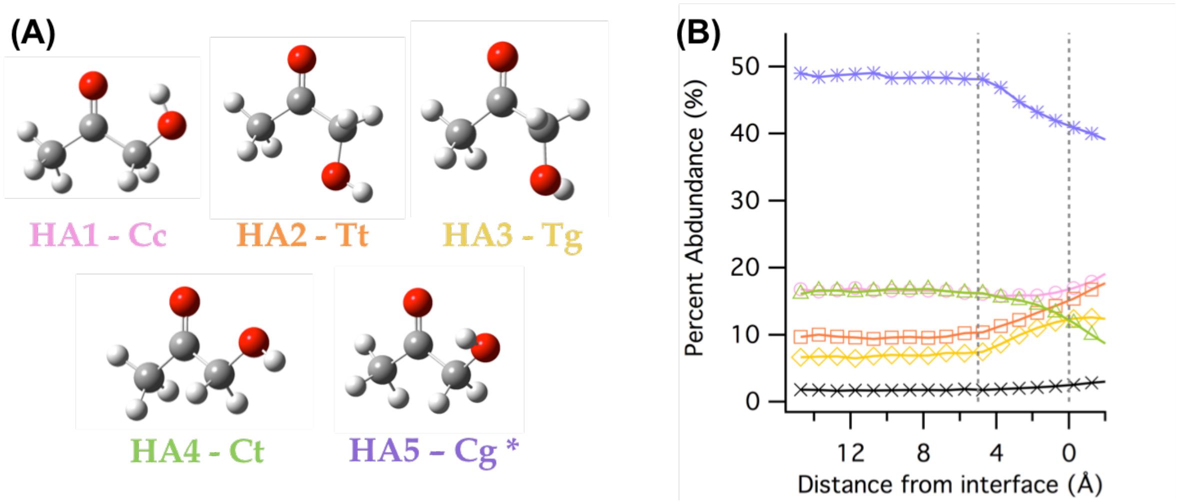

Figure 5.5. Percent abundance of the HA conformers as a function of depth: (A) Gas phase DFT structures of HA at the B3LYP/6-311++G(2d,2p) level of theory. (* Not a minimum on the gas phase potential energy surface.) (B) Percent abundance of the HA conformers as a function of depth from the interface (16 HA molecules, ~1M). HA1-Cc (red, circles), HA2-Tt (orange, squares), HA3-Tg (green, diamonds), HA4-Ct (blue, triangles), HA5-Cg (purple, stars), and unassigned conformations (X's). The dotted gray lines denote the approximate boundary between the surface (0 Å) and subsurface (5 Å).

The MD simulations support the presence of multiple conformers at the interface. Figure 5.5B illustrates how the relative abundance of the five conformers varies as a function of depth from the interface. Little change was observed at different simulation concentrations, so only the results for the HA 16 (~1M) simulation are presented. Note that while HA5-Cg is the most abundant conformer for both the bulk and interface, its relative abundance decreases slightly near the interface (as does HA4-Ct, to a lesser extent). This is consistent with HA5-Cg not being a stable gas phase conformer and with HA4-Ct being the least energetically favorable in gas phase. At ~5 Å these two conformers decline in abundance, while the two *trans* conformers, HA2-Tt and HA3-Tg, begin to increase. This is the same depth at which the sub-surface enhancement was observed in the density profiles (Fig. 5.4B), supporting that this change in preference is surface mediated. Intriguingly, HA5-Cg is still the dominant conformer at the interface (accounting for ~40%); the relative abundance of the remaining conformers tracks more closely to their gas phase hierarchy (with HA1-Cc, the dominant gas phase conformer, leading at ~20%). The ratio between the most abundant *cis* and *trans* conformers (HA5- Cg and HA2-Tt, respectively) is higher in the bulk (~5:1) than at the interface (~3:1), further emphasizing the behavior changes at the interface.

The depth dependent orientation of HA was analyzed in each simulation to determine average distributions of specific bond angles (with respect to the surface normal) within each 1 Å slice of the box (Figure 5.6). It is important to emphasize that the aqueous HA interface is highly dynamic and that these are very much statistical averages. As such, the peak of the distribution signifies a preference to tend towards that orientation, but as evidenced by the broadness of the distributions, the molecules are also continually moving and reorienting. Examination of the angle distributions for the individual HA conformers reveals orientations that are both depth and conformer dependent.

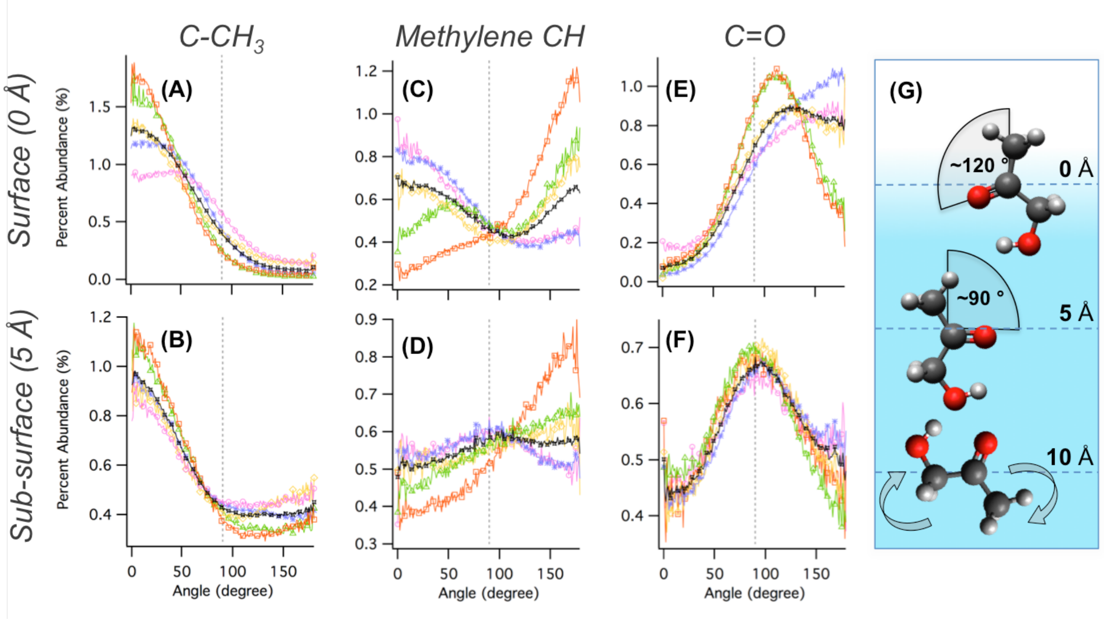

Figure 5.6. Normalized distributions of HA bond angles (relative to the surface normal into the vapor phase) for a simulation with 80 HA molecules (~5M). Percent abundance for the total HA system (black, open x's) and individual HA conformers (HA1–Cc (pink, circles), HA2-Tt (orange, squares), HA3-Tg (gold, diamonds), HA4-Ct (olive, triangles), HA5-Cg (purple, stars) are displayed for the C-CH$_3$ (A,B), methylene CH (C,D), and C=O (E,F) bond angles at the surface (0 Å, top) and sub-surface (5 Å, bottom), respectively. (G): Visual representation of the C=O bond angle orientation as a function of depth from the interface. In the bulk (~10 Å), the orientation is isotropic and HA has no average net orientation (indicated by the curved arrows.)

Figure 5.6 shows percent abundance per conformer for the C-CH$_3$ (A,B), methylene CH (C,D), and C=O (E,F) bond angles at the subsurface and surface, respectively. In each plot, the black lines represent the percent distribution across all conformers while the colored lines correspond to angles distribution for individual conformers. Figure 5.6G provides a graphic representation of the overall C=O bond angle orientation as a function of depth (black lines in Fig. 5.6 E,F). The C=O bond angle shifts from ~90˚ at the sub-surface (~5 Å deep) to ~120˚ at the surface (~0 Å deep). However, the individual conformations reveal additional variation for a given depth.

With the C=O bond angle, the conformers all have a similar orientation in the subsurface region centered at ~90˚ (Fig 5.6 F). But at the surface (Fig 5.6 E), the HA2-Tt and HA4-Ct species both show a well-defined peak at ~120˚ while the other three conformers have shifted into a broader peak, centered closer to ~180˚. The methylene CH bond angles show a similar trend. At ~5 Å deep (Fig 5.6 D), the HA2-Tt conformer, and to a lesser extent, HA3-Tg and HA4-Ct, tend to have methylene CH bonds pointed toward the vapor phase while the HA1-Cc and HA5-Cg show a minute enhancement parallel to the interface at ~90˚. At the interface (Fig 5.6 C) again the HA2-Tt conformer shows little change, but HA1-Cc and HA5-Cg strongly reorient towards ~0˚ (where methylene CH bonds would be pointed out of the interface) while HA3-Tg and HA4-Ct take on a bimodal distribution, with preferences for orientation at ~45˚ and ~180˚ (one methylene CH bond pointed into the vapor phase with the other pointed into the condensed phase.) The orientation of the methyl group is more consistent between the subsurface and surface (Fig 5.6 A and B, respectively), with a strong preference to point into the vapor phase. But the HA1-Cc distribution (and to lesser degree HA5-Cg) broadens somewhat, peaking closer to ~45˚, indicating a more variable orientation.

From Figure 5.6, it is evident that the broadened angle distributions observed in the total system (black lines) cannot be viewed in the context of a uniform change in orientation. The individual conformer orientations are far more complicated, in support of the VSF spectra, which suggest multiple conformers in different orientations. It is worth noting that the HA4-Ct conformer tracks more closely with the HA2-Tt conformer than with the other two *cis* conformers, whereas the HA3-Tt conformer tends to fall somewhere between the others. This indicates that the C-C-O-H dihedral (lower case letter) has a larger role in the interfacial orientation of HA than the O=C-C-O dihedral (capital letter). Since external hydrogen bonding is the factor most likely to involve the orientation of the OH group, this arrangement signifies a tendency for HA to form ordered hydrogen-bonded aggregates at the interface, as has been proposed in the literature.[59, 62,65]

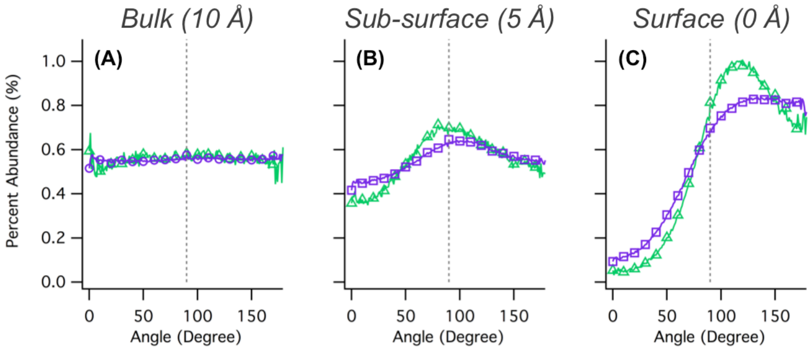

Figure 5.7. Depth variation in concentration dependent C=O bond angle: The concentration dependence in the C=O bond angle orientation for (A) the bulk (10 Å), (B) the sub-surface (5 Å), and (C) the surface (0 Å, bottom), for simulations with 8 HA (~0.5M) (green) and 80 HA (~5M) (purple).

Intuitively, one might expect this tendency to aggregate to be amplified with increasing [HA]: as HA further populates the interface, more water is in turn excluded and other HA molecules become more abundant for aggregation. This increased HA population also creates additional favorable ways for HA orient itself, as indicated in Figure 5.7 by the broadening of the angle distributions at higher [HA]. This could explain some of changes in intensity with [HA] observed in the experimental VSF spectra.

Application of Computational Results with Spectral Interpretations

The results discussed in the previous section provide a deeper understanding of the depth, concentration, and conformation dependent population and orientation dynamics of HA. Here the experimental VSF spectra can be reconsidered in context of these findings and agreement with calculated VSF spectra. Assessment of calculated VSF spectra enable further analysis by decoupling the spectral contributions arising from each HA conformer and providing insight into how these contributions convolve together to produce the overall spectrum. It is important to note that the current implementation of the methodology does not include contributions to the experimental intensity arising from water. Additionally, only contributions from fundamental vibrations are calculated, so intensity from any Fermi Resonance, overtone or combination bands is excluded. Barring these limitations, the calculated spectra are able to reproduce the experimental VSF data for spectral regions arising from fundamental modes that are insensitive to solvation as previously demonstrated.[36, 89-90, 92, 97]

Figure 5.8 shows both experimental and calculated 1M HA spectra in two different vibrational regions (CO stretching and CH stretching) and for both polarizations schemes (*ssp* and *sps*). The blue (topmost) traces in A,B,E,F are the experimental results for 1M HA in H_2O. Directly beneath each of these are the spectral individual contributions calculated for each of the five individual HA conformers (colored traces) plus the calculated total spectrum (black). In both polarizations and for each region, the calculated spectra are a good overall match to experiment.

The intensity and phase of the modes giving rise to these calculated spectra are displayed in the bottom of Figure 5.8 (C,D,G,H). These intermediate results (referred to as 'stick spectra') are the initial outputs of the VSF calculation routine, which are broadened according to Eq. 2 to generate the calculated spectra. The stick spectra provide a guide to the phases and intensities of these modes that explains the resulting destructive or constructive interference in the resulting total VSF spectrum.

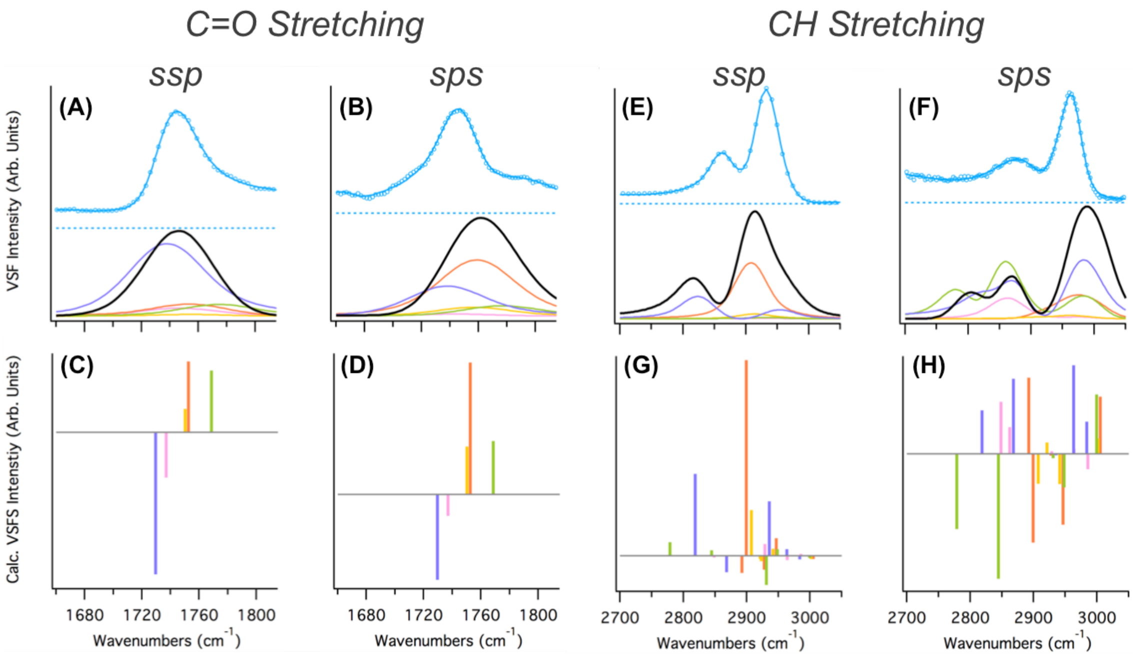

Figure 5.8. Experimental VSFS vs. Calculated HA VSF spectra from the 16 HA (~1 M) simulation in the CO stretching (A-D) and CH stretching (E-H) regions. **Top:** *ssp* (A,E) and *sps* (B,F) polarized experimental VSF of 1 M HA spectra (offset, blue, data=circles, fit= line) and the calculated VSF spectra for: the total spectrum with all HA conformers (black) and the individual conformer contributions of HA1–Cc (pink), HA2-Tt (orange), HA3-Tg (gold), HA4-Ct (olive), HA5-Cg (purple) stretching region compared to the calculated spectra of the full 16 HA (~1 M). **Bottom**: Calculated intensities and phases in the *ssp* (C,G) and *sps* (D,H) polarization for the HA conformers (positive and negative intensities represent phases of zero and pi, respectively.)

A few specifics immediately stand out in these calculated spectra. In general, the HA5-Cg (purple) and HA3-Tt (orange) conformers contribute the most in the calculated

VSF spectra, which agrees with the previous literature predictions regarding the dominant condensed phase species.[65] It is not surprising that HA5-Cg has a dominant conformation since it was revealed by the MD simulations to be the most abundant conformer at the interface. (For clarity, only these two most abundant conformers will be discussed here.) The phase information revealed by the stick spectra provides significant new insights into how these conformers combine to produce the resulting line shape.

In the C=O stretching region, the underlying stick spectra (Fig 5.8 C,D) displays the frequency and phase of the C=O mode for each conformer. In both polarizations, the HA5-Cg (and HA1-Cc) is lower in frequency with a negative phase while HA2-Tt (and the other two conformers) is at a higher frequency with a positive phase. Additionally, HA5-Cg has the greatest relative intensity in the *ssp* spectrum, while HA2-Tt is the most intense in the *sps* spectrum. Recall that the experimental C=O spectra were fit to two peaks with opposite phase: a negative peak at ~1725 cm^{-1} (attributed to a more strongly H-bonded carbonyl) and a positive peak at ~1737 cm^{-1} (attributed to a less strongly H- bonded carbonyl). This agreement between the calculated spectra and experimental fits provide significant evidence of more than one species of carbonyl at the interface. Due to the lack of solvation effects included in our methodology, this alone cannot differentiate if the agreement is due to the conformation or solvation environment, but it does clearly indicate that the experimental C=O is in a continuum of hydrogen bonding environments at the interface.

In the CH stretching region (Fig 5.8 E-H), HA5-Cg and HA2-Tt also have significant contributions in both polarizations. In fact, HA5-Cg and HA2-Tt are the main sources of intensity in the *ssp* polarization calculated VSF spectra (Fig. 5.8 E), and the stick spectra (Fig. 5.8 G) show that the most intense peak arises from HA2-Tt at ~2900 cm^{-1} (CH_2 sym. stretch). Once broadened, this positive phase peak interferes constructively with the positive HA5-Cg peak at ~2935 cm^{-1} (CH_3 sym. stretch). Thus, both methylene and methyl modes contribute to the single tall, broad peak to the high frequency side of the total spectrum. The remaining feature at ~2850 cm^{-1} largely arises from CH_2 sym. stretching modes (positive phase) of HA5-Cg.

The CH stretching region is more complicated in the *sps* polarization (Fig. 5.8 F) due to larger contributions from the other conformers, as well. Surprisingly, the low frequency side of the HA4-Ct spectrum (Fig 5.8 F, green) is slightly more intense than HA5-Cg, but the total calculated spectrum (Fig 5.8 F, black) does not reflect this additional intensity. The stick spectra in Figure 5.8H reveals that these HA4-Ct modes are out of phase with those of the other two *cis* conformers, bringing down the intensity of the total VSF feature there. On the high frequency side of the CH region (~3000 cm^{-1}), the intensity arises from the positive phases of CH_3 asymmetric stretching modes of all five conformers interfering constructively. These two clusters of positive phase modes on either side of the spectrum border an intense cluster of negative phase peaks between ~2900-2950 cm^{-1}. These negative phases in the stick spectra are due to the CH_2 and CH_3 symmetric stretches of the two *trans* conformers, as well as the methyl asymmetric stretch of HA4-Ct. These negative phase modes line up extremely well with the sharp dip seen in the experimental spectrum.

Overall, the agreement between the calculated and experimental spectra indicates that both the open form *cis* and *trans* conformers of HA are present at the air-water interface. With the phase information provided by the stick spectra, the experimental spectra can be examined in context of the underlying conformational contributions. The resulting experimental VSF spectral assignments are displayed in Table 5.1.

Table 5.1. Fit assignments for HA. Frequencies and assignments of peaks from experimental *ssp* and *sps* polarized VSF spectra.

Mode no. ν_i	*ssp* Exp. Freq. (cm^{-1})*		*sps* Exp. Freq. (cm^{-1})*		Bulk IR (cm^{-1})[62]	Gas phase IR (cm^{-1})[62]	Assignment (mode)**
ν_{12}	1363	π	-	-	1359	1356.56	Sym-δCH_3 Sym, CH_2 wag +/ νCCC AS
ν_{11}	-	-	1380	π	1378	1411.35	CH_3 scissors + δCOH
ν_{10}	1405	0	1405	0	1405	1446.53	CH_2 δHCO/ CH_2 wag + δCOH
ν_9	1420	0	1420	0	1418	1448.69	δCH_3 AS' + CH_2 Scissors
ν_8	1442	0	1442	π	1438	1469	δCH_3 AS" / CH_2 Scissors
ν_7	1725	π	1725	π	1724	-	C=O Stretch (more H-Bonded)
$\nu_{7'}$	1737	0	1739	0	-	1741.49	C=O Stretch (less H-Bonded)
$2\nu_{10}$	2808	0	-	-	2810	2803	Overtone ($2\nu_{10}$)
ν_6	2855	0	-	-	2842	2862	νCH_2 SS (*cis*-HA)
ν_5	2902	π	2907	0	2897	2885	νCH_2 SS (*trans*-HA), νCH_2 AS (*cis*-HA)
ν_4	2915	0	2912	π	2921	2917	νCH_2 AS (*trans*-HA)
ν_3	-	-	2954	π	2939	2973	νCH_3 AS, νCH_3 SS (*trans*-HA)
ν_2	-	0	2966	0	2989	3022	νCH_3 AS
$\nu_{1'}$	~3250	0	~3550	0	3417	-	νOH (H-Bonded)
ν_1	3604	0	3610	0	-	3523.68	νOH (HA)

* Exp. Fit frequencies ± *10 cm^{-1}*

** δ = bend; ν=stretching; AS'=(in plane); AS"=(out of plane), "+" = "and"; "/ " = "or";

Conclusions and Atmospheric Implications

Calculated and experimental VSF spectra have been presented and demonstrate that HA (a small organic molecule and not a traditional surfactant) demonstrates a substantial surface activity. HA is oriented at the air-water interface, but also highly dynamic in regards to conformation, concentration, and depth dependent behavior. The system transitions from a diffusion limited regime into a surface excess limited regime around 0.5 M HA. The relatively large surface area per molecule and calculated density profile support the presence of solvated water in a surface layer that is largely HA. The continued presence of water is evidenced in experimental VSF spectra by the loss of key spectral features when solvating HA in D_2O. The contributions of water modes to the VSF spectra demonstrates that the interfacial water is coordinating in an ordered way, even at the highest HA concentrations.

The VSF spectra also show evidence of either multiple HA conformers or solvation environments at the interface. Analysis of MD simulations shows that the open *cis* form of HA (with the hydroxyl H at a *gauche* offset to the carbonyl) is the most abundant conformer in the bulk (~50%) and at the interface (~40%). The lack of an internal H-bond in the open form signifies the formation of H-bonded aggregates throughout the system. This *cis* conformer and the open form *trans* conformer (with the hydroxyl H fully *trans* to the carbonyl) contribute most strongly to the calculated VSF spectra. These two conformers exhibit differing orientations as well as depth dependent reorientations between the subsurface and surface. Interestingly, the position of the hydroxyl group was shown to have a greater effect on interfacial orientation than the *cis* or *trans* configuration. This suggests that the resulting orientation of HA may be dependent on its aggregation interactions. The ratio of open form *cis* to *trans* conformers is lower at the interface (~3:1) than in the bulk (~5:1). Since the *trans* conformer is not populated in the gas phase, this may be a sign of stabilizing interactions unique to the interface.

Together, these results create a picture of a coordinated interface composed of HA forming dynamic external hydrogen bonds with other HA and water. Furthermore, they suggest that there may be one or more preferred aggregation structures at the interface. In the future, aggregation structures could potentially be investigated by incorporating explicit micro-solvation into the computational methodology and examining HA H-bonded dimer and trimer systems. This would also serve to further isolate spectral features arising from the external solvation environment from internal conformational dependencies.

HA's tendency to form surface specific coordinated aggregates may have significant implication for atmospheric interfaces, as it could impact surface properties, such as gas-to-particle partitioning and cloud condensation nuclei activity. Furthermore, because of the potential variability of these H-bonded aggregates, unanticipated cooperative effects may arise in systems of mixed organics. This work provides the foundation for HA as a quantified organic model system to use as a control in future studies of organic-salt or mixed organic systems at the air-water interface.

CHAPTER VI

PYRUVIC ACID AND ITS SURFACE-ACTIVE OLIGOMERS

The contents of this chapter have been previously published in whole or in part. The text presented here has been modified from the publication below:

Gordon, B. P., Moore, F. G., Scatena, L. F., Richmond, G. L. On the Rise: Experimental and Computational VSFS Studies of Pyruvic Acid and its Surface Active Oligomer Species at the Air-Water Interface. *J. Phys. Chem. A* **2019***, Just Accepted Manuscript* **(**DOI: 10.1021/acs.jpca.9b0885)

Bridge

It is well known that atmospheric aerosol play important roles in the environment. However, there is still much to learn about the processes that form aerosols, particularly aqueous secondary organic aerosols (aqSOA). While pyruvic acid (PA) is often better known for its biological significance, it is also an abundant atmospheric secondary organic. It has been shown that in bulk aqueous environments, PA exists in equilibrium between unhydrated α-keto carboxylic acid (PYA) and singly hydrated geminal diol carboxylic acid (PYT), favoring the diol. These studies have also identified oligomer products in the bulk, including zymonic acid (ZYA) and parapyruvic acid (PPA). The surface behavior of these oligomers has not been studied and their contributions (if any) to the interface are unknown. Here, we address this knowledge gap by examining the molecular species present at the interface of aqueous PA systems using vibrational sum- frequency spectroscopy (VSFS), a surface sensitive technique. VSFS provides information about interfacial molecular populations, orientations and behaviors. Computational studies using classical molecular dynamics (MD) and quantum mechanical density functional theory (DFT) are employed in combination to afford further insights into these systems. Our studies indicate populations of at least two intensely surface active oligomeric species at the interface. Computational results demonstrate that along with PYA and PYT, both PPA and ZYA are surface active with strong VSF responses that can account for features in the experimental spectra.

Introduction

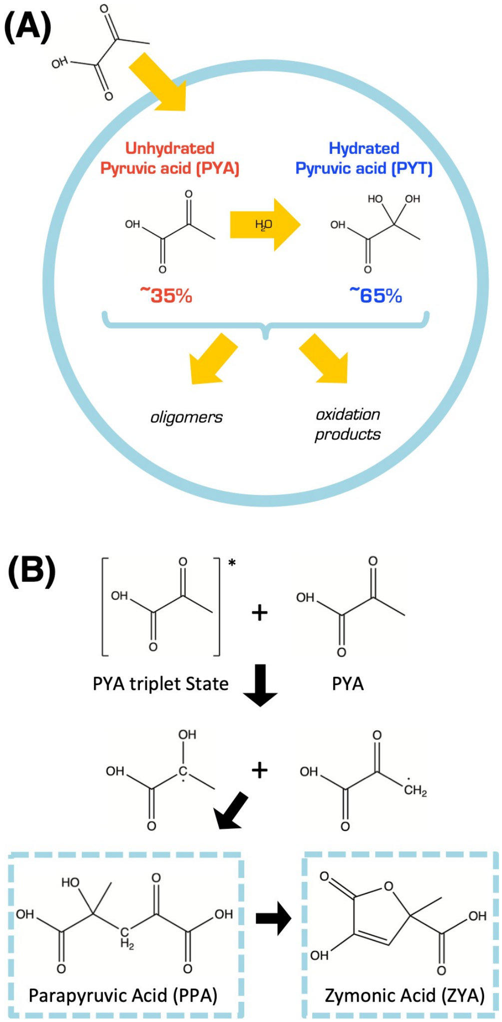

Figure 6.1. Aqueous phase processing of PA[41] (A) and (B) mechanism of PA oligomer formation from Perkins et al.,[48] with zymonic acid (ZYA) and parapyruvic acid (PPA) highlighted in the dotted blue boxes.

Aqueous secondary organic aerosols are among the most ubiquitous environmental systems and have far-reaching impacts on the climate. Solvated organics are known to have significant roles in the formation, structure, and characteristics of aqueous secondary organic aerosol (aqSOA).[1-32] However, much of the aqueous phase processing of these organics remains poorly understood.[18, 27, 28, 31] Many of the small atmospheric carbonyls found in aqSOA can further react in the aqueous phase to form hydrated species and oligomers.[16,33-54] Due to the complexity of these systems, the molecular nature of many of these organics at aerosol interfaces is largely unknown.[31, 32, 55-58] This is particularly true for pyruvic acid (PA). Beyond its biological significance, PA is also one of the most abundant atmospheric secondary organic ketoacids and is known to be involved in aqSOA formation.[41-54, 59-63] Because of this, PA has been studied extensively in this context and as a model atmospheric α-dicarbonyl.

In aqueous solutions PA has two populated hydration species (depicted in Figure 6.1A): the unhydrated α-keto acid (PYA) and the singly hydrated triol (PYT).[41] However, the factors that determine equilibrium conditions and corresponding abundances of these hydration species are known to be complex. For example, in a nonpolar solvent as well as low pH aqueous solutions the PYA:PYT ratio is 35%:65%.[41] Whereas in dilute solutions or at higher pH this ratio has been reported to vary by as much as 50%:50% to 90%:10%.[50] Compounding this complexity, it is likely there is a depth-dependent shift in the hydration equilibrium between the bulk and the interface. Such behavior has been reported in similar a system by Wren et al. in which methylglyoxal (MG) was determined to exhibit preference for its less-hydrated diol form at the interface relative to the bulk.[34] As surface properties are plausibly related to the ratio of these species, characterizing the nature of this equilibrium at the air-water interface will provide valuable information to atmospheric scientists.

Furthermore, PA has recently been established to favorably form oligomeric species.[45, 47, 48, 50, 53, 54] The Vaida group has pioneered the characterization and mechanistic studies of PA and its oligomer species, demonstrating that due to the variety of favorable pathways through which each monomeric hydration species can react, these higher order oligomer products are numerous.[45, 48, 50] The abundance of these reaction products can vary greatly depending on solution and environmental conditions (such as pH[48, 50] and photochemistry[42-54]) and some of these oligomer species are also in equilibrium with favorable hydration species.[48] Aqueous PA favorably forms larger molecular weight oligomeric species, as demonstrated in Figure 6.1B,[48] where the polar medium lessens the tendency to form intramolecular hydrogen bonds and enhances intermolecular hydrogen bonding.[41] In fact, the formation of such oligomeric species is favorable enough to occur on metal oxide surfaces where unhydrated PA reacts with surface hydroxyl groups to produce pyruvate, which can go on to yield several higher-molar-mass oligomeric species.[54]

For purposes of clarity, this work focuses on only two of the unhydrated oligomer products highlighted in Figure 6.1B: the keto acid parapyruvic acid, (PPA), and PPA's closed ring lactone enol form zymonic acid, (ZYA). PPA and ZYA were chosen because they have repeatedly been established to form spontaneously from PA precursors, even in the dark.[42-54]

While these literature studies provide precedence and insight into the PA oligomeric reaction products, the relative surface affinity of such species at the air-water interface has not been previously studied. Here, we report novel insights obtained using vibrational sum-frequency spectroscopy (VSFS) in combination with surface tensiometry and computational chemistry to examine the molecular species present at the air-water interface of aqueous PA systems. VSFS is a surface sensitive technique, which provides information about interfacial molecular character, population, and orientation.

In the present study, aqueous PA solutions reveal higher than anticipated surface activity at the air-water interface. Moreover, VSF spectra provide significant evidence of ordered, surface-active oligomeric species (PPA and ZYA) in addition to the monomeric PYA and PYT. Computational results demonstrate that along with PYA and PYT, both

PPA and ZYA are surface active and that they have strong VSF responses that can account for the increased surface-activity and additional features observed in the experimental spectra.

Experimental Methods

Vibrational Sum Frequency Spectroscopy

Vibrational sum frequency (VSF) spectroscopy is an inherently surface-selective nonlinear optical technique that provides a vibrational spectrum of surface–active molecules that are anisotropically ordered, and noncentrosymmetric.[64-67] at asymmetric interfaces VSF spectroscopy is a well-established technique has been used extensively by the Richmond lab[34, 68-79] and others[80-99] to study liquid interfaces. By overlapping a fixed visible and a tunable-frequency IR beam in time and space, a third sum frequency beam is generated, which is the sum of the incident frequencies.

Depending on the polarizations of the incident beams, VSF can probe molecular dipole components perpendicular (*ssp*) or parallel (*sps*) to the air-water interface, where the three letters denote the polarizations of the sum frequency, visible and IR beams respectively. All VSF spectra discussed within were collected in either the *ssp* or *sps* polarization scheme.

The intensity of the VSF response is proportional to the absolute square of the nonlinear second-order macroscopic susceptibility ($\chi^{(2)}$), which contains both resonant ($\chi_{R\nu}^{(2)}$) and non-resonant ($\chi_{NR}^{(2)}$) components. Included within the resonant component is molecular information regarding both population and orientation at the interface. The numerous contributions to the VSF spectra is described as a convolution of a Gaussian and Lorentzian distribution described by Bain et al.[64]:

$$\chi^{(2)} = \chi_{NR}^{(2)} e^{i\varphi} + \sum_{v} \int_{-\infty}^{\infty} \frac{A_v e^{-[(\omega_L - \omega_v)/\Gamma_v]^2}}{\omega_L - \omega_{IR} + i\Gamma_L} d\omega_L \qquad (7.1)$$

Equation 1 is utilized as the fitting equation for spectral analysis of the VSF data. As per convention, reported vibrational lifetimes of the specific transitions are used to inform mode specific fixed Lorentzian widths for the CH (2 cm^{-1}), coordinated OH and C=O (5 cm^{-1}), and ‘free’ OH (12 cm^{-1}) modes.[100-103]

Laser System

The VSF spectra discussed within were acquired using a picosecond laser system, which has been previously described.[78] In short, the sum frequency (SF) beam is generated by overlapping a fixed visible beam (12500 cm^{-1}) with a tunable IR beam (4000 cm^{-1} to 1200 cm^{-1}, with a 3 cm^{-1} wavenumber step) at the air-water interface. The resolution of the VSF system used herein is ~18 cm^{-1}. The incident angles of the visible and IR beams are set relative to the surface normal at 45° and 60°, respectively. The resulting SF beam is collected using a curved mirror set at its focal length and directed into a thermoelectrically cooled CCD camera (Pixas, Princeton Instruments). All experimental spectra are normalized for VSF power using that day’s nonresonant SF response of an uncoated gold substrate. Daily frequency calibration of the tunable IR beam is accomplished by measuring the absorption of a polystyrene standard and fitting to the known assignments.

All VSF measurements were acquired at room temperature (~22 °C) under ambient conditions in sample cells consisting of shallow glass dishes (≥ 8mm depth) that are cleaned according to a rigorous protocol.[34, 78] No changes in intensity or spectral shape were observed between scans of the equilibrated sample for any PA concentration. This indicates that if the laser is inducing photoinitiated reactions, any resulting reaction products at the interface are not ordered and/or abundant enough to be detectable by VSFS. Furthermore, any resulting perturbations to the net interfacial orientation or populations of the reactant species are not significantly deviating within the ~1 to 3 hours required for data collection. For these reasons, laser induced reactions are not considered to be a concern in this work.

Surface Tension

Experimental Wilhelmy plate surface tensiometry measurements provide a measure of surface population, which is used to decouple contributions from number density and molecular orientation in the VSF signal. This technique uses a force balance (KSV) to quantify surface tension (γ) by measuring the force exerted on the plate by the solution under ambient conditions at room temperature (~22°C). Surface tension is converted to surface pressure (π) by subtracting the daily-measured surface tension of neat water. The platinum plate is cleaned in 18.2 MΩ cm nanopure water and then dried under flame between measurements.

Sample Preparation

Aqueous PA solutions (0.05 – 1M) were prepared volumetrically by diluting PA stock solution (98%, Sigma Aldrich) with nanopure (18.2 MΩ cm) water or D_2O (99.9%, Cambridge Isotope Laboratories, Inc.). Solutions were prepared ≥ 24h before use and stored in Pyrex flasks, since PA is known to have numerous photoinitiated reaction mechanisms.[42-54] Therefore, solutions were kept in the dark when not in use.

Computational Methods

Calculated VSF responses are generated using a combination of computational techniques. These techniques also provide vital structural and behavioral insights about the simulated system, such as depth dependent molecular partitioning. This approach has been shown to be robust, efficient, and highly adaptable for numerous and varied chemical systems when compared with experimental spectra.[34, 71-78]

Classical Molecular Dynamics

Molecular dynamics (MD) simulations are performed using the Amber 12 suite of programs,[104] using parameters and force fields derived in the same manner as in previous studies[34, 71-78] and starting configurations were generated by PACKMOL.[105] In each simulation, a specific number of PA and water molecules are arranged to form a 30 Å cube within a 30 Å x 120 Å x 30 Å simulation box, with periodic boundary conditions, forming a water slab with two interfaces. To maintain a consistent simulation volume with a total of ~2700 atoms, the number of water molecules is decreased as the number of is PA molecules is increased. Simulations were performed for configurations of 2, 4, 8, and 16 PA molecules per box, corresponding to concentrations of ~0.125, 0.25, 0.5 and 1 M PA, respectively. Each simulation was energy minimized at 0 K and equilibrated from 0 K to 298 K over 2 ns. The simulations were then further evolved at 298 K in 1 fs time steps for a minimum of 10 ns, which was evaluated to be sufficient as the conformational sampling of these initial studies has been intentionally limited by design.

Quantum Mechanical Calculations

The Gaussian 09[106] program package was used to perform density functional theory (DFT) calculations using the B3LYP exchange-correlation functional at the 6-311++G(2d,2p) level of theory for a limited subset of PYA, PYT, PPA, and ZYA gas phase conformers. These include geometry optimizations, dihedral potential energy scans, and harmonic vibrational frequency calculations and anharmonic corrections, as well as polarizabilities and dipole moments at displaced geometries along each normal mode. The results of these calculations are provided in Appendix D (Tables D1 & D2).

Calculated VSF responses

An in-house code[73] calculates VSF intensities and phases by first inspecting the MD trajectories at every time-step, where molecule conformations are analyzed and matched to a library of gas-phase DFT structures. The DFT library includes polarizabilities and dipole moment derivatives calculated using three-point finite differentiation, which are combined according to Equation (2) to approximate the second- order nonlinear susceptibility response tensor for each normal mode of the represented

PA monomeric and oligomeric conformers.

$$!^{(!)}_{!"!} \propto \sum_{!,!,!} !_{!"\#} \frac{!!_{!"}}{!!_{!}} \frac{!!_{!}}{!!_{!}} \qquad (6.2)$$

In Equation (2), α is the molecular polarizability, μ is the dipole moment, Q_q is the normal coordinate of the mode q, and C is a geometrical factor relating the molecular and laboratory reference frames.

Results and Discussion

Experimental VSF Spectra

VSF spectra were acquired for neat water and a series of PA concentrations (0.01, 0.05, 0.1, 0.25, 0.50, and 1 M) in the *ssp* and *sps* polarizations for the C=C/C=O (Fig. 2A,C) and CH/OH (Fig. 2B,D) stretching regions. For clarity, only a subset of spectra of these PA solutions (0.05, 0.25 and 1M) is shown in Figure 6.2. Spectra of full concentration series are provided in the Appendix D in Figure D1. As detailed and thorough discussions of neat-water at the air-water interface are numerous,[70, 81-99] it will only be addressed briefly in Appendix D Figure D1. This work will focus primarily on the organic contribution to the VSF spectra presented within. The strong VSF response in each spectral region demonstrates a large, oriented surface population. However, some of these responses cannot be attributed to modes from either of the PA hydration species, as is discussed below.

In the OH stretching region, both the *ssp* and *sps* spectra of PA solutions show strong features centered at ~3600 cm^{-1} that are attributed to the OH stretching modes of PA. The loss of intensity in the coordinated-OH stretching region (~3000-3400 cm^{-1}),[70] most clearly observed in the *ssp* polarization scheme, indicates that the addition of PA suppresses the coordination of and/or excludes water. However, it is possible that less coordinated interfacial water still present and oriented at the interface is also contributing to the ~3600 cm^{-1} feature in PA solutions, as has been demonstrated with HA.[78] This can be further investigated by examining the water bending modes, as is discussed below.

It is worth briefly discussing pH considerations at this point. Aqueous solutions of PA are known to be acidic, even at low concentrations. The bulk pH of the aqueous PA

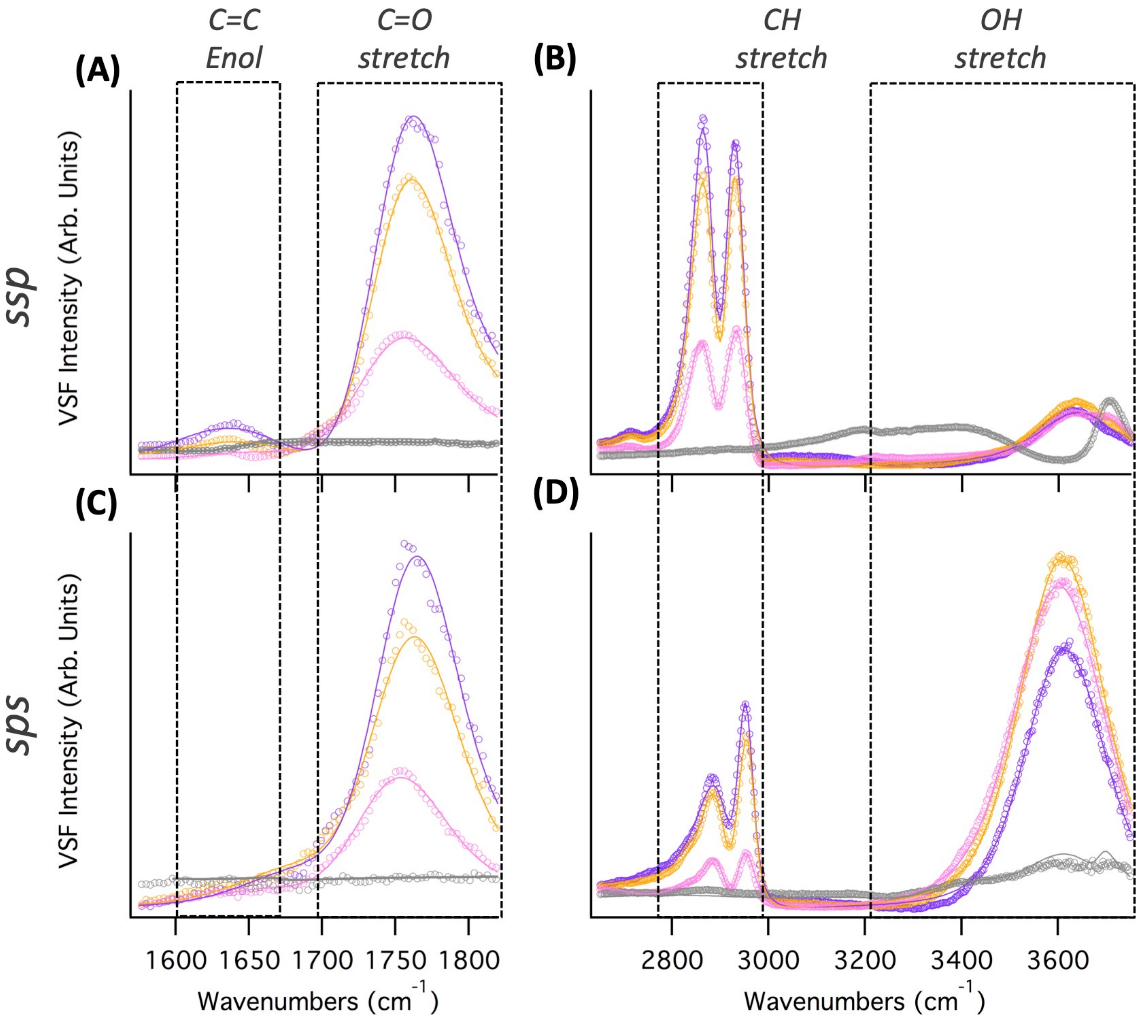

Figure 6.2. VSF spectra for water and aqueous PA: VSF Experimental data (open circles) and corresponding fits (solid lines) for water and aqueous PA solutions in the *ssp* (A,B) and *sps* (C,D) polarization schemes for the C=C/C=O stretching region (left), and the CH/OH stretching region (right). Water (gray), 0.05M PA (pink,), 0.25M PA (orange), and 1M PA (purple). Dotted boxes provide visual reference of approximate spectral regions.

solutions in this work was not further adjusted, therefore reflecting the low pH of atmospheric SOA. Rapf et al. reported pH=2.36 and 2.06 for 0.01M and 0.1M PA solutions, respectively, and that the effective acid dissociation constant of pyruvic acid was determined to be 2.51. [50] However the authors note that because the monomeric forms of PA are relatively strong acids, both PYA and PYT can deprotonate at even at fairly low bulk solution pH. They determined that at 0.01M PA (pH= ~2.36), ~36% of monomeric PA species in solution will be deprotonated, while at 0.1M PA (pH= ~2.06) the majority of species are protonated.

As the PA solutions studied here are all of higher PA concentration than this, it can be assumed that the pH of these sample are all ≤ 2.4 and that < 36% of monomeric PA species are deprotonated. Furthermore, it is known that charged species at the interface, such as deprotonated PA, would enhance the VSF intensity in the coordinated- OH region.[80] Examination of the OH stretching region then provides a means to qualitatively evaluate the presence of charged species without needing to know the actual percentage of deprotonated species. Figure 6.2B,D shows no appreciable change in the intensity of the coordinated-OH stretching region as the PA increases from the lowest (0.05M) to the highest (1M) concentration solutions. With regards to the surface charge specifically, this indicates that the amount of surface-active deprotonated species (either monomeric or oligomeric) is negligible and thus the interface can be considered neutral.

In the *ssp* CH stretching region (Fig. 6.2B), two broad features are present at ~2870 cm^{-1} and ~2930 cm^{-1}. For small dicarbonyls like PA, these frequency positions are generally attributed to methylene and methyl stretching modes, respectively.[78] Similarly, the *sps* CH stretching region (Fig. 6.2D) has two broad features: the lower frequency peak also at ~2870 cm^{-1} while the higher frequency peak appears higher at ~2950 cm^{-1}. In both the *ssp* and *sps* spectra, a broad low energy peak occurs at ~2750 cm^{-1}, which is attributed to OH modes from carboxylic acid dimers, in agreement with literature assignments.[41]

The CH stretching regions of both polarization schemes were fit to three peaks at 2872, 2928, and 2957 cm^{-1}. Literature assignments of PYA's CH_3-SS have been reported between 2932 and 2941 cm^{-1} but to our knowledge, experimental measurements of the PYT vibrational modes have not been previously reported.[107-110] However, insight can be gained from VSFS studies of methylglyoxal (MG), a similar dicarbonyl with both diol and tetrol hydration species. The MG diols's ketonic methyl symmetric stretching (CH_3- SS) modes were reported between 2936-2949 cm^{-1}, while the tetrol (hydrated at the ketonic carbonyl to form a geminal diol) had its methyl CH_3-SS slightly blue-shifted to 2972 cm^{-1}.[34] Therefore, the resonances at 2928 and 2957 cm^{-1} were assigned to the CH_3- SS modes of PYA and PYT, respectively. These assignments are further supported by the computational work discussed below.

As previously stated, for a small dicarbonyl like PA, the lower frequency at 2872 cm^{-1} would generally be associated with methylene stretching modes. [78] As neither PYA nor PYT contain CH_2 moieties, and no PA methyl stretching modes have been reported below 2900 cm^{-1}, this indicates the presence of surface-active PA oligomers with methylene moieties.

PA has been shown to form a number of stable oligomeric species, two of which are parapyruvic acid (PPA) and zymonic acid (ZYA).[45, 47, 48, 50, 53, 54] The formation of these species has been speculated to be surface mediated, but have not been previously examined specifically at the air-water interface. Furthermore, the formation of ZYA, PPA, and other oligomeric PA species are complex and subject to similar pH considerations discussed above for monomeric PA. However, for the purposes of this work, ZYA and PPA are assumed to be predominately protonated and therefore neutral.

Similarly, assessing if oligomers are present and ordered at the interface does not require determining absolute abundances of ZYA or PPA. Instead sufficient abundance can be extrapolated by determining if their contributions can account for this unassigned intensity in the VSF spectra.

ZYA does not contain methylene groups, but PPA does, making it a likely candidate for these modes. As such, the resonance at 2872 cm^{-1} has been tentatively assigned to the symmetric CH_2 stretching mode of PPA. Additionally, PPA and ZYA both have methyl groups, which would likely contribute some intensity to the ~2930 cm^{-1} and 2957 cm^{-1} features as well, but cannot be decoupled from those of PYA and PYT from experimental VSF alone.

Looking to the C=O stretching region (Fig. 6.2A,C), an intense broad feature at ~1750 cm^{-1} can be observed in both polarizations. This feature contains contributions from both the acid and keto C=O stretching modes of PYA, the C=O stretching mode of PYT, and potentially contributions and/or interferences from underlying water bending modes. This spectral congestion obfuscates attempts to interpret and assign these underlying features.

The *ssp* spectra (Fig. 6.2A) shows an additional peak to the red of the C=O at about ~1640 cm^{-1}. This is significantly lower than any reported values for either of the C=O stretching modes for either PA monomer, but is within the vicinity of the bending mode of water. The specific nature of the water bending modes is an active area of research, but in brief, water is currently thought to have two contributions at ~1640 and ~1750 cm^{-1}, corresponding to less-coordinated and more-coordinated water, respectively.[89-91, 93, 95, 96] While the specific contributions of water to the VSF H_2O

bending region is still not fully understood, the presence of water modes can be qualitatively probed via isotopic dilution studies.

Figure 6.3 displays VSF isotopic dilution spectra of PA solvated in H_2O (circles) versus D_2O (triangle) offset by concentration for 0.05M (pink), 0.25M (orange), and 1M (purple) PA. While the *ssp* data (Fig. 6.3A) does not show a clear change in intensity between the H_2O and D_2O in the lower frequency region (though an apparent red-shift in peak position is observed when solvated in D_2O, discussed further below), there is decreased intensity in the region underlying the C=O (~1750 cm^{-1}). The *sps* data (Fig. 6.3B) also demonstrate a change in intensity that indicates water contributions in the C=O region, as well as a clear decrease in intensity in the lower frequency region (~1640 cm^{-1}). These results confirm that ordered water is present at the air-water interface, even at higher PA concentrations. This is anticipated for these sorts of systems and has previously been reported in VSF studies of hydroxyacetone by Gordon et al..[78]

In addition to facilitating the identification of underlying water modes, isotopic dilution studies also show that the feature at ~1640 cm^{-1} persists in D_2O solutions (albeit slightly red-shifted), demonstrating that it must be arising from species other than monomeric PA or water. Thus, this peak is likely arising from a PA oligomer species. Additionally, the lack of *sps* response indicates that this mode must be predominately perpendicular to the air-water interface.

The presence of oligomeric species is supported by the studies by Perkins et al.[45] , in which abundant PPA and ZYA (as well as other oligomeric species) were isolated from PA solutions via distillation. This isolate will herein be referred to as ‘crude PPA and ZYA’. Perkins et al. reported a similar peak at ~1660 cm^{-1} in the FTIR spectrum of crude PPA and ZYA solutions, which the authors attributed to the C=C stretching mode of ZYA. That value is somewhat higher than the frequency seen here, but well within range for the C=C stretching modes of furan derivatives which extends to much lower wavenumbers, often being observed as low as ~1500 cm^{-1} [111, 112] and occasionally even below that.[113, 114]

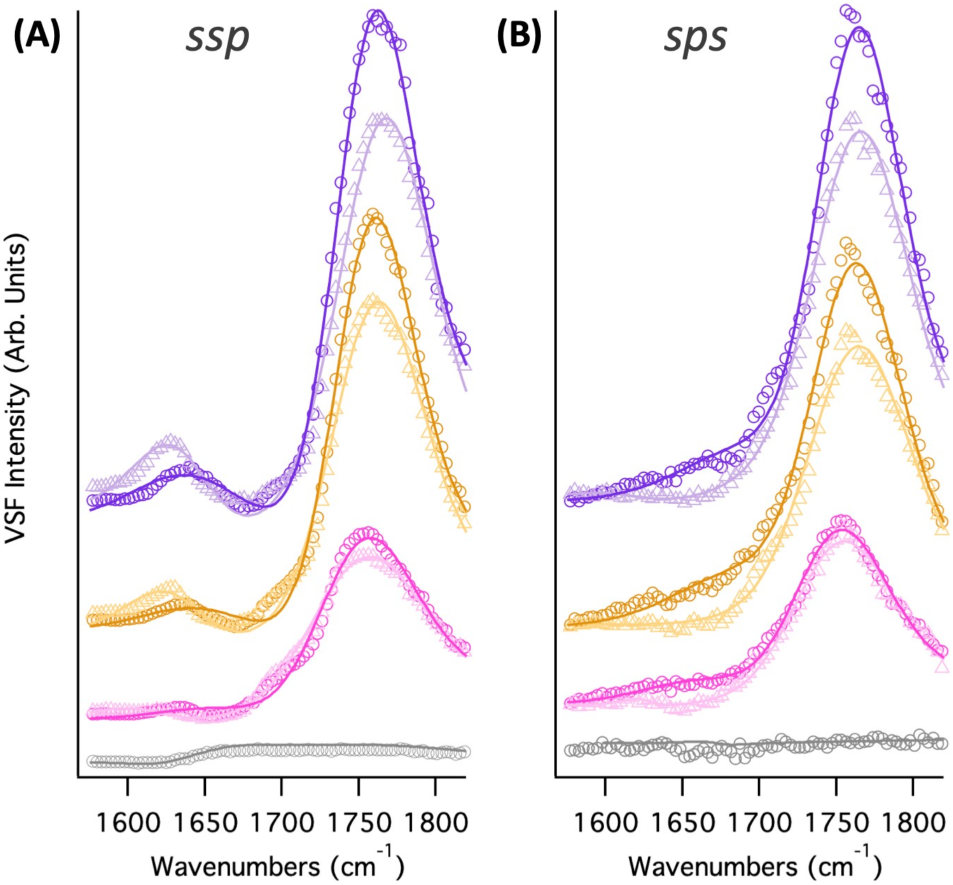

Figure 6.3. VSF spectra for PA in H_2O and D_2O: VSF Experimental spectra for PA in H_2O (open circles) and D_2O (open triangles) and corresponding fits (solid lines) in the C=C/C=O stretching regions in the *ssp* (A) and *sps* (B) polarization schemes for water (gray), 0.05M PA (pink), 0.25M PA (orange), 1M PA (Purple). Spectra are vertically offset for clarity.

As for the apparent shift in the C=C peak position in the experimental VSF *ssp* spectrum when solvated by D_2O (Fig. 6.3A), fitting confirms that the feature at ~1640 cm^{-1} undergoes a >10cm^{-1} shift to the red. This shift is not explainable by subtle differences in interference effects between H_2O and D_2O solvation and is most likely due to H to D isotopic exchange of ZYA hydroxyl groups. This is supported by DFT calculations of isotopically substituted ZYA, which confirmed that the C=C stretch frequency position is sensitive to such exchanges (Appendix D, Table D3.)

The VSF data provides solid evidence for the presence of oligomers at the water surface and is supported by characterization of oligomer species in previous literature studies.[45, 47, 48, 50, 53, 54] A combination of complementary surface tensiometry and computational methods can provide further details necessary to more thoroughly understand the molecular environment giving rise to these complicated VSF spectra.

Surface Tensiometry

Surface pressure isotherms for PA solutions (Fig. 6.4A) reveal higher surface activity than might be intuitively expected, given either the PYA or PYT monomeric forms, especially when compared to similar surface active species such as methylglyoxal (MG)[34] and hydroxyacetone HA.[78]

MG is another dicarbonyl with two populated hydration states and significant oligomer formation. While the MG diol to tetrol ratio was 60:40 in bulk,[35] at the air-water interface it was found to shift to 80:20.[34] Bulk studies also found that 53% of aqueous MG solutions consisted of dimers or oligomers.[16, 35-38] We recently reported on HA as a model system, due to its relative simplicity of being 96-98% in an unhydrated monomeric state.[78, 115]

It is interesting to note that HA, which has the most hydrophobic moieties of these organics, actually has the lowest surface activity. As previously stated, HA is also the only molecule that does not favor oligomer formation. With the context provided by MG and HA, it does appear as though surface activity and oligomer formation are correlated, the presence of interfacially active PA oligomers is likely the cause of this relatively high surface pressure.

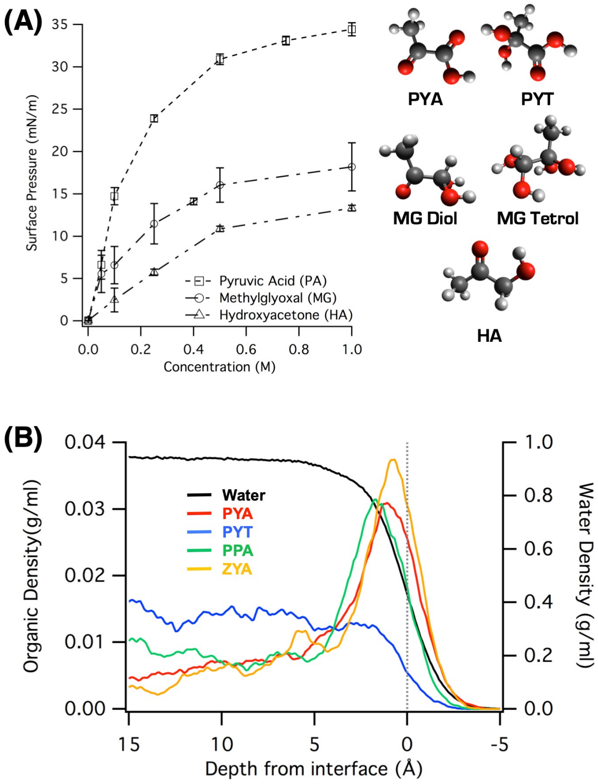

Figure 6.4. Experimental surface pressure isotherms and calculated density profiles: (A) Surface pressure as a function of organic concentration for PA, MG[34], and HA[78] at the air/water interface. (B) Density profiles of water (black) and organic residues obtained from the mixed PA simulation of 4 PYA (red), 4 PYT (blue), 4 PPA (green), and 4 ZYA. Each PA species has approximated 0.25M concentration and the four combined results in 16 total organics for ~1M total concentration. The dotted gray lines denote the approximate boundary between the surface (0 Å) and subsurface (5 Å).

Computational Results

The experimental results discussed in the previous section provide substantial evidence of additional molecular diversity at the surface of aqueous PA solutions. However, due to the complex equilibria (both hydration and oligomerization) and resulting spectral congestion endemic to this system, experiments alone cannot fully isolate the individual contribution and behavior of each species.

To bridge this gap, classical molecular dynamics (MD) simulations and quantum mechanical density functional theory (DFT) were used in combination to explore the depth dependent dynamics of each species considered in this work. Simulations of aqueous PYA, PYT, PPA, and ZYA in isolation (not shown) where not found to differ appreciably from mixed simulations containing one or more of the above residues. As such, this discussion will focus only on the mixed system of equal parts PYA, PYT, PPA, and ZYA, containing 4 of each species and totaling 16 molecules per simulation (corresponding to ~1M organic concentration.)

Density Profiles

Figure 6.4B displays the density profiles from the mixed simulation of PYA, PYT, PPA, and ZYA (left) as well as that of water (right). The interface, 0 Å, is defined as the 50% dividing line of the density profile of water.

PYA and PYT show a surface enhancement and a subsurface depletion, respectively. This depth dependent behavior of PYA and PYT is strikingly similar to that of the methylglyoxal diol (MGD) and tetrol (MGT), respectively.[34] That work concluded that the interfacial ratio of MGD to MGT was deviated from that of the bulk to favor the less hydrated MGD. Given the aforementioned similarities, it is plausible that a similar shift is occurring here, with a higher ratio of PYA to PYT at the air-water interface relative to the bulk.

What is notable however, are the density profiles of PPA and ZYA, which show substantial surface enhancement similar to that of PYA. Given the results of Figure 4B, PPA and ZYA would have enhanced surface population relative to the bulk, as well. This supports the conclusion that the presence of oligomeric PA species at the interface likely accounts for the higher than expected surface activity observed in experimental surface tensiometry of PA solutions shown in Figure 4A.

Calculated VSF responses

The density profiles demonstrated the favorable surface partitioning of the oligomeric PPA and ZYA species, in addition to PYA, but does not explain how they contribute to the observed experimental VSF spectrum. This question has been explored by calculating the VSF response for a representative subset of conformers of PYA, PYT, PPA, and ZYA. While significant work has been done in the literature on the conformational space of the monomeric forms of PA,[109, 110, 116-119] the same has yet to be done for ZYA and PPA. With the degree of spectral congestion arising from the numerous PA species, the interfacial conformational space of PYA and PYT cannot be computationally evaluated without considering ZYA and PPA, as well. However, generating responses for each of the multitude of conformers populated by PA and its oligomeric products is a significant undertaking and beyond the scope of the present work. Thus, for this initial treatment, the VSF responses have been calculated for a limited subset of conformers of PYA, PYT, PPA, and ZYA. The results of the DFT calculations and computed VSF responses for each of these is provided in Appendix E (Tables D1-D3).

Calculated VSF spectra generated using the computational methodology utilized here have been shown to reproduce the experimental VSF data for spectral regions arising from modes that are insensitive to solvation (such as CH stretching modes).[34, 71-78] This technique references only the gas-phase DFT structures of the organics and does not include contributions arising from water nor variations in those organic modes sensitive to their solvation environment. For this reason, the calculated response of the OH stretching region cannot be relied upon to the reproduce the experimental spectra. While not shown here, the calculated VSF responses of the organic OH stretching modes (as well as those of the other modes discussed here) are provided in Table D2.

Figure 6.5 shows the experimental VSF spectra for solutions of 1M PA (compared to the published FTIR spectrum of crude PPA and ZYA[45]) and calculated VSF responses for the mixed PA species simulation in the C=C/C=O stretching (Fig. 6.5A,B) and CH stretching regions (Fig. 6.5 C-F) and for both the *ssp* (Fig. 6.5 A-D) and *sps* (Fig. 6.5 E,F) polarization schemes. The calculated VSF responses in Figure 6.5 (B,D,F) are displayed in the form of 'stick spectra'. These stick spectra represent intensities and phases (positive intensity indicating positive phase, and vice versa) of the VSF response for the individual modes of each conformation of each species. This allows for comparison of pertinent areas of the experimental spectra with the corresponding stick spectra. As VSF is highly sensitive to phase, variations in local intensity can be explained by a superposition of resonances with mixed positive and negative amplitude (i.e. constructive or destructive interference). Examination of the phases and relative intensities of the calculated stick spectra can provide the context needed to decouple such interactions in the experimental results.

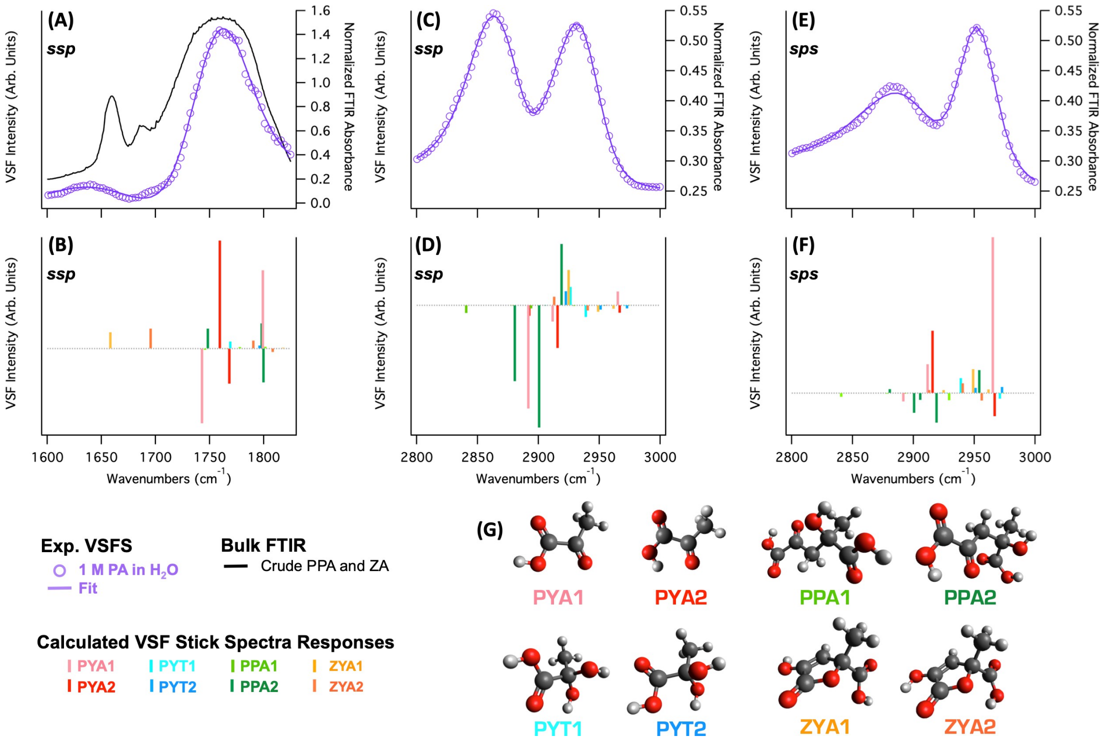

Figure 6.5. Experimental vs. Calculated *ssp* PAVSF spectra from the mixed PA species simulation in the C=C/C=O (A,B) and CH (C-F) stretching regions.
TOP (A,C,E): Bulk FTIR spectra of crude PPA and ZYA[45] (black) compared to *ssp* (A,C) and *sps* (E) experimental VSF spectra of 1M PA (purple, data=markers, fit= lines).
MIDDLE (B,D,F): Calculated intensities and phases for the individual conformer contributions in the *ssp* (B,D) and *sps* (F) polarizations for each PA species, color coded to their respective structures in (G), where positive and negative intensities represent phases of zero and pi, respectively. DFT frequencies x-scaled by 0.9875 for the CH stretching region.
BOTTOM (G) Gas phase DFT structures of each PA species considered at the B3LYP/6-311++G (2d,2p) level of theory.

The calculated stick spectra (Fig. 6.5B) show that all four PA species contribute to the feature observed in the experimental C=O stretching region at ~1750 cm^{-1} (Fig. 6.5A). However, only ZYA has resonances in the lower frequency C=C stretching region. As previously discussed, in the C=C/C=O stretching region Perkins et al. identified a peak at ~1660 cm^{-1} in the FTIR spectrum of crude PPA and ZYA (Fig. 6.5A) as arising from a C=C oscillation.[45] Based on that work, the feature at ~1640 cm^{-1} in the experimental VSF spectrum of aqueous PA (Fig. 6.5A) is also attributed to a C=C stretching mode of ZYA oligomers naturally occurring within PA solutions. Figure 6.5B shows that the calculated VSF responses support this assignment, as the C=C modes of ZYA1 and ZYA2 at 1658 and 1695 cm^{-1}, respectively, are the only spectral contributions of any species below 1700 cm^{-1}. Interestingly, closer examination of the FTIR spectrum shows a second peak at ~1685 cm^{-1}, which is intriguingly close to both the dip centered at ~1685 cm^{-1} in the experimental VSF spectrum and the calculated VSF response at 1695 cm^{-1} from the C=C stretching mode of ZYA2. Further work will need to be done to explore if in fact a second, higher frequency C=C resonance could be present at the interface, and if so, perhaps destructively interfering with adjacent modes to produce the dip observed in the experimental VSF spectrum.

In the CH stretching region, the experimental *ssp* VSF spectra (Fig. 6.5C) shows two regions of significant intensity (~2860 and ~2940 cm^{-1}) on either side of a lower intensity region (~2900 cm^{-1}). Insight is gained once again from the calculated VSF responses: the corresponding stick spectra (Fig. 6.5D) show both PYA and PYT contribute little to no intensity to the feature at ~2860 cm^{-1}, while PPA does, particularly the PYA2 conformer. Furthermore, it can be seen that when including the resonances of both monomeric and oligomeric species, the combined phase interactions reproduce the observed experimental intensities: the responses in the ~2860 and ~2940 cm^{-1} are largely negative in phase while the ~2900 cm^{-1} is predominantly positive, resulting in constructive interferences in the high and low frequency sides of the spectrum and destructive interferences in the central region.

Similar results are seen for the *sps* CH stretching region (Fig. 6.5 E,F), where once again the inclusion of PPA resonances provide intensity to the lower frequency region where a feature is observed at ~2860 cm^{-1} in the experimental VSF spectrum. Likewise, destructive interference from the intense and oppositely phased responses at ~2920 cm^{-1} line up well with the dip in the experimental spectrum at the same position.

Notably, in both the *ssp* and *sps* calculated CH spectra, it can be seen that the CH_3-SS modes of PYT occur slightly to the blue of PYA's (supporting the experimental fits). Additionally, the calculated responses indicate the asymmetric stretching (AS) modes of all constituents have strong *sps* responses, but are negligible in the *ssp*. This is in agreement with known selection rules of VSFS[84] and could account for the apparent frequency shift between polarization schemes of the ~2940 cm^{-1} feature in the experimental VSF spectra. While AS modes have not been included in the experimental fits, these results indicate their likely contribution to the *sps* spectrum.

The computational results demonstrate that along with PYA and PYT, both PPA and ZYA are surface active. With this additional evidence, it becomes clear that these oligomers are significant contributors to interfacial population. Even with only a limited subset of conformers, PPA and ZYA have been shown to have strong VSF responses that can account for the additional features observed in the experimental spectra, and thus merit a full computational workup in the future.

Conclusions

Surface tensiometry (ST) and vibrational sum frequency (VSF) experimental results of aqueous PA solutions along with computational results for simulations of monomeric PA (PYA, PYT) and two PA oligomer species (PPA and ZYA) have been presented. These results demonstrate that the experimental VSF spectra contain strong responses arising from vibrational modes of functional groups not found in the monomeric forms, suggesting the presence of oligomeric species at the interface. ST of the neat-PA systems revealed higher than anticipated surface activity, further indicating the contributions of additional interfacially active species. While the formation of favorable PA oligomeric reaction products in the bulk have been well documented, their presence at the air-water interface and relative surface affinity had not been previously established. The computational results demonstrate that along with PYA and PYT, both PPA and ZYA are surface active and have strong VSF responses that can account for the additional features observed in the experimental spectra.

As previously stated, PPA and ZYA are just two of many possible oligomeric species known to form from PA. Furthermore, numerous other secondary organics have been shown to form favorable oligomer species This system and many others would benefit from further and more detailed exploration using more focused experimental and computational techniques, such as, respectively, phase sensitive Heterodyne-Detected sum frequency generation spectroscopy (HD-SFG) [93,98] and DFT calculations of microsolvated structures.[75]

As larger molecular weight species can have substantial impact on aerosol properties, these are significant findings for the atmospheric community. The specific implications of the presence of interfacially active oligomers and their affect on the chemistry of said interfaces will require further work, but the current finding are sufficient to demonstrate the presence of these oligomers at the interface.

CHAPTER VII

The Influence of NaCl on Methylglyoxal Surface Adsorption and Hydration State at the Air-Water Interface

The contents of this chapter have been or are intended to be published in whole or in part. The text presented here has been modified from the publication below:

Gordon, B. P., Wren, S. N., Moore, F. G., Scatena, L. F., Richmond, G. L. Diol it up: The Influence of NaCl on Methylglyoxal Surface Adsorption and Hydration State at the Air-Water Interface. **To be submitted to Journal of Physical Chemistry A in December 2019*

Bridge

Methylglyoxal (MG) – an atmospherically important α-dicarbonyl implicated in the aqueous-phase secondary organic aerosol formation – is known to be surface active. Due to the presence of carbonyl moieties, MG can hydrate to form geminal diols in solution. Recently, it has been shown that MG exists predominantly as methylglyoxal monohydrate at the neat air-water interface. However, inorganic aerosol constituents have the potential to 'salt-out' methylglyoxal to the interface, shift its hydration equilibria, and catalyze self- and cross-oligomerization reactions. Here, we study the influence of the non-reactive salt, sodium chloride (NaCl), on MG's surface adsorption and hydration state using vibrational sum frequency (VSF) spectroscopy. We show that the presence of NaCl significantly enhances MG's surface activity, while perturbing the water structure at the interface. Possible shifts in MG's hydration state are discussed. This work builds on the published studies on MG in pure water and allows identification of how the system is perturbed by the presence of NaCl, which has important implications for understanding MG's atmospheric fate.

Introduction

Secondary organic aerosols (SOA) have far reaching effects on both the climate and human health. Aerosols influence the climate directly by scattering and absorbing light and indirectly by acting as nucleation sites in cloud formation. [1, 2] Aerosol composition is complex and varied, and consists of both inorganic and organic constituents. [3-6] Due to the high surface area to volume ratio of aerosols, molecules at aerosol surfaces play a particularly large role in their atmospheric chemistry. [7,8] Additionally, the presence of organics and salts can significantly affect SOA properties.[1-8] However, because of the complexity of SOA, much of how these components (individually or in concert) affect aerosol behavior remains unknown. This lack of knowledge makes predicting formation and aging of SOA in the atmosphere very challenging and currently a large source of error in atmospheric modeling.

Methylglyoxal (MG) is an atmospherically import and abundant α-dicarbonyl and the uptake and aqueous phase processing of MG has been shown to be an important source SOA. However, the chemistry underlying this SOA formation and subsequent aging is still uncertain due to the inherent complexity of MG, as it has multiple populated hydration states (a single hydrated diol and a doubly hydrated tetrol) [9, 10] and also forms stable oligomer products with itself and other molecules.[x]5, 11-14

The unhydrated methylglyoxal monomer (MGM) hydrates preferably at the aldehydic carbon (α-C) to form methylglyoxal monohydrate (or methylglyoxal diol, MGD) in aqueous solution. The monohydrate can subsequently be hydrated at the ketonic carbon (β-C) to form methylglyoxal dihydrate (or methylglyoxal tetrol, MGT). Both experimental studies [9] and thermodynamic calculations [15] suggest that methylglyoxal exists in a hydrated form in the bulk, with a MGD to MGT ratio of ~60:40. The hydration of MG has also been shown to be depth dependent as well. Wren et al. [10] demonstrated that this ratio is shifted at the air-water interface to favor the diol (~90% MGD to ~10%

MGT). This is due to the less favorable solvation environment at the water surface and the lower surface affinity of MGT relative to MGD.

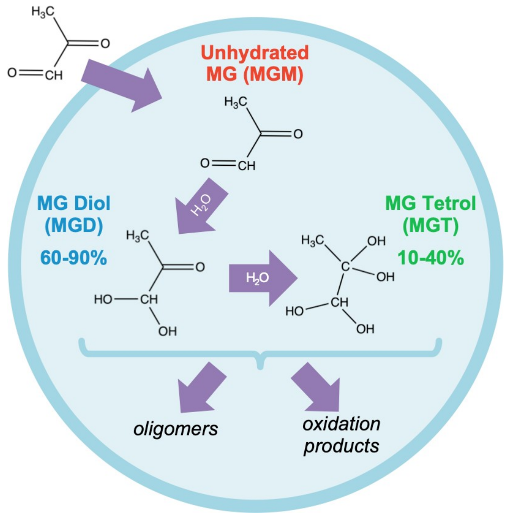

Figure 7.1: In-cloud aqueous phase processing[9-10] of unhydrated (MGM), singly hydrated (MGD), and doubly hydrated (MGT) methylglyoxal.

We have previously reported on the identification of oligomer species at the interface.[16] MG readily forms a large variety of oligomers which include self reactions with other MG as well as combining with other organics and reactive-salts. [5, 11-14, 17] In fact, De Haan et al. reported that in aqueous MG solutions, only 53% of the actual molecular species were monomeric MG. [12] Of the remaining constituents MG dimer and oligomer products were found to account for 37% and pyruvic acid (PA) and hydroxyacetone (HA) each accounted for ~5%.[12] However, those experiments were performed in neat water, which is not representative of the high ionic strength found in atmospheric particulates. [1-8, 18] Alone, atmospheric salts can affect water structure at the air-water interface (i.e., the aerosol surface), in turn altering aerosol hygroscopicity and surface tension. . [3-5] The presence of salts, and corresponding change in the activity of water, can also shift the hydration equilibrium of organics with multiple hydration states. [11, 19] Salts also have the potential to influence the uptake of MG and other organics to the condensed phase (via 'salting-in' and 'salting-out' effects), as well as to catalyze and participate in oligomerization reactions leading to SOA formation. [3, 6,20]

Here, 'salting-out' refers to enhanced bulk to surface partitioning of organics component to the interface. Conversely, 'salting-in' refers to instances where salt increases the solubility of a molecule, which can increase uptake of organics to aerosol from the gas phase. [3, 6, 18, 20-22]

Considering the multiple favorable hydration and oligomer species that form spontaneously in MG solutions, it is clear that this system cannot be treated as a single organic and instead should be viewed as a mixed system. This distinction is important as it has been observed that aerosols with multiple organic species can have unpredicted synergistic effects on aerosol surface tension and hygroscopicity, particularly in the presence of salt. [6, 23] These effects have been ascribed to the adsorption of mixed organics to the particle interface and exceed what would be expected based on predictions from bulk properties.[6,23] Changes in these properties can have important atmospheric consequences, such as enhancing aerosol cloud nucleation activity. [1-3, 6, 23]

In this study, the influence of the non-reactive salt NaCl on MG's surface behavior at the air-water interface is examined using vibrational sum frequency (VSF) spectroscopy and surface tensiometry. A combination of computational density functional theory (DFT) and molecular dynamics (MD) are employed to further decouple and understand the interfacial species of this system. The results indicated the hydration equilibrium of MG is further shifted to favor the diol as the predominant species at the interface, with lesser amounts MGT. However, MGD is not alone at the interface and is joined by what is likely a multitude of oligomeric species in lower concentrations. This work has implications for understanding the atmospheric fate of methylglyoxal and other important α-dicarbonyls.

Methods

Vibrational Sum Frequency (VSF) Spectroscopy Theory

Vibrational sum frequency (VSF) spectroscopy is a surface selective technique ideally suited to the study of molecules at interfaces. VSF spectroscopy is a well- established technique .[10, 24-59] and only a brief description is provided here. A fixed- frequency visible (VIS) is overlapped spatially and temporally with a tunable IR beam at an aqueous surface, producing a third beam at the sum of the two incident frequencies (the sum frequency beam). When the IR field is coincident with a vibrational mode that is both IR and Raman active there is a resonant enhancement in the intensity of the sum frequency (SF) beam. Selection rules additionally require that the vibrational mode reside in a region of broken symmetry, hence molecules residing in an asymmetric environment (such as that present at an interface) give rise to a SF response while those residing in a symmetric environment (the isotropic bulk) do not.

The intensity of generated SF signal is proportional to the square modulus of the second-order susceptibility, $\chi^{(2)}$, which has both resonant and nonresonant components. The resonant component is proportional to the number of contributing molecules, *N*, and the orientational average of the molecular hyperpolarizability, β. Therefore VSF spectra contain information about surface population and orientation.

VSF spectroscopy is a coherence technique leading to the constructive and destructive interference of overlapping modes. A standard fitting routine is used to deconvolve the nonresonant signal and the individual resonant modes.[24]:

$$!^{(!)} = !^{(!)}_{!''} !^{!''} + \sum_{!} \int^{!}_{!!} \frac{!_!! \, ! \, ! \, !^{!!! \, -[! \, !!!/!!]^{!}}}{!!!!!'' !!!!} \, !! \qquad (7.1)$$

The first term is the nonresonant second-order susceptibility and is described by an amplitude and a phase, ψ. The second term describes the resonant contribution and is a sum over the individual resonant vibrational modes. The line shape of each mode is fit as convolution of empirical homogenous, Γ_L, and inhomogeneous broadening, Γ_v. The amplitude, A_v, describes the transition strength and contains the product of the number of contributing molecules and the IR and Raman transition probabilities. The frequencies of the Lorentzian, IR, and resonant vibrational mode are given by ω_L, ω_{IR}, and ω_v respectively. The phase of each resonant mode is given by φ_v and is either 0 or π. In this work, Lorentzians of 2 cm^{-1}, 5 cm^{-1} and 12 cm^{-1} were used to describe the CH, both the coordinated OH and C=O, and the 'free OH' vibrational modes respectively. [60-63]

Laser System

VSF spectra were obtained using a picosecond sum frequency system that has been fully described elsewhere. Gordon, 2018 #326; Gordon, 2019 #373} Briefly, a mode-locked Ti:Sapphire system in tandem with an ultrafast regenerative amplifier is used to produce a pulsed visible (VIS) beam centered at 800 nm. A portion of the visible beam is sent through an optical parametric amplifier (OPA) in tandem with a difference frequency generator (DFG) to produce a tunable IR beam (2.5 – 12 µm). The visible and IR beams are copropagated to the interface at 63° and 55°from the surface normal, respectively. The resulting sum frequency beam is detected using a thermoelectrically-cooled CCD camera. Samples are held in scrupulously clean, shallow glass dishes on a translatable stage.

Spectral Analysis

VSF spectra were acquired by measuring the intensity of the SF beam as the tunable IR beam was scanned in 3 cm^{-1} increments over the relevant spectral range (~2700 – 3850 cm^{-1} for the CH/OH stretching region, ~1500 – 1850 cm^{-1} for the C=C/C=O stretching region). Spectra were acquired in the *ssp* and *sps* polarization schemes where the three letters denote the polarizations of the sum frequency, visible and IR beams respectively. The different polarization schemes allow different molecular orientations to be probed with *ssp* and *sps* probing molecular dipole components perpendicular and parallel to the interface respectively. All spectra presented here have been normalized to the nonresonant response off an uncoated gold surface. IR wavelengths were calibrated daily against a polystyrene standard. Presented spectra are averages from > 3 scans. All measurements were performed at ambient temperature (~20 ˚C).

Surface Tensions Measurements

Surface tension measurements were performed using the Wilhelmy plate method. Solutions were placed in a clean glass dish, and a Pt plate was lowered to the air-water water interface. A force balance (KSV Instruments) measuring the force acting on the Pt plate, was used to obtain surface tension (mN m^{-1}) data as a function of time (s). Surface tensions (γ) were converted to surface pressures (π) by subtracting the daily-measured surface tension of water. The Pt plate was rinsed with nanopure water and cleaned under flame between measurements.

Sample Preparation

Aqueous MG solutions were prepared volumetrically by diluting an aqueous stock MG solution (40 wt%, Sigma Aldrich) in nanopure (18.2 MΩ cm) water. The NaCl salt (ACS grade > 99.0%, EMD Chemicals) was baked at 220 ˚C for at least 48 hours before use to eliminate organic contaminants. Solutions were prepared ≥ 24 hours before use and stored in Pyrex glass flasks. Solutions were not further protected since photochemical degradation was not a concern. [3]

Computational Methods

Molecular dynamics (MD) simulations are performed using the Amber 12[64] suite of programs from starting configurations generated by PACKMOL. .[65] Parameters and force fields are derived in the same manner described in previous studies. [10, 31-38] Simulations of pure systems refer to those previously reported for neat-MG and were not repeated here. Classical molecular dynamics (MD) simulations were performed for systems of isolated nonreactive MG hydration species and 1M NaCl. In each simulation, 16 MG, 16 NaCl, and 900 water molecules are arranged to form a 30 Å cube within a 30 Å x 120 Å x 30 Å simulation box (corresponding to ~1M organic and salt concentrations) with periodic boundary conditions, creating a water slab with two interfaces. These simulations are energy minimized at 0 K and then equilibrated from 0 K to 298 K over 2 ns followed by subsequent evolution at 298 K for 50 ns in 1 fs time steps.

The results of these simulations were combined with quantum mechanical density functional theory (DFT) conformer libraries created for the previously reported neat-MG using the Gaussian 09[66] program package at the B3LYP /6-311++G(2d,2p) level of theory. These DFT libraries include energy optimized stationary point structures, harmonic frequencies and anharmonic correction, as well as polarizabilities and dipole moment derivatives calculated using three-point finite differentiation. MD trajectories are analyzed at every time-step to match molecule conformations the library of gas-phase DFT structures using an in-house code. [31] Density profiles, and bond angle orientations are determined for each MG hydration species.

To generate VSF intensities and phases, the code combines the MD and DFT results to approximate the second-order nonlinear susceptibility response tensor for each normal mode of a given MG conformer according to Equation (2).

$$!^{(!)}_{!"\#} \propto \sum_{!,!,!} !_{!"\#} \frac{!!_{!"}}{!!_{!}} \frac{!!_{!}}{!!_{!}} \tag{7.2} $$

In Equation (2), α is the molecular polarizability, μ is the dipole moment, Q_q is the normal coordinate of the mode q, and C is a geometrical factor relating the molecular and laboratory reference frames.

The results from simulations of mixed MGD and MGT were not found to differ appreciably from simulations of “pure” hydration species. As such, this discussion will include only the results of the pure simulations of 16 molecules (~1M organic concentration) of MGM, MGD, or MGT (only one type of hydration species per simulation.)

Experimental Results and Discussion

Surface Tension

Surface pressure isotherms at constant NaCl concentration (0 M and 3 M) and varying MG concentration are shown in Figure 7.2A. Methylglyoxal in neat water has previously [3, 10] been shown to be strongly surface active, with a maximum surface pressure > 15 mN/m. The addition of 1M NaCl further increases this surface activity by ~3 to 5 mN/m on average. Sareen et al. [3] also measured the surface tension of mixed NaCl-MG systems and found that the presence of NaCl enhances MG's surface activity (up to 10 mN/m for 5.1M salt). They attribute the enhanced surface activity to a salting- out influence of NaCl. However, it is important to note that the salting-out affect of NaCl is significantly less than other salts. [3, 18] Indeed, the overall increase in SP with the addition of salt is somewhat minimal when viewed in context of the surface pressure isotherm of other similar organics.

The surface pressures isotherms of pyruvic acid (PA)[16] and hydroxyacetone (HA) [38] are also displayed in Figure 7.2A. Similar to MG, PA is a dicarboxylic acid with two favorable hydration states (unhydrated PA and a hydrated PA triol, Fig. 7.2B, top) as well as a multitude of oligomer products such as zymonic acid and parapyruvic acid. [16, 19, 67-79] Conversely, HA is an α-hydroxyketone that is known to exist 96-98% in its unhydrated monomeric form in aqueous solutions (Fig. 7.2B, bottom). [38, 80] HA is very similar in structure to the MG diol, differing only in having a second hydrogen atom in place of one of MGD's geminal diols.

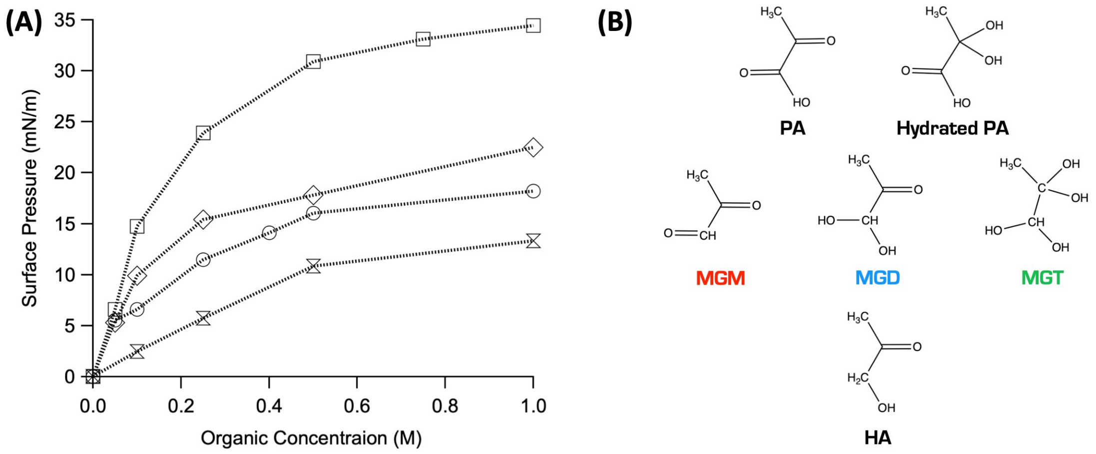

Figure 7.2. Surface pressure isotherm vs. organic concentration for MG and MG-NaCl: **(A)** Surface pressure as a function of bulk methylglyoxal concentration for aqueous solutions with 0 M NaCl (circles, from Wren et al., 2015[10]) and 1 M NaCl (diamonds). SP isotherms of hydroxyacetone (hourglasses)[38] and pyruvic acid (squares)[16] are provided for context. **(B)** Structures of PA, MG, and HA.

Even with the addition of salt, the SP values of MG are significantly lower than those of PA for the same concentration while HA is definitively lower than neat-MG. This is interesting given the more polar character of PA, particularly in its triol form, would ostensibly be more soluble than MG while HA, being slightly more hydrophobic with its additional CH, would be expected to be more surface-active than HA. However, this is clearly not the case.

Given that MG and PA share the preference to hydrate and form oligomers while HA does not, it seems likely that these additional products are contributing to the measured surface pressures. In fact, Gordon et al. have recently published work demonstrating the presence of surface-active PA oligomers at the air-water interface. It is also worth noting that VSF studies of both PA and HA show ordered water at the interface at 1M. Given that water remains at the interface at higher SP than those seen for MG-NaCl, it is unlikely that the ~3-5 mN/m increase upon the addition of NaCl is enough to exclude water from the interface in MG solutions. Overall, it becomes clear that while salt definitely increases surface partitioning in MG solutions, other factors are at play as well.

VSF Spectroscopy Results

We have previously reported on MG's surface behavior at the air-water interface. [10] However, since that time a significant number of improvements to the picosecond laser system have resulted in much-increased signal to noise, yielding superior data and revealing spectral features previously buried in, or nearly in, the noise level. This has allowed for a more in-depth analysis and resulting fits than was previously available. As such, updated spectra (Figure 7.3) and fitting assignments (Table 7.1) of the MG-Neat water system will be included this discussion.

VSF spectra were acquired in the *ssp* and *sps* polarizations of the C=C/C=O (Fig. 7.3A,D), C-H (Fig. 7.3B,E), and O-H (Fig. 7.3C,F) stretching regions for neat water and 1M MG with varying NaCl concentration (0.01, 0.05, 0.1, 0.25, 0.50, and 1 M). A brief discussion on the VSF spectra of neat water is provided in the Appendix E. Each spectral region contains strong VSF responses arising from MG and dramatic changes are observed upon the addition of NaCl.

In Brief, at the neat air-water interface, shows strong contributions from MG are visible in the C=O, CH, and OH stretching regions. A notable feature in the neat-MG spectrum is the enhancement of coordinated OH stretching modes between 3100 -3600 cm^{-1}. The additional of salt appears to suppress this coordination while also the intensity of the lower frequency CH stretching modes increases. While the reasons for these changes may initially seem straightforward, such as increased surface partitioning, careful examination of the results reveal a much more interesting picture.

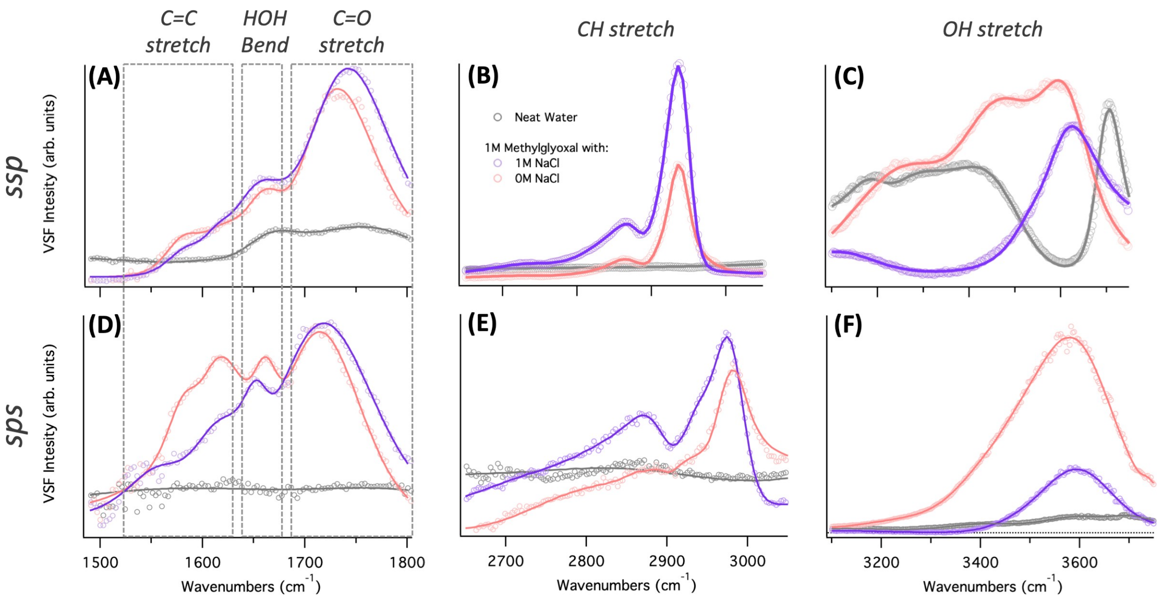

Figure 7.3. VSF Experimental spectra for MG and MG-NaCl in H_2O: VSF Experimental data (open circles) and corresponding fits (solid lines) for water and aqueous MG and MG-NaCl in the *ssp* (A,B,C) and *sps* (D,E,F) polarization schemes for the C=C/C=O stretching region (left), and the CH stretching region (middle), and the OH stretching region (right). Water (gray), 1M MG (pink,) and 1M MG with 1M NaCl (purple). Dotted boxes (A,D) provide visual reference of approximate spectral regions.

CH Stretching Region

As has been previously reported, MGD and MGT have distinctive spectra contributions in the CH stretching region, as is demonstrated in Figure 7.4 by comparison of the experimental spectra (Fig. 7.4A,C) to the calculated sum frequency responses (Fig. 7.4B,D) The calculated VSF intensities and phases (herein referred to as ‘stick spectra’) of each individual mode of each conformer MGM, MGD, and MGT (color coded to their respective structure in Fig. 7.3E, with positive intensities indicating positive phases, and vice versa. These stick spectra provide invaluable insight into the how individual contributions give rise to the overall spectrum and were used in combination with the calculated density profiles to determine he diol to tetrol ratio is greater at the interface than in the bulk, favoring the diol (40% MGD to 60% MGT in the bulk [9] versus 90% MGD to 10% MGT at the interface[10]

For the neat-MG system, two broad features dominate the CH stretching region (Fig 7.4A,C). In both polarizations, a broad lower frequency peak between 2860 cm^{-1} and 2870 cm^{-1} is attributed primarily to the α-CH stretching mode of MGD (blue). The higher frequency peak is centered at ~2935 cm^{-1} and ~2975 cm^{-1} for the *ssp* and *sps* polarizations, respectively, and is contains contributions from both the symmetric methyl stretching mode of MGD (blue) and the α-CH stretching mode of MGT (MGT). Another important feature in the *ssp* polarization, spectrum is the lower energy shoulder centered at ~2980 cm^{-1} which has previously been found to primarily arise from the symmetric methyl stretching mode of MGT. Similarly, the *sps* polarization spectrum also exhibits a shoulder on the high energy side of the region. This shoulder is centered at ~3000 cm^{-1} and contains responses from the asymmetric methyl stretching modes of both MGD and MGT.

The addition of salt creates distinct intensity changes in CH stretching region, but fits revealed no appreciable shift in frequency position. In both polarizations, the two dominant spectral features dramatically increase in intensity with increasing salt but the intensity of the high frequency shoulders also sharply decreases. Spectral fitting indicates the intensity changes observed in the coordinated OH region (discussed further below) do not affect the CH stretching fit intensities and thus do not account for this behavior. As these intensity changes are consistent between polarizations, they cannot be explained by

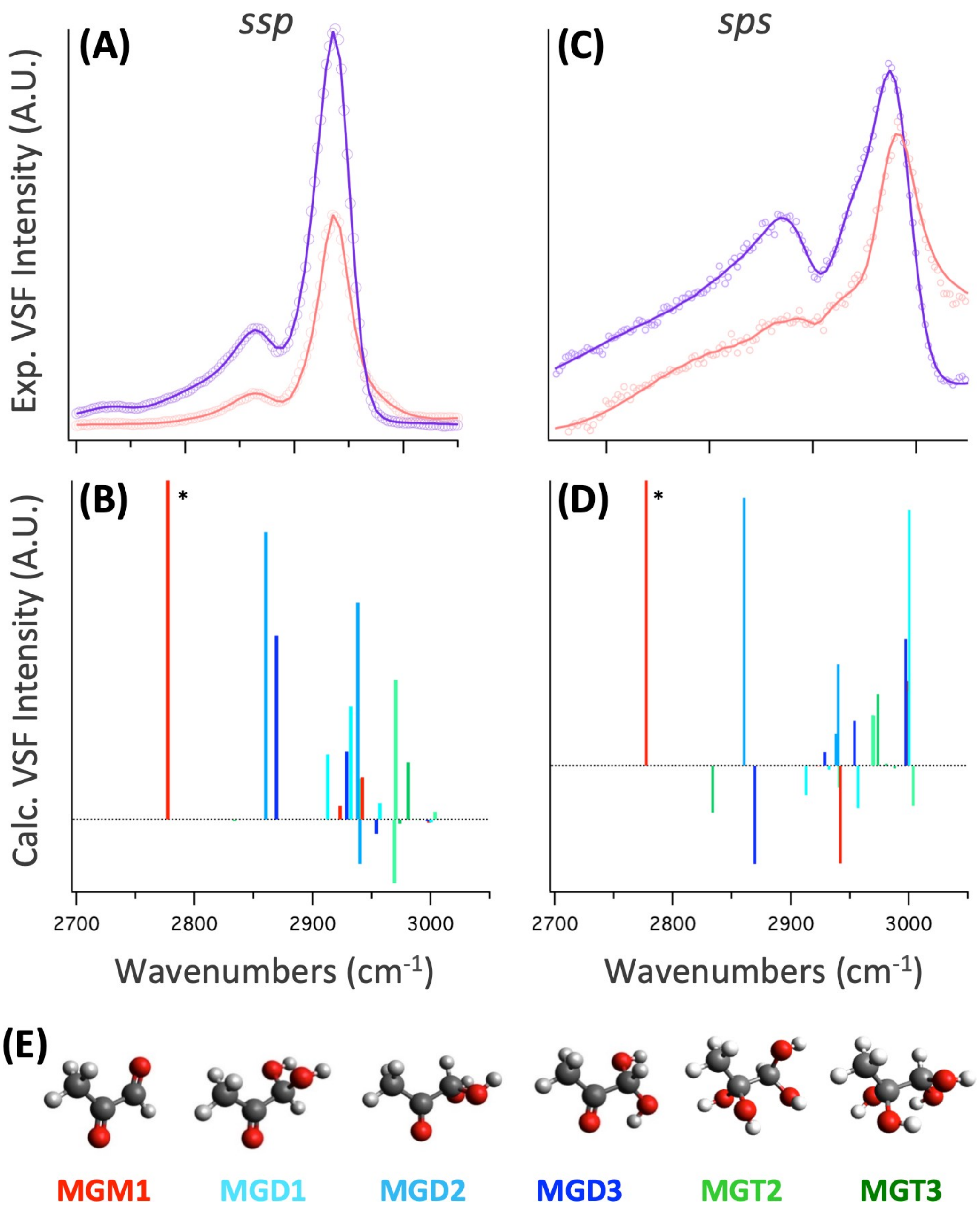

Figure 7.4. Experimental VSFS MG and MG-NaCl vs. Calculated VSF stick spectra: Experimental vs. Calculated VSF spectra from MG species simulation in CH stretching regions.

TOP (A,C): *ssp* (A) and *sps* (C) experimental VSF spectra of 1M MG (pink) and 1M MG with 1M NaCl (purple)

MIDDLE (B,D): Calculated intensities and phases for the individual conformer contributions in the *ssp* (B) and *sps* (D) polarizations for each MG conformer, color coded to their respective structures in (E), where positive and negative intensities represent phases of zero and pi, respectively.

BOTTOM (E): Gas phase DFT structures of each MG conformer at the B3LYP/6-311++G (2d,2p) level of theory.

reorientation. Likewise, the intensity does not uniformly increase and so cannot be entirely justified by increased surface population, either.

As previously stated and demonstrated in Figure 7.4B,D, the lower frequency feature at 2870 cm^{-1} is arises primarily from MGD while the majority of MGT contribution occur above 2940 cm^{-1}. Given this, it becomes clear in the MG-NaCl system, there is an overall increase in intensity for modes associated with MGD (and potentially MGM). Conversely, modes associated with MGT decreased in intensity, indicating that these changes are related to MG's hydration equilibrium.

It is worth noting that in both polarizations a broad low intensity region centered around ~2725 cm^{-1} extends to the low frequency side of the spectrum, which also increases with added NaCl. This intensity could be arising from two potential sources: (1) the aldehydic CH stretching mode of MGM[10] and/or (2) OH stretching modes from hydrogen bonded carboxylic acid dimers of MG oligomer products. [67] Option 1 would be in line with a shift in the MG equilibrium towards its less hydrated forms while option 2 could indicate an increase in MG oligomer formation, which has been observed with the loss of water in drying studies of MG. While the source of this mode cannot be resolved here, either of these options indicates noteworthy chemistry is occurring at the interface.

C=C/C=O Stretching & HOH Bending Region

The region from ~1500-1800cm^{-1} has a high degree of spectral density, containing modes from MG C=O stretching, water bending, and (as will be demonstrated below) C=C stretching modes from MG oligomers.

Based on the evidence in the CH stretching of a further hydration shift, it is important to determine if water is still contributing to the interface. While the intensity in the coordinated OH stretching region is largely suppressed in the MG-NaCl system, it is possible that less coordinated water is contributing to the peak at ~3650 cm^{-1}. While such contributions cannot be experimentally decoupled from those of the MG-OH stretching modes of MGD and MGT, the bending modes of water are spectrally distinct from those of MG. However, for both the *sps* and *ssp* polarizations, there still appears to be a contribution at ~1664 cm^{-1} when NaCl is present in the bending region. This is coincident the water bending mode of water (Fig. E1) so this is likely arising from ordered interfacial water. This is supported by comparison to PA and HA.

Figure 7.5A shows the C=C/C=O stretching region of water, neat 1M MG, and 1M MG with 1M NaCl. Also in Figure 7.5 and offset for clarity are 1M HA (orange) and 1M PA (green) solvated in H_2O (circles) and D_2O (triangles). While the water bending mode is less clear in PA, its absence can be seen in decreased intensity in C=O stretching region when solvated in D_2O.

In this region, both polarizations exhibit a broad peak at ~1575 cm^{-1}. Comparison to PA can once again lend insight, as a similar feature at ~1630 was found to arise surface-active PA oligomers including zymonic acid (ZYA). Numerous studies has established the production and mechanistic pathways of MG oligomers that contain C=C moieties. While it is not possible to identify the specific oligomer from this alone, we are confident in attributing this feature to general C=C stretching modes of MG oligomers.

Interestingly, the intensity of this peak decreases in both polarizations with the addition of salt. As the decrease in intensity in one polarization does not correspond to increase in the other, this loss is not simply a due reorientation. An intriguing possibility is that the higher ionic strength drives the oligomerization equilibrium to favor these species less. However further work would need to be done to better understand the mechanisms producing such species as well as how they may be affected by non-reactive salts.

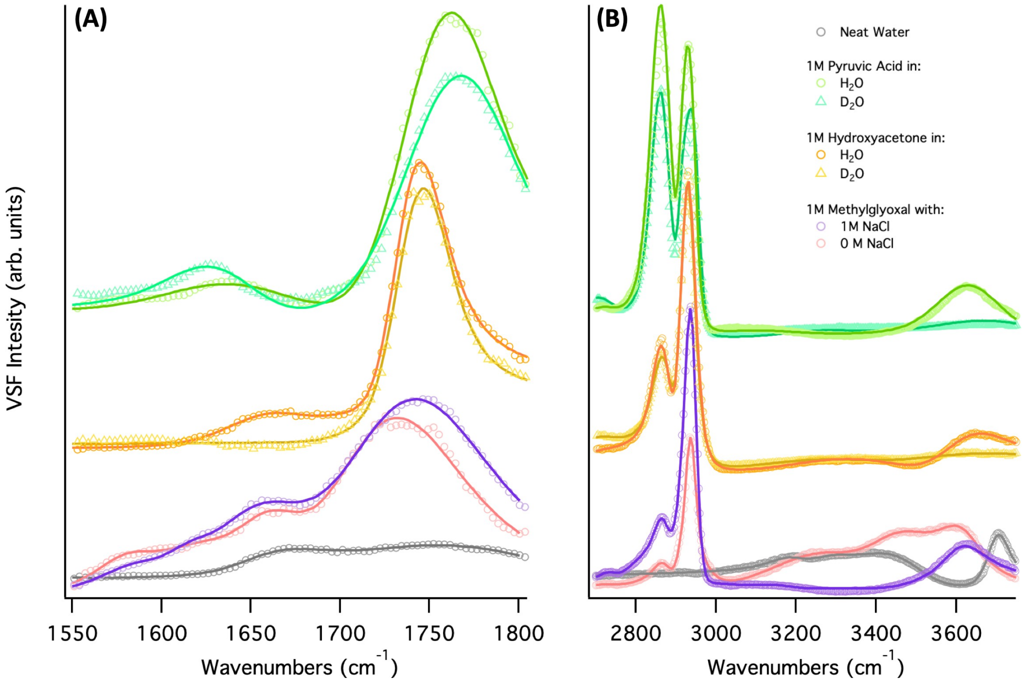

Figure 7.5. VSF spectra for MG and MG-NaCl vs. HA and PA in H2O and D2O: VSF Experimental *ssp* spectra in H_2O (open circles) and D_2O (open triangles) with corresponding fits (solid lines) in the (A) C=C/C=O and (B) CH/OH stretching regions for: **(BOTTOM)** 1M MG and 1M MG (pink) with 1M NaCl (purple); **(MIDDLE)** Offset 1M HA in H_2O[38] (yellow) and 1M HA in D_2O[38] (Orange); **(TOP)** Offset 1M PA in H_2O[16] (dark green) and 1M PA in D_2O (light green).

This suggestion of oligomers is compelling, but unlike PA, there are no other clear indications of oligomeric species at the interface. Additionally, the C=C mode observed here is significantly broader than that in PA. Likely, this means that there is a larger assortment of oligomeric species populated. Thus instead of yielding strong, relatively sharp resonances, MG oligomers contribute to a continuum of modes that serve to further broaden and obscure the spectra. Likewise, any MG oligomer species present that share similar resonance frequencies to those of the monomeric MG will contribute to the overall spectral broadening and congestion in their respective regions. Exploring the potential oligomeric products of MG is beyond the scope of this work, significant insight can be gained by computationally examining the MG hydration equilibrium.

OH stretching region

In both polarizations, the OH stretching region of neat MG is substantially enhanced above that of neat water. This was previously observed for MG but a definitive cause could not be identified.

In the more distinctive *ssp* spectra, much of the characteristic spectral shape and underlying frequencies of coordinated OH modes are preserved in the enhanced MG OH stretching spectra. Additionally, this region's intensity is not extended to lower frequencies, as is generally seen when the response of coordinated OH modes is enhanced due to field effects from charged species. However, here it can be seen that this enhancement diminishes with increasing salt concentration, as shown in Figure 7.6, providing us insight into this previously enigmatic observation.

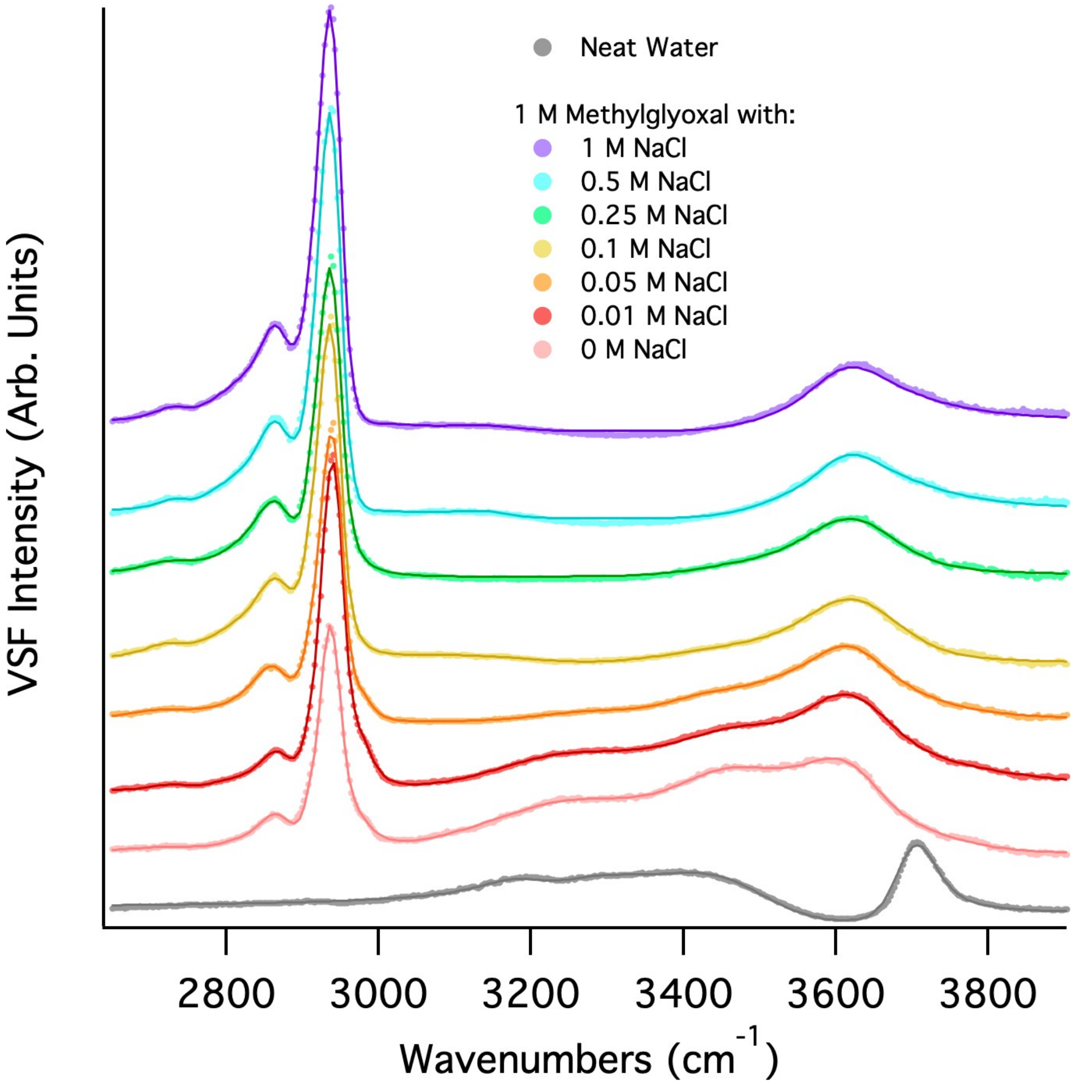

Figure 7.6. VSF spectra of MG and MG-NaCl CH/OH stretching region: Offset VSF Experimental data (open circles) and corresponding fits (solid lines) for water (gray) and aqueous 1 M MG solutions with increasing NaCl concentration in the *ssp* CH/OH stretching region. Offset traces correspond to 1M MG with 0M NaCl (pink), 0.01M NaCl (red), 0.05M NaCl (orange), 0.1M NaCl (yellow), 0.25M NaCl (greener), 0.5M NaCl (blue), and 1M NaCl (purple).

Figure 7.5B shows the CH/OH stretching region of water, neat 1M MG, and 1M MG with 1M NaCl compared to offset 1M HA (orange) and 1M PA (green) solvated in H_2O (circles) versus D_2O (triangles). Looking at the OH stretching region of both HA and PA, it is clear that the enhancement observed with neat-MG and low ionic strength

MG-NaCl is not the norm for these system. Again, this suggests that the loss of coordinated OH intensity with increasing salt is actually a return to the conventional line shape for these kinds of molecule.

Given this as well as the changes observed in the CH stretching region provides a potential explanation: The salt, as well as the increased overall MG surface presence from salting out effects, has decreased the total amount of water at the interface available for hydration, making it less favorable to hydrate MGD an additional time to form MGT. As MGT has four OH groups, it has the ability enhance the ordered hydrogen bonding beyond that of any of the other hydration species of MG and PA or of HA. As the hydration equilibrium shifts with increasing NaCl to further favor MGD, this heightened H-bonding is decreases until the coordinated OH stretching returns to the more expected line shape at ~0.1M NaCl and above.

Thus, we conclude that the presence of salt, as well as the increased overall MG surface presence from salting out effects, has decreased the total amount/activity of water at the interface available for hydration, making it less favorable to hydrate MGD an additional time to form MGT.

Table 1: Fit assignments for MG-NaCl: Frequencies (cm^{-1}) and assignments for peaks contributing intensity to experimental and calculated *sps* spectra. Reported experimental frequencies obtained from global fitting of the experimental spectra. The strongest peaks are shown in bold. Experimental uncertainty = ± 10 cm^{-1}

ssp Expt. Freq.	Calc. Freq.	Assignment (mode, species)	*sps* Expt. Freq.	Calc. Freq.	Assignment (mode, species)
~1575	-	C=C MG Oligomer	~1575	-	C=C MG Oligomer
1664	-	HOH bend	1664	-	HOH bend
1742	1738 1751 1752 1768 1781	α-C=O, MGM1 β-C=O, MGD1 β-C=O, MGD3 β-C=O, MGM1 β-C=O, MGD2	1737	1738 1751 1752 1768 1781	α-C=O, MGM1 β-C=O, MGD1 β-C=O, MGD3 β-C=O, MGM1 β-C=O, MGD2
~2750	2777	α-CH, MGM1 COOH dimers	~2775	2777	α-CH, MGM1 COOH dimers
2878	2834 2860 2870	α-CH, MGT3 α-CH, MGD2 α-CH, MGD3	2878	2834 2860 2870	α-CH, MGT3 α-CH, MGD2 α-CH, MGD3
2940	2929 2932 2938 2941	CH$_3$-SS, MGD2 CH$_3$-SS, MGD1 CH$_3$-SS, MGD2 α-CH, MGT2	2940	2940 2942	CH$_3$-AS, MGD2 CH$_3$-AS, MGM1
2972	2970 2981	CH$_3$-SS, MGT2 CH$_3$-SS, MGT3	2988	2969 2973 2998 2997 3000 3000	CH$_3$-AS, MGT2 CH$_3$-AS, MGT3 CH$_3$AS', MGM1 CH$_3$-AS', MGD3 CH$_3$-AS', MGD1 CH$_3$-AS', MGD2
3540, 3544	3460 3633 3646 3667	MG-OH, MGD3 MG-OH, MGD3 MG-OH, MGD1 MG-OH, MGD2	3517, 3538	3633 3647 3667	MG-OH, MGD3 MG-OH, MGD1 MG-OH, MGD2

NMR Results

To rule out the possibility contamination and confirm that the stock MG hydration matched that reported in the literature, ^{1}H and ^{13}C NMR, 2D HSQC, and ^{15}N NMR NMR (Figures E5-7) was performed on solutions of MG. The results showed the bulk MGD:MGT ration was ~60-65% to 35-40%, in aggrrement with the literature. Since the

N–H bending modes of primary amines occur in the 1650-1580 cm^{-1} region, ^{15}N NMR was performed as well (Figures E8), which confirmed no nitrogen contamination is present.

Calculated Results

Calculated Density Profiles

To further explore this complex system, MD simulations were examined to determine the depth dependent partitioning and orientation of each MG species. The density profiles depicted in Figure 7.7A provide information about the density of each MG hydration state (Mol/L, left) as well as that of water (g/ml, right) as a function of depth from the interface for both "pure" (dotted) and ~1M NaCl solutions (solid). The interface, 0 Å, is defined as the 50% dividing line of the density profile of water.

Like the experimental surface tensiometry, the density profiles show minimal overall change in surface partitioning with the addition of salt. Immediately apparent is the strong surface activity of MGM (red). In both the pure and 1M NaCl simulations, MGM is largely centered at the interface with minimal bulk concentration. In fact, the tail of this peak stretches past the aqueous surface and nearly to -5 Å, indicating that MGM is partitioning between the liquid and vapor phases, with a significant percentage of its population existing 1-3 Å above the water interface. The changes to this depth profile with the addition of salt are negligible, indicating that NaCl is not perturbing the solubility of MGM.

The same is true when comparing the pure and NaCl MGD simulations. In each, MGD shows moderate bulk population at >5 Å but is significantly enhanced approaching the interface (0 Å). MGT shows the largest variation, having a slightly greater preference for bulk solvation in the presence of salt. However both the neat and salt simulations follow the same overall trend with the majority of the population in the bulk (>5 Å) and a sub-surface depletion approaching the interface. Overall, any changes observed in the presence of NaCl are too minimal to be considered significant.

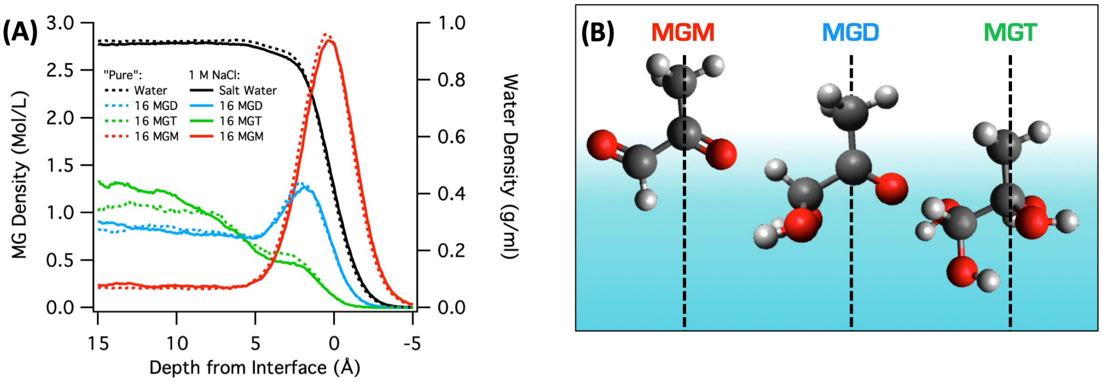

Figure 7.7. Calculated MG density profiles and orientations: **(A)** Density profiles from simulations of 16 MG (~1M) in pure water (dotted) and with 16 (~1M) NaCl (solid) for MGM (red), MGD (blue), MGT (green), and water (black). (**B**) Depiction of the orientations of the MGM, MGD, and MGT C-CH_3 bond angle relative to surface normal at the air-water interface calculated from molecular dynamics (MD) simulations of both neat- MG and MG-NaCl

MG Orientation and Angle Distributions

The indications of a shift in hydration equilibrium discussed above merit a more careful analysis of each MG species in both neat and salt solutions. For each simulation, 1Å slices of the box were analyzed to determine the average distributions of specific bond angles of MG (with respect to the surface normal) as a function of depth from the interface (Figures 7.8 and E2-4 in Appendix E.) The angle profiles reported here differ from those previously reported[x] as they have now been normalized by the sin(ø) and reported as percent abundance, allowing for clearer determination of preferred orientation. It is important to note that these are not traditional surfactants and have highly dynamic surface behavior. Hence, these distributions are very much statistical averages, with the peak of the distribution signifying a preference towards that orientation, but with the molecules also continually moving and reorienting, as evidenced by the breadth of the distributions.

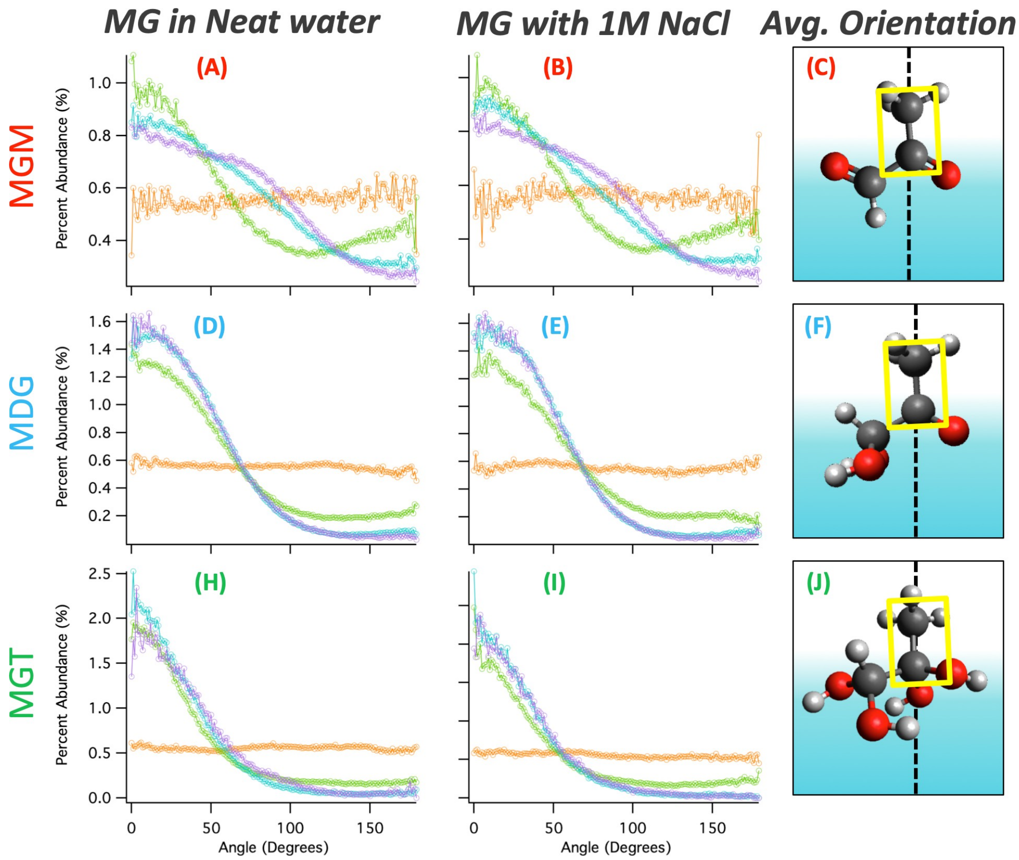

Figure 7.8. Calculated MG depth dependent angle distributions: Depth dependent Angle distributions of the MG β-C-CH_3 bond angle with respect to surface normal. Colored traces correspond to depth from the interface, describing the distribution for the bulk (10 Å, orange), subsurface (3 Å, green), surface (0 Å, blue), and supersurface (-1Å, purple)**.**

As with the density profiles, the addition of salt did not cause any significant change in orientation compared to the neat-MG results. In both neat-MG and Mg-NaCl simulations, MGM, MGD, and MGT each prefer to orient with their methyl groups pointing out of the interface between ~0-45^o (centered at ~0^o), as depicted in Figure 7.7B. From this, it is clear that the addition of salt does not by itself induce orientational changes in MG at the interface. MGM is the least ordered (broadest distribution) while

MGT is the most constrained (narrowest distribution). We attribute this to MGT's enhanced hydrogen bonding ability maximizing its preferred orientation compared to the methyl orientation of MGM (and to a lesser extent, MGD) being largely driven by hydrophobic forces.

Given MG's preference to hydrate and the density profiles discussed above, in experimental studies any population of MGM will likely occur near or above the interface. As might be expected, the simulations show the orientation of MGM becomes increasing broad as it partitions further into the gas-phase. At 1-2 Å above the interface, the preferred range of MGM methyl angle expands to up to 90º, beyond which the percent abundance precipitously drops. In this region, the decrease in hydrophobic forces on the methyl group allow a greater degree of freedom while the proximity to the aqueous phase below still exerts repulsion that prevents MGM from fully flipping its orientation. This indicates that gas-phase MGM can take on some degree of order as it approaches the interface and is thus able to contribute to the VSFS spectra. However, it still does not provide sufficient evidence to conclusively assign the ~2750 cm^{-1} mode seen in the VSF spectra to MGM.

Conclusions

To assess the effects of nonreactive salts on MG's surface behavior at the air- water interface, VSF measurements were performed on aqueous solutions of MG and NaCl. Our previous studies[1] on MG in neat water determined that MG is present at the interface as both the diol (MGD) and the tetrol (MGT) in a ratio of ~90:10, a greater monohydrate ratio than the 60:40 ratio reported in the bulk[2]. This work builds on those studies and allows identification of how the system is perturbed by the presence of NaCl.

VSF spectra showed that the presence of NaCl significantly depresses the coordinated-OH stretching region relative to the MG-neat water system. The MG-NaCl system also demonstrated an increase in intensity for modes associated with MGD (and potentially unhydrated MG (MGM). Conversely, modes associated with MGT decreased in intensity, implying changes not directly related to MG's hydration equilibrium and only the total organic number density at the interface.

The recent improvements to the picosecond laser system have also provided access to the bending region in the *sps* polarization, which was previously buried in the noise level. This has revealed spectral features and trends that were not observed during the original data collection of MG at the neat air-water interface. For example, in both polarization schemes, the feature assigned to water bending is now well defined when solvating MG in water. In combination, these new data sets confirm the assignment of the water bending mode, and thus, the presence of oriented interfacial water for both neat and salt solutions. The presence of C=C stretching modes in the VSF results also indicate the presence of larger oligomer species in the bending region, which requires further exploration.

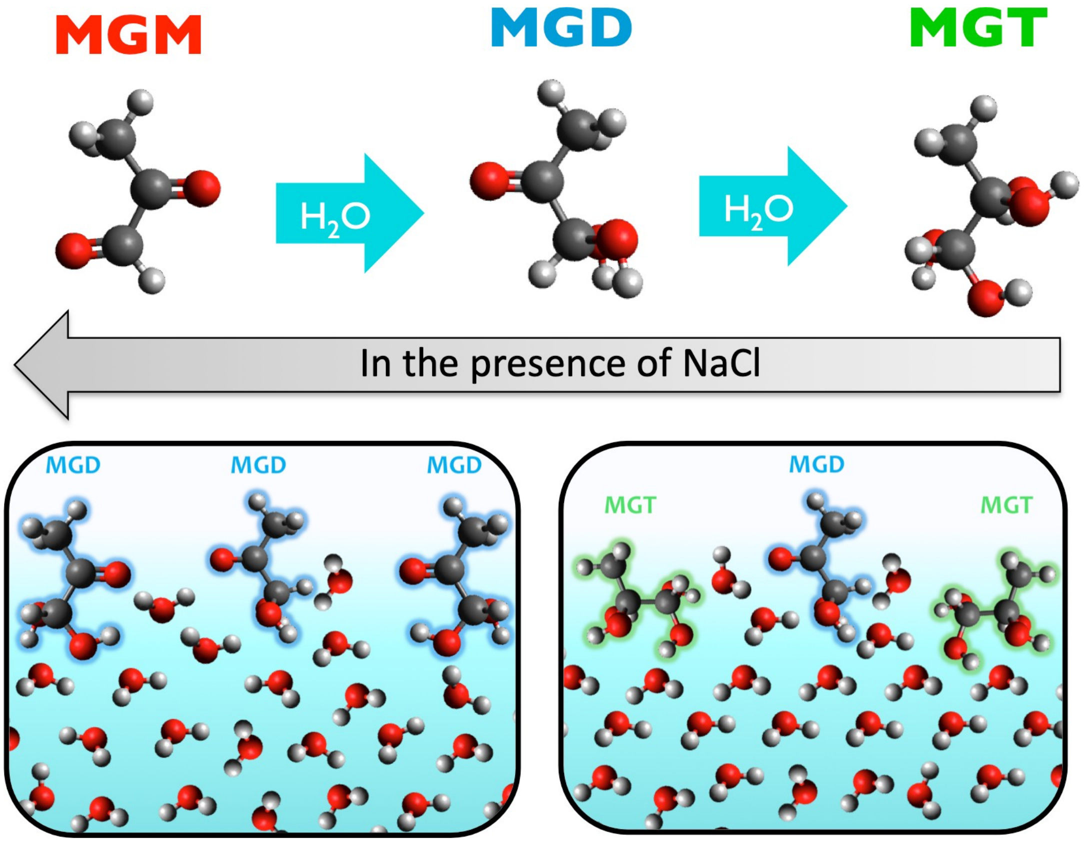

Figure 7.9. Depiction of the potential explanation of a shift in MG hydration equilibrium underlying the enhancement of coordinated interfacial OH stretching modes in neat-MG and subsequent depletion with added salt: (BOTTOM RIGHT) With 4 OH-groups, MGT enhances the OH-coordination at the interface. (TOP) The addition of NaCl shifts the hydration equilibrium at the interface back towards MGD. (BOTTOM LEFT) MGD has less OH-groups and does not solvate as neatly, disrupting the OH-coordination.

The continued presence of a water mode in the bending region indicates that the observed changes in the stretching region are not merely due to increased surface partitioning and surface coverage from the salting out effects. This is supported by surface pressure measurements, which show a relatively small increase in the presence of NaCl, < 5 mN/m, as compared to the MG in neat water system. The computational results also show little change in depth specific behavior or density relative to the pure MG- water system, in agreement with a minimal salting out affect. Analysis of MG bond angles also shows that orientational changes were minimal for both the all three MG hydration species. In combination, these results demonstrate that the local hydration equilibrium is shifted to even further favor MGD (and potentially minimal amounts of MGM) at the air-water interface, with little to none MGT, present at the interface.

This exploration of perturbations to MG by non-reactive NaCl salts will serve as a foundation for investigating aqueous systems of MG in the presence of atmospherically relevant reactive salts, such as ammonium sulfate (AS).

CHAPTER VIII

GLYOXAL AND ITS OLIGOMERS

This chapter includes preliminary data intended for the publication below:

Gordon, B. P., Moore, F. G., Scatena, L. F., Richmond, G. L. Mix and Match: VSF studies of Glyoxal and its Surface Active Oligomers at the Air-Water Interface. **In Preparation*

Bridge

Preliminary work is presented here for glyoxal (GL) at the air-water interface. This work continues the theme of previous chapters regarding the interfacial contributions of surface-active oligomer products.

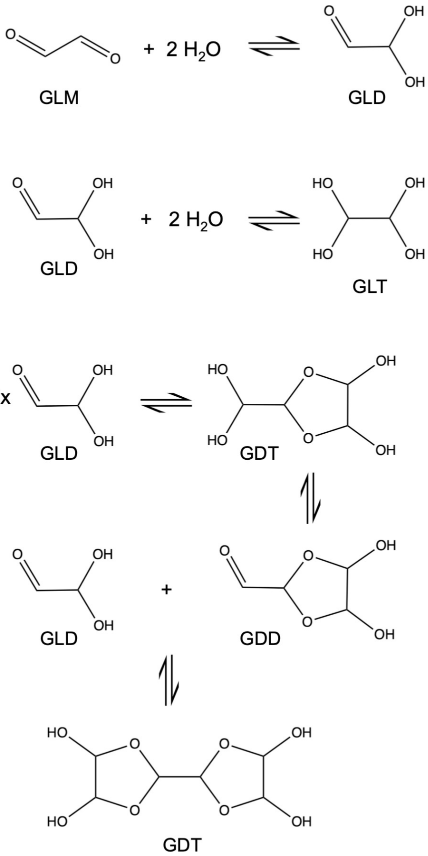

Figure 8.1. Mechanistic pathways of Glyoxal (GL) hydration and oligomer production.[1]

Introduction

Glyoxal (GL) is an ubiquitous atmospheric organic with both biogenic and anthropogenic sources and is the second most abundant atmospheric aldehyde in atmospheric rainwater after formaldehyde. [1, 2] GL is known to play a significant role in secondary organic aerosol (SOA) formation, particularly aqueous aerosol. [1, 2] However, the full scope of this role and its far- reaching effects are as of yet poorly understood. This is in part because GL undergoes extensive aqueous processing to produce a myriad of hydration and oligomerization products, [1, 2] as shown in Figure 8.1.

Glyoxal is known to have a high solubility in water due its preference to hydrate. [1, 2] GL has three hydration states: an unhydrated (GLM), a singly hydrated diol (GLD), and a doubly hydrated tetrol (GLT). Additionally, GL forms multiple favorable oligomer species including a hydrated tetrol dimer (GDT), which is in equilibrium with its unhydrated diol form (GDD), and tetrol trimer (GTT). Figure 1 demonstrates the mechanistic pathways through which these species form. [1]

Surface Tensiometry

The surface pressure (SP) isotherm of GL as a function of concentration is displayed in Figure 8.2 along with those of neat HA, PA, and MG that were previously discussed in chapters 5, 6, and 7, respectively. The SP of GL plateaus above 0.75M at ~7mN/m. While this is quite low compared HA, [3] MG, [4] and PA [5] it is higher than

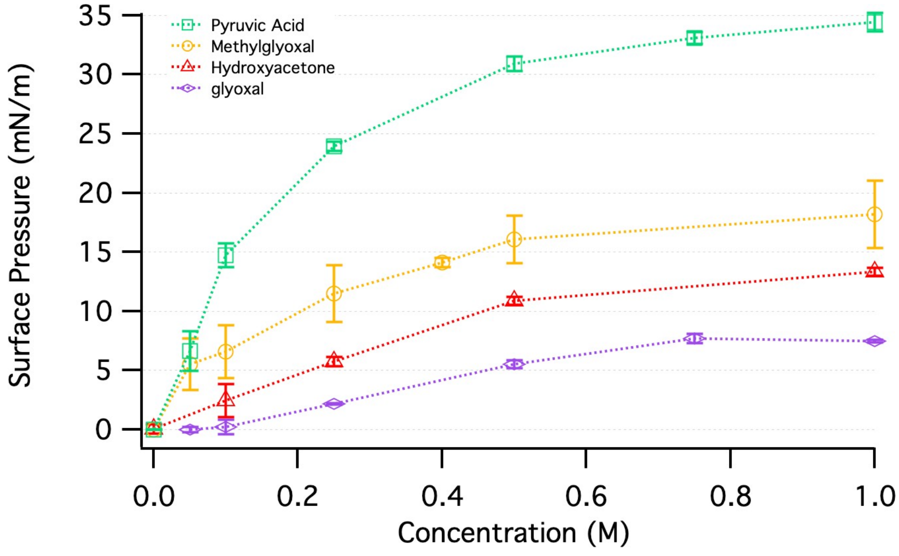

Figure 8.2. Surface pressure isotherm vs. organic concentration for GL (purple diamonds) compared to hydroxyacetone[3] (red triangles), methylglyoxal[4] (orange circles), and pyruvic acid [5] (green squares).

might be expected for the highly soluble monomeric forms of GL. This suggests that surface-active oligomer species may be contributing to the surface population.

VSF Spectra

Considering GL's high solubility and relatively low SP values, the experimental VSF spectra of aqueous GL solutions have intriguingly intense responses, as can be seen in Figure 8.3. Additionally, there are contributions not consistent with monomeric GL, much as we have seen before with PA and MG.

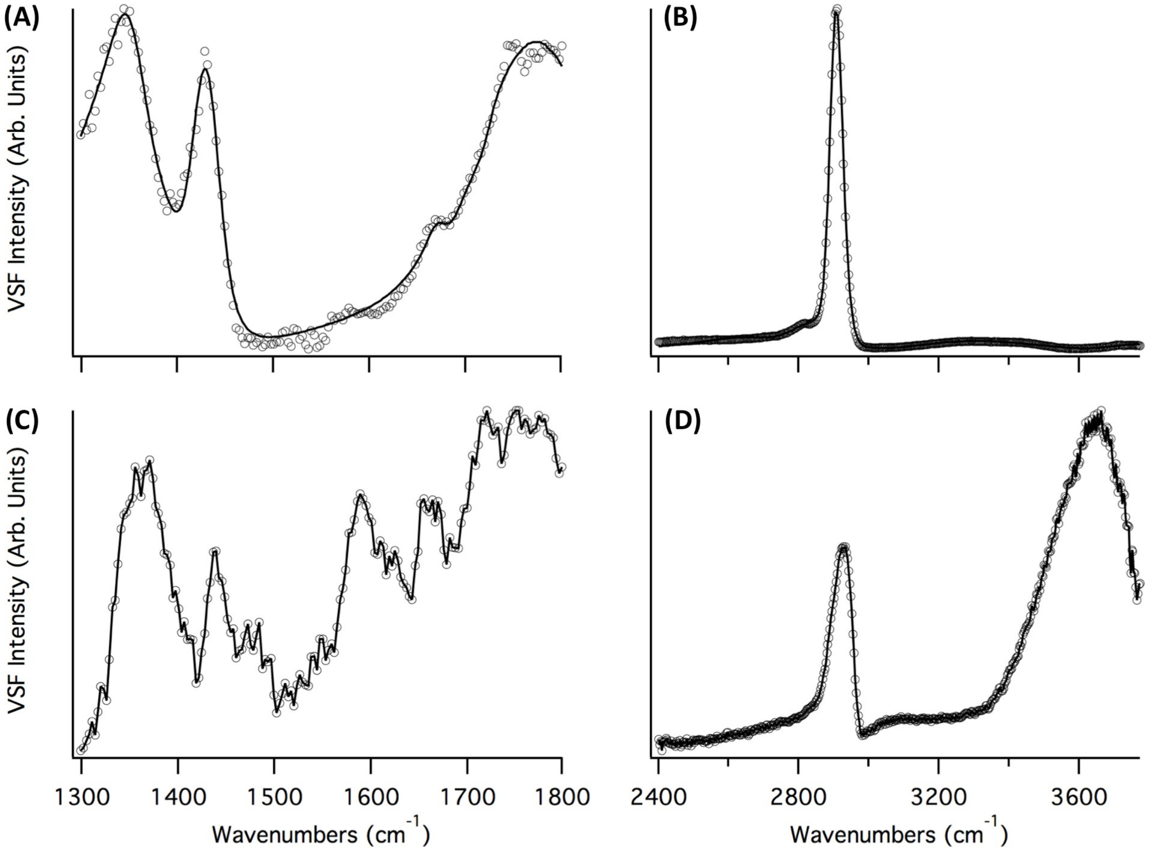

Figure 8.3. VSF Experimental spectra for 1M GL in H_2O (open circles) and corresponding fits (solid lines) in the CH bending/C=O stretching (A,C) and CH/OH stretching (B,D) regions in the *ssp* (top) and *sps* (bottom) polarization schemes.

In particular, the intense and relatively narrow peak at ~2950 cm^{-1} is unlikely to come from an aldehydic CH of monomeric GL as these modes would be expected to exhibit a high degree of spectral broadening due to both conformational variability and inductive effects arising from solvation of its neighboring oxygens. This indicates that species other than GL monomers are present. However, the rigid ring structures found in GDD, GDT, and GTT (Figure 1) would have CH moieties that would be highly restricted and of differing frequency than those of the monomer GL species.

To investigate this, simulations were performed for a sampling of representative conformations monomeric GLM, GLD, and GLT and oligomeric GDT, GTT* were performed to generate calculated VSF responses using our standard computational methodology (See Chapter 2). The preliminary analysis discussed below was performed for each simulation after a 2ns evolution.

Preliminary calculated VSF responses (displayed as stick spectra) are compared to the experimental ssp spectra in Figure 8.4. It is immediately apparent that the oligomers GDT (orange) and GTT (purple) exhibit strong VSF responses in regions where the monomeric GLM (red), GLD (blue), and GLT (green) have minimal intensity.

Their density profiles show that the oligomers heavily sample the bulk and visual analysis of the MD trajectories reveal that GDT and GTT readily cluster together when in proximity. This could be an artifact arising from the size of the water box relative to the larger GL oligomers. However, if accurate, this behavior could lead to significant behavioral changes to other GL species when in the presence of these oligomers.

---

* The simulations of GDD were not completed at the time of writing.

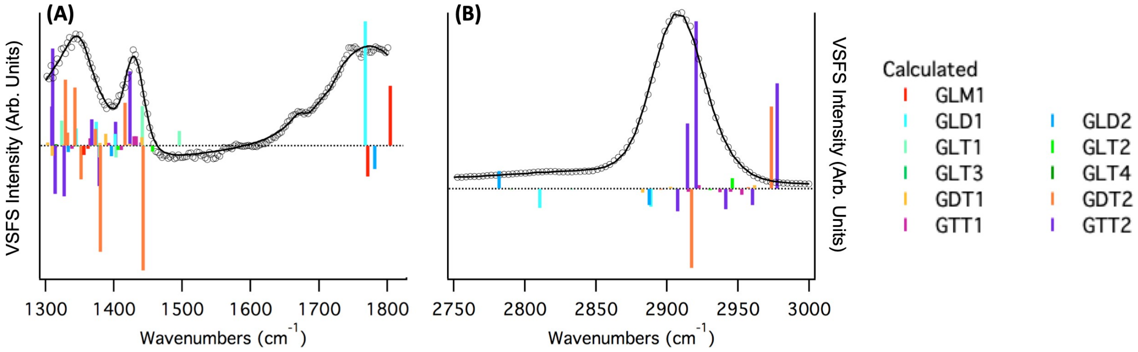

Figure 8.4. Experimental vs. calculated VSF GL spectra: Experimental VSFS 1M GL(gray) vs. Calculated VSF stick spectra from each 16 GL (~1 M) simulation in the CH bending/CO stretching (A) and CH stretching (B) regions. The calculated stick spectra are color coded to their corresponding conformer according to the legend.

Thus, future work includes moving to a larger simulation box (30x30x45) as well as simulating mixed systems with varying ratios of both monomeric (GLM, GLD, GLT) and oligomeric GL residues (GDT, GDD, GTT). Simulations will also be reanalyzed after continuing their evolutions for a full 50 ns, as per convention.[6] Other potential GL reaction products may also be considered.

While this work is ongoing, it is already clear that it provides valuable insight about a system with immense atmospheric importance and has the potential improve the communities understanding of GL's function in SOA formation and aging.

CHAPTER IX

COMPUTATIONAL METHODOLOGY IMPROVEMENTS

This chapter includes contents that are currently being prepared for the publication below:

Gordon, B. P., Moore, F. G., Valley, N. A., Richmond, G. L. Level Up: Methodology Improvements for Calculation of VSF Spectra of Aqueous Organic Interfaces Using Gas-Phase Water Microclusters. **In Preparation*

Bridge

To complement our experimental work, we are also improving our computational methodology. In order to generate calculated VSF spectra of coordinated water, we are building a library of gas-phase density functional theory (DFT) microclusters. Improvements to the description of the organic molecules in the classical molecular dynamics (MD) simulations are also currently being pursued, and several MD water models for the simulation of the air-water interface

Simulating VSF Water Spectra with Gas-Phase DFT Water Microclusters

In order to better describe calculated VSF spectra for solvated organics, we seek to improve the underlying methodology used for calculating VSF water spectra. Since organic-OH and water modes interfere with each other, experimental VSF spectra in the OH-region are convolutions of contributions from both types of modes. Prior to this work, our computational methodology did not inherently include solvation effects, thus we have been unable to make use of calculated spectra in those regions.

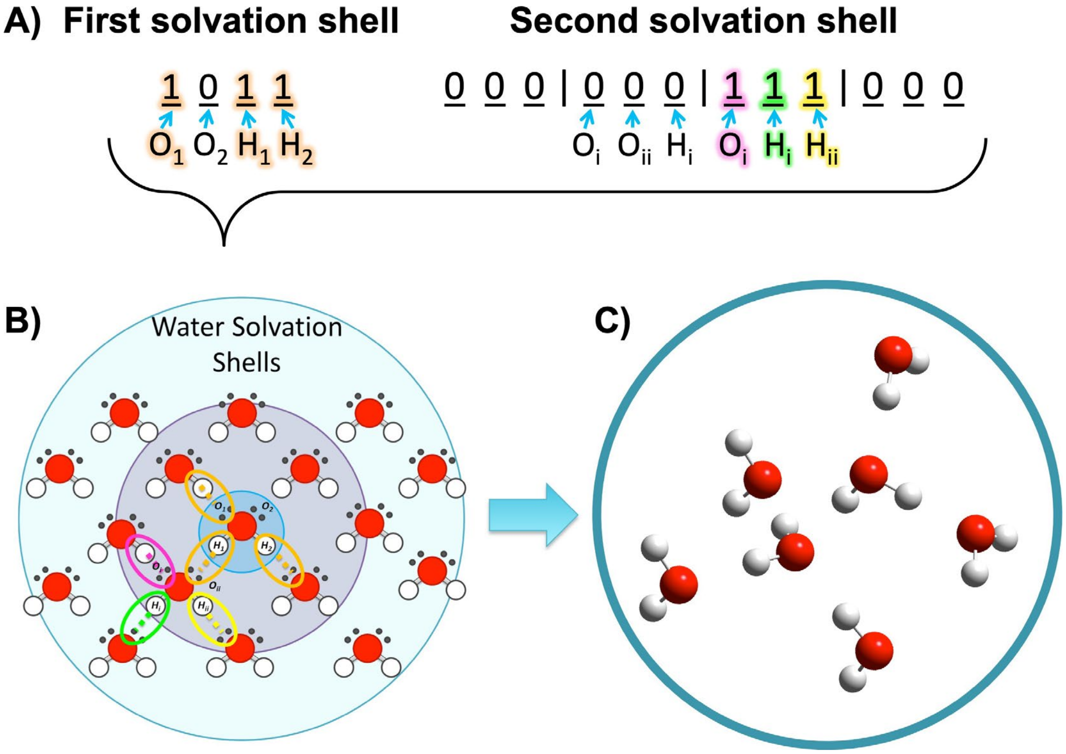

Figure 9.1. Graphical depiction the 16-digit binary code and of how it (A) maps to the solvating water molecules in the first and second solvation shells (B) to describe the corresponding DFT microcluster (C).

Due to the highly coordinated nature and the broad solvation environment of water, a single isolated gas phase water molecule cannot reproduce the observed neat air/water spectra of water. In fact, it has been shown that it is necessary to include both the first and second solvation shells of water in order to reproduce the water intramolecular vibrations of water [4]. The first solvation shell includes four waters that can potentially hydrogen bond with the central water.

Each of those four waters can then potentially hydrogen bond with 3 more waters in the second solvation shell, giving a total of 16 possible water molecules in the first and second solvation shells.

In order to define these various solvation environments, a 16-digit binary code was developed to describe the solvation shells, where 1 indicates the presence of a water molecule in a given position and 0 indicates an empty position. Digits 1-4 define the first solvation shell and digits 5-16 define the second solvation shell. Using this 16-digit code, an initial library of 191 DFT structures was created spanning 8 possible first solvation shell environments, each with various second solvation shell water environments, allowing us to represent the coordinated nature of water in a controlled way.

An initial library of 191 DFT structures has been created at the B3LYP/6-311++G(2d,2p) level of theory, allowing us to represent the coordinated nature of water in a controlled way. The DFT microcluster library is currently being extended to include additional microclusters, currently totaling 304 conformers and which will eventually total 500 in all. This allows us to reproduce both the coordinated nature of water as well as the homogenous broadening produced by the varying solvation environments.

Investigating the MD Water Models

In addition our efforts to improve the underlying methodology used for calculating VSF water spectra, we are also investigating the impact of the molecular descriptions of water in the classical MD. With this work, we investigate the applicability of various MD water models for systems with small organics. Conventionally, we have utilized a three-point polarizable water model (POL3 [5]) for our MD simulations. However, four-point non-polarizable models, which have an additional point to describe electron density, can be better at reproducing structural characteristics of water. It is possible that improved descriptions of water structure afforded by four-point non-polarizable models may play a more important role than explicit polarization on properties of the MD simulation concerned with simulating VSF spectra. For this reason, six other rigid non-polarizable water models have been used in this work to simulate water. As outlined in Figure 9.2A, the models used include 2 three- point models (TIP3P [6], SPC/E [7]) and 4 four-point models (TIP4P [6], TIP4P-ew [8], TIP4/2005[9], and OPC [10]).

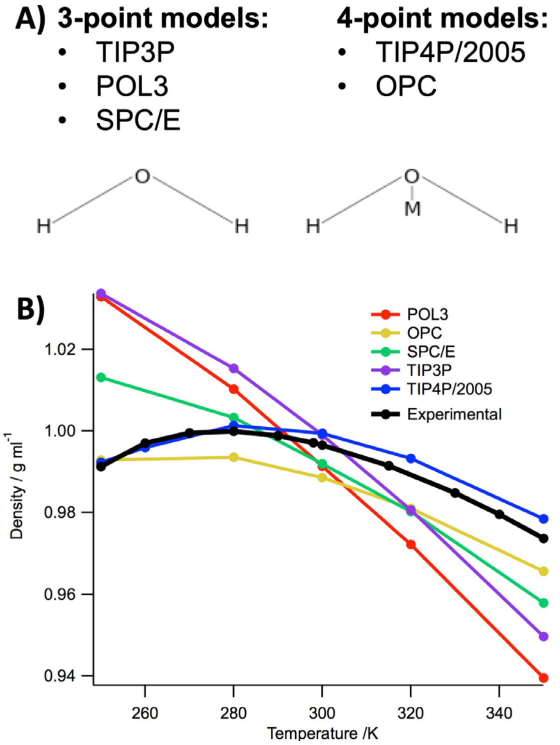

Figure 9.2. 3-point vs. 4-point MD water models (A), where the 'M' in the 4 point model represents a 'dummy atom' used to describe electron density. (B) Calculated density vs. temperature for each of the MD water molecules.

Harmonic and anharmonic *ssp* polarized VSF spectra of water have been calculated for these 7 water models. Experimental spectra serve as a metric for evaluating the differing methodologies that use various water models. From this work, we can see that the harmonic calculations do a poor job of reproducing the experimental spectra for all water models. (Appendix F, Figure F1) The anharmonic frequencies were a much closer match for all of water models. In particular, POL3 and TIP4P/2005 were best able to reproduce the relative intensities of the experimental spectra. Future work includes evaluating the effect of hydrogen bonding length for each water model as well incorporating implicit solvation, which is discussed further, below.

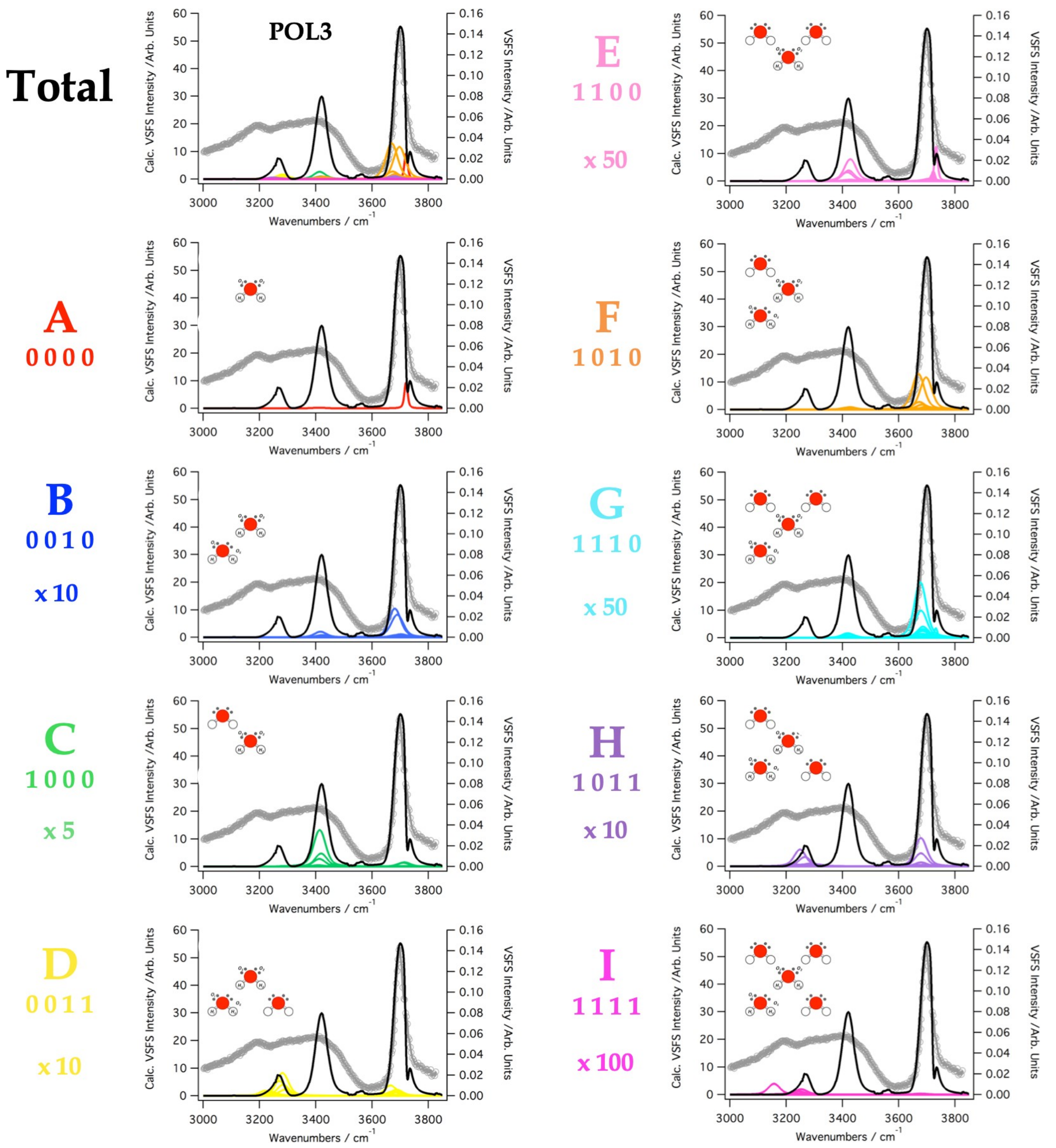

Figure 9.3. Experimental vs. calculated VSF spectra of neat water: Experimental neat water VSF spectra (gray markers) vs. the calculated VSF spectral contributions from individual water microcluster conformations (colored lines) of each first solvation shell subtype (given a letter designate A-I for clarity) with varying degrees of second shell solvation.

Evaluating our DFT functional

Finally, we are also currently evaluating other DFT methods that have been previously benchmarked in the literature [11] for small water clusters to confirm the rigor of our current level of theory for calculating the frequencies and response properties of these microclusters compared. These DFT functionals include a pure functional (M06L), a hybrid functional (SOGGA11X), and 2 range-separated hybrid functional (ωB97 and ωB97X). These functionals, as well as the B3LYP hybrid functional we employ for our library, will be calculated for a subset of 24 microclusters using a mixed aug-cc-pVX Z: cc-pVX Z basis set (aug-cc-pVX Z for O and cc-pVX Z for H). We will examine harmonic frequencies as well as the resulting calculated VSF spectra as our metric for accuracy.

Linear least squares regression fits of the resulting harmonic frequencies from each higher-level calculation versus our standard level of theory have been calculated for each of the 24 conformers. Differences in fundamental frequencies were found to be different only by a linear offset, as shown in Appendix F for two representative structures containing seven and eleven water molecules. (Figure F2) This demonstrates that for our purposes, our current level of theory is sufficient and can simply be linearly scaled to match the results of more these expensive functionals and basis sets. Future analysis includes calculating VSF spectra and compared to both experiment as a metric for performance with regards to the response calculations used to generate our calculated beta tensor.

Evaluation of Improvements: Hydroxyacetone as a Model System

A more accurate description of the water structure in our MD simulations will allow us to improve our simulated VSF spectra, including all resonant modes due to both the solute and solvent molecules, by convolving the organic modes with the water modes. This may also allow us to analyze the effects organics have on water structure. In order to evaluate the success of the aforementioned methodology improvements, we need a well-behaved model system that we can use as a metric.

As previously discussed in Chapter 5, Hydroxyacetone (HA) is a common semi-volatile surface-active atmospheric secondary organic that we have released published on.[12] It has been observed experimentally in situ in aerosol along with other atmospheric organics of interest, such as methylglyoxal and acetaldehyde.[13] HA can be hydrated to form a geminal diol, but the hydration is not favorable: 96-98% of HA is unhydrated in the bulk only 2-4% in the hydrated form.[3] This allows us to make the assumption that HA is entirely in its unhydrated state, meaning that HA is not subject to the same hydration equilibrium complications as methylglyoxal. For this reason, direct comparison can be made between the calculated free energy of simulated non- reactive HA-water systems and experimental values. Thus, in additon to being an excellent model system for our ongoing atmospheric research, HA is also ideal for testing new computational methodologies.

To that end, both a polarized and an un-polarized force field were created for Hydroxyacetone MD simulations. Seven separate MD simulations were performed with HA and each of the water models discussed above. For simulations with non-polarizable water models, the organic force fields are parameterized using the FF99SB non-polarizable force field[14] without charge scaling. The simulations were analyzed to generate VSF spectra using the same DFT optimizations, frequency calculations, and aharmonic frequency corrections created for our initial published treatment of HA.

The experimental HA-neat water VSF spectra were used to directly compare to the calculated spectra to gauge the applicability of each water model for the calculation of VSF spectra of the organics. Here, it was also found that the POL3 and TIP4/2005 models best reproduced the observed spectral features.

Future work involves running analogous MD simulations with implicitly polarized HA. Implicit polarization effects can be produced by scaling parameters to reproduce experimentally determined solvation free energies, as previously demonstrated by the Roeselova group.[15] This will be done for each water model by pushing a single HA molecule through a water slab and using the weighted histogram algorithm method (WHAM) to calculate a potential of mean force from which we can derive calculated free energies of hydration. The process will be repeated while iteratively scaling the charges on the organic until the calculated free energy of hydration is in good agreement with the experimental values.

Conclusions

Upon the completion of this work, we intend to use the HA, MG, PA, and GL and systems as a foundation to build upon for future studies. In particular, we are interested in furthering our understanding of how the hydration equilibrium and oligomer products of these species affect water coordination at the interface. Another avenue of interest is any potential effects of temperature. Literature studies on similar small geminal diols have shown a shift in hydration equilibrium with varying temperature and having water models more suited to a wider temperature range will be beneficial for these studies.

Once we are able to simulate water and improve our organic representation, we can begin to incorporate these improvements into our future simulations. The ability to depict changes in water structure in the presence of organics will be vital for understanding the chemistry of the interface. The surface chemistry at the air-water interface is of great atmospheric significance since it could greatly influence aerosol hydrophobicity and gas to bulk phase partitioning. With this improved methodology and experimental knowledge base, we can move towards investigating more complicated systems.

CHAPTER X

CONCLUSIONS

An improved understanding of the interfacial chemistry of aqueous secondary organic aerosols is needed to address the current knowledge gaps in atmospheric representations. This research will help to lower the uncertainties associated with atmospheric aerosol formation by providing results that can inform atmospheric chemists about complex cooperative behaviors, thereby aiding the development of more accurate models. These studies of glyoxal (GL), methylglyoxal (MG), hydroxyacetone (HA), and Pyruvic acid (PA) in neat water and MG with NaCl have made valuable strides towards this goal. Furthermore, they have laid the foundation for future studies of more complicated systems that are more representative the chemical diversity inherent to SOA. These studies will be aided by the new computational methodologies developed in this work.

APPENDIX A
SUPPLEMENTAL INFORMATION FOR NEAT WATER

Table A1: VSF fitting parameters for neat-water in the HOH bending region

#	Fit Parameter	*ssp*	*sps**	Assignment
1	Intensity	0.15	0.059	Librational Overtone
	Phase	3.14	0	
	Lorentzian (cm^{-1})	5	5	
	Frequency (cm^{-1})	1480	1603	
	Gaussian (cm^{-1})	246	38	
2	Intensity	0.078	0.015	HOH bending modes
	Phase	3.14	3.14	
	Lorentzian (cm^{-1})	5	5	
	Frequency (cm^{-1})	1640.2	1642	
	Gaussian (cm^{-1})	24	77	
3	Intensity	0.30	0.024	TBD
	Phase	0	0	
	Lorentzian (cm^{-1})	5	5	
	Frequency (cm^{-1})	1732	1704	
	Gaussian (cm^{-1})	121	56	
Nonresonant (NR)	NR Intensity	0.065	0.16	-
	NR Phase	3.14	3.14	

* Tentative Assignments

Table A2: VSF fitting parameters for neat-water in the OH stretching region.

Mode	Fit Parameter	*ssp*	*sps*	Assignment
1	Intensity	0.016	0.072	More coordinated water
	Phase	3.14	0	
	Lorentzian (cm^{-1})	5	5	
	Frequency (cm^{-1})	3200	3136	
	Gaussian (cm^{-1})	43	159	
2	Intensity	0.061	0.105	coordinated water
	Phase	3.14	0	
	Lorentzian (cm $^{-1}$)	5	5	
	Frequency (cm^{-1})	3335	3390	
	Gaussian (cm^{-1})	114	120	
3	Intensity	0.11	0.11	Companion OH
	Phase	3.14	0	
	Lorentzian (cm^{-1})	5	5	
	Frequency (cm^{-1})	3475	3572	
	Gaussian (cm^{-1})	94	98	
4	Intensity	0.25	0.05	Free OH
	Phase	0	0	
	Lorentzian (cm^{-1})	12	12	
	Frequency (cm^{-1})	3696	3682	
	Gaussian (cm^{-1})	26.64	42	
Non-resonant (NR)	NR Intensity	0.07	0.03	-
	NR Phase	3.14	3.14	

APPENDIX B

SUPPLEMENTAL INFROMATION FOR MG

The contents of this appendix have been previously published in whole or in part.

Wren, S. N., Gordon, B. P., Valley, N. A., McWilliams, L. E., Richmond, G. L. Hydration, Orientation, and Conformation of Methylglyoxal at the Air-Water Interface. *J. Phys. Chem. A* **2015** *119* (24), 6391-6403

B1. Quantum Mechanical Calculations

Table B1. DFT structures and energies calculated at B3LYP/6-311++G(2d,2p) level of theory. Conformer definitions and percent abundances for MD simulations.

MD Conformer	DFT energy (Hartree)	Relative DFT energy[a] (kcal mol^{-1})	DFT Dihedral Angle[b] (°)		Dihedral Range (°) for MD assignments[c]		% Abundance[d]
			D1	D2	D1	D2	
MGM1	-267.242	0	0	-	0 – 30	-	100
MGD1	-343.713	4.7	180	-	150 – 180	-	26
MGD2[e]	-343.705	9.9	0	-	0 – 30	-	3
MGD3	-343.720	0	56.5	-	30 – 90	-	26
MGD4	-	-	NF	-	90 – 150	-	12
MGT1	-	-	NF	NF	0 – 120	0 – 120	0
MGT2	-420.185	0.2	34	156	0 – 60	120 – 180	52
MGT3	-420.186	0	76	165	60 – 120	120 – 180	47

[a] Relative to the lowest energy structure for each MG species

[b] D1 for MGM is γC-βC-αC=O, D1 for MGD is γC-βC-αC-H, D1 and D2 for MGT are both γC-βC-αC-OH

[c] Angles apply to rotation in both directions

[d] Based on MD simulation with 16 MG molecules, integrated over entire box

[e] Converged at saddle point on potential energy landscape

NF = not found (no minimum located)

B2. Surface Orientation of MGD

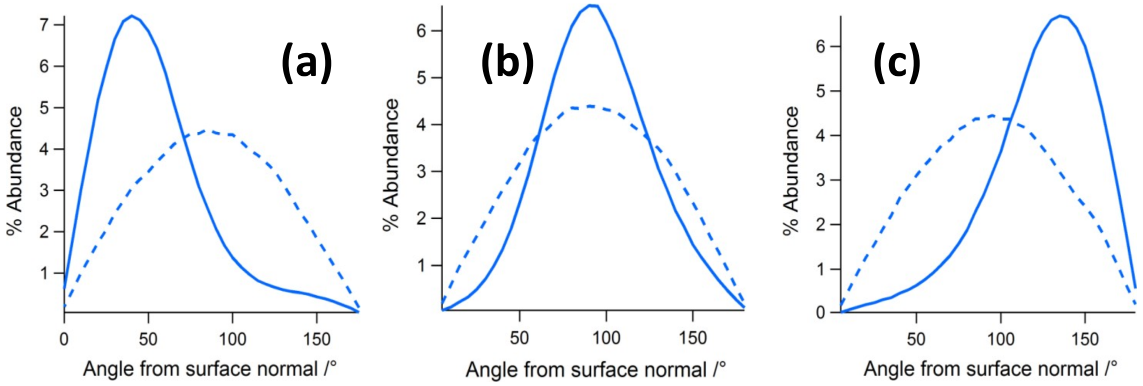

Figure B2. Normalized distribution of MGD bond angles relative to the surface normal into the vapor phase (0˚) in the bulk (-10 Å, dashed) and at the interface (0 Å, solid) for (a) βC-Me, (b) βC=O, (c) βC-αC (pure simulation with 16 MG molecules).

B3. Surface Tensiometry

Surface pressure, π, is plotted as a function of methylglyoxal concentration, [MG], in Figure C3a. Maximum surface excess was calculated from the surface pressure data according to the Gibbs adsorption equation[5]:

!!" = (1/!")(!"/! ln !!")! (C1)

where Γ_{MG} is the maximum surface excess, π is the surface pressure in mN m^{-1}, and a_{MG} is the activity. From Eq. S1, it is clear that a plot of surface pressure against the natural log of the activity will yield a slope equivalent to the maximum surface excess (Figure C3b). Strictly, activities should be used in Eq. S1, however, concentrations not corrected for activity were used here (a_{MG} = [MG]). Inverting the surface excess gives the minimum area per molecule, which was calculated here to be 73 Å^2 per molecule.

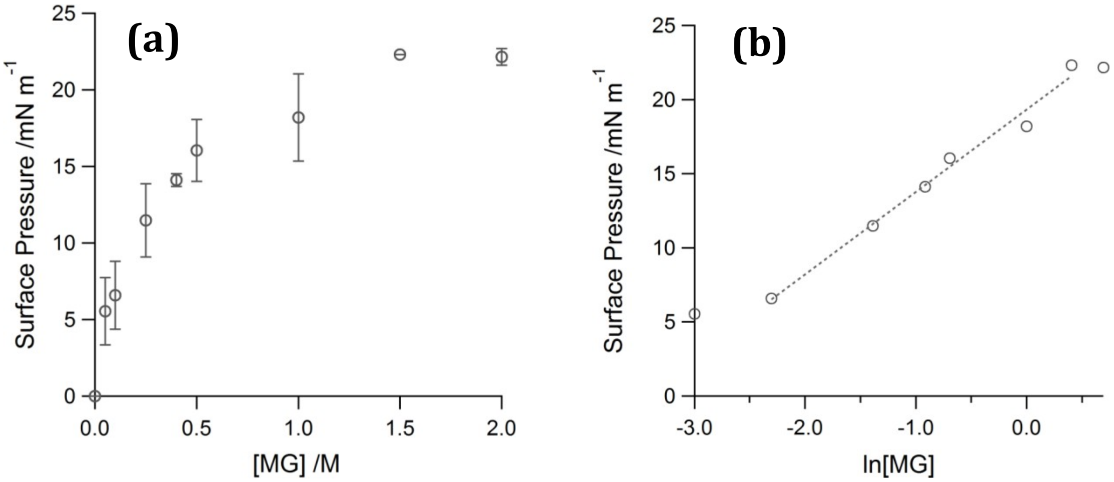

Figure B3. (a) Methylglyoxal surface pressure as a function of bulk MG concentration, [MG]. Each point represents the average of 3-7 individual samples and the vertical error bars represents the standard deviation. (b) Methylglyoxal surface pressure as a function of the natural log of the bulk MG concentration. The dotted line is a fit to the linear portion of the curve.

B4. Pyruvic Acid Contamination

There is a small possibility that trace amounts of pyruvic acid impurity contribute to the observed spectral response. Acids are known to induce changes to the surface electric field thereby increasing the ordering of interfacial water molecules and leading to an enhancement in the 3200 – 3400 cm^{-1} spectral region.[6] However, given that the intensity in this region decreases at higher bulk MG surface concentrations (and therefore higher pyruvic acid concentrations and lower pH) this may not be the case. The concentration of pyruvic acid in the most concentrated MG solution (0.50 M) was also calculated to be $< 5 \times 10^{-3}$ M, which is relatively low. Furthermore, we obtained a rudimentary *sps* spectrum of ~1 M pyruvic acid: no enhancement at ~3200 cm^{-1} was observed. Therefore we conclude that the observed changes to the water structure in the presence of methylglyoxal are predominantly due to methylglyoxal (and its hydrates) rather than pyruvic acid. However, it is possible that trace amounts of pyruvic acid may play a role in catalyzing the hydrolysis of methylglyoxal.[7-8]

APPENDIX C
SUPPLEMENTAL INFORMATION FOR HA

C1. EXPERIMENTAL VSF SPECTRA

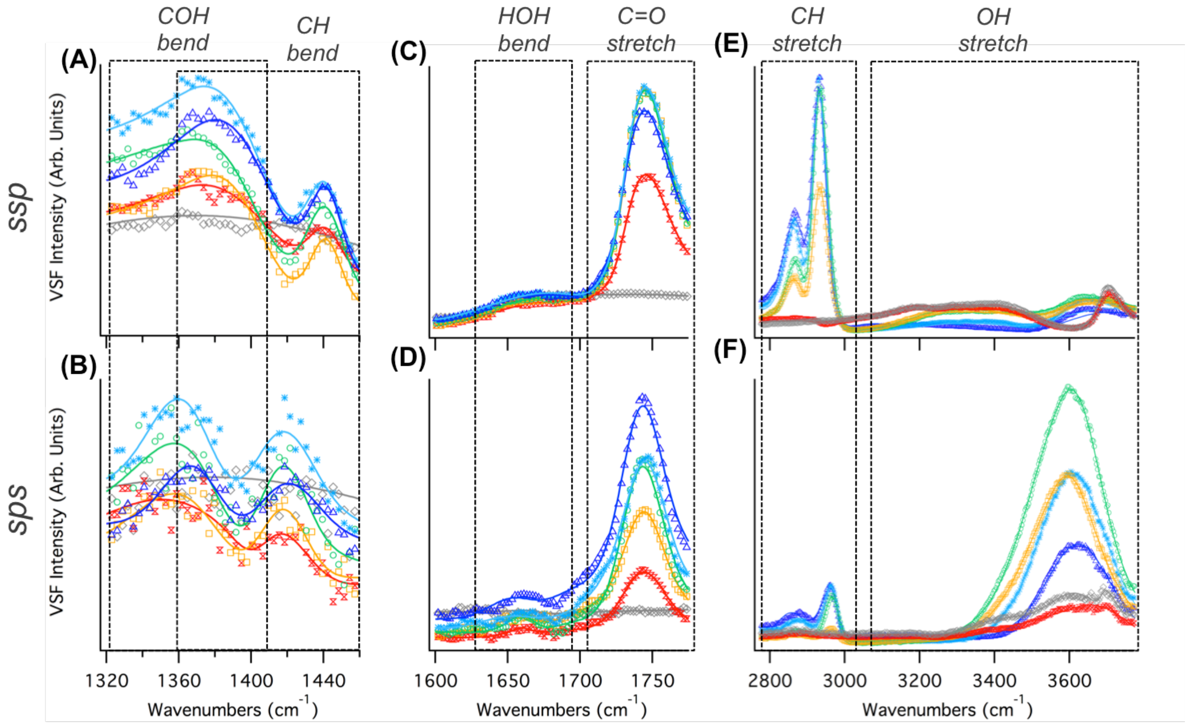

Figure C1. VSF Experimental data (open circles) and corresponding fits (solid lines) for water and aqueous HA solutions in the COH/CH bending region (A,B), C=O stretching region (C,D), and the CH/OH stretching region (E,F) in the *ssp* polarization (top) and *sps* polarization (bottom). Water (gray, diamonds), 0.1M HA (red, hourglasses). 0.25M HA (orange, squares), 0.5M HA (green, circles), 1M HA (blue, stars), and 2M HA (dark blue, triangles). Dotted boxes are for visual reference of approximate spectral regions.

C1 Neat water VSFS spectra

The OH stretching region (3200 - 3700 cm^{-1}) displays the characteristic air-water *ssp* spectrum (Fig. D1E) that has been extensively studied in the literature.[1-9] While discussions of some assignments are ongoing,[8, 10-12] a general consensus has arisen. The region is dominated by sharp, well-defined peak at ~3700 cm^{-1}, arising from "free" OH oscillators, and a very broad feature from ~3600-3200 cm^{-1}, attributed to OH stretching modes in a continuum of hydrogen bonded states and environments. Though less visually characteristic, the same modes give rise to the *sps* neat water spectrum (Fig. D1F), which also agrees with literature findings.[9, 12]

Fig D1C and D displays the spectrum arising from HOH bending modes of water (gray) in the *ssp* and *sps* polarization, respectively. The spectrum of neat water in the bending region has only been accessible by VSF in the *ssp* polarization relatively recently [13-15] and no features have been observed above the noise level in the *sps* polarization in this work or the literature. The specific contributions to the spectral shape of the *ssp* polarized water-bending region are currently an ongoing matter of discussion.[16-17] This is due to the complex and still undetermined interferences contributing to the intensity in this region. Our results agree with the spectral shape reported in the existing literature. [13- 17] In brief, the *ssp* spectra of neat water consists of a feature at ~1640 cm^{-1} (arising HOH bending from water in a continuum of solvation environments) and an underlying broad, low intensity feature centered around ~1440 cm^{-1} (due to librational overtones, Fig. S1A).[15, 18] As consistently reported in the literature, to the higher frequency side the water bending region (> 1700 cm^{-1}), the background fails to return to zero. While this phenomenon has yet to be fully understood, it is generally thought to be an interference effect. [16]

D2. SURFACE TENSIOMETRY

Surface pressure, π, is plotted as a function time for neat water and hydroxyacetone solutions between 0.1 M and 2M in Figure D2A. For each HA solution, the equilibrated surface pressure value (> 15 hours) is plotted as a function of the natural log of bulk hydroxyacetone concentration, [HA], in Figure D2B. From this surface pressure isotherm, the maximum surface excess was calculated according to the Gibbs adsorption equation[19]:

$$\text{!}_{\text{!"}} = (1/\text{!"})(\text{!"}/\text{!}\ln \text{!}_{\text{!"}})_{\text{!}} \qquad \text{(D1)}$$

where Γ_{HA} is the maximum surface excess, π is the surface pressure in mN m^{-1}, and a_{HA} is the activity. However, since experimental data for the activity of HA has not been reported to our knowledge, concentrations not corrected for activity were used instead (a_{HA} = [HA]). The slope of a linear fit of the surface pressure versus the natural log of the activity (here, [HA]) is equivalent to the maximum surface excess. The minimum area per molecule can then be found by inverting the surface excess, which was calculated here to be 83 $Å^2$ per molecule.

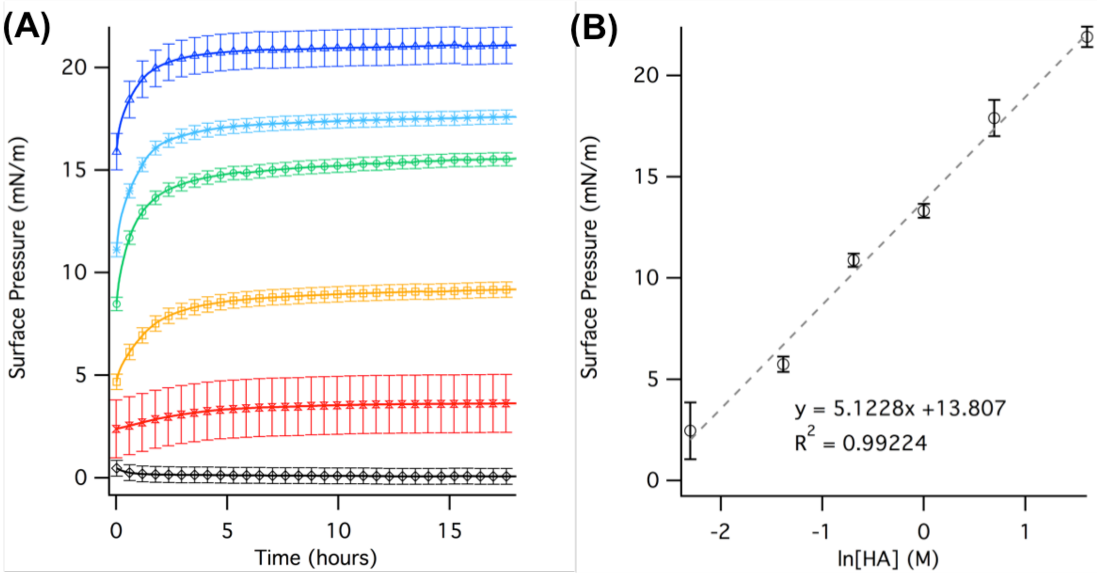

Figure C2. (A) Surface pressure vs time data for water (gray, diamonds), 0.1M HA (red, hourglasses). 0.25M HA (orange, squares), 0.5M HA (green, circles), 1M HA (blue, stars), and 2M HA (dark blue, triangles). **(B)** HA surface pressure as a function of the natural log of the bulk HA concentration (markers) and linear fit (dotted line).

C3. COMPUTATIONAL DETAILS

C3.1 HA dihedrals and conformers

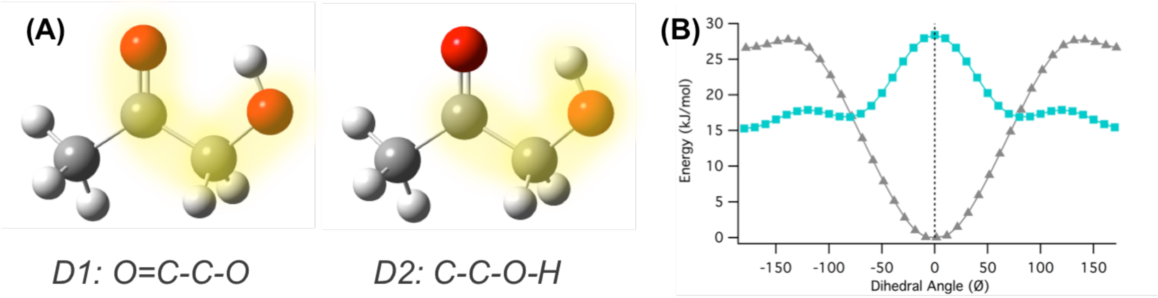

Figure C3: (A) HA dihedral definitions**. (B)** 1D potential energy scans of the hydroxyl dihedral angle (D2, C-C-OH) for *cis*- (gray triangles) and *trans*- (blue squares) D1 (O=C-C-O) configurations at the B3LYP/6-311++G(2d,2p) level of theory.

Table C2: HA DFT structures and energies calculated at B3LYP/6-311++G(2d,2p) level of theory. Conformer definitions and percent abundances for MD simulations.

HA conformer	DFT energy (Hartree)	Relative DFT energy[a] (kJ mol^{-1})	DFT dihedral angle (°)		Dihedral range (°) for MD assignments[b]		% Abundance[c]	
			D1	D2	D1	D2	Bulk	Surface
HA1-Cc	266.811	0	2.96	2.91	0-90	0-45	~16	~16
HA2-Tt	-266.807	10.1869	180.00	180	90-180	120-180	~10	~14
HA3-Tg	-266.806	11.7858	168.81	83.01	90-180	45-120	~7	~12
HA4-Ct	-266.800	29.2688	5.93	177.56	0-90	135-180	~16	~13
HA5-Cg*	-268.463*	14.3658*	2.96	70*	0-90	45-135	~49	~42

[a] Relative to the lowest energy structure for each HA species

[b] Angles apply to rotation in both directions

[c] Based on MD simulation with 16 HA molecules (~1M HA), measured at 0 Å (surface) and 10 Å (bulk)

*Not found (not a stable gas-phase conformer), energy calculated from D2 dihedral potential energy scan

C3.2 HA conformer DFT molecular coordinates:

Table C3: Molecular coordinates from DFT structures calculated at B3LYP/6-311++G(2d,2p) level of theory.

HA1-Cc

#	Atom	X	Y	Z
1	C	-1.848868	-0.456463	0.013456
2	H	-1.903805	-1.341367	-0.620969

3	H	-2.590557	0.275296	-0.294892
4	H	-2.074496	-0.773477	1.034458
5	C	-0.474012	0.158908	-0.013742
6	C	0.722724	-0.775523	-0.027559
7	H	0.638189	-1.469374	0.817495
8	H	0.667946	-1.382806	-0.94043
9	O	1.935123	-0.074806	0.030748
10	H	1.700374	0.866049	0.01928
11	O	-0.289712	1.357825	-0.011732

HA2-Tt

#	Atom	X	Y	Z
1	C	0.78337	1.338994	0.000001
2	H	0.288013	1.769246	0.871724
3	H	0.288026	1.769246	-0.871729
4	H	1.840398	1.588155	0.000006
5	C	0.620314	-0.157251	0.000000
6	C	-0.792056	-0.733284	0.000003
7	H	-0.877306	-1.37248	-0.884142
8	H	-0.877306	-1.372471	0.884154
9	O	-1.767379	0.302109	-0.000003
10	H	-2.643058	-0.091441	-0.000002
11	O	1.556312	-0.924736	-0.000002

HA3-Tg

#	Atom	X	Y	Z
1	C	0.804628	1.336419	0.045518
2	H	0.300349	1.757439	0.916214
3	H	0.339878	1.798798	-0.827723
4	H	1.865075	1.570398	0.062974
5	C	0.618955	-0.159099	0.002518
6	C	-0.80112	-0.716794	0.128329
7	H	-0.900927	-1.549873	-0.570652
8	H	-0.885534	-1.132521	1.134512
9	O	-1.847033	0.235021	-0.005781
10	H	-2.027597	0.380654	-0.937469
11	O	1.543779	-0.933528	-0.098724

HA4-Ct

#	Atom	X	Y	Z
1	C	1.813664	-0.56466	0.026325
2	H	1.785581	-1.479282	-0.567138
3	H	2.023417	-0.851081	1.059668
4	H	2.614197	0.082676	-0.321022
5	C	0.497545	0.186528	-0.018851
6	C	-0.744955	-0.692424	-0.050149
7	H	-0.713089	-1.258131	-0.991504
8	H	-0.659101	-1.424384	0.764187
9	O	-1.9103	0.089946	0.058288
10	H	-2.676535	-0.485534	-0.002759
11	O	0.4388	1.389939	-0.018961

HA5-Cg*				
#	Atom	X	Y	Z
1	C	-1.847427	-0.474899	0.043742
2	H	-1.902448	-1.369072	-0.577544
3	H	-2.609655	0.239484	-0.255118
4	H	-2.041538	-0.782097	1.074179
5	C	-0.484952	0.164158	-0.026391
6	C	0.727625	-0.749163	-0.058507
7	H	0.676866	-1.432985	0.797357
8	H	0.660768	-1.36952	-0.961731
9	O	1.928344	-0.026493	-0.040146
10	H	1.995342	0.357143	0.847987
11	O	-0.322195	1.366052	-0.044628

C3.3. Calculated frequencies and VSF intensities

Table D4: DFT harmonic and anharmonic frequencies calculated at B3LYP/6-311++G(2d,2p) level of theory and calculated VSF intensities

HA1-Cc				
#	DFT harmonic frequencies (cm^{-1})	DFT anharmonic frequencies (cm^{-1})	ssp intensity (arb. units)	sps intensity (arb. units)
1	1207.81	1163.504	-5603.86	912.912
2	1258.28	1225.721	635.291	-1109.67
3	1309.37	1277.301	-10701.6	10991.8
4	1397.35	1354.997	1306.7	281.509
5	1443.1	1395.484	2975	-4389.59
6	1469.9	1438.411	-2787.03	-2914.53
7	1482.26	1445.515	57.7226	2128.36
8	1486.2	1470.28	-9180.68	1065.61
9	1770.11	1737.052	-38501.4	-26245.8
10	2988.43	2862.156	-1162.2	13915.5
11	3009.59	2848.665	-3051.33	27209.5
12	3041.34	2928.386	22762.5	1333.43
13	3096.8	2963.758	-8186.68	2315.37
14	3145.61	2985.723	4012.26	-8107.86
15	3695.39	3504.935	95256.1	11516
HA2-Tt				
#	DFT harmonic	DFT anharmonic	ssp intensity	sps intensity

	frequencies (cm^{-1})	frequencies (cm^{-1})	(arb. units)	(arb. units)
1	1254.46	1228.781	4397.92	-4648.13
2	1267.27	1221.729	42397.5	10198.3
3	1393.21	1358.275	-14929.6	12711.6
4	1424.26	1393.945	-9751.3	7830.24
5	1463.85	1416.304	6262.42	39014.9
6	1470.39	1437.72	-1683.35	2980.11
7	1483.22	1474.01	24762.3	-16913.5
8	1778.5	1752.564	60021.9	159024
9	3010.43	2899.221	372372	-46308.8
10	3044.9	2892.064	-32492.9	39737.3
11	3047.18	2927.139	-25859.5	-994.14
12	3099.07	2946.303	33778.1	-37116
13	3152.24	3004.851	-5719.35	29926.2
14	3854.75	3648.731	203191	145252

HA3-Tg

#	DFT harmonic frequencies (cm^{-1})	DFT anharmonic frequencies (cm^{-1})	ssp intensity (arb. units)	sps intensity (arb. units)
1	1202.96	1172.802	4180.62	5216.39
2	1241.26	1198.132	12572.4	-8989.58
3	1363.71	1331.609	3200.13	207.208
4	1383.73	1336.773	9151.82	695.74
5	1392.89	1361.491	-5077.53	3988.24
6	1460.11	1426.492	-910.513	10359.9
7	1465.98	1426.091	9342.52	378.198
8	1473.3	1442.362	-9.3031	-1776.16
9	1776.35	1750.161	19908.8	57634.4
10	3040.13	2907.433	87241.7	-15599.2
11	3043.51	2922.907	-10205.1	-56.692
12	3081.97	2921.159	-5915.12	5892.31
13	3094.73	2940.994	13695.7	-15849
14	3150.74	3001.511	-5958.65	8021.47
15	3850.76	3670.124	45668.1	23471.9

HA4-Ct

#	DFT harmonic frequencies (cm^{-1})	DFT anharmonic frequencies (cm^{-1})	ssp intensity (arb. units)	sps intensity (arb. units)
1	1235.34	1225.429	-10346.2	20406.3
2	1267.1	1233.013	660.161	-1646.79
3	1390.63	1356.551	-4195.6	2113.97
4	1438.7	1416.224	-1390.79	352.329
5	1470.8	1426.125	-1737.58	6578.98
6	1482.93	1450.528	2164.3	-3739.64
7	1488.35	1445.553	18529.7	6900.52
8	1803.06	1768.692	52527.3	64229.1
9	2970.02	2778.773	25747.7	-39379
10	2992.37	2844.458	10456.4	-65318.6
11	3038.14	2931.083	-55469.5	-2278.79
12	3092.47	2948.34	12809.7	-17516.1
13	3144.16	2999.333	-3982.09	31009.5
14	3854.06	3669.399	112928	76191.5

HA5-Cg*				
#	DFT harmonic frequencies (cm^{-1})	DFT anharmonic frequencies (cm^{-1})	ssp intensity (arb. units)	sps intensity (arb. units)
1	1066.96	1042.26	2452.33	-4124.43
2	1119.53	1092.831	-3323.8	-10525
3	1204.63	1164.103	-24960.5	10166.2
4	1242.16	1214.662	2185.2	-829.534
5	1385.65	1347.611	-1272.01	-15536.1
6	1397.5	1352.682	7464.22	8074.57
7	1438.37	1400.415	528.791	27664.9
8	1466.95	1435.232	-4294.02	-4094.97
9	1474.21	1438.459	-2615.26	-34299.6
10	1483.67	1449.756	15339.1	-7157.09
11	1764.34	1729.487	-120787	-103211
12	2986.18	2818.498	155692	22643.7
13	3023.53	2868.119	-31281.7	39265.5
14	3039.48	2935.465	103840	-742.576
15	3094.51	2962.946	13019.2	46282.9
16	3145.02	2983.738	-6699.41	16741.3
17	3727.27	3537.297	149182	75563.1

APPENDIX D

SUPPLEMENTAL INFORMATION FOR PA

D1. Experimental VSF Spectra

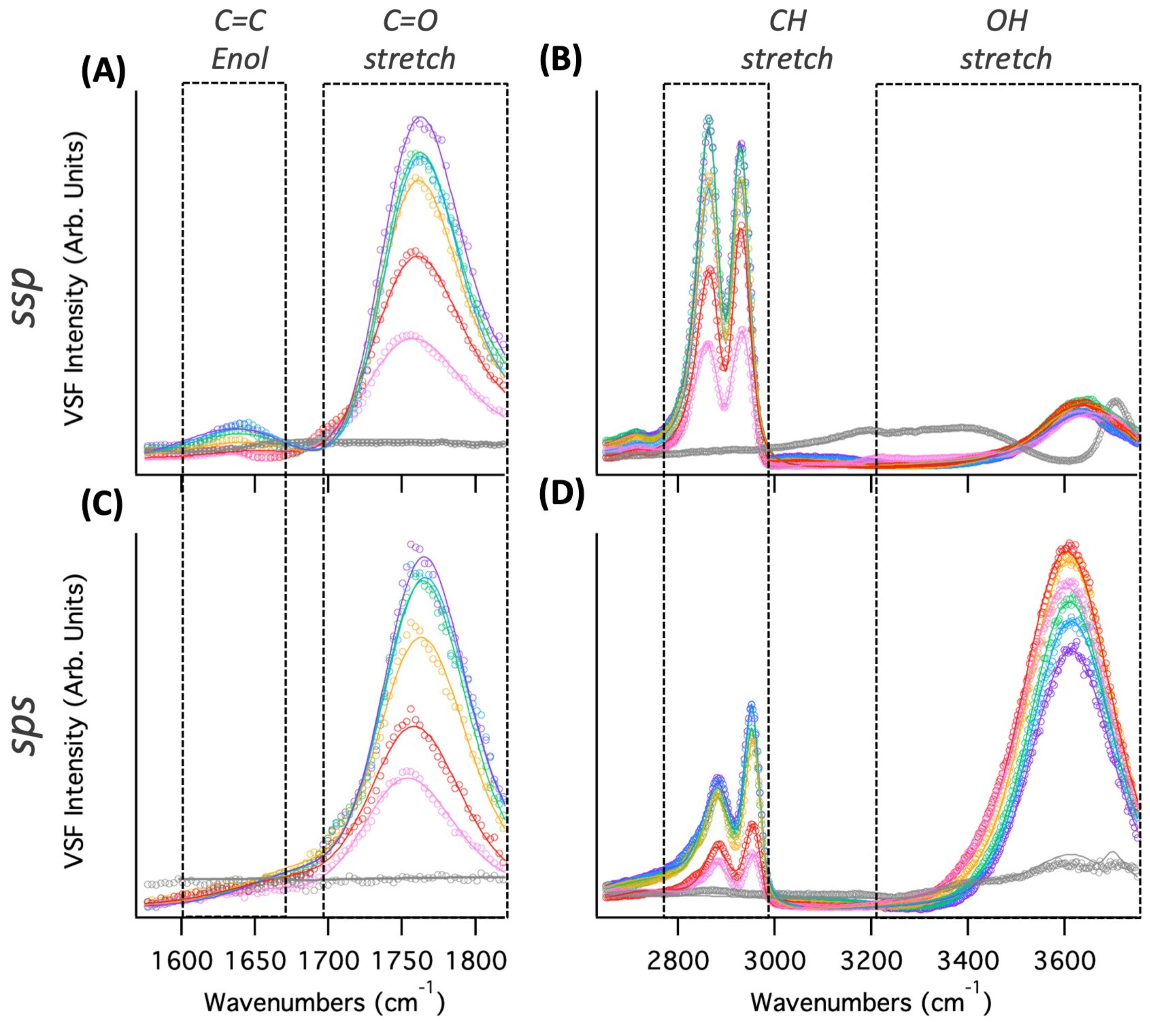

Figure D1. VSF Experimental data (open circles) and corresponding fits (solid lines) for water and aqueous PA solutions in the C=C/C=O stretching region (A,C), and the CH/OH stretching region (B,D) in the *ssp* polarization (top) and *sps* polarization (bottom). Water (gray), 0.05M PA (pink), 0.1M PA (red), 0.25M PA (orange), 0.5M PA (green), 0.75M HA (blue), and 1M HA (purple). Dashed boxes provide visual reference of approximate spectral regions.

E2. COMPUTATIONAL DETAILS

D2.1 PA species DFT molecular coordinates:

Table D1: Molecular coordinates from DFT structures calculated at B3LYP/6-311++G(2d,2p) level of theory.

PYA1

#	Atom	X	Y	Z
1	C	1.769783	0.749761	-0.000009
2	H	1.668251	1.386235	0.871728
3	H	2.738013	0.270021	0.000014
4	H	1.668275	1.386198	-0.871776
5	C	0.699315	-0.307252	0.000001
6	C	-0.744684	0.219606	0.000001
7	O	0.90256	-1.474287	0.00001
8	O	-0.99637	1.379077	0.000011
9	O	-1.644995	-0.739055	-0.00001
10	H	-2.510591	-0.341021	-0.000015

PYA2

#	Atom	X	Y	Z
1	C	1.801577	0.679507	0.000001
2	H	1.736389	1.321219	-0.871315
3	H	1.736388	1.321214	0.871321
4	H	2.737755	0.14014	0.000002
5	C	0.663708	-0.295661	-0.000001
6	C	-0.761392	0.285898	0
7	O	0.776075	-1.482053	-0.000001
8	O	-0.963891	1.449606	-0.000001
9	O	-1.703213	-0.630445	0.000002
10	H	-1.305659	-1.497891	-0.000004

PYT1

#	Atom	X	Y	Z
1	C	1.20809	1.07541	-0.83037
2	H	0.88984	2.04801	-0.46652
3	H	2.29349	1.00339	-0.76318
4	H	0.92223	0.96404	-1.87525
5	C	0.59656	-0.03107	0.01433
6	C	-0.94547	-0.08383	-0.05005
7	O	-1.5544	-1.11429	-0.1844
8	O	-1.52438	1.11666	0.07857
9	H	-2.48342	0.98085	0.07247
10	O	1.10145	-1.25408	-0.43166
11	H	0.43735	-1.93242	-0.24247
12	O	0.85441	0.16113	1.40215
13	H	1.76883	-0.1023	1.55431

PYT2

#	Atom	X	Y	Z
1	C	1.41591	1.17614	-0.23536
2	H	1.20923	1.91288	0.53536
3	H	2.47168	0.9055	-0.21348
4	H	1.18998	1.60782	-1.20738
5	C	0.58775	-0.07134	-0.00055
6	C	-0.92497	0.24578	0.00662
7	O	-1.40642	1.34421	0.03442
8	O	-1.65731	-0.88889	-0.04118
9	H	-2.59044	-0.63256	-0.03475
10	O	0.88716	-0.9787	-1.03615
11	H	0.33901	-1.76277	-0.91226
12	O	0.8189	-0.64792	1.27173
13	H	1.76975	-0.76393	1.37767

PPA1

#	Atom	X	Y	Z
1	O	-3.81139	-0.17865	-0.12817
2	H	-3.5434	-1.10715	-0.00107
3	C	-2.69787	0.5556	-0.08955
4	C	-1.42613	-0.30876	0.14611
5	C	-0.1308	0.44752	0.22995
6	H	-0.18953	1.2793	-0.47137
7	H	-0.09054	0.91788	1.21613
8	C	1.14662	-0.36047	-0.0224
9	C	2.3372	0.60924	0.084
10	O	3.36723	0.22117	-0.70346
11	H	4.09449	0.84292	-0.5566
12	O	1.02626	-0.87623	-1.34276
13	H	1.86615	-1.26241	-1.61048
14	O	2.3933	1.56493	0.8108
15	O	-1.58668	-1.50152	0.27341
16	O	-2.67275	1.74796	-0.21299
17	C	1.39654	-1.48095	1.00264
18	H	1.44117	-1.07966	2.01505
19	H	0.59562	-2.21052	0.93963
20	H	2.34494	-1.97469	0.7897

PPA2

#	Atom	X	Y	Z
1	O	3.45787	-0.85779	-0.14372
2	H	2.89205	-1.62051	-0.36197
3	C	2.65151	0.17714	0.09426
4	C	1.15192	-0.18701	-0.05102
5	C	0.16245	0.89768	0.2644
6	H	0.17973	1.03753	1.34893
7	H	0.52308	1.83434	-0.16258
8	C	-1.26902	0.60732	-0.19818

9	C	-1.81175	-0.66101	0.50205
10	O	-2.39503	-1.55606	-0.30027
11	H	-2.23683	-1.2726	-1.21656
12	O	-1.27969	0.37101	-1.61801
13	H	-1.63487	1.14155	-2.06937
14	O	-1.76181	-0.78752	1.69538
15	O	0.87201	-1.3143	-0.38674
16	O	3.03215	1.27694	0.38537
17	C	-2.19481	1.77221	0.16279
18	H	-2.22192	1.91529	1.24053
19	H	-1.83696	2.69423	-0.29959
20	H	-3.21001	1.57391	-0.18133

ZYA1

#	Atom	X	Y	Z
1	C	1.421578	0.623272	0.445193
2	C	1.456052	-0.567999	-0.455433
3	C	0.263173	-1.127451	-0.467482
4	O	0.181386	0.695585	0.94342
5	H	-0.068709	-1.99702	-1.000748
6	O	2.290599	1.368941	0.709556
7	O	2.606082	-0.862394	-1.051897
8	H	2.516907	-1.62603	-1.607058
9	C	-1.754526	0.290631	-0.433184
10	O	-2.778059	-0.268668	-0.656023
11	O	-1.430238	1.456743	-0.95646
12	H	-2.146942	1.745214	-1.514122
13	C	-0.652034	-0.323569	0.429208
14	C	-1.248941	-1.116135	1.58394
15	H	-0.447038	-1.548792	2.168753
16	H	-1.834914	-0.464609	2.220661
17	H	-1.889278	-1.902924	1.210287

ZYA2

#	Atom	X	Y	Z
1	C	-1.947193	0.05987	0.139257
2	C	-0.537764	0.516683	-0.269035
3	C	0.512813	-0.549085	0.195218
4	C	1.920713	0.037062	0.140393
5	O	2.660708	0.0574	1.069241
6	O	-2.620363	0.618329	0.938925
7	O	-2.365858	-1.012197	-0.516241
8	H	-3.247259	-1.209404	-0.213393
9	O	-0.575593	0.627437	-1.66401
10	H	0.249947	0.976479	-1.97437
11	O	0.221037	-0.850595	1.525237
12	H	1.008818	-0.779461	2.052902
13	O	2.26561	0.486778	-1.061205

14	H	3.165059	0.801814	-1.023219
15	C	0.530224	-1.837608	-0.639845
16	H	-0.400608	-2.364711	-0.508756
17	H	0.674716	-1.635373	-1.690985

ED.2. Calculated frequencies and VSF intensities

Table D2: DFT harmonic and anharmonic frequencies calculated at B3LYP/6-311++G(2d,2p) level of theory and calculated VSF intensities

PYA1

#	DFT harmonic frequencies (cm^{-1})	DFT anharmonic frequencies (cm^{-1})	*ssp* intensity (arb. units)	*sps* intensity (arb. units)
1	1789.93	1759.43	1133372.5	429232.5
2	1801.25	1768.3	-367860	-551490
3	3050.48	2928.97	-33217	-155.1815
4	3102.04	2952.46	-136750.25	120046.5
5	3158.45	3004.26	-23123.5	-43963.75
6	3756.62	3556.07	321925	306765

PYA2

#	DFT harmonic frequencies (cm^{-1})	DFT anharmonic frequencies (cm^{-1})	*ssp* intensity (arb. units)	*sps* intensity (arb. units)
1	1772.66	1743.02	-780968	-67324.08188
2	1834.7	1799.28	822324	-295148.4039
3	3050.69	2928.28	-332026	-15971.16202
4	3100.91	2948.52	-51857.8	55504.75858
5	3159.8	3002.8	45430	330290.1669
6	3641.66	3423.9	-809762	280178.6082

PYT1

#	DFT harmonic frequencies (cm^{-1})	DFT anharmonic frequencies (cm^{-1})	*ssp* intensity (arb. units)	*sps* intensity (arb. units)
1	1804.73	1769.13	73075.5	44352.5
2	3054.95	2963.41	59929.5	714.0275
3	3118.01	2976.07	-37022.25	29389.5
4	3150.07	3008.63	-1686.29	-10403.75
5	3738.83	3527.05	-80137	-13666.05
6	3751.92	3549.56	19472.225	15064.225
7	3811.82	3628.78	88413.75	52580.75

PYT2

#	DFT harmonic frequencies (cm^{-1})	DFT anharmonic frequencies (cm^{-1})	*ssp* intensity (arb. units)	*sps* intensity (arb. units)
1	1825.85	1796.01	32751.75	18448.975
2	3059.1	2959.47	46281.75	977.18

3	3128.73	2988.24	-13069.125	10407.325
4	3154.39	3010.43	-9685.825	12299.925
5	3763.83	3583.52	48088.25	41409
6	3798.84	3603.79	64228	48138.25
7	3805.65	3633.31	36792	10936.1

PPA1

#	DFT harmonic frequencies (cm^{-1})	DFT anharmonic frequencies (cm^{-1})	*ssp* intensity (arb. units)	*sps* intensity (arb. units)
1	1773.42	1745.63	-13480.3	-4012.4
2	1809.05	1777.95	15449.4	3328.81
3	1835.34	1801.37	19742.9	12057.5
4	3049.1	2876.7	-24096.6	-7100.76
5	3058.08	2930.59	-9649.3	-657.076
6	3102	2914.8	841.022	-684.748
7	3108.4	2966.47	-1027.68	-13593.3
8	3158.5	3011.54	-859.226	-513.863
9	3639.37	3420.47	62976.4	-69.7406
10	3760.56	3559.94	-27401.5	-16328.8
11	3827.57	3639.98	30075.8	23272.6

PPA2

#	DFT harmonic frequencies (cm^{-1})	DFT anharmonic frequencies (cm^{-1})	*ssp* intensity (arb. units)	*sps* intensity (arb. units)
1	1778.8	1748.21	211045	142721
2	1830.19	1798.08	266224	201555
3	1832.65	1799.62	-353396	-322926
4	3036.75	2937.34	-393306	-37810.8
5	3051.39	2916.97	-244166	7891.26
6	3090.57	2942.4	-328.534	-12721.6
7	3101.25	2955.77	198371	-56652.1
8	3133.6	2991.46	-508.702	44739.3
9	3646.83	3432.32	-906328	-86044.6
10	3676.47	3465.7	720556	121794
11	3842.33	3628.92	318443	207736

ZYA1

#	DFT harmonic frequencies (cm^{-1})	DFT anharmonic frequencies (cm^{-1})	*ssp* intensity (arb. units)	*sps* intensity (arb. units)
1	1700.22	1658.33	169739	-12811.3
2	1794.8	1765.4	-672.509	-10916.2
3	1853	1817.99	9176.33	61488.6
4	3059.18	2961.89	114319	5972.27
5	3129.15	2986.25	-20378.7	46221
6	3143.87	2999.05	-9976.41	7073.36
7	3226.14	3106.04	-17111.3	3405.14
8	3753.12	3550.68	138143	100462
9	3825.49	3656.24	120791	70765.3

ZYA2

#	DFT harmonic frequencies (cm^{-1})	DFT anharmonic frequencies (cm^{-1})	*ssp* intensity (arb. units)	*sps* intensity (arb. units)
1	1734.17	1695.36	210638	-24766.4
2	1823.55	1790.43	83196.3	130823
3	1839.72	1808.3	-35037.5	-14506.5
4	3056.53	2949.81	28128.7	5938
5	3127.2	2977.74	-16178.8	19057.8
6	3142.39	2993.53	1375.62	-13902.6
7	3251.63	3114.56	2399.49	24469.5
8	3724.97	3517.18	-63057	-31456.8
9	3739.7	3537.44	-127001	25578.4

Table E3: DFT harmonic and anharmonic frequencies calculated at B3LYP/6-311++G(2d,2p) level of theory and calculated VSF intensities

Deuterated ZYA1

#	DFT harmonic frequencies (cm^{-1})	DFT anharmonic frequencies (cm^{-1})
1	1699.50	1663.658
2	1787.81	1756.907
3	1852.68	1817.698
4	2729.95	2622.074
5	2784.84	2695.84
6	3059.18	2961.24
7	3129.15	2986.348
8	3143.87	2998.87
9	3226.14	3105.43

Deuterated ZYA2

#	DFT harmonic frequencies (cm^{-1})	DFT anharmonic frequencies (cm^{-1})
1	1723.10	1686.95
2	1822.01	1791.266
3	1833.28	1797.918
4	2710.54	2601.788
5	2721.70	2615.932
6	3056.53	2949.348
7	3127.20	2977.757
8	3142.39	2993.629
9	3251.64	3112.622

APPENDIX E

SUPPLEMENTAL INFORMATION FOR MG-NaCl

The contents of this chapter have been or are intended to be published in whole or in part. The text presented here has been modified from the publication below:

Gordon, B. P., Wren, S. N., Moore, F. G., Scatena, L. F., Richmond, G. L. Diol it up: The Influence of NaCl on Methylglyoxal Surface Adsorption and Hydration State at the Air-water interface. **To be submitted to Journal of Physical Chemistry A in December 2019*

E1: NMR Results

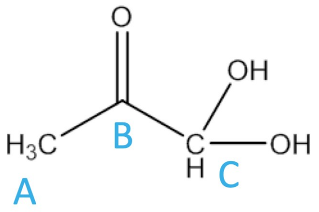

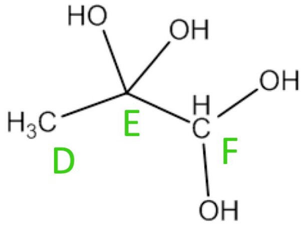

Table E1: NMR Assignments for methylglyoxal

Assignment		^{1}H Chemical Shift (ppm)			^{13}C Chemical Shift (ppm)	
		Here	Donarski et al.[a]	Nemet et al.[b]	Here	Nemet et al.[b]
A	CH_3	2.31	2.31	2.3	25.4	25.4
B	C=O				209.9	209.9
C	CH	5.28	5.29	5.25	90.6	90.6
D	CH_3	1.38	1.38	1.19	22.2	22.2
E	$C(OH)_2$				96.0	96.0
F	CH	4.8	4.81	4.3	92.7	92.7

a: Donarski, J. A., Roberts, D. P. T., & Charlton, A. J. (2010). *Anal. Methods*, *2*(10), 1479–1483.
b: Nemet, I., Vikić-Topić, D., & Varga-Defterdarović, L. (2004). *Bioorganic Chemistry*, *32*(6), 560–570.

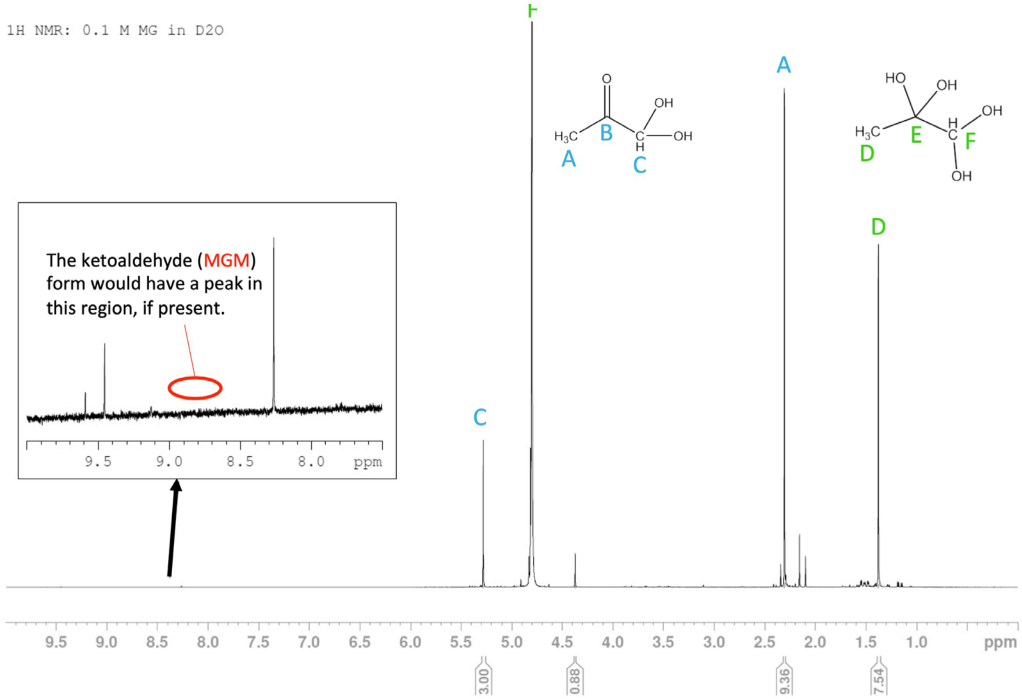

The ketoaldehyde (MGM) form would have a peak in this region, if present.

Figure E1. ^{1}H NMR spectrum of MG

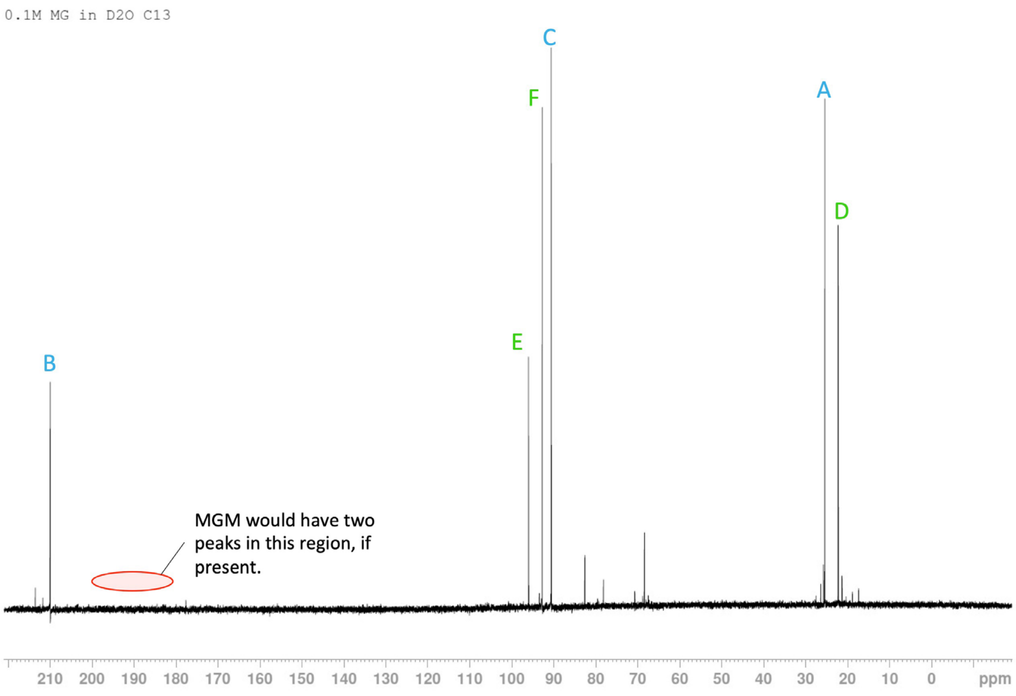

MGM would have two peaks in this region, if present.

Figure E2. ^{13}C NMR of MG

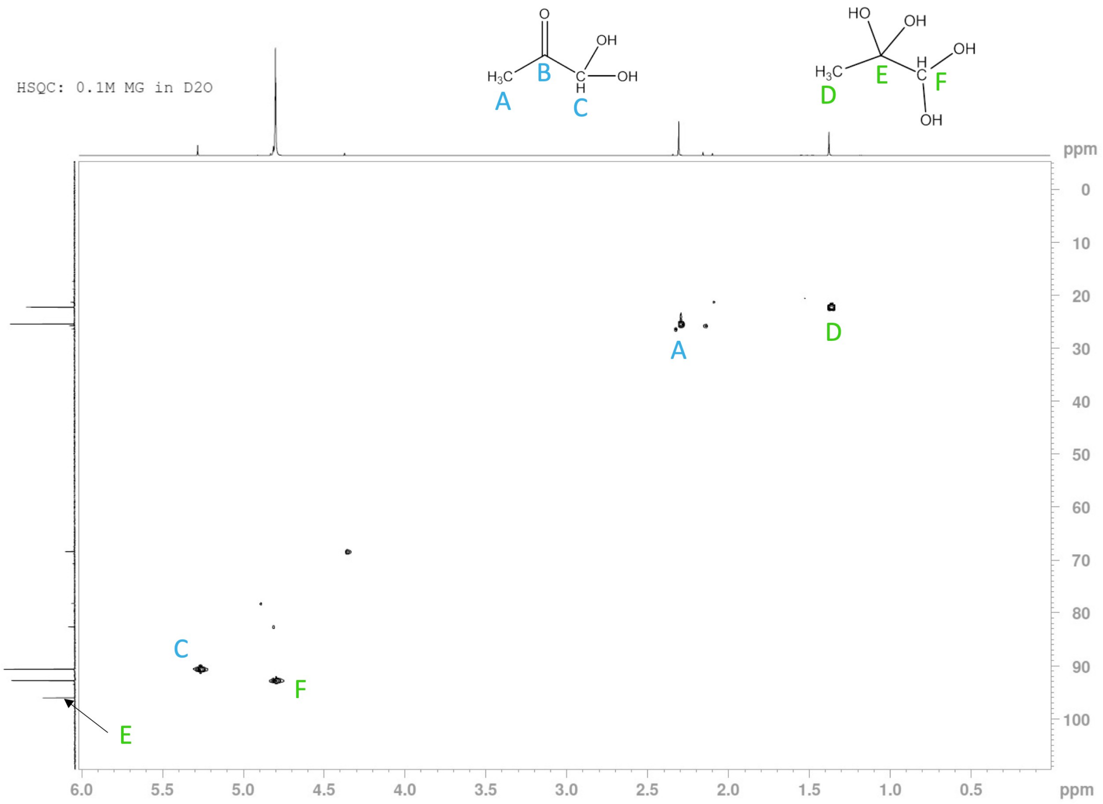

Figure E3. HSQC of MG

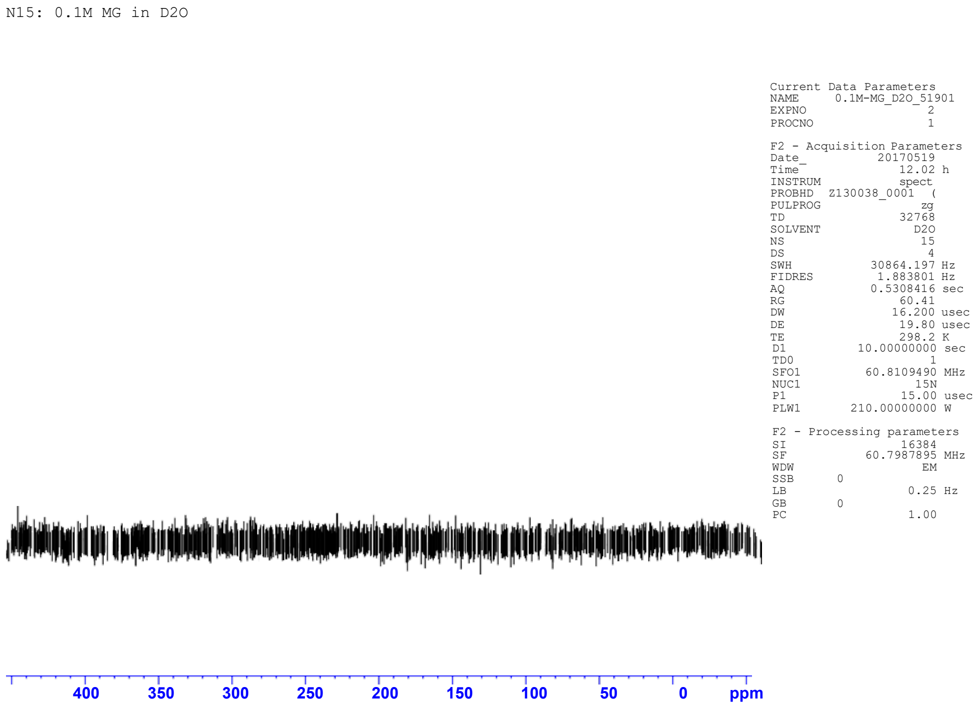

N15: 0.1M MG in D2O

```
Current Data Parameters
NAME     0.1M-MG_D2O_51901
EXPNO                    2
PROCNO                   1

F2 - Acquisition Parameters
Date_             20170519
Time                 12.02 h
INSTRUM              spect
PROBHD  Z130038_0001  (
PULPROG                 zg
TD                   32768
SOLVENT                D2O
NS                      15
DS                       4
SWH              30864.197 Hz
FIDRES            1.883801 Hz
AQ               0.5308416 sec
RG                   60.41
DW                  16.200 usec
DE                   19.80 usec
TE                   298.2 K
D1             10.00000000 sec
TD0                      1
SFO1            60.8109490 MHz
NUC1                   15N
P1                   15.00 usec
PLW1          210.00000000 W

F2 - Processing parameters
SI                   16384
SF              60.7987895 MHz
WDW                     EM
SSB      0
LB                    0.25 Hz
GB       0
PC                    1.00
```

Figure E4. ^{15}N NMR Confirming that there are no nitrogen containing contaminants in the stock MG.

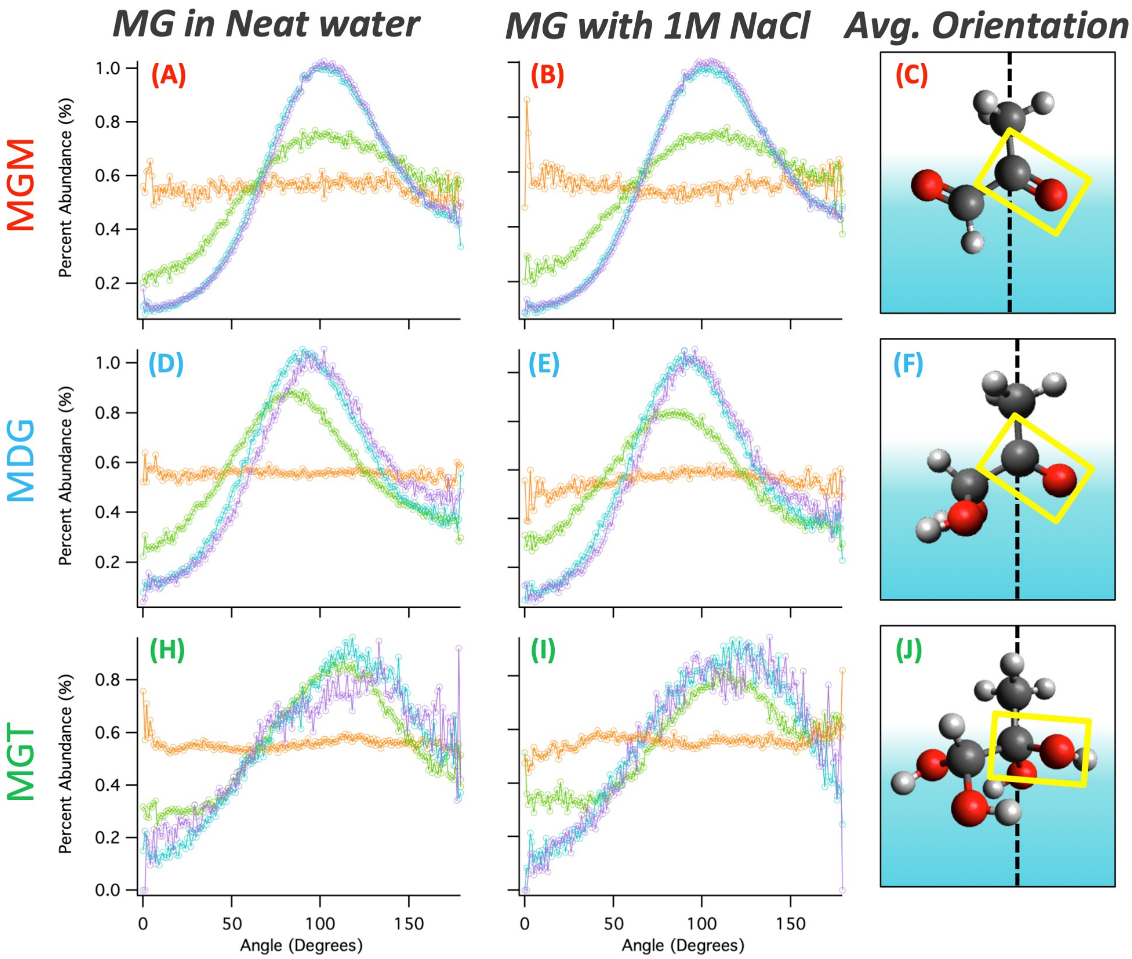

Figure E5. Normalized distributions of HA bond angles (relative to the surface normal into the vapor phase) for a simulation with 80 HA molecules (~5M). Percent abundance for the total HA system (black, open x's) and individual HA conformers (HA1–Cc (pink, circles), HA2-Tt (orange, squares), HA3-Tg (gold, diamonds), HA4-Ct (olive, triangles), HA5-Cg (purple, stars) are displayed for the C-CH_3 (A,B), methylene CH (C,D), and C=O (E,F) bond angles at the surface (0 Å, top) and sub-surface (5 Å, bottom), respectively. (G): Visual representation of the C=O bond angle orientation as a function of depth from the interface. In the bulk (~10 Å), the orientation is isotropic and HA has no average net orientation (indicated by the curved arrows.)

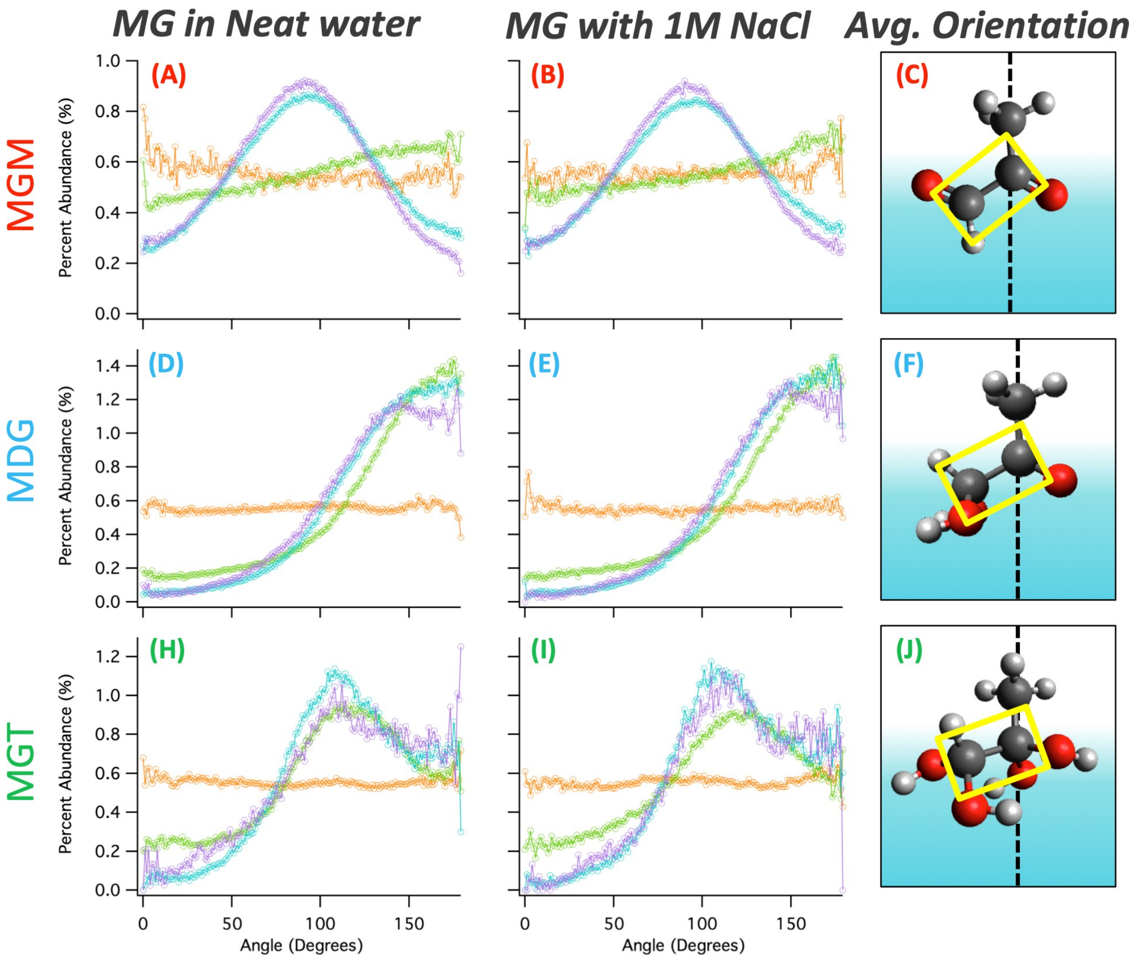

Figure E6. Normalized distributions of HA bond angles (relative to the surface normal into the vapor phase) for a simulation with 80 HA molecules (~5M). Percent abundance for the total HA system (black, open x's) and individual HA conformers (HA1–Cc (pink, circles), HA2-Tt (orange, squares), HA3-Tg (gold, diamonds), HA4-Ct (olive, triangles), HA5-Cg (purple, stars) are displayed for the C-CH_3 (A,B), methylene CH (C,D), and C=O (E,F) bond angles at the surface (0 Å, top) and sub-surface (5 Å, bottom), respectively. (G): Visual representation of the C=O bond angle orientation as a function of depth from the interface. In the bulk (~10 Å), the orientation is isotropic and HA has no average net orientation (indicated by the curved arrows.)

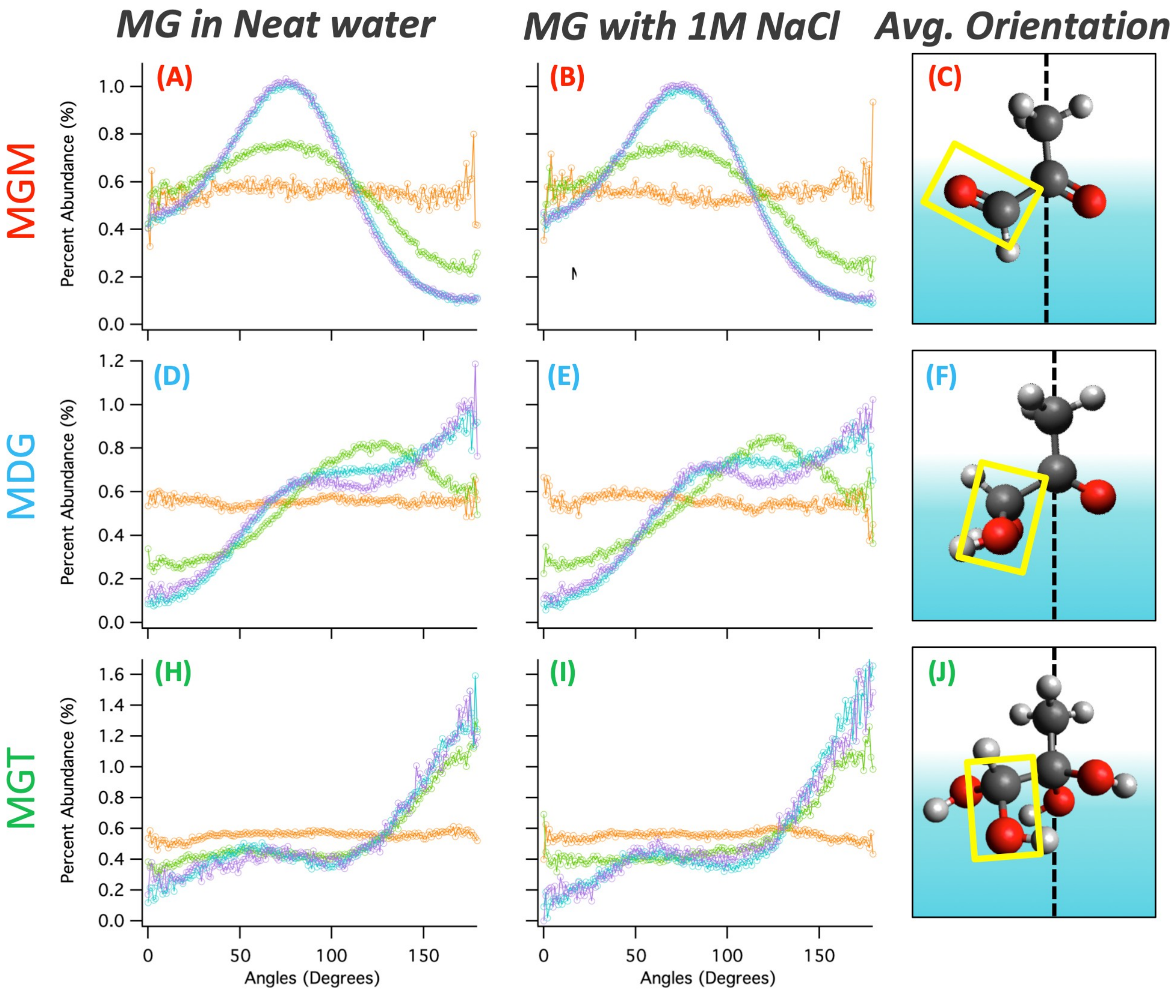

Figure E7. Normalized distributions of HA bond angles (relative to the surface normal into the vapor phase) for a simulation with 80 HA molecules (~5M). Percent abundance for the total HA system (black, open x's) and individual HA conformers (HA1–Cc (pink, circles), HA2-Tt (orange, squares), HA3-Tg (gold, diamonds), HA4-Ct (olive, triangles), HA5-Cg (purple, stars) are displayed for the C-CH_3 (A,B), methylene CH (C,D), and C=O (E,F) bond angles at the surface (0 Å, top) and sub-surface (5 Å, bottom), respectively. (G): Visual representation of the C=O bond angle orientation as a function of depth from the interface. In the bulk (~10 Å), the orientation is isotropic and HA has no average net orientation (indicated by the curved arrows.)

E2. COMPUTATIONAL DETAILS

E2.1 DFT molecular coordinates of gas-phase MG species:

Table E2: Molecular coordinates from DFT structures calculated at B3LYP/6-311++G(2d,2p) level of theory.

MGM1

#	Atom	X	Y	Z
1	C	0.89811	1.261974	-0.000002
2	C	0.517082	-0.188487	-0.000002
3	H	0.470022	1.757903	0.872799
4	H	0.469918	1.757937	-0.872732
5	H	1.97934	1.361283	-0.000059
6	C	-0.981113	-0.532864	0.000003
7	O	1.298514	-1.11164	-0.000001
8	O	-1.850412	0.297324	0
9	H	-1.180846	-1.619999	0.000009

MGD1

#	Atom	X	Y	Z
1	C	1.402379	1.05925	-0.240098
2	C	0.778528	-0.278511	0.045738
3	H	1.080083	1.781843	0.510578
4	H	1.054047	1.427228	-1.205907
5	H	2.484595	0.968098	-0.237682
6	C	-0.758721	-0.331855	0.080067
7	O	1.408787	-1.289417	0.245029
8	H	-1.056194	-1.359277	0.296847
9	O	-1.178868	0.543612	1.104541
10	O	-1.213733	0.068564	-1.194747
11	H	-2.039571	0.272098	1.435388
12	H	-2.081994	-0.306735	-1.36581

MGD2

#	Atom	X	Y	Z
1	C	-1.89091	-0.769276	0.007074
2	C	-0.747127	0.213013	-0.001925
3	H	-1.82788	-1.424022	-0.865314
4	H	-2.838476	-0.238668	0.002153
5	H	-1.827945	-1.407844	0.891379
6	C	0.67697	-0.396027	0.003707
7	O	-0.895845	1.40582	-0.012897
8	H	0.623025	-1.490095	0.013896
9	O	1.299616	0.064505	1.178784
10	O	1.299523	0.042529	-1.179807
11	H	2.068501	-0.47971	1.37228
12	H	2.068297	-0.5053	-1.363281

MGD3

#	Atom	X	Y	Z
1	C	-1.868963	-0.638463	-0.200898
2	C	-0.706654	0.292473	-0.028682
3	H	-1.917283	-0.987669	-1.234461
4	H	-2.795032	-0.137502	0.065633
5	H	-1.719765	-1.520036	0.423709
6	C	0.699696	-0.243977	-0.373655
7	O	-0.80425	1.426155	0.381618
8	H	0.729748	-0.609362	-1.405856
9	O	0.908884	-1.323356	0.525842
10	O	1.652098	0.75538	-0.252267
11	H	1.833146	-1.583803	0.454828
12	H	1.25295	1.462186	0.280387

MGT2

#	Atom	X	Y	Z
1	C	0.867998	0.058065	-0.458665
2	C	-0.618519	-0.042686	-0.008203
3	H	0.902551	0.026253	-1.547505
4	O	1.398692	1.262234	0.044742
5	O	1.624495	-1.046	-0.026852
6	C	-1.32406	1.299217	0.062659
7	O	-0.710334	-0.632008	1.277527
8	O	-1.206766	-0.898497	-0.973185
9	H	-2.14819	-0.960091	-0.779687
10	H	-0.460358	-1.557865	1.170902
11	H	2.309819	1.32908	-0.257933
12	H	1.672781	-0.988353	0.936094
13	H	-2.379156	1.13461	0.285372
14	H	-0.893768	1.91854	0.84408
15	H	-1.238273	1.820845	-0.888238

MGT3

#	Atom	X	Y	Z
1	C	0.837428	0.10253	-0.490977
2	C	-0.62155	-0.018687	0.01784
3	H	0.835911	0.289305	-1.570411
4	O	1.590081	-1.045519	-0.206025
5	O	1.407229	1.198398	0.188762
6	C	-1.533435	1.035833	-0.589743
7	O	-0.659895	0.049488	1.42556
8	O	-1.033285	-1.326111	-0.36736
9	H	-1.697303	-1.61228	0.268579
10	H	0.158952	0.464898	1.725923

11	H	0.971388	-1.788491	-0.179479
12	H	2.362299	1.147317	0.079629
13	H	-1.58678	0.92014	-1.671411
14	H	-1.166415	2.033088	-0.351996
15	H	-2.534305	0.927047	-0.173654

E2.2 Calculated frequencies and VSF intensities

Table E2: DFT harmonic and anharmonic frequencies calculated at B3LYP/6-311++G(2d,2p) level of theory and calculated VSF intensities

MGM1

#	DFT harmonic frequencies (cm^{-1})	DFT anharmonic frequencies (cm^{-1})	*ssp* intensity (arb. units)	*sps* intensity (arb. units)
1	1775.85	1717.065	817435.7779	429232.5
2	1794.38	1746.94675	-760403.6841	-551490
3	2940.68	2742.692375	15545684.65	-155.1815
4	3046.68	2886.6205	490518.8181	120046.5
5	3098.43	2905.3435	1501983.39	
6	3156.51	2960.841	-100263.9628	

MGD1

#	DFT harmonic frequencies (cm^{-1})	DFT anharmonic frequencies (cm^{-1})	*ssp* intensity (arb. units)	*sps* intensity (arb. units)
1	1795.28	1751.37	54715.36263	44352.5
2	3050.52	2932.05	1532068.705	714.0275
3	3055.86	2912.63	566761.755	29389.5
4	3107.9	2956.99	187636.7842	-10403.75
5	3152.63	3000.23	-7734.48809	-13666.05
6	3834.45	3646.48	15694872.2	15064.225
7	3834.81	3646.48	-2461231.351	52580.75

MGD2

#	DFT harmonic frequencies (cm^{-1})	DFT anharmonic frequencies (cm^{-1})	*ssp* intensity (arb. units)	*sps* intensity (arb. units)
1	1815.69	1781.14	-121910.9531	18448.975
2	2996.93	2860.31	3900284.757	977.18
3	3032.32	2938.12	3108675.225	10407.325
4	3083.61	2940	-603137.3279	12299.925
5	3149.5	2999.99	-71853.0917	
6	3827.3	3667.44	1741001.139	
7	3827.7	3667.3	-304317.1579	

MGD3

#	DFT harmonic	DFT anharmonic	*ssp* intensity	*sps* intensity

	frequencies (cm^{-1})	frequencies (cm^{-1})	(arb. units)	(arb. units)
1	1787.8	1752.47	-130459.963	-4012.4
2	3009.09	2869.31	2420216.139	3328.81
3	3044.14	2928.73	899294.4056	12057.5
4	3100.51	2953.88	-209269.735	-7100.76
5	3151.84	2997.29	2084.07896	-657.076
6	3680.3	3460.2	-3393882.452	-684.748
7	3819.21	3633.56	3829886.603	

MGT2

#	DFT harmonic frequencies (cm^{-1})	DFT anharmonic frequencies (cm^{-1})	*ssp* intensity (arb. units)	*sps* intensity (arb. units)
1	3050.86	2933.102125	4584496.567	142721
2	3079.57	2904.089375	1355992.061	201555
3	3119.98	2932.2825	-1977560.618	-322926
4	3152.09	2966.064875	153843.1382	-37810.8
5	3770.27	3532.74175	-19871.35972	7891.26
6	3786.25	3553.963125	-987914.1087	
7	3811.74	3581.1885	-4247100.42	
8	3823.52	3584.76325	5361074.288	

MGT3

#	DFT harmonic frequencies (cm^{-1})	DFT anharmonic frequencies (cm^{-1})	*ssp* intensity (arb. units)	*sps* intensity (arb. units)
1	3003.17	2798.545375	-494448.2782	-12811.3
2	3049.74	2943.619	856060.6677	-10916.2
3	3120.17	2936.43	-77790.93504	61488.6
4	3125.38	2950.659875	95859.01725	5972.27
5	3745.82	3519.538875	-3149277.332	46221
6	3762.81	3574.45375	2720519.165	7073.36
7	3822.88	3595.122125	-2794563.548	
8	3826.29	3601.531	2688742.194	

APPENDIX F
SUPPLEMENTAL INFORMATION FOR COMPUTATIONAL WORK

This chapter includes contents that are currently being prepared for the publication below:

Gordon, B. P., Moore, F. G., Valley, N. A., Richmond, G. L. Level Up: Methodology Improvements for Calculation of VSF Spectra of Aqueous Organic Interfaces Using Gas-Phase Water Microclusters. **In Preparation*

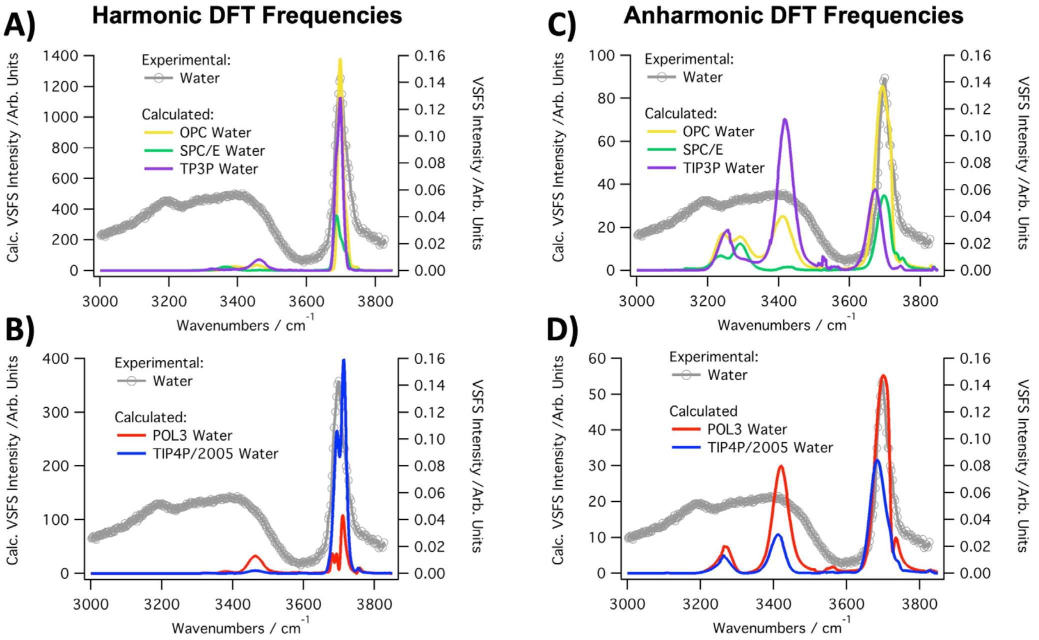

Figure F1. Experimental VSF spectra of neat water (gray) in the CH stretching region compared to calculated VSF spectra (colored lines) arising from either harmonic (left, A-B) or anharmonically corrected (left, A-B) DFT frequency positions. Calculated VSF spectra were generated from simulations each MD water model and are color-coded as follows: OPC (yellow), SPC/E (green), TP3P (purple), POL3 (red), and TIP4P/2005 (blue). Poorer agreeing models displayed in the top row (A,C) and better agreeing models displayed in the bottom row (B,D). Harmonic Calculated spectra are scaled by 0.9925 and anharmonic Calculated spectra are scaled by 1.035.

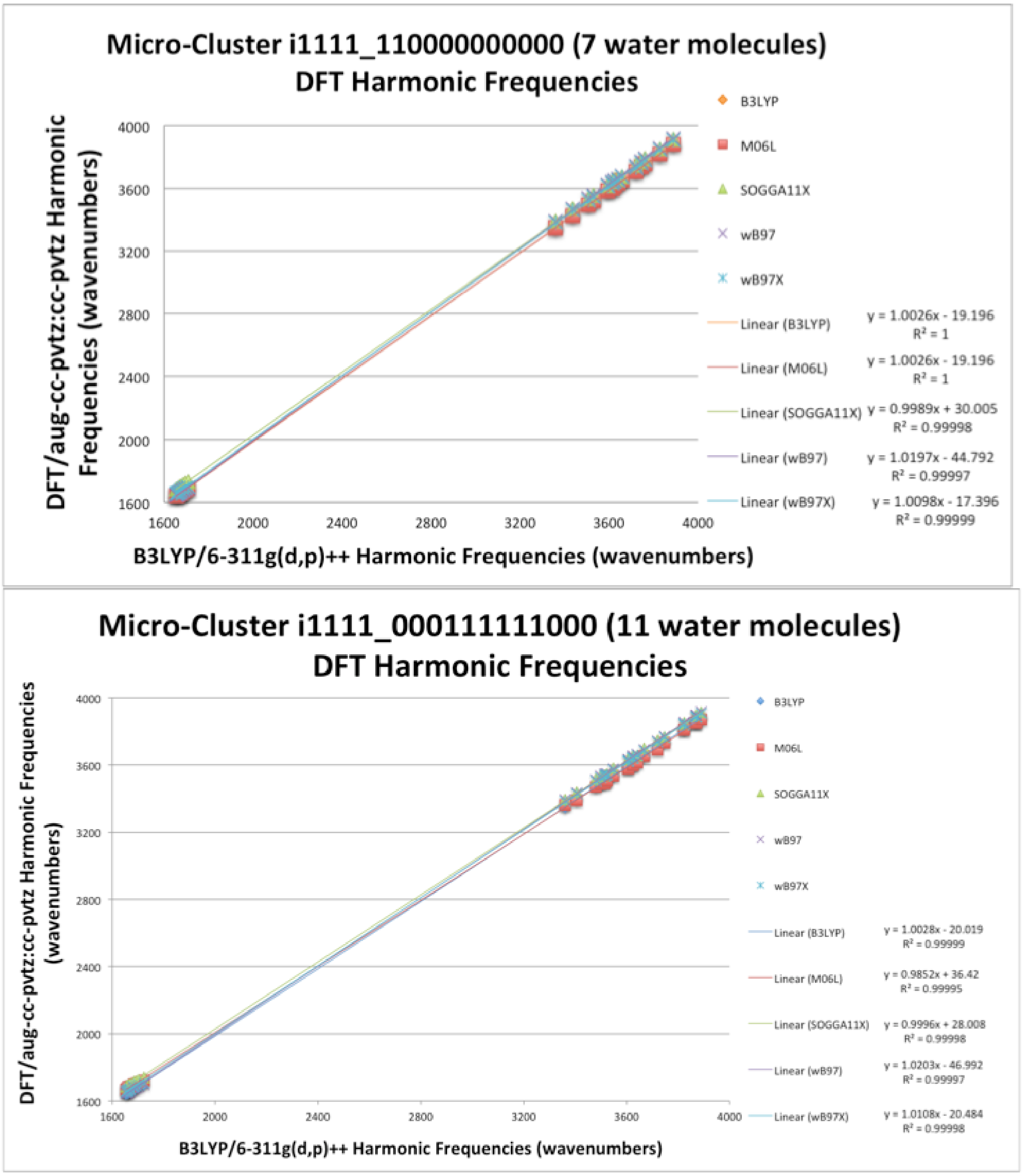

Figure F2. Testing a subset of 24 micro-clusters with our current method and basis set against the same clusters calculated with 5 DFT methods benchmarked to be better in the literature for representative clusters of 7 **(TOP)** and 11 **(BOTTOM)** water molecules.

REFERENCES CITED

CHAPTER I: Introduction

1. Ervens, B.; Volkamer, R., Glyoxal Processing by Aerosol Multiphase Chemistry: Towards a Kinetic Modeling Framework of Secondary Organic Aerosol Formation in Aqueous Particles. *Atmos. Chem. Phys.* **2010,** *10*, 8219-8244.

2. Ervens, B.; Turpin, B. J.; Weber, R. J., Secondary Organic Aerosol Formation in Cloud Droplets and Aqueous Particles (AqSOA): A Review of Laboratory, Field and Model Studies. *Atmos. Chem. Phys.* **2011,** *11*, 11069-11102.

3. Sareen, N.; Schwier, A. N.; Shapiro, E. L.; Mitroo, D.; McNeill, V. F., Secondary Organic Material Formed by Methylglyoxal in Aqueous Aerosol Mimics. *Atmos. Chem. Phys.* **2010,** *10*, 997-1016.

4. Noziere, B.; Dziedzic, P.; Cordova, A., Inorganic Ammonium Salts and Carbonate Salts Are Efficient Catalysts for Aldol Condensation in Atmospheric Aerosols. *Phys. Chem. Chem. Phys.* **2010,** *12*, 3864-3872.

5. De Haan, D. O.; Hawkins, L. N.; Kononenko, J. A.; Turley, J. J.; Corrigan, A. L.; Tolbert, M. A.; Jimenez, J. L., Formation of Nitrogen-Containing Oligomers by Methylglyoxal and Amines in Simulated Evaporating Cloud Droplets. *Environ. Sci. Technol.* **2011,** *45*, 984-991.

6. Sareen, N.; Schwier, A. N.; Lathem, T. L.; Nenes, A.; McNeill, V. F., Surfactants from the Gas Phase May Promote Cloud Droplet Formation. *P. Natl. Acad. Sci. USA* **2013,** *110*, 2723-2728.

7. Gopalakrishnan, S.; Jungwirth, P.; Tobias, D. J.; Allen, H. C., Air-Liquid Interfaces of Aqueous Solution Containing Ammonium and Sulfate: Spectroscopic and Molecular Dynamics Studies. *J. Phys. Chem. B.* **2005,** *109*, 8861-8872.

8. Jungwirth, P.; Tobias, D. J., Specific Ion Effects at the Air/Water Interface. *Chem. Review.* **2006,** *106*, 1259-1281.

9. Heald, C. L.; Jacob, D. J.; Park, R. J.; Russell, L. M.; Huebert, B. J.; Seinfeld, J. H.; Liao, H.; Weber, R. J., A Large Organic Aerosol Source in the Free Troposphere Missing from Current Models. *Geophys. Res. Lett.* **2005,** *32*, No. L188091.

10. Kroll, J. H.; Ng, N. L.; Murphy, S. M.; Varutbangkul, V.; Flagan, R. C.; Seinfeld, J. H., Chamber Studies of Secondary Organic Aerosol Growth by Reactive Uptake of Simple Carbonyl Compound. *J. Geophys. Res.-Atmos.* **2005,** *110*, No. D23207.

11. Loeffler, K. W.; Koehler, C. A.; Paul, N. M.; De Haan, D. O., Oligomer Formation in Evaporating Aqueous Glyoxal and Methyl Glyoxal Solutions. *Environ. Sci. Technol.* **2006,** *40*, 6318-6323.

12. Yu, G.; Bayer, A. R.; Galloway, M. M.; Korshavn, K. J.; Fry, C. G.; Keutsch, F. N., Glyoxal in Aqueous Ammonium Sulfate Solutions: Products, Kinetics, and Hydration Effects. *Environ. Sci. Technol.* **2011,** *45*, 6336–6342.

13. Li, Z.; Schwier, A.N.; Sareen, N.; McNeill, V. F., Reactive processing of formaldehyde and acetaldehyde in aqueous aerosol mimics: Surface tension depression and secondary organic products. *Atmos. Chem. Phys.* **2011**, *11*, 11617-11629.

14. Cappa, C. D.; Edward, R. L.; Ravishankara, A. R., Evidence for Liquid-Like and Nonideal Behavior of a Mixture of Organic Aerosol Components. *P.N.A.S.* **2008,** *105*, 18687-18691.

15. Prisle, N. L.; Raatikainen, T.; Laaksonen, A.; Bilde, M., Surfactants in Cloud Droplet Activation: Mixed Organic-Inorganic Particles. *Atmos. Chem. Phys.* **2010,** *10*, 5663-5683.

16. Romakkaniemi, S.; Kokkola, H.; Smith, J. N.; Prisle, N. L.; Schwier, A. N.; McNeill, V. F.; Laaksonen, A., Partitioning of Semivolatile Surface-Active Compounds between Bulk, Surface and Gas Phase. *Geophys. Res. Lett.* **2011,** *38*, No. L03807.

17. Kampf, C. J.; Waxman, E. M.; Slowik, J. G.; Dommen, J.; Pfaffenberger, L.; Praplan, A. P.; Prevot, A. S. H.; Baltensperger, U.; Hoffmann, T.; Volkamer, R., Effective Henry's Law Partitioning and the Salting Constant of Glyoxal in Aerosols Containing Sulfate. *Environ. Sci. Technol.* **2013,** *47*, 4236-4244.

18. Wren, S. N.; Valley, N. A.; Gordon, B. P.; McWilliams, L. E.; Richmond, G. L. Hydration, Orientation, and Conformation of Methylglyoxal at the Air-Water Interface. *J. Phys. Chem. A* **2015,** *119*, 6391-6403.

CHAPTER II

1. Bain, C. D.; Davies, P. B.; Ong, T. H.; Ward, R. N.; Brown, M. A. Quantitative Analysis of Monolayer Composition by Sum-Frequency Vibrational Spectroscopy. *Langmuir* **1991,** *7*, 1563-1566.

2. Moore, F. G.; Becraft, K. A.; Richmond, G. L. Challenges in Interpreting Vibrational Sum Frequency Spectra: Deconvoluting Spectral Features as Demonstrated in the Calcium Fluoride-Water-Sodium Dodecylsulfate System. *Appl. Spectrosc.* **2002,** *56*, 1575-1578.

3. Chieffo, L.; Shattuck, J.; Amsden, J. J.; Erramilli, S.; Ziegler, L. D. Ultrafast Vibrational Relaxation of Liquid H2O Following Librational Combination Band Excitation. *Chem. Phys.* **2007,** *341*, 71-80.

4. Knop, S.; Lindner, J.; Vöhringer, P. OH and NH Stretching Vibrational Relaxation of Liquid Ethanolamine. *Z. Phys. Chem.* **2011,** *225*, 913-926.

5. Monson, P. R.; Patumtev, S.; Kaufmann, K. J.; Robinson, G. W. Dominance of Methyl-Groups in Picosecond Vibrational-Relaxation in Hydrocarbons. *Chem. Phys. Lett.* **1974,** *28*, 312-315.

6. Nienhuys, H. K.; van Santen, R. A.; Bakker, H. J. Orientational Relaxation of Liquid Water Molecules as an Activated Process. *J. Chem. Phys.* **2000,** *112*, 8487-8494.

7. Woutersen, S.; Emmerichs, U.; Bakker, H. J. Femtosecond mid-IR pump-probe spectroscopy of liquid water: Evidence for a two-component structure. *Science* **1997,** *278*, 658-660.

8. Wren, S. N.; Valley, N. A.; Gordon, B. P.; McWilliams, L. E.; Richmond, G. L. Hydration, Orientation, and Conformation of Methylglyoxal at the Air-Water Interface. *J. Phys. Chem. A* **2015,** *119*, 6391-6403.

9. McWilliams, L. E.; Valley, N. A.; Vincent, N. M.; Richmond, G. L. Interfacial Insights into a Carbon Capture System: CO_2 Uptake to an Aqueous Monoethanolamine Surface. *J. Phys. Chem. A* **2017,** *121*, 7956-7967.

10. McWilliams, L. E.; Valley, N. A.; Wren, S. N.; Richmond, G. L. A Means to an Interface: Investigating Monoethanolamine Behavior at an Aqueous Surface. *Phys. Chem. Chem. Phys.* **2015,** *17*, 21458-21469.

11. Gordon, B. P.; Moore, F. G.; Scatena, L. F.; Valley, N. A.; Wren, S. N.; Richmond, G. L., Model Behavior: Characterization of Hydroxyacetone at the Air–Water Interface Using Experimental and Computational Vibrational Sum Frequency Spectroscopy. *J. Phys. Chem. A* **2018,** *122* (15), 3837-3849.

12. Gordon, B. P.; Moore, F. G.; Scatena, L. F.; Richmond, G. L., On the Rise: Experimental and Computational Vibrational Sum Frequency Spectroscopy Studies of Pyruvic Acid and Its Surface-Active Oligomer Species at the Air–Water Interface. *J. Phys. Chem. A* **2019**, *123* (49), 10609-10619.

13. Blower, P. G.; Ota, S. T.; Valley, N. A.; Wood, S. R.; Richmond, G. L. Sink or Surf: Atmospheric Implications for Succinic Acid at Aqueous Surfaces. *J. Phys. Chem. A* **2013,** *117*, 7887-7903.

14. Valley, N. A.; Richmond, G. L. Solvation Station: Microsolvation for Modeling Vibrational Sum-Frequency Spectra of Acids at Aqueous Interfaces. *J. Chem. Theory Comput.* **2015,** *11*, 4780-4790.

15. Valley, N. A.; Robertson, E. J.; Richmond, G. L. Twist and Turn: Effect of Stereoconfiguration on the Interfacial Assembly of Polyelectrolytes. *Langmuir* **2014,** *30*, 14226-14233.

16. Valley, N. V.; Blower, P. G.; Wood, S. R.; Plath, K. L.; McWilliams, L. E.; Richmond, G. L. Doubling Down: Delving into the Details of Diacid Adsorption at Aqueous Surfaces. *J. Phys. Chem. A* **2014,** *118*, 4778-4789.

17. Davies, J. T.; Rideal, E. K. *Interfacial Phenomena*. Academic Press: New York, 1963.

18. Rosen, M. J., In *Surfactants and Interfacial Phenomena 3rd ed.*, John Wiley & Sons, Inc.: New York, 2004.

19. Case, D. A.; Darden, T. A.; Cheatham, T. E., III; Simmerling, C. L.; Wang, J.; Duke, R. E.; Luo, R.; Walker, R. C.; Zhang, W.; Merz, K. M., et al., *Amber 12*. University of Californa, San Francisco: **2012**.

20. Calwell, J. W.; Kollman, P. A., Structure and Properties of Neat Liquids Using Nonadditive Molecular Dynamics: Water, Methanol, and *N*-Methylacetamide. *J. Phys. Chem.* **1995,** *99*, 6208-6219.

21. Case, D. A.; Cheatham, E. J.; Gohlke, H.; Luo, R.; Merz, K. M.; Onufriev, A.; Simmerlinfg, C.; Wang, B.; Woods, R. J., The Amber Biomolecular Simulation Programs. *J. Comp. Chem.* **2006,** *26*, 1668-1688.

22. Bayly, C. I.; Cieplak, P.; Cornell, W. D.; Kollman, P. A., A Well-Behaved Electrostatic Potential Based Method Using Charge Restraints for Deriving Atomic Charges: The RESP Model. *J. Phys. Chem.* **1993,** *97*, 10269-10280.

23. Martinez, L.; Andrade, R.; Birgin, E. G., Martinez, J. M., Packmol: A Package for Building Initial Configurations for Molecular Dynamics Simulations. *J. Comput. Chem.* **2009,** *30*, 2157-2164.

24. Valiev, M.; Bylaska, E. J.; Govind, N.; Kowalski, K.; Straatsma, T. P.; Dam, H. J. J. V.; Wang, D.; Nieplocha, J.; Apra, E.; Windus, T. L., et al., Nwchem: A Comprehensive and Scalable Open-Source Solution for Large Scale Molecular Simulations. *Comput. Phys. Commun.* **2010,** *181*, 1477 - 1489.

25. Frisch, M. J.; Trucks, G. W.; Schlegel, H. G.; Scuseria, G. E.; Robb, M. A.; Cheeseman, J. R.; Scalmani, G.; Barone, V.; Mennucci, B.; Petersson, G. A., et al., *Gaussian 09*. Gaussian Inc.: Wallingford CT, **2009**.

26. Sulpizi, M.; Salanne, M.; Sprik, M.; Gaigeot, M. P., Vibrational Sum Frequency Generation Spectroscopy of the Water Liquid−Vapor Interface from Density Functional Theory-Based Molecular Dynamics Simulations. *J. Phys. Chem. Lett.* **2013**, *4*, 83-87.

27. Ishiyama, T.; Takahashi, H.; Morita, A., Vibrational Spectrum at a Water Surface: A Hybrid Quantum Mechanics/Molecular Mechanics Molecular Dynamics Approach. *J. Phys.: Condens. Matter*, **2012**, *24*, 124107.

28. Ishiyama, T.; Imamura, T.; Morita, A., Theoretical Studies of Structures and Vibrational Sum Frequency Generation Spectra at Aqueous Interfaces. *Chem. Rev.* **2014**, *114*, 8447-8470.

29. Valley, N. V.; Blower, P. G.; Wood, S. R.; Plath, K. L.; McWilliams, L. E.; Richmond, G. L., Doubling Down: Delving into the Details of Diacid Adsorption at Aqueous Surfaces. *J. Phys. Chem. A* **2014,** *118*, 4778-4789.

30. Blower, P. G.; Ota, S. T.; Valley, N. A.; Wood, S. R.; Richmond, G. L., Sink or Surf: Atmospheric Implications for Succinic Acid at Aqueous Surfaces. *J. Phys. Chem. A* **2013,** *117*, 7887-7903.

31. Blower, P. G.; Shamay, E. S.; Kringle, L.; Ota, S. T.; Richmond, G. L., Surface Behavior of Malonic Acid Adsorption at the Air/Water Interface. *J. Phys. Chem. A* **2013,** *117*, 2529-2542.

CHAPER III: Water

1. Du, Q.; Superfine, R.; Freysz, E.; Shen, Y. R. Vibrational Spectroscopy of Water at the Vapor/Water Interface. *Phys. Rev. Lett.* **1993,** *70*, 2313-2316.

2. Ishiyama, T.; Imamura, T.; Morita, A. Theoretical Studies of Structures and Vibrational Sum Frequency Generation Spectra at Aqueous Interfaces. *Chem. Rev.* **2014,** *114*, 8447-8470.

3. Medders, G. R.; Paesani, F. Dissecting the Molecular Structure of the Air/Water Interface from Quantum Simulations of the Sum-Frequency Generation Spectrum. *J. Am.Chem. Soc.* **2016,** *138*, 3912-3919.

4. Perakis, F.; Marco, L. D.; Shalit, A.; Tang, F.; Kann, Z. R.; Kühne, T. D.; Torre, R.; Bonn, M.; Nagata, Y. Vibrational Spectroscopy and Dynamics of Water. *Chem. Rev.* **2016,** *116*, 7590-7607.

5. Raymond, E. A.; Tarbuck, T. L.; Brown, M. G.; Richmond, G. L. Hydrogen-Bonding Interactions at the Vapor/Water Interface Investigated by Vibrational Sum-Frequency Spectroscopy of HOD/H_2O/D_2O Mixtures and Molecular Dynamics Simulations. *J. Phys. Chem. B* **2003,** *107*, 546-556.

6. Raymond, E. A.; Tarbuck, T. L.; Richmond, G. L. Isotopic Dilution Studies of the Vapor/Water Interface as Investigated by Vibrational Sum-Frequency Spectroscopy. *J. Phys. Chem. B* **2002,** *106*, 2817-2820.

7. Richmond, G. L. Molecular Bonding and Interactions at Aqueous Surfaces as Probed by Vibrational Sum Frequency Spectroscopy. *Chem. Rev.* **2002,** *102*, 2693-2724.

8. Tang, F.; Ohto, T.; Hasegawa, T.; Xie, W. J.; Xu, L.; Bonn, M.; Nagata, Y. Definition of Free O–H Groups of Water at the Air–Water Interface. *J. Chem. Theory Comput.* **2018,** *14*, 357-364.

9. Shen, Y. R.; Ostroverkhov, V. Sum-Frequency Vibrational Spectroscopy on Water Interfaces: Polar Orientation of Water Molecules at Interfaces. *Chem. Rev.* **2006,** *106*, 1140-1154.

10. Pezzotti, S.; Galimberti, D. R.; Gaigeot, M.P. 2D H-Bond Network as the Topmost Skin to the Air–Water Interface. *J. Phys. Chem. Lett* **2017,** *8*, 3133-3141.

11. Schaefer, J.; Backus, E. H. G.; Nagata, Y.; Bonn, M. Both Inter- and Intramolecular Coupling of O–H Groups Determine the Vibrational Response of the Water/Air Interface. *J. Phys. Chem. Lett.* **2016,** *7*, 4591-4595.

12. Suzuki, Y.; Nojima, Y.; Yamaguchi, S. Vibrational Coupling at the Topmost Surface of Water Revealed by Heterodyne-Detected Sum Frequency Generation Spectroscopy. *J. Phys. Chem. Lett.* **2017,** *8*, 1396-1401.

13. Nagata, Y.; Hsieh, C.S.; Hasegawa, T.; Voll, J.; Backus, E. H. G.; Bonn, M. Water Bending Mode at the Water–Vapor Interface Probed by Sum-Frequency Generation Spectroscopy: A Combined Molecular Dynamics Simulation and Experimental Study. *J. Phys. Chem. Lett.* **2013,** *4*, 1872-1877.

14. Ni, Y.; Skinner, J. L. IR and SFG vibrational spectroscopy of the water bend in the bulk liquid and at the liquid-vapor interface, respectively. *J. Chem. Phys.* **2015,** *143* (1), 014502.

15. Vinaykin, M.; Benderskii, A. V. Vibrational Sum-Frequency Spectrum of the Water Bend at the Air/Water Interface. *J. Phys. Chem. Lett.* **2012,** *3,* 3348-3352.

16. Dutta, C.; Benderskii, A. V. On the Assignment of the Vibrational Spectrum of the Water Bend at the Air/Water Interface. *J. Phys. Chem. Lett.* **2017,** *8,* 801-804.

17. Kundu, A.; Tanaka, S.; Ishiyama, T.; Ahmed, M.; Inoue, K.I.; Nihonyanagi, S.; Sawai, H.; Yamaguchi, S.; Morita, A.; Tahara, T. Bend Vibration of Surface Water Investigated by Heterodyne-Detected Sum Frequency Generation and Theoretical Study: Dominant Role of Quadrupole. *J. Phys. Chem. Lett.* **2016,** *7*, 2597-2601.

18. Khatib, R.; Hasegawa, T.; Sulpizi, M.; Backus, E. H. G.; Bonn, M.; Nagata, Y. Molecular Dynamics Simulations of SFG Librational Modes Spectra of Water at the Water–Air Interface. *J. Phys. Chem. C* **2016,** *120*, 18665-18673.

19. Rosen, M. J., In *Surfactants and Interfacial Phenomena 3rd ed.*, John Wiley & Sons, Inc.: New York, 2004.

CHAPTER IV: Neat -MG

1. Pankow, J. F., An Absorption-Model of the Gas Aerosol Partitioning Involved in the Formation of Secondary Organic Aerosol. *Atmos. Environ.* **1994,** *28*, 189-193.

2. Odum, J. R.; Hoffmann, T.; Bowman, F.; Collins, D.; Flagan, R. C.; Seinfeld, J. H., Gas/Particle Partitioning and Secondary Organic Aerosol Yields. *Environ. Sci. Technol.* **1996,** *30*, 2580-2585.

3. Pankow, J. F., An Absorption-Model of Gas-Particle Partitioning of Organic-Compounds in the Atmosphere. *Atmos. Environ.* **1994,** *28*, 185-188.

4. Volkamer, R.; Jimenez, J. L.; San Martini, F.; Dzepina, K.; Zhang, Q.; Salcedo, D.; Molina, L. T.; Worsnop, D. R.; Molina, M. J., Secondary Organic Aerosol Formation from Anthropogenic Air Pollution: Rapid and Higher Than Expected. *Geophys. Res. Lett.* **2006,** *33*, No. L17811.

5. Volkamer, R.; Martini, F. S.; Molina, L. T.; Salcedo, D.; Jimenez, J. L.; Molina, M. J., A Missing Sink for Gas-Phase Glyoxal in Mexico City: Formation of Secondary Organic Aerosol. *Geophys. Res. Lett.* **2007,** *34*, No. L19807.

6. Heald, C. L.; Jacob, D. J.; Park, R. J.; Russell, L. M.; Huebert, B. J.; Seinfeld, J. H.; Liao, H.; Weber, R. J., A Large Organic Aerosol Source in the Free Troposphere Missing from Current Models. *Geophys. Res. Lett.* **2005,** *32*, No. L188091.

7. de Gouw, J. A.; Middlebrook, A. M.; Warneke, C.; Goldan, P. D.; Kuster, W. C.; Roberts, J. M.; Fehsenfeld, F. C.; Worsnop, D. R.; Canagaratna, M. R.; Pszenny, A. A. P., et al., Budget of Organic Carbon in a Polluted Atmosphere: Results from the New England Air Quality Study in 2002. *J. Geophys. Res.-Atmos.* **2005,** *110,* No. D16305.

8. Trainic, M.; Riziq, A. A.; Lavi, A.; Rudich, Y., Role of Interfacial Water in the Heterogeneous Uptake of Glyoxal by Mixed Glycine and Ammonium Sulfate Aerosols. *J. Phys. Chem. A* **2012,** *116*, 5948-5957.

9. Ervens, B.; Volkamer, R., Glyoxal Processing by Aerosol Multiphase Chemistry: Towards a Kinetic Modeling Framework of Secondary Organic Aerosol Formation in Aqueous Particles. *Atmos. Chem. Phys.* **2010,** *10*, 8219-8244.

10. Waxman, E. M.; Dzepina, K.; Ervens, B.; Lee-Taylor, J.; Aumont, B.; Jimenez, J. L.; Madronich, S.; Volkamer, R., Secondary Organic Aerosol Formation from Semi- and Intermediate-Volatility Organic Compounds and Glyoxal: Relevance of O/C as a Tracer for Aqueous Multiphase Chemistry. *Geophys. Res. Lett.* **2013,** *40*, 978-982.

11. Fu, T. M.; Jacob, D. J.; Wittrock, F.; Burrows, J. P.; Vrekoussis, M.; Henze, D. K., Global Budgets of Atmospheric Glyoxal and Methylglyoxal, and Implications for Formation of Secondary Organic Aerosols. *J. Geophys. Res.-Atmos.* **2008,** *113*, No. D15303.

12. Ervens, B.; Turpin, B. J.; Weber, R. J., Secondary Organic Aerosol Formation in Cloud Droplets and Aqueous Particles (AqSOA): A Review of Laboratory, Field and Model Studies. *Atmos. Chem. Phys.* **2011,** *11*, 11069-11102.

13. Betterton, E. A.; Hoffmann, M. R., Henry Law Constants of Some Environmentally Important Aldehydes. *Environ. Sci. Technol.* **1988,** *22*, 1415-1418.

14. Zhou, X. L.; Mopper, K., Apparent Partition-Coefficients of 15 Carbonyl-Compounds between Air and Seawater and between Air and Fresh-Water - Implications for Air Sea Exchange. *Environ. Sci. Technol.* **1990,** *24*, 1864-1869.

15. Lim, Y. B.; Tan, Y.; Turpin, B. J., Chemical Insights, Explicit Chemistry, and Yields of Secondary Organic Aerosol from OH Radical Oxidation of Methylglyoxal and Glyoxal in the Aqueous Phase. *Atmos. Chem. Phys.* **2013,** *13*, 8651-8667.

16. Ervens, B.; Sorooshian, A.; Lim, Y. B.; Turpin, B. J., Key Parameters Controlling Oh-Initiated Formation of Secondary Organic Aerosol in the Aqueous Phase (AqSOA). *J. Geophys. Res.-Atmos.* **2014,** *119*, 3997-4016.

17. Zhao, R.; Lee, A. K. Y.; Abbatt, J. P. D., Investigation of Aqueous-Phase Photooxidation of Glyoxal and Methylglyoxal by Aerosol Chem. Ionization Mass Spectrometry: Observation of Hydroxyhydroperoxide Formation. *J. Phys. Chem. A* **2012,** *116*, 6253-6263.

18. Sareen, N.; Moussa, S. G.; McNeill, V. F., Photochemical Aging of Light-Absorbing Secondary Organic Aerosol Material. *J. Phys. Chem. A* **2013,** *117*, 2987-2996.

19. Sareen, N.; Schwier, A. N.; Shapiro, E. L.; Mitroo, D.; McNeill, V. F., Secondary Organic Material Formed by Methylglyoxal in Aqueous Aerosol Mimics. *Atmos. Chem. Phys.* **2010,** *10*, 997-1016.

20. Schwier, A. N.; Sareen, N.; Mitroo, D.; Shapiro, E. L.; McNeill, V. F., Glyoxal-Methylglyoxal Cross-Reactions in Secondary Organic Aerosol Formation. *Environ. Sci. Technol.* **2010,** *44*, 6174-6182.

21. Shapiro, E. L.; Szprengiel, J.; Sareen, N.; Jen, C. N.; Giordano, M. R.; McNeill, V. F., Light-Absorbing Secondary Organic Material Formed by Glyoxal in Aqueous Aerosol Mimics. *Atmos. Chem. Phys.* **2009,** *9*, 2289-2300.

22. Sedehi, N.; Takano, H.; Blasic, V. A.; Sullivan, K. A.; De Haan, D. O., Temperature- and Ph-Dependent Aqueous-Phase Kinetics of the Reactions of Glyoxal and Methylglyoxal with Atmospheric Amines and Ammonium Sulfate. *Atmos. Environ.* **2013,** *77*, 656-663.

23. Yu, G.; Bayer, A. R.; Galloway, M. M.; Korshavn, K. J.; Fry, C. G.; Keutsch, F. N., Glyoxal in Aqueous Ammonium Sulfate Solutions: Products, Kinetics, and Hydration Effects. *Environ. Sci. Technol.* **2011,** *45*, 6336–6342.

24. Galloway, M. M.; Chhabra, P. S.; Chan, A. W. H.; Surratt, J. D.; Flagan, R. C.; Seinfeld, J. H.; Keutsch, F. N., Glyoxal Uptake on Ammonium Sulphate Seed Aerosol: Reaction Products and Reversibility of Uptake under Dark and Irradiated Conditions. *Atmos. Chem. Phys.* **2009,** *9*, 3331-3345.

25. Noziere, B.; Cordova, A., A Kinetic and Mechanistic Study of the Amino Acid Catalyzed Aldol Condensation of Acetaldehyde in Aqueous and Salt Solutions. *J. Phys. Chem. A* **2008,** *112*, 2827-2837.

26. Noziere, B.; Dziedzic, P.; Cordova, A., Inorganic Ammonium Salts and Carbonate Salts Are Efficient Catalysts for Aldol Condensation in Atmospheric Aerosols. *Phys. Chem. Chem. Phys.* **2010,** *12*, 3864-3872.

27. Nozière, B.; Dziedzic, P.; Còrdova, A., Products and Kinetics of the Liquid-Phase Reaction of Glyoxal Catalyzed by Ammonium Ions (NH_4^+). *J Phys Chem A* **2009,** *113*, 231-237.

28. Noziere, B.; Esteve, W., Light-Absorbing Aldol Condensation Products in Acidic Aerosols: Spectra, Kinetics, and Contribution to the Absorption Index. *Atmos. Environ.* **2007,** *41*, 1150-1163.

29. Barsanti, K. C.; Pankow, J. F., Thermodynamics of the Formation of Atmospheric Organic Particulate Matter by Accretion Reactions - 2. Dialdehydes, Methylglyoxal, and Diketones. *Atmos. Environ.* **2005,** *39*, 6597-6607.

30. Connelly, B. M.; De Haan, D. O.; Tolbert, M. A., Heterogeneous Glyoxal Oxidation: A Potential Source of Secondary Organic Aerosol. *J. Phys. Chem. A* **2012,** *116*, 6180-6187.

31. Corrigan, A. L.; Hanley, S. W.; Haan, D. O., Uptake of Glyoxal by Organic and Inorganic Aerosol. *Environ. Sci. Technol.* **2008,** *42*, 4428-4433.

32. De Haan, D. O.; Corrigan, A. L.; Smith, K. W.; Stroik, D. R.; Turley, J. J.; Lee, F. E.; Tolbert, M. A.; Jimenez, J. L.; Cordova, K. E.; Ferrell, G. R., Secondary Organic Aerosol-Forming Reactions of Glyoxal with Amino Acids. *Environ. Sci. Technol.* **2009,** *43*, 2818-2824.

33. De Haan, D. O.; Corrigan, A. L.; Tolbert, M. A.; Jimenez, J. L.; Wood, S. E.; Turley, J. J., Secondary Organic Aerosol Formation by Self-Reactions of Methylglyoxal and Glyoxal in Evaporating Droplets. *Environ. Sci. Technol.* **2009,** *43*, 8184-8190.

34. De Haan, D. O.; Hawkins, L. N.; Kononenko, J. A.; Turley, J. J.; Corrigan, A. L.; Tolbert, M. A.; Jimenez, J. L., Formation of Nitrogen-Containing Oligomers by Methylglyoxal and Amines in Simulated Evaporating Cloud Droplets. *Environ. Sci. Technol.* **2011,** *45*, 984-991.

35. De Haan, D. O.; Tolbert, M. A.; Jimenez, J. L., Atmospheric Condensed-Phase Reactions of Glyoxal with Methylamine. *Geophys. Res. Lett.* **2009,** *36*, No. L11819.

36. Hastings, W. P.; Koehler, C. A.; Bailey, E. L.; De Haan, D. O., Secondary Organic Aerosol Formation by Glyoxal Hydration and Oligomer Formation: Humidity Effects and Equilibrium Shifts During Analysis. *Environ. Sci. Technol.* **2005,** *39*, 8728-8735.

37. Loeffler, K. W.; Koehler, C. A.; Paul, N. M.; De Haan, D. O., Oligomer Formation in Evaporating Aqueous Glyoxal and Methyl Glyoxal Solutions. *Environ. Sci. Technol.* **2006,** *40*, 6318-6323.

38. Galloway, M. M.; Powelson, M. H.; Sedehi, N.; Wood, S. E.; Millage, K. D.; Kononenko, J. A.; Rynaski, A. D.; De Haan, D. O., Secondary Organic Aerosol Formation During Evaporation of Droplets Containing Atmospheric Aldehydes, Amines, and Ammonium Sulfate. *Environ. Sci. Technol.* **2014,** *48*, 14417-14425.

39. Lee, A. K. Y.; Zhao, R.; Li, R.; Liggio, J.; Li, S. M.; Abbatt, J. P. D., Formation of Light Absorbing Organo-Nitrogen Species from Evaporation of Droplets Containing Glyoxal and Ammonium Sulfate. *Environ. Sci. Technol.* **2013,** *47*, 12819-12826.

40. Esteve, W.; Noziere, B., Uptake and Reaction Kinetics of Acetone, 2-Butanone, 2,4-Pentanedione, and Acetaldehyde in Sulfuric Acid Solutions. *J. Phys. Chem. A* **2005,** *109*, 10920-10928.

41. Casale, M. T.; Richman, A. R.; Elrod, M. J.; Garland, R. M.; Beaver, M. R.; Tolbert, M. A., Kinetics of Acid-Catalyzed Aldol Condensation Reactions of Aliphatic Aldehydes. *Atmos. Environ.* **2007,** *41*, 6212-6224.

42. Liggio, J.; Li, S. M.; Mclaren, R., Reactive Uptake of Glyoxal by Particulate Matter. *J. Geophys. Res.-Atmos.* **2005,** *110*, No. D10304.

43. Ortiz-Montalvo, D. L.; Hakkinen, S. A. K.; Schwier, A. N.; Lim, Y. B.; McNeill, V. F.; Turpin, B. J., Ammonium Addition (and Aerosol pH) Has a Dramatic Impact on the Volatility and Yield of Glyoxal Secondary Organic Aerosol. *Environ. Sci. Technol.* **2014,** *48*, 255-262.

44. Liggio, J.; Li, S. M.; Mclaren, R., Heterogeneous Reactions of Glyoxal on Particulate Matter: Identification of Acetals and Sulfate Esters. *Environ. Sci. Technol.* **2005,** *39*, 1532-1541.

45. Noziere, B.; Chabert, P., Abiotic C-C Bond Formation under Environmental Conditions: Kinetics of the Aldol Condensation of Acetaldehyde in Water Catalyzed by Carbonate Ions (CO_3^{2-}). *Int. J. Chem. Kinet.* **2010,** *42*, 676-686.

46. Woo, J. L.; Kim, D. D.; Schwier, A. N.; Li, R. Z.; McNeill, V. F., Aqueous Aerosol SOA Formation: Impact on Aerosol Physical Properties. *Faraday Discuss.* **2013,** *165*, 357-367.

47. Trainic, M.; Riziq, A. A.; Lavi, A.; Flores, J. M.; Rudich, Y., The Optical, Physical and Chemical Properties of the Products of Glyoxal Uptake on Ammonium Sulfate Seed Aerosols. *Atmos. Chem. Phys.* **2011,** *11*, 9697-9707.

48. Kampf, C. J.; Jakob, R.; Hoffmann, T., Identification and Characterization of Aging Products in the Glyoxal/Ammonium Sulfate System - Implications for Light-Absorbing Material in Atmospheric Aerosols. *Atmos. Chem. Phys.* **2012,** *12*, 6323-6333.

49. Drozd, G. T.; McNeill, V. F., Organic Matrix Effects on the Formation of Light-Absorbing Compounds from Alpha-Dicarbonyls in Aqueous Salt Solution. *Environ. Sci. Process. Impact* **2014,** *16*, 741-747.

50. Kroll, J. H.; Ng, N. L.; Murphy, S. M.; Varutbangkul, V.; Flagan, R. C.; Seinfeld, J. H., Chamber Studies of Secondary Organic Aerosol Growth by Reactive Uptake of Simple Carbonyl Compound. *J. Geophys. Res.-Atmos.* **2005,** *110*, No. D23207.

51. Kampf, C. J.; Waxman, E. M.; Slowik, J. G.; Dommen, J.; Pfaffenberger, L.; Praplan, A. P.; Prevot, A. S. H.; Baltensperger, U.; Hoffmann, T.; Volkamer, R., Effective Henry's Law Partitioning and the Salting Constant of Glyoxal in Aerosols Containing Sulfate. *Environ. Sci. Technol.* **2013,** *47*, 4236-4244.

52. Romakkaniemi, S.; Kokkola, H.; Smith, J. N.; Prisle, N. L.; Schwier, A. N.; McNeill, V. F.; Laaksonen, A., Partitioning of Semivolatile Surface-Active Compounds between Bulk, Surface and Gas Phase. *Geophys. Res. Lett.* **2011,** *38*, No. L03807.

53. Köhler, H., The Nucleus in the Growth of Hygroscopic Droplets. *J. Chem. Soc, Faraday Trans.* **1936,** *32*, 1152 - 1161.

54. Prisle, N. L.; Raatikainen, T.; Laaksonen, A.; Bilde, M., Surfactants in Cloud Droplet Activation: Mixed Organic-Inorganic Particles. *Atmos. Chem. Phys.* **2010,** *10*, 5663-5683.

55. Prisle, N. L.; Asmi, A.; Topping, D.; Partanen, A. I.; Romakkaniemi, S.; Dal Maso, M.; Kulmala, M.; Laaksonen, A.; Lehtinen, K. E. J.; McFiggans, G., et al., Surfactant Effects in Global Simulations of Cloud Droplet Activation. *Geophys. Res. Lett.* **2012,** *39*, No. L05802.

56. Sorjamaa, R.; Svenningsson, B.; Raatikainen, T.; Henning, S.; Bilde, M.; Laaksonen, A., The Role of Surfactants in Kohler Theory Reconsidered. *Atmos. Chem. Phys.* **2004,** *4*, 2107-2117.

57. Sareen, N.; Schwier, A. N.; Lathem, T. L.; Nenes, A.; McNeill, V. F., Surfactants from the Gas Phase May Promote Cloud Droplet Formation. *P. Natl. Acad. Sci. USA* **2013,** *110*, 2723-2728.

58. Donaldson, D. J.; Vaida, V., The Influence of Organic Films at the Air-Aqueous Boundary on Atmospheric Processes. *Chem. Rev.* **2006,** *106*, 1445-1461.

59. Krizner, H. E.; De Haan, D. O.; Kua, J., Thermodynamics and Kinetics of Methylglyoxal Dimer Formation: A Computational Study. *J. Phys. Chem. A* **2009,** *113*, 6994-7001.

60. Jang, M.; Czoschke, N. M.; Lee, S.; Kamens, R. M., Heterogeneous Atmospheric Aerosol Production by Acid-Catalyzed Particle-Phase Reactions. *Science* **2002,** *298*, 814-817.

61. Hazra, M. K.; Francisco, J. S.; Sinha, A., Hydrolysis of Glyoxal in Water-Restricted Environments: Formation of Organic Aerosol Precursors through Formic Acid Catalysis. *J. Phys. Chem. A* **2014,** *118*, 4095-4105.

62. Nemet, I.; Vikic-Topic, D.; Varga-Defterdarovic, L., Spectroscopic Studies of Methylglyoxal in Water and Dimethylsulfoxide. *Bioorg. Chem.* **2004,** *32*, 560-570.

63. Raymond, E. A.; Tarbuck, T. L.; Brown, M. G.; Richmond, G. L., Hydrogen-Bonding Interactions at the Vapor/Water Interface Investigated by Vibrational Sum-Frequency Spectroscopy of HOD/H_2O/D_2O Mixtures and Molecular Dynamics Simulations. *J. Phys. Chem. B* **2003,** *107*, 546-556.

64. Raymond, E. A.; Tarbuck, T. L.; Richmond, G. L., Isotopic Dilution Studies of the Vapor/Water Interface as Investigated by Vibrational Sum-Frequency Spectroscopy. *J. Phys. Chem. B* **2002,** *106*, 2817-2820.

65. Walker, D. S.; Hore, D. K.; Richmond, G. L., Understanding the Population, Coordination, and Orientation of Water Species Contributing to the Nonlinear Optical Spectroscopy of the Vapor-Water Interface through Molecular Dynamics Simulations. *J. Phys. Chem. B* **2006,** *110*, 20451-20459.

66. Walker, D. S.; Richmond, G. L., Understanding the Effects of Hydrogen Bonding at the Vapor-Water Interface: Vibrational Sum Frequency Spectroscopy of H_2O/HOD/D_2O Mixtures Studied Using Molecular Dynamics Simulations. *J. Phys. Chem. C* **2007,** *111*, 8321-8330.

67. Du, Q.; Superfine, R.; Freysz, E.; Shen, Y. R., Vibrational Spectroscopy of Water at the Vapor/Water Interface. *Phys. Rev. Lett.* **1993,** *70*, 2313-2316.

68. Tian, C. S.; Shen, Y. R., Sum-Frequency Vibrational Spectroscopic Studies of Water/Vapor Interfaces. *Chem. Phys. Lett.* **2009,** *470*, 1-6.

69. Lambert, A. G.; Davies, P. B.; Neivandt, D. J., Implementing the Theory of Sum Frequency Generation Vibrational Spectroscopy: A Tutorial Review. *Appl. Spectrosc. Rev.* **2005,** *40*, 103-145.

70. Bain, C. D.; Davies, P. B.; Ong, T. H.; Ward, R. N.; Brown, M. A., Quantitative-Analysis of Monolayer Composition by Sum-Frequency Vibrational Spectroscopy. *Langmuir* **1991,** *7*, 1563-1566.

71. Case, D. A.; Darden, T. A.; Cheatham, T. E., III; Simmerling, C. L.; Wang, J.; Duke, R. E.; Luo, R.; Walker, R. C.; Zhang, W.; Merz, K. M., et al., *Amber 12*. University of Californa, San Francisco: 2012.

72. Valley, N. V.; Blower, P. G.; Wood, S. R.; Plath, K. L.; McWilliams, L. E.; Richmond, G. L., Doubling Down: Delving into the Details of Diacid Adsorption at Aqueous Surfaces. *J. Phys. Chem. A* **2014,** *118*, 4778-4789.

73. Blower, P. G.; Ota, S. T.; Valley, N. A.; Wood, S. R.; Richmond, G. L., Sink or Surf: Atmospheric Implications for Succinic Acid at Aqueous Surfaces. *J. Phys. Chem. A* **2013,** *117*, 7887-7903.

74. Blower, P. G.; Shamay, E. S.; Kringle, L.; Ota, S. T.; Richmond, G. L., Surface Behavior of Malonic Acid Adsorption at the Air/Water Interface. *J. Phys. Chem. A* **2013,** *117*, 2529-2542.

75. Plath, K. L.; Valley, N. A.; Richmond, G. L., Ion-Induced Reorientation and Distribution of Pentanone in the Air-Water Boundary Layer. *J. Phys. Chem. A* **2013,** *117*, 11514-11527.

76. Martinez, L.; Andrade, R.; Birgin, E. G.; Martinez, J. M., Packmol: A Package for Building Initial Configurations for Molecular Dynamics Simulations. *J. Comput. Chem.* **2009,** *30*, 2157-2164.

77. Valiev, M.; Bylaska, E. J.; Govind, N.; Kowalski, K.; Straatsma, T. P.; Dam, H. J. J. V.; Wang, D.; Nieplocha, J.; Apra, E.; Windus, T. L., et al., Nwchem: A Comprehensive and Scalable Open-Source Solution for Large Scale Molecular Simulations. *Comput. Phys. Commun.* **2010,** *181*, 1477 - 1489.

78. Frisch, M. J.; Trucks, G. W.; Schlegel, H. G.; Scuseria, G. E.; Robb, M. A.; Cheeseman, J. R.; Scalmani, G.; Barone, V.; Mennucci, B.; Petersson, G. A., et al., *Gaussian 09*. Gaussian Inc.: Wallingford CT, 2009.

79. Profeta, L. T. M.; Sams, R. L.; Johnson, T. J., Quantitative Infrared Intensity Studies of Vapor-Phase Glyoxal, Methylglyoxal, and 2,3-Butanedione (Diacetyl) with Vibrational Assignments. *J. Phys. Chem. A* **2011,** *115*, 9886-9900.

80. Mucha, M.; Mielke, Z., Complexes of Atmospheric Alpha-Dicarbonyls with Water: Ftir Matrix Isolation and Theoretical Study. *J. Phys. Chem. A* **2007,** *111*, 2398-2406.

81. Axson, J. L.; Takahashi, K.; De Haan, D. O.; Vaida, V., Gas-Phase Water-Mediated Equilibrium between Methylglyoxal and Its Geminal Diol. *P. Natl. Acad. Sci. USA* **2010,** *107*, 6687-6692.

82. Vinaykin, M.; Benderskii, A. V., Vibrational Sum-Frequency Spectrum of the Water Bend at the Air/Water Interface. *J. Phys. Chem. Lett.* **2012,** *3*, 3348-3352.

83. Richmond, G. L., Molecular Bonding and Interactions at Aqueous Surfaces as Probed by Vibrational Sum Frequency Spectroscopy. *Chem. Rev.* **2002,** *102*, 2693-2724.

84. Johnson, C. M.; Tyrode, E.; Leygraf, C., Atmospheric Corrosion of Zinc by Organic Constituents I. The Role of the Zinc/Water and Water/Air Interfaces Studied by Infrared Reflection/Absorption Spectroscopy and Vibrational Sum Frequency Spectroscopy. *J. Electrochem. Soc.* **2006,** *153*, B113-B120.

85. Gopalakrishnan, S.; Liu, D.; Allen, H. C.; Kuo, M.; Shultz, M. J., Vibrational Spectroscopic Studies of Aqueous Interfaces: Salts, Acids, Bases, and Nanodrops. *Chem. Rev.* **2006,** *106*, 1155-1175.

86. Plath, K. L.; Axson, J. L.; Nelson, G. C.; Takahashi, K.; Skodje, R. T.; Vaida, V., Gas-Phase Vibrational Spectra of Glyoxylic Acid and Its Gem Diol Monohydrate. Implications for Atmospheric Chemistry. *React. Kinet. Catal. Lett.* **2009,** *96*, 209-224.

87. Maron, M. K.; Takahashi, K.; Shoemaker, R. K.; Vaida, V., Hydration of Pyruvic Acid to Its Geminal-Diol, 2,2-Dihydroxypropanoic Acid, in a Water-Restricted Environment. *Chem. Phys. Lett.* **2011,** *513*, 184-190.

88. Mikhailov, E.; Vlasenko, S.; Martin, S. T.; Koop, T.; Poschl, U., Amorphous and Crystalline Aerosol Particles Interacting with Water Vapor: Conceptual Framework and Experimental Evidence for Restructuring, Phase Transitions and Kinetic Limitations. *Atmos. Chem. Phys.* **2009,** *9*, 9491-9522.

CHAPTER V: HA

1. Kawamura, K.; Okuzawa, K.; Aggarwal, S. G.; Irie, H.; Kanaya, Y.; Wang, Z. Determination of Gaseous and Particulate Carbonyls (Glycolaldehyde, Hydroxyacetone, Glyoxal, Methylglyoxal, Nonanal and Decanal) in the Atmosphere at Mt. Tai. *Atmos. Chem. Phys.* **2013,** *13*, 5369-5380.

2. Waxman, E. M.; Dzepina, K.; Ervens, B.; Lee-Taylor, J.; Aumont, B.; Jimenez, J. L.; Madronich, S.; Volkamer, R. Secondary Organic Aerosol Formation from Semi- and Intermediate-Volatility Organic Compounds and Glyoxal: Relevance of O/C as a Tracer for Aqueous Multiphase Chemistry. *Geophys. Res. Lett.* **2013,** *40*, 978-982.

3. Ervens, B.; Turpin, B. J.; Weber, R. J. Secondary Organic Aerosol Formation in Cloud Droplets and Aqueous Particles (AqSOA): A Review of Laboratory, Field and Model Studies. *Atmos. Chem. Phys.* **2011,** *11*, 11069-11102.

4. Ervens, B.; Volkamer, R. Glyoxal Processing by Aerosol Multiphase Chemistry: Towards a Kinetic Modeling Framework of Secondary Organic Aerosol Formation in Aqueous Particles. *Atmos. Chem. Phys.* **2010,** *10*, 8219-8244.

5. Fu, T. M.; Jacob, D. J.; Wittrock, F.; Burrows, J. P.; Vrekoussis, M.; Henze, D. K. Global Budgets of Atmospheric Glyoxal and Methylglyoxal, and Implications for Formation of Secondary Organic Aerosols. *J. Geophys. Res.* **2008,** *113*, No. D15303.

6. Ervens, B.; Sorooshian, A.; Lim, Y. B.; Turpin, B. J. Key Parameters Controlling OH-Initiated Formation of Secondary Organic Aerosol in the Aqueous Phase (AqSOA). *J. Geophys. Res.-Atmos.* **2014,** *119*, 3997-4016.

7. Galloway, M. M.; Chhabra, P. S.; Chan, A. W. H.; Surratt, J. D.; Flagan, R. C.; Seinfeld, J. H.; Keutsch, F. N. Glyoxal Uptake on Ammonium Sulphate Seed Aerosol: Reaction Products and Reversibility of Uptake under Dark and Irradiated Conditions. *Atmos. Chem. Phys.* **2009,** *9*, 3331-3345.

8. Galloway, M. M.; Powelson, M. H.; Sedehi, N.; Wood, S. E.; Millage, K. D.; Kononenko, J. A.; Rynaski, A. D.; De Haan, D. O. Secondary Organic Aerosol Formation During Evaporation of Droplets Containing Atmospheric Aldehydes, Amines, and Ammonium Sulfate. *Environ. Sci. Technol.* **2014,** *48*, 14417-14425.

9. Jang, M.; Czoschke, N. M.; Lee, S.; Kamens, R. M. Heterogeneous Atmospheric Aerosol Production by Acid-Catalyzed Particle-Phase Reactions. *Science* **2002,** *298*, 814-817.

10. Odum, J. R.; Hoffmann, T.; Bowman, F.; Collins, D.; Flagan, R. C.; Seinfeld, J. H. Gas/Particle Partitioning and Secondary Organic Aerosol Yields. *Environ. Sci. Technol.* **1996,** *30*, 2580-85.

11. Sareen, N.; Schwier, A. N.; Lathem, T. L.; Nenes, A.; McNeill, V. F. Surfactants from the Gas Phase May Promote Cloud Droplet Formation. *Proc. Natl. Acad. Sci. U. S. A.* **2013,** *110*, 2723-2728.

12. Woo, J. L.; Kim, D. D.; Schwier, A. N.; Li, R. Z.; McNeill, V. F. Aqueous Aerosol SOA Formation: Impact on Aerosol Physical Properties. *Faraday Discuss.* **2013,** *165*, 357-367.

13. McNeill, V. F. Aqueous Organic Chemistry in the Atmosphere: Sources and Chemical Processing of Organic Aerosols. *Environ. Sci. Technol.* **2015,** *49*, 1237-1244.

14. Kroll, J. H.; Ng, N. L.; Murphy, S. M.; Varutbangkul, V.; Flagan, R. C.; Seinfeld, J. H. Chamber Studies of Secondary Organic Aerosol Growth by Reactive Uptake of Simple Carbonyl Compound. J. Geophys. Res. 2005, 110, No. 23207.

15. Heald, C. L.; Jacob, D. J.; Park, R. J.; Russell, L. M.; Huebert, B. J.; Seinfeld, J. H.; Liao, H.; Weber, R. J. A Large Organic Aerosol Source in the Free Troposphere Missing from Current Models. *Geophys. Res. Lett.* **2005,** *32*, L18809.

16. Volkamer, R.; San Martini, F.; Molina, L.; Salcedo, D.; L Jimenez, J.; Molina, M.; Martini, S. A Missing Sink for Gas-Phase Glyoxal in Mexico City: Formation of Secondary Organic Aerosol. *Geophys. Res. Lett.* **2007,** *34*, L19807.

17. Volkamer, R.; Jimenez, J. L.; San Martini, F.; Dzepina, K.; Zhang, Q.; Salcedo, D.; Molina, L. T.; Worsnop, D. R.; Molina, M. J. Secondary Organic Aerosol Formation from Anthropogenic Air Pollution: Rapid and Higher than Expected. *Geophys. Res. Lett.* **2006,** *33*, L17811.

18. Axson, J. L.; Takahashi, K.; De Haan, D. O.; Vaida, V. Gas-Phase Water-Mediated Equilibrium between Methylglyoxal and Its Geminal Diol. *Proc. Natl. Acad. Sci. U. S. A.* **2010,** *107*, 6687-6692.

19. Corrigan, A. L.; Hanley, S. W.; Haan, D. O. Uptake of Glyoxal by Organic and Inorganic Aerosol. *Environ. Sci. Technol.* **2008,** *42*, 4428-4433.

20. De Haan, D. O.; Corrigan, A. L.; Smith, K. W.; Stroik, D. R.; Turley, J. J.; Lee, F. E.; Tolbert, M. A.; Jimenez, J. L.; Cordova, K. E.; Ferrell, G. R. Secondary Organic Aerosol-Forming Reactions of Glyoxal with Amino Acids. *Environ. Sci. Technol.* **2009,** *43*, 2818-2824.

21. De Haan, D. O.; Corrigan, A. L.; Tolbert, M. A.; Jimenez, J. L.; Wood, S. E.; Turley, J. J. Secondary Organic Aerosol Formation by Self-Reactions of Methylglyoxal and Glyoxal in Evaporating Droplets. *Environ. Sci. Technol.* **2009,** *43*, 8184-8190.

22. De Haan, D. O.; Hawkins, L. N.; Kononenko, J. A.; Turley, J. J.; Corrigan, A. L.; Tolbert, M. A.; Jimenez, J. L. Formation of Nitrogen-Containing Oligomers by Methylglyoxal and Amines in Simulated Evaporating Cloud Droplets. *Environ. Sci. Technol.* **2011,** *45*, 984-991.

23. De Haan, D. O.; Tolbert, M. A.; Jimenez, J. L. Atmospheric Condensed-Phase Reactions of Glyoxal with Methylamine. *Geophys. Res. Lett.* **2009,** *36*, L11819.

24. Hastings, W. P.; Koehler, C. A.; Bailey, E. L.; De Haan, D. O. Secondary Organic Aerosol Formation by Glyoxal Hydration and Oligomer Formation: Humidity Effects and Equilibrium Shifts During Analysis. *Environ. Sci. Technol.* **2005,** *39*, 8728-8735.

25. Hazra, M. K.; Francisco, J. S.; Sinha, A. Hydrolysis of Glyoxal in Water-Restricted Environments: Formation of Organic Aerosol Precursors through Formic Acid Catalysis. *J. Phys. Chem. A* **2014,** *118*, 4095-4105.

26. Johnson, C. M.; Tyrode, E.; Leygraf, C. Atmospheric Corrosion of Zinc by Organic Constituents I. The Role of the Zinc/Water and Water/Air Interfaces Studied by Infrared Reflection/Absorption Spectroscopy and Vibrational Sum Frequency Spectroscopy. *J. Electrochem. Soc.* **2006,** *153*, B113-B120.

27. Krizner, H. E.; De Haan, D. O.; Kua, J. Thermodynamics and Kinetics of Methylglyoxal Dimer Formation: A Computational Study. *J. Phys. Chem. A* **2009,** *113*, 6994-7001.

28. Liggio, J.; Li, S. M.; McLaren, R. Reactive Uptake of Glyoxal by Particulate Matter. *J. Geophys. Res.* **2005,** *110*, No. D10304.

29. Liggio, J.; Li, S. M.; McLaren, R. Heterogeneous Reactions of Glyoxal on Particulate Matter: Identification of Acetals and Sulfate Esters. *Environ. Sci. Technol.* **2005,** *39*, 1532-1541.

30. Loeffler, K. W.; Koehler, C. A.; Paul, N. M.; De Haan, D. O. Oligomer Formation in Evaporating Aqueous Glyoxal and Methyl Glyoxal Solutions. *Environ. Sci. Technol.* **2006,** *40*, 6318-6323.

31. Maron, M. K.; Takahashi, K.; Shoemaker, R. K.; Vaida, V. Hydration of Pyruvic Acid to Its Geminal-Diol, 2,2-Dihydroxypropanoic Acid, in a Water-Restricted Environment. *Chem. Phys. Lett.* **2011,** *513*, 184-190.

32. Mucha, M.; Mielke, Z. Complexes of Atmospheric Alpha-Dicarbonyls with Water: FTIR Matrix Isolation and Theoretical Study. *J. Phys. Chem. A* **2007,** *111*, 2398-2406.

33. Nemet, I.; Vikic-Topic, D.; Varga-Defterdarovic, L. Spectroscopic Studies of Methylglyoxal in Water and Dimethylsulfoxide. *Bioorg. Chem.* **2004,** *32*, 560-570.

34. Plath, K. L.; Axson, J. L.; Nelson, G. C.; Takahashi, K.; Skodje, R. T.; Vaida, V. Gas-Phase Vibrational Spectra of Glyoxylic Acid and Its Gem Diol Monohydrate. Implications for Atmospheric Chemistry. *React. Kinet. Catal. Lett.* **2009,** *96*, 209-224.

35. Romakkaniemi, S.; Kokkola, H.; Smith, J. N.; Prisle, N. L.; Schwier, A. N.; McNeill, V. F.; Laaksonen, A. Partitioning of Semivolatile Surface-Active Compounds between Bulk, Surface and Gas Phase. *Geophys. Res. Lett.* **2011,** *38*, No. L03807.

36. Wren, S. N.; Valley, N. A.; Gordon, B. P.; McWilliams, L. E.; Richmond, G. L. Hydration, Orientation, and Conformation of Methylglyoxal at the Air-Water Interface. *J. Phys. Chem. A* **2015,** *119*, 6391-6403.

37. Pocker, Y.; Meany, J. E.; Nist, B. J.; Zadorojny, C. Reversible Hydration of Pyruvic Acid. I. Equilibrium Studies. *J. Phys. Chem.* **1969,** *73*, 2879-2882.

38. Betterton, E. A.; Hoffmann, M. R. Henry Law Constants of Some Environmentally Important Aldehydes. *Environ. Sci. Technol.* **1988,** *22*, 1415-1418.

39. Sareen, N.; Schwier, A. N.; Shapiro, E. L.; Mitroo, D.; McNeill, V. F. Secondary Organic Material Formed by Methylglyoxal in Aqueous Aerosol Mimics. *Atmos. Chem. Phys.* **2010,** *10*, 997-1016.

40. Casale, M. T.; Richman, A. R.; Elrod, M. J.; Garland, R. M.; Beaver, M. R.; Tolbert, M. A. Kinetics of Acid-Catalyzed Aldol Condensation Reactions of Aliphatic Aldehydes. *Atmos. Environ.* **2007,** *41*, 6212-6224.

41. Renard, P.; Reed Harris, A. E.; Rapf, R. J.; Ravier, S.; Demelas, C.; Coulomb, B.; Quivet, E.; Vaida, V.; Monod, A. Aqueous Phase Oligomerization of Methyl Vinyl Ketone by Atmospheric Radical Reactions. *J. Phys. Chem. C* **2014,** *118*, 29421-29430.

42. Schwier, A. N.; Sareen, N.; Mitroo, D.; Shapiro, E. L.; McNeill, V. F. Glyoxal-Methylglyoxal Cross-Reactions in Secondary Organic Aerosol Formation. *Environ. Sci. Technol.* **2010,** *44*, 6174-6182.

43. Yu, G.; Bayer, A. R.; Galloway, M. M.; Korshavn, K. J.; Fry, C. G.; Keutsch, F. N. Glyoxal in Aqueous Ammonium Sulfate Solutions: Products, Kinetics, and Hydration Effects. *Environ. Sci. Technol.* **2011,** *45*, 6336-6342.

44. Zhao, R.; Lee, A. K. Y.; Abbatt, J. P. D. Investigation of Aqueous-Phase Photooxidation of Glyoxal and Methylglyoxal by Aerosol Chemical Ionization Mass Spectrometry: Observation of Hydroxyhydroperoxide Formation. *J. Phys. Chem. A* **2012,** *116*, 6253-6263.

45. Rapf, R. J.; Perkins, R. J.; Carpenter, B. K.; Vaida, V. Mechanistic Description of Photochemical Oligomer Formation from Aqueous Pyruvic Acid. *J. Phys. Chem. A* **2017,** *121*, 4272-4282.

46. Donaldson, D. J.; Vaida, V. The Influence of Organic Films at the Air-Aqueous Boundary on Atmospheric Processes. *Chem. Rev.* **2006,** *106*, 1445-1461.

47. Donaldson, D. J.; Valsaraj, K. T. Adsorption and Reaction of Trace Gas-Phase Organic Compounds on Atmospheric Water Film Surfaces: A Critical Review. *Environ. Sci. Technol.* **2010,** *44*, 865-873.

48. Köhler, H. The Nucleus in the Growth of Hygroscopic Droplets. *Trans. Faraday Soc.* **1936,** *32*, 1152-1161.

49. Prisle, N. L.; Asmi, A.; Topping, D.; Partanen, A. I.; Romakkaniemi, S.; Dal Maso, M.; Kulmala, M.; Laaksonen, A.; Lehtinen, K. E. J.; McFiggans, G. Surfactant Effects in Global Simulations of Cloud Droplet Activation. *Geophys. Res. Lett.* **2012,** *39*, L05802.

50. Prisle, N. L.; Raatikainen, T.; Laaksonen, A.; Bilde, M. Surfactants in Cloud Droplet Activation: Mixed Organic-Inorganic Particles. *Atmos. Chem. Phys.* **2010,** *10*, 5663-5683.

51. Sorjamaa, R.; Svenningsson, B.; Raatikainen, T.; Henning, S.; Bilde, M.; Laaksonen, A. The Role of Surfactants in Kohler Theory Reconsidered. *Atmos. Chem. Phys.* **2004,** *4*, 2107-2117.

52. Rapf, R. J.; Dooley, M. R.; Kappes, K.; Perkins, R. J.; Vaida, V. pH Dependence of the Aqueous Photochemistry of α-Keto Acids. *J. Phys. Chem. A* **2017,** *121*, 8368-8379.

53. Reed Harris, A. E.; Pajunoja, A.; Cazaunau, M.; Gratien, A.; Pangui, E.; Monod, A.; Griffith, E. C.; Virtanen, A.; Doussin, J.-F.; Vaida, V. Multiphase Photochemistry of Pyruvic Acid under Atmospheric Conditions. *J. Phys. Chem. A* **2017,** *121*, 3327-3339.

54. Rodriguez, A. A.; de Loera, A.; Powelson, M. H.; Galloway, M. M.; De Haan, D. O. Formaldehyde and Acetaldehyde Increase Aqueous-Phase Production of Imidazoles in Methylglyoxal/Amine Mixtures: Quantifying a Secondary Organic Aerosol Formation Mechanism. *Environ. Sci. Technol. Lett.* **2017,** *4*, 234-239.

55. Shrivastava, M.; Cappa, C. D.; Fan, J.; Goldstein, A. H.; Guenther, A. B.; Jimenez, J. L.; Kuang, C.; Laskin, A.; Martin, S. T.; Ng, N. L.; et al. Recent Advances in Understanding Secondary Organic Aerosol: Implications for Global Climate Forcing. *Rev. Geophys.* **2017,** *55*, 509-559.

56. Ortiz-Montalvo, D. L.; Hakkinen, S. A. K.; Schwier, A. N.; Lim, Y. B.; McNeill, V. F.; Turpin, B. J. Ammonium Addition (and Aerosol pH) Has a Dramatic Impact on the Volatility and Yield of Glyoxal Secondary Organic Aerosol. *Environ. Sci. Technol.* **2014,** *48*, 255-262.

57. Bell, S. Ab Initio Study of the Barriers to Methyl Torsion and Torsional Frequencies of Acetyl Molecules. *Spectrochim. Acta, Part A* **2005,** *61*, 1471-1477.

58. Braakman, R.; Drouin, B. J.; Widicus Weaver, S. L.; Blake, G. A. Extended Analysis of Hydroxyacetone in the Torsional Ground State. *J. Mol. Spectros.* **2010,** *264*, 43-49.

59. Jetzki, M.; Luckhaus, D.; Signorell, R. Fermi Resonance and Conformation in Glycolaldehyde Particles. *Can. J. Chem.* **2004,** *82*, 915-924.

60. Kattija-Ari, M.; Harmony, M. D. The Microwave Spectrum and Conformation of Hydroxyacetone: The Influence of Hydrogen Bonding on the Barrier to Internal Rotation of the Methyl Group. *Int. J. Quantum Chem.* **1980,** *18*, 443-453.

61. Lasne, J.; Laffon, C.; Parent, P. Interaction of Acetone, Hydroxyacetone, Acetaldehyde and Benzaldehyde with the Surface of Water Ice and $HNO_{3}73H_{2}O$ Ice. *Phys. Chem. Chem. Phys.* **2012,** *14*, 697-704.

62. Lindenmaier, R.; Tipton, N.; Sams, R. L.; Brauer, C. S.; Blake, T. A.; Williams, S. D.; Johnson, T. J. Assignment of the Fundamental Modes of Hydroxyacetone Using Gas-Phase Infrared, Far-Infrared, Raman, and ab Initio Methods: Band Strengths for Atmospheric Measurements. *J. Phys. Chem. A* **2016,** *120*, 5993-6003.

63. Mohaček-Grošev, V. Vibrational Analysis of Hydroxyacetone. *Spectrochim. Acta, Part A* **2005,** *61*, 477-484.

64. Petitjean, M.; Darvas, M.; Picaud, S.; Jedlovszky, P.; Le Calve, S. Adsorption of Hydroxyacetone on Pure Ice Surfaces. *Chemphyschem* **2010,** *11*, 3921-3927.

65. Sharma, A.; Reva, I.; Fausto, R. Matrix-insolation Study and Ab Initio Calculations of the Structure and Spectra of Hydroxyacetone. *J. Phys. Chem. A* **2008,** *112*, 5935-5946.

66. Sharma, A.; Reva, I.; Fausto, R. Conformational Switching Induced by Near-infrared Laser Irradiation. *J. Am. Chem. Soc.* **2009,** *131*, 8752-8753.

67. Sharma, A.; Reva, I.; Fausto, R.; Hesse, S.; Xue, Z.; Suhm, M. A.; Nayak, S. K.; Sathishkumar, R.; Pal, R.; Guru Row, T. N. Conformation-changing Aggregation in Hydroxyacetone: A Combined Low-temperature FTIR, Jet, and Crystallographic Study. *J. Am. Chem. Soc.* **2011,** *133*, 20194-20207.

68. Glushonok, G. K.; Glushonok, T. G.; Maslovskaya, L. A.; Shadyro, O. I. A ^{1}H and ^{13}C NMR and UV Study of the State of Hydroxyacetone in Aqueous Solutions. *Russ. J. Gen. Chem.* **2003,** *73*, 1027-1031.

69. Dutta, C.; Benderskii, A. V. On the Assignment of the Vibrational Spectrum of the Water Bend at the Air/Water Interface. *J. Phys. Chem. Lett.* **2017,** *8*, 801-804.

70. Eisenthal, K. B. Liquid Interfaces Probed by Second-Harmonic and Sum-Frequency Spectroscopy. *Chem. Rev.* **1996,** *96*, 1343-1360.

71. Feng, R. R.; Guo, Y.; Lü, R.; Velarde, L.; Wang, H. F. Consistency in the Sum Frequency Generation Intensity and Phase Vibrational Spectra of the Air/Neat Water Interface. *J. Phys. Chem. A* **2011,** *115*, 6015-6027.

72. Lambert, A. G.; Davies, P. B.; Neivandt, D. J. Implementing the Theory of Sum Frequency Generation Vibrational Spectroscopy: A Tutorial Review. *Appl. Spectrosc. Rev.* **2005,** *40*, 103-145.

73. Morita, A.; Hynes, J. T. A Theoretical Analysis of the Sum Frequency Generation Spectrum of the Water Surface. *Chem. Phys.* **2000,** *258*, 371-390.

74. Perakis, F.; Marco, L. D.; Shalit, A.; Tang, F.; Kann, Z. R.; Kühne, T. D.; Torre, R.; Bonn, M.; Nagata, Y. Vibrational Spectroscopy and Dynamics of Water. *Chem. Rev.* **2016,** *116*, 7590-7607.

75. Richmond, G. L. Molecular Bonding and Interactions at Aqueous Surfaces as Probed by Vibrational Sum Frequency Spectroscopy. *Chem. Rev.* **2002,** *102*, 2693-2724.

76. Schaefer, J.; Backus, E. H. G.; Nagata, Y.; Bonn, M. Both Inter- and Intramolecular Coupling of O–H Groups Determine the Vibrational Response of the Water/Air Interface. *J. Phys. Chem. Lett.* **2016,** *7*, 4591-4595.

77. Shen, Y. R. Basic Theory of Surface Sum-Frequency Generation. *J. Phys. Chem. C* **2012,** *116*, 15505-15509.

78. Tian, C. S.; Shen, Y. R. Sum-Frequency Vibrational Spectroscopic Studies of Water/Vapor Interfaces. *Chem. Phys. Lett.* **2009,** *470*, 1-6.

79. Verreault, D.; Hua, W.; Allen, H. C. From Conventional to Phase-Sensitive Vibrational Sum Frequency Generation Spectroscopy: Probing Water Organization at Aqueous Interfaces. *J. Phys. Chem. Lett.* **2012,** *3*, 3012-3028.

80. Lu, R.; Gan, W.; Wu, B.H.; Zhang, Z.; Guo, Y.; Wang, H.F. C−H Stretching Vibrations of Methyl, Methylene and Methine Groups at the Vapor/Alcohol (n = 1−8) Interfaces. *J. Phys. Chem. B* **2005,** *109*, 14118-14129.

81. Ishiyama, T.; Imamura, T.; Morita, A. Theoretical Studies of Structures and Vibrational Sum Frequency Generation Spectra at Aqueous Interfaces. *Chem. Rev.* **2014,** *114*, 8447-8470.

82. Bain, C. D.; Davies, P. B.; Ong, T. H.; Ward, R. N.; Brown, M. A. Quantitative Analysis of Monolayer Composition by Sum-Frequency Vibrational Spectroscopy. *Langmuir* **1991,** *7*, 1563-1566.

83. Moore, F. G.; Becraft, K. A.; Richmond, G. L. Challenges in Interpreting Vibrational Sum Frequency Spectra: Deconvoluting Spectral Features as Demonstrated in the Calcium Fluoride-Water-Sodium Dodecylsulfate System. *Appl. Spectrosc.* **2002,** *56*, 1575-1578.

84. Chieffo, L.; Shattuck, J.; Amsden, J. J.; Erramilli, S.; Ziegler, L. D. Ultrafast Vibrational Relaxation of Liquid H2O Following Librational Combination Band Excitation. *Chem. Phys.* **2007,** *341*, 71-80.

85. Knop, S.; Lindner, J.; Vöhringer, P. OH and NH Stretching Vibrational Relaxation of Liquid Ethanolamine. *Z. Phys. Chem.* **2011,** *225*, 913-926.

86. Monson, P. R.; Patumtev, S.; Kaufmann, K. J.; Robinson, G. W. Dominance of Methyl-Groups in Picosecond Vibrational-Relaxation in Hydrocarbons. *Chem. Phys. Lett.* **1974,** *28*, 312-315.

87. Nienhuys, H. K.; van Santen, R. A.; Bakker, H. J. Orientational Relaxation of Liquid Water Molecules as an Activated Process. *J. Chem. Phys.* **2000,** *112*, 8487-8494.

88. Woutersen, S.; Emmerichs, U.; Bakker, H. J. Femtosecond mid-IR pump-probe spectroscopy of liquid water: Evidence for a two-component structure. *Science* **1997,** *278*, 658-660.

89. McWilliams, L. E.; Valley, N. A.; Vincent, N. M.; Richmond, G. L. Interfacial Insights into a Carbon Capture System: CO_2 Uptake to an Aqueous Monoethanolamine Surface. *J. Phys. Chem. A* **2017,** *121*, 7956-7967.

90. McWilliams, L. E.; Valley, N. A.; Wren, S. N.; Richmond, G. L. A Means to an Interface: Investigating Monoethanolamine Behavior at an Aqueous Surface. *Phys. Chem. Chem. Phys.* **2015,** *17*, 21458-21469.

91. Davies, J. T.; Rideal, E. K. *Interfacial Phenomena*. Academic Press: New York, 1963.

92. Blower, P. G.; Ota, S. T.; Valley, N. A.; Wood, S. R.; Richmond, G. L. Sink or Surf: Atmospheric Implications for Succinic Acid at Aqueous Surfaces. *J. Phys. Chem. A* **2013,** *117*, 7887-7903.

93. Plath, K. L.; Valley, N. A.; Richmond, G. L. Ion-Induced Reorientation and Distribution of Pentanone in the Air–Water Boundary Layer. *J. Phys. Chem. A* **2013,** *117*, 11514-11527.

94. Valley, N. A.; Richmond, G. L. Solvation Station: Microsolvation for Modeling Vibrational Sum-Frequency Spectra of Acids at Aqueous Interfaces. *J. Chem. Theory Comput.* **2015,** *11*, 4780-4790.

95. Valley, N. A.; Richmond, G. L. Computational Vibrational Sum Frequency Spectra of Formaldehyde and Hydroxymethanesulfonate at Aqueous Interfaces. *J. Phys. Chem. C* **2016,** *120*, 14122-14129.

96. Valley, N. A.; Robertson, E. J.; Richmond, G. L. Twist and Turn: Effect of Stereoconfiguration on the Interfacial Assembly of Polyelectrolytes. *Langmuir* **2014,** *30*, 14226-14233.

97. Valley, N. V.; Blower, P. G.; Wood, S. R.; Plath, K. L.; McWilliams, L. E.; Richmond, G. L. Doubling Down: Delving into the Details of Diacid Adsorption at Aqueous Surfaces. *J. Phys. Chem. A* **2014,** *118*, 4778-4789.

98. Case, D. A.; Darden, T. A.; T.E. Cheatham, I.; Simmerling, C. L.; Wang, J.; Duke, R. E.; Luo, R.; Walker, R. C.; Zhang, W.; Merz, K. M. *Amber 12*; University of California: San Francisco, 2012.

99. Martinez, L.; Andrade, R.; Birgin, E.; Martinez, J. Packmol: A Package for Building Initial Configurations for Molecular Dynamics Simulations. *J. Comput. Chem.* **2009,** *30*, 2157-2164.

100. Frisch, M. J.; Trucks, G. W.; Schlegel, H. B.; Scuseria, G. E.; Robb, M. A.; Cheeseman, J. R.; Scalmani, G.; Barone, V.; Mennucci, B.; Petersson, G. A.; et al., *Gaussian 09;* Gaussian Inc.: Wallingford, CT. 2009.

101. Nagata, Y.; Hsieh, C.S.; Hasegawa, T.; Voll, J.; Backus, E. H. G.; Bonn, M. Water Bending Mode at the Water–Vapor Interface Probed by Sum-Frequency Generation Spectroscopy: A Combined Molecular Dynamics Simulation and Experimental Study. *J. Phys. Chem. Lett.* **2013,** *4*, 1872-1877.

102. Ni, Y.; Skinner, J. L. IR and SFG Vibrational Spectroscopy of the Water Bend in the Bulk Liquid and at the Liquid-Vapor Interface, Respectively. *J. Chem. Phys.* **2015,** *143* (1), 014502.

103. Vinaykin, M.; Benderskii, A. V. Vibrational Sum-Frequency Spectrum of the Water Bend at the Air/Water Interface. *J. Phys. Chem. Lett.* **2012,** *3*, 3348-3352.

104. Rosen, M. J. In *Surfactants and Interfacial Phenomena 3rd ed.*, John Wiley & Sons, Inc.: New York, 2004.

CHAPTER VI: PA

1. Talbot, R. W.; Andreae, M. O.; Berresheim, H.; Jacob, D. J.; Beecher, K. M., Sources and Sinks of Formic, Acetic, and Pyruvic Acids Over Central Amazonia: 2. Wet Season. *J. Geophys. Res.-Atmos.* **1990,** *95* (D10), 16799-16811.

2. Odum, J. R.; Hoffmann, T.; Bowman, F.; Collins, D.; Flagan, R. C.; Seinfeld, J. H., Gas/Particle Partitioning and Secondary Organic Aerosol Yields. *Environ. Sci. Technol.* **1996,** *30* (8), 2580-2585.

3. Betterton, E. A.; Hoffmann, M. R., Henry Law Constants of Some Environmentally Important Aldehydes. *Environ. Sci. Technol.* **1988,** *22* (12), 1415-1418.

4. Ellison, G. B.; Tuck, A. F.; Vaida, V., Atmospheric Processing of Organic Aerosols. *J. Geophys. Res.-Atmos.* **1999,** *104* (D9), 11633-11641.

5. Jang, M.; Czoschke, N. M.; Lee, S.; Kamens, R. M., Heterogeneous Atmospheric Aerosol Production by Acid-Catalyzed Particle-Phase Reactions. *Science* **2002,** *298* (5594), 814-817.

6. Gao, S.; Ng, N. L.; Keywood, M.; Varutbangkul, V.; Bahreini, R.; Nenes, A.; He, J.; Yoo, K. Y.; Beauchamp, J. L.; Hodyss, R. P.; Flagan, R. C.; Seinfeld, J. H., Particle Phase Acidity and Oligomer Formation in Secondary Organic Aerosol. *Environ. Sci. Technol.* **2004,** *38* (24), 6582-6589.

7. Kalberer, M.; Paulsen, D.; Sax, M.; Steinbacher, M.; Dommen, J.; Prevot, A. S. H.; Fisseha, R.; Weingartner, E.; Frankevich, V.; Zenobi, R.; Baltensperger, U., Identification of Polymers as Major Components of Atmospheric Organic Aerosols. *Science* **2004,** *303* (5664), 1659-1662.

8. Tolocka, M. P.; Jang, M.; Ginter, J. M.; Cox, F. J.; Kamens, R. M.; Johnston, M. V., Formation of Oligomers in Secondary Organic Aerosol. *Environ. Sci. Technol.* **2004,** *38* (5), 1428-1434.

9. Hastings, W. P.; Koehler, C. A.; Bailey, E. L.; De Haan, D. O., Secondary Organic Aerosol Formation by Glyoxal Hydration and Oligomer Formation: Humidity Effects and Equilibrium Shifts During Analysis. *Environ. Sci. Technol.* **2005,** *39* (22), 8728-8735.

10. Kroll, J. H.; Ng, N. L.; Murphy, S. M.; Varutbangkul, V.; Flagan, R. C.; Seinfeld, J. H., Chamber Studies of Secondary Organic Aerosol Growth by Reactive Uptake of Simple Carbonyl Compound. *J. Geophys. Res.-Atmos.* **2005,** *110* (D23), No. 23207.

11. Heald, C. L.; Jacob, D. J.; Park, R. J.; Russell, L. M.; Huebert, B. J.; Seinfeld, J. H.; Liao, H.; Weber, R. J., A Large Organic Aerosol Source in the Free Troposphere Missing from Current Models. *Geophys. Res. Lett.* **2005,** *32* (18), No. L18809.

12. Altieri, K. E.; Carlton, A. G.; Lim, H. J.; Turpin, B. J.; Seitzinger, S. P., Evidence for Oligomer Formation in Clouds: Reactions of Isoprene Oxidation Products. *Environ. Sci. Technol.* **2006,** *40* (16), 4956-4960.

13. Carlton, A. G.; Turpin, B. J.; Lim, H. J.; Altieri, K. E.; Seitzinger, S., Link Between Isoprene and Secondary Organic Aerosol (SOA): Pyruvic Acid Oxidation Yields Low Volatility Organic Acids in Clouds. *Geophys. Res. Lett.* **2006,** *33* (6), No. L06822.

14. Donaldson, D. J.; Vaida, V., The Influence of Organic Films at the Air-Aqueous Boundary on Atmospheric Processes. *Chem. Rev.* **2006,** *106* (4), 1445-1461.

15. Guzman, M. I.; Colussi, A. J.; Hoffmann, M. R., Photoinduced Oligomerization of Aqueous Pyruvic Acid. *J. Phys. Chem. A* **2006,** *110* (10), 3619-3626.

16. Loeffler, K. W.; Koehler, C. A.; Paul, N. M.; De Haan, D. O., Oligomer Formation in Evaporating Aqueous Glyoxal and Methyl Glyoxal Solutions. *Environ. Sci. Technol.* **2006,** *40* (20), 6318-6323.

17. Volkamer, R.; Jimenez, J. L.; San Martini, F.; Dzepina, K.; Zhang, Q.; Salcedo, D.; Molina, L. T.; Worsnop, D. R.; Molina, M. J., Secondary Organic Aerosol Formation from Anthropogenic Air Pollution: Rapid and Higher Than Expected. *Geophys. Res. Lett.* **2006,** *33* (17), No. L17811.

18. Volkamer, R.; San Martini, F.; Molina, L.; Salcedo, D.; L Jimenez, J.; Molina, M.; Martini, S., *A missing sink for gas-phase glyoxal in Mexico City: Formation of secondary organic aerosol. Geophys. Res. Lett.* **2007,** *34* (19), No. L19807.

19. Mucha, M.; Mielke, Z., Complexes of Atmospheric α-Dicarbonyls with Water: FTIR Matrix Isolation and Theoretical Study. *J. Phys. Chem. A* **2007,** *111* (12), 2398-2406.

20. Fu, T. M.; Jacob, D. J.; Wittrock, F.; Burrows, J. P.; Vrekoussis, M.; Henze, D. K., Global Budgets of Atmospheric Glyoxal and Methylglyoxal, and Implications for Formation of Secondary Organic Aerosols. *J. Geophys. Res.-Atmos.* **2008,** *113* (D15), No. D15303.

21. De Haan, D. O.; Corrigan, A. L.; Tolbert, M. A.; Jimenez, J. L.; Wood, S. E.; Turley, J. J., Secondary Organic Aerosol Formation by Self-Reactions of Methylglyoxal and Glyoxal in Evaporating Droplets. *Environ. Sci. Technol.* **2009,** *43* (21), 8184-8190.

22. Donaldson, D. J.; Valsaraj, K. T., Adsorption and Reaction of Trace Gas-Phase Organic Compounds on Atmospheric Water Film Surfaces: A Critical Review. *Environ. Sci. Technol.* **2010,** *44* (3), 865-873.

23. Ervens, B.; Volkamer, R., Glyoxal Processing by Aerosol Multiphase Chemistry: Towards a Kinetic Modeling Framework of Secondary Organic Aerosol Formation in Aqueous Particles. *Atmos. Chem. Phys.* **2010,** *10* (17) 8219-8244.

24. Ervens, B.; Turpin, B. J.; Weber, R. J., Secondary Organic Aerosol Formation in Cloud Droplets and Aqueous Particles (AqSOA): A Review of Laboratory, Field and Model Studies. *Atmos. Chem. Phys.* **2011,** *11* (21), 11069-11102.

25. Kawamura, K.; Okuzawa, K.; Aggarwal, S. G.; Irie, H.; Kanaya, Y.; Wang, Z., Determination of Gaseous and Particulate Carbonyls (Glycolaldehyde, Hydroxyacetone, Glyoxal, Methylglyoxal, Nonanal and Decanal) in the Atmosphere at Mt. Tai. *Atmos. Chem. Phys.* **2013,** *13* (10), 5369-5380.

26. Waxman, E. M.; Dzepina, K.; Ervens, B.; Lee-Taylor, J.; Aumont, B.; Jimenez, J. L.; Madronich, S.; Volkamer, R., Secondary Organic Aerosol Formation from Semi- and Intermediate-Volatility Organic Compounds and Glyoxal: Relevance of O/C as a Tracer for Aqueous Multiphase Chemistry. *Geophys. Res. Lett.* **2013,** *40* (5), 978-982.

27. Woo, J. L.; Kim, D. D.; Schwier, A. N.; Li, R. Z.; McNeill, V. F., Aqueous Aerosol SOA Formation: Impact on Aerosol Physical Properties. *Faraday Discuss.* **2013,** *165*, 357-367.

28. Sareen, N.; Schwier, A. N.; Lathem, T. L.; Nenes, A.; McNeill, V. F., Surfactants from the Gas Phase May Promote Cloud Droplet Formation. *Proc. Natl. Acad. Sci. U. S. A.* **2013,** *110*,(8), 2723-2728.

29. Ervens, B.; Sorooshian, A.; Lim, Y. B.; Turpin, B. J., Key Parameters Controlling OH-Initiated Formation of Secondary Organic Aerosol in the Aqueous Phase (Aqsoa). *J. Geophys. Res.-Atmos.* **2014,** *119* (7), 3997-4016.

30. Galloway, M. M.; Powelson, M. H.; Sedehi, N.; Wood, S. E.; Millage, K. D.; Kononenko, J. A.; Rynaski, A. D.; De Haan, D. O., Secondary Organic Aerosol Formation During Evaporation of Droplets Containing Atmospheric Aldehydes, Amines, and Ammonium Sulfate. *Environ. Sci. Technol.* **2014,** *48* (24), 14417-14425.

31. McNeill, V. F., Aqueous Organic Chemistry in the Atmosphere: Sources and Chemical Processing of Organic Aerosols. *Environ. Sci. Technol.* **2015,** *49* (3), 1237-1244.

32. Kawamura, K.; Bikkina, S., A Review of Dicarboxylic Acids and Related Compounds in Atmospheric Aerosols: Molecular Distributions, Sources and Transformation. *Atmos. Res.* **2016,** *170*, 140-160.

33. Kua, J.; Hanley, S. W.; De Haan, D. O., Thermodynamics and Kinetics of Glyoxal Dimer Formation: A Computational Study. *J. Phys. Chem. A* **2008,** *112* (1), 66-72.

34. Wren, S. N.; Valley, N. A.; Gordon, B. P.; McWilliams, L. E.; Richmond, G. L., Hydration, Orientation, and Conformation of Methylglyoxal at the Air-Water Interface. *J. Phys. Chem. A* **2015,** *119* (24), 6391-6403.

35. Axson, J. L.; Takahashi, K.; De Haan, D. O.; Vaida, V., Gas-Phase Water-Mediated Equilibrium between Methylglyoxal and Its Geminal Diol. *Proc. Natl. Acad. Sci. U. S. A.* **2010,** *107* (15), 6687-6692.

36. Nemet, I.; Vikic-Topic, D.; Varga-Defterdarovic, L., Spectroscopic Studies of Methylglyoxal in Water and Dimethylsulfoxide. *Bioorg. Chem.* **2004,** *32*, (6) 560-570.

37. Krizner, H. E.; De Haan, D. O.; Kua, J., Thermodynamics and Kinetics of Methylglyoxal Dimer Formation: A Computational Study. *J. Phys. Chem. A* **2009,** *113* (25), 6994-7001.

38. Schwier, A. N.; Sareen, N.; Mitroo, D.; Shapiro, E. L.; McNeill, V. F., Glyoxal-Methylglyoxal Cross-Reactions in Secondary Organic Aerosol Formation. *Environ. Sci. Technol.* **2010,** *44* (16), 6174-6182.

39. Schnitzler, E. G.; Seifert, N. A.; Ghosh, S.; Thomas, J.; Xu, Y. J.; Jager, W., Hydration of the Simplest α-Keto Acid: a Rotational Spectroscopic and Ab Initio Study of the Pyruvic Acid-Water Complex. *Phys. Chem. Chem. Phys.* **2017,** *19* (6), 4440-4446.

40. Rodigast, M.; Mutzel, A.; Herrmann, H., A Quantification Method for Heat-Decomposable Methylglyoxal Oligomers and its Application on 1,3,5-Trimethylbenzene SOA. *Atmos. Chem. Phys.* **2017,** *17* (6), 3929-3943.

41. Maron, M. K.; Takahashi, K.; Shoemaker, R. K.; Vaida, V., Hydration of Pyruvic Acid to Its Geminal-Diol, 2,2-Dihydroxypropanoic Acid, in a Water-Restricted Environment. *Chem. Phys. Lett.* **2011,** *513* (4-6), 184-190.

42. Larsen, M. C.; Vaida, V., Near Infrared Photochemistry of Pyruvic Acid in Aqueous Solution. *J. Phys. Chem. A* **2012,** *116* (24), 5840-5846.

43. Griffith, E. C.; Carpenter, B. K.; Shoemaker, R. K.; Vaida, V., Photochemistry of Aqueous Pyruvic Acid. *Proc. Natl. Acad. Sci. U. S. A.* **2013,** *110* (29), 11714-11719.

44. Reed Harris, A. E.; Ervens, B.; Shoemaker, R. K.; Kroll, J. A.; Rapf, R. J.; Griffith, E. C.; Monod, A.; Vaida, V., Photochemical Kinetics of Pyruvic Acid in Aqueous Solution. *J. Phys. Chem. A* **2014,** *118* (37), 8505-8516.

45. Perkins, R. J.; Shoemaker, R. K.; Carpenter, B. K.; Vaida, V., Chemical Equilibria and Kinetics in Aqueous Solutions of Zymonic Acid. *J. Phys. Chem. A* **2016,** *120* (51), 10096-10107.

46. Reed Harris, A. E.; Doussin, J. F.; Carpenter, B. K.; Vaida, V., Gas-Phase Photolysis of Pyruvic Acid: The Effect of Pressure on Reaction Rates and Products. *J. Phys. Chem. A* **2016,** *120* (51), 10123-10133.

47. Reed Harris, A. E.; Pajunoja, A.; Cazaunau, M.; Gratien, A.; Pangui, E.; Monod, A.; Griffith, E. C.; Virtanen, A.; Doussin, J. F.; Vaida, V., Multiphase Photochemistry of Pyruvic Acid under Atmospheric Conditions. *J. Phys. Chem. A* **2017,** *121* (18), 3327-3339.

48. Rapf, R. J.; Perkins, R. J.; Carpenter, B. K.; Vaida, V., Mechanistic Description of Photochemical Oligomer Formation from Aqueous Pyruvic Acid. *J. Phys. Chem. A* **2017,** *121* (22), 4272-4282.

49. Rapf, R. J.; Perkins, R. J.; Yang, H. S.; Miyake, G.; Carpenter, B. K.; Vaida, V., Photochemical Synthesis of Oligomeric Amphiphiles from Alkyl Oxoacids in Aqueous Environments. *J. Am. Chem. Soc.* **2017,** *139* (20), 6946-6959.

50. Rapf, R. J.; Dooley, M. R.; Kappes, K.; Perkins, R. J.; Vaida, V., pH Dependence of the Aqueous Photochemistry of α-Keto Acids. *J. Phys. Chem. A* **2017,** *121* (44), 8368-8379.

51. Reed Harris, A. E.; Cazaunau, M.; Gratien, A.; Pangui, E.; Doussin, J. F.; Vaida, V., Atmospheric Simulation Chamber Studies of the Gas-Phase Photolysis of Pyruvic Acid. *J. Phys. Chem. A* **2017,** *121* (44), 8348-8358.

52. Rapf, R. J.; Perkins, R. J.; Dooley, M. R.; Kroll, J. A.; Carpenter, B. K.; Vaida, V., Environmental Processing of Lipids Driven by Aqueous Photochemistry of α-Keto Acids. *Acs Central Science* **2018,** *4* (5), 624-630.

53. Fang, Y.; Lesnicki, D.; Wall, K. J.; Gaigeot, M. P.; Sulpizi, M.; Vaida, V.; Grassian, V. H., Heterogeneous Interactions between Gas-Phase Pyruvic Acid and Hydroxylated Silica Surfaces: A Combined Experimental and Theoretical Study. *J. Phys. Chem. A* **2019,** *123* (5), 983-991.

54. Alves, M. R.; Fang, Y.; Wall, K. J.; Vaida, V.; Grassian, V. H., Chemistry and Photochemistry of Pyruvic Acid Adsorbed on Oxide Surfaces. *J. Phys. Chem. A* **2019,** *123* (35), 7661-7671.

55. Salameh, A.; Vorka, F.; Daskalakis, V., Correlation between Surface Tension and the Bulk Dynamics in Salty Atmospheric Aquatic Droplets. *J. Phys. Chem. C* **2016,** *120* (21), 11508-11518.

56. Tang, M. J.; Larish, W. A.; Fang, Y.; Gankanda, A.; Grassian, V. H., Heterogeneous Reactions of Acetic Acid with Oxide Surfaces: Effects of Mineralogy and Relative Humidity. *J. Phys. Chem. A* **2016,** *120* (28), 5609-5616.

57. Han, Y.; Kawamura, K.; Chen, Q.; Mochida, M., Formation of High-Molecular-Weight Compounds Via the Heterogeneous Reactions of Gaseous C_8–C_{10} n-Aldehydes in the Presence of Atmospheric Aerosol Components. *Atmos. Environ.* **2016,** *126*, 290-297.

58. Shrivastava, M.; Cappa, C. D.; Fan, J.; Goldstein, A. H.; Guenther, A. B.; Jimenez, J. L.; Kuang, C.; Laskin, A.; Martin, S. T.; Ng, N. L.; et al., Recent Advances in Understanding Secondary Organic Aerosol: Implications for Global Climate Forcing. *Revs. Geophys.* **2017,** *55* (2), 509-559.

59. Eugene, A. J.; Guzman, M. I., Reactivity of Ketyl and Acetyl Radicals from Direct Solar Actinic Photolysis of Aqueous Pyruvic Acid. *J. Phys. Chem. A* **2017,** *121* (15), 2924-2935.

60. Mekic, M.; Brigante, M.; Vione, D.; Gligorovski, S., Exploring the Ionic Strength Effects on the Photochemical Degradation of Pyruvic Acid in Atmospheric Deliquescent Aerosol Particles. *Atmos. Environ.* **2018,** *185*, 237-242.

61. Mekic, M.; Loisel, G.; Zhou, W. T.; Jiang, B.; Vione, D.; Gligorovski, S., Ionic-Strength Effects on the Reactive Uptake of Ozone on Aqueous Pyruvic Acid: Implications for Air-Sea Ozone Deposition. *Environ. Sci. Technol.* **2018,** *52* (21), 12306-12315.

62. Eugene, A. J.; Pillar, E. A.; Colussi, A. J.; Guzman, M. I., Enhanced Acidity of Acetic and Pyruvic Acids on the Surface of Water. *Langmuir* **2018,** *34* (31), 9307-9313.

63. Fu, Y.; Zhang, Y. Y.; Zhang, F.; Chen, J. M.; Zhu, Z. H.; Yu, X. Y., Does Interfacial Photochemistry Play a Role in the Photolysis of Pyruvic Acid in Water? *Atmos. Environ.* **2018,** *191*, 36-45.

64. Bain, C. D.; Davies, P. B.; Ong, T. H.; Ward, R. N.; Brown, M. A., Quantitative Analysis of Monolayer Composition by Sum-Frequency Vibrational Spectroscopy. *Langmuir* **1991,** *7* (8), 1563-1566.

65. Eisenthal, K. B., Liquid Interfaces Probed by Second-Harmonic and Sum-Frequency Spectroscopy. *Chem. Rev.* **1996,** *96* (4), 1343-1360.

66. Lambert, A. G.; Davies, P. B.; Neivandt, D. J., Implementing the Theory of Sum Frequency Generation Vibrational Spectroscopy: A Tutorial Review. *Appl. Spectrosc. Rev.* **2005,** *40* (2), 103-145.

67. Shen, Y. R., Basic Theory of Surface Sum-Frequency Generation. *J. Phys. Chem. C* **2012,** *116* (29), 15505-15509.

68. Scatena, L. F.; Brown, M. G.; Richmond, G. L., Water at Hydrophobic Surfaces: Weak Hydrogen Bonding and Strong Orientation Effects. *Science* **2001,** *292* (5518), 908-912.

69. Moore, F. G.; Becraft, K. A.; Richmond, G. L., Challenges in interpreting vibrational sum frequency spectra: Deconvoluting spectral features as demonstrated in the calcium fluoride-water-sodium dodecylsulfate system. *Appl. Spectrosc.* **2002,** *56* (12), 1575-1578.

70. Richmond, G. L., Molecular Bonding and Interactions at Aqueous Surfaces as Probed by Vibrational Sum Frequency Spectroscopy. *Chem. Rev.* **2002,** *102* (8), 2693-2724.

71. Blower, P. G.; Ota, S. T.; Valley, N. A.; Wood, S. R.; Richmond, G. L., Sink or Surf: Atmospheric Implications for Succinic Acid at Aqueous Surfaces. *J. Phys. Chem. A* **2013,** *117* (33), 7887-7903.

72. Valley, N. A.; Robertson, E. J.; Richmond, G. L., Twist and Turn: Effect of Stereoconfiguration on the Interfacial Assembly of Polyelectrolytes. *Langmuir* **2014,** *30* (47), 14226-14233.

73. Valley, N. V.; Blower, P. G.; Wood, S. R.; Plath, K. L.; McWilliams, L. E.; Richmond, G. L., Doubling Down: Delving into the Details of Diacid Adsorption at Aqueous Surfaces. *J. Phys. Chem. A* **2014,** *118* (26), 4778-4789.

74. McWilliams, L. E.; Valley, N. A.; Wren, S. N.; Richmond, G. L., A Means to an Interface: Investigating Monoethanolamine Behavior at an Aqueous Surface. *Phys. Chem. Chem. Phys.* **2015,** *17*, 21458-21469.

75. Valley, N. A.; Richmond, G. L., Solvation Station: Microsolvation for Modeling Vibrational Sum-Frequency Spectra of Acids at Aqueous Interfaces. *J. Chem. Theory Comput.* **2015,** *11* (10), 4780-4790.

76. Valley, N. A.; Richmond, G. L., Computational Vibrational Sum Frequency Spectra of Formaldehyde and Hydroxymethanesulfonate at Aqueous Interfaces. *J. Phys. Chem. C* **2016,** *120* (26), 14122-14129.

77. McWilliams, L. E.; Valley, N. A.; Vincent, N. M.; Richmond, G. L., Interfacial Insights into a Carbon Capture System: CO_2 Uptake to an Aqueous Monoethanolamine Surface. *J. Phys. Chem. A* **2017,** *121* (41), 7956-7967.

78. Gordon, B. P.; Moore, F. G.; Scatena, L. F.; Valley, N. A.; Wren, S. N.; Richmond, G. L., Model Behavior: Characterization of Hydroxyacetone at the Air–Water Interface Using Experimental and Computational Vibrational Sum Frequency Spectroscopy. *J. Phys. Chem. A* **2018,** *122* (15), 3837-3849.

79. Schabes, B. K.; Altman, R. M.; Richmond, G. L., Come Together: Molecular Details into the Synergistic Effects of Polymer–Surfactant Adsorption at the Oil/Water Interface. *J. Phys. Chem. B* **2018,** *122* (36), 8582-8590.

80. Wen, Y.; Zha, S.; Xing, L.; Yang, S.; Guo, P.; Shi, G.; Fang, H.; Shen, Y. R.; Tian, C., Unveiling Microscopic Structures of Charged Water Interfaces by Surface-Specific Vibrational Spectroscopy. *Phys. Rev. Lett.* **2016,** *116* (1-8), 016101.

81. Du, Q.; Superfine, R.; Freysz, E.; Shen, Y. R., Vibrational Spectroscopy of Water at the Vapor/Water Interface. *Phys. Rev. Lett.* **1993,** *70* (15), 2313-1316.

82. Morita, A.; Hynes, J. T., A theoretical analysis of the sum frequency generation spectrum of the water surface. *Chem. Phys.* **2000,** *258* (2-3), 371-390.

83. Raymond, E. A.; Tarbuck, T. L.; Brown, M. G.; Richmond, G. L., Hydrogen-Bonding Interactions at the Vapor/Water Interface Investigated by Vibrational Sum-Frequency Spectroscopy of HOD/H_2O/D_2O Mixtures and Molecular Dynamics Simulations. *J. Phys. Chem. B* **2003,** *107* (2), 546-556.

84. Lu, R.; Gan, W.; Wu, B.-h.; Chen, H.; Wang, H.-f., Vibrational Polarization Spectroscopy of CH Stretching Modes of the Methylene Group at the Vapor/Liquid Interfaces with Sum Frequency Generation. *J. Phys. Chem. B* **2004,** *108* (22), 7297-7306.

85. Shen, Y. R.; Ostroverkhov, V., Sum-Frequency Vibrational Spectroscopy on Water Interfaces: Polar Orientation of Water Molecules at Interfaces. *Chem. Rev.* **2006,** *106* (4), 1140-1154.

86. Tian, C. S.; Shen, Y. R., Sum-Frequency Vibrational Spectroscopic Studies of Water/Vapor Interfaces. *Chem. Phys. Lett.* **2009,** *470* (1-3), 1-6.

87. Feng, R. r.; Guo, Y.; Lü, R.; Velarde, L.; Wang, H. f., Consistency in the Sum Frequency Generation Intensity and Phase Vibrational Spectra of the Air/Neat Water Interface. *J. Phys. Chem. A* **2011,** *115* (23), 6015-6027.

88. Verreault, D.; Hua, W.; Allen, H. C., From Conventional to Phase-Sensitive Vibrational Sum Frequency Generation Spectroscopy: Probing Water Organization at Aqueous Interfaces. *J. Phys. Chem. Lett.* **2012,** *3* (20), 3012-3028.

89. Vinaykin, M.; Benderskii, A. V., Vibrational Sum-Frequency Spectrum of the Water Bend at the Air/Water Interface. *J. Phys. Chem. Lett.* **2012,** *3* (22), 3348-3352.

90. Nagata, Y.; Hsieh, C.-S.; Hasegawa, T.; Voll, J.; Backus, E. H. G.; Bonn, M., Water Bending Mode at the Water–Vapor Interface Probed by Sum-Frequency Generation Spectroscopy: A Combined Molecular Dynamics Simulation and Experimental Study. *J. Phys. Chem. Lett.* **2013,** *4* (11), 1872-1877.

91. Ni, Y.; Skinner, J. L., IR and SFG Vibrational Spectroscopy of the Water Bend in the Bulk Liquid and at the Liquid-Vapor Interface, Respectively. *J. Chem. Phys.* **2015,** *143* (1), 014502.

92. Medders, G. R.; Paesani, F., Dissecting the Molecular Structure of the Air/Water Interface from Quantum Simulations of the Sum-Frequency Generation Spectrum. *J. Am. Chem. Soc.* **2016,** *138* (11), 3912-3919.

93. Kundu, A.; Tanaka, S.; Ishiyama, T.; Ahmed, M.; Inoue, K.-i.; Nihonyanagi, S.; Sawai, H.; Yamaguchi, S.; Morita, A.; Tahara, T., Bend Vibration of Surface Water Investigated by Heterodyne-Detected Sum Frequency Generation and Theoretical Study: Dominant Role of Quadrupole. *J. Phys. Chem. Lett.* **2016,** *7* (13), 2597-2601.

94. Perakis, F.; Marco, L. D.; Shalit, A.; Tang, F.; Kann, Z. R.; Kühne, T. D.; Torre, R.; Bonn, M.; Nagata, Y., Vibrational Spectroscopy and Dynamics of Water. *Chem. Rev.* **2016,** *116* (13), 7590-7607.

95. Khatib, R.; Hasegawa, T.; Sulpizi, M.; Backus, E. H. G.; Bonn, M.; Nagata, Y., Molecular Dynamics Simulations of SFG Librational Modes Spectra of Water at the Water–Air Interface. *J. Phys. Chem. C* **2016,** *120* (33), 18665-18673.

96. Dutta, C.; Benderskii, A. V., On the Assignment of the Vibrational Spectrum of the Water Bend at the Air/Water Interface. *J. Phys. Chem. Lett.* **2017,** *8* (4), 801-804.

97. Pezzotti, S.; Galimberti, D. R.; Gaigeot, M.-P., 2D H-Bond Network as the Topmost Skin to the Air–Water Interface. *J. Phys. Chem. Lett.* **2017,** *8* (13), 3133-3141.

98. Suzuki, Y.; Nojima, Y.; Yamaguchi, S., Vibrational Coupling at the Topmost Surface of Water Revealed by Heterodyne-Detected Sum Frequency Generation Spectroscopy. *J. Phys. Chem. Lett.* **2017,** *8* (7), 1396-1401.

99. Tang, F.; Ohto, T.; Hasegawa, T.; Xie, W. J.; Xu, L.; Bonn, M.; Nagata, Y., Definition of Free O–H Groups of Water at the Air–Water Interface. *J. Chem. Theory Comput.* **2018,** *14* (1), 357-364.

100. Woutersen, S.; Emmerichs, U.; Bakker, H. J., Femtosecond mid-IR pump-probe spectroscopy of liquid water: Evidence for a two-component structure. *Science* **1997,** *278* (5338), 658-660.

101. Monson, P. R.; Patumtev, S.; Kaufmann, K. J.; Robinson, G. W., Dominance of Methyl-Groups in Picosecond Vibrational-Relaxation in Hydrocarbons. *Chem. Phys. Lett.* **1974,** *28* (3), 312-315.

102. Chieffo, L.; Shattuck, J.; Amsden, J. J.; Erramilli, S.; Ziegler, L. D., Ultrafast Vibrational Relaxation of Liquid H_2O Following Librational Combination Band Excitation. *Chem. Phys.* **2007,** *341* (3), 71-80.

103. Knop, S.; Lindner, J.; Vöhringer, P., OH and NH Stretching Vibrational Relaxation of Liquid Ethanolamine. *Z. Phys. Chem.* **2011,** *225*, (9-10) 913-926.

104. Case, D. A.; Darden, T. A.; T.E. Cheatham, I.; Simmerling, C. L.; Wang, J.; Duke, R. E.; Luo, R.; Walker, R. C.; Zhang, W.; Merz, K. M., *AMBER 12; University of California: San Francisco*. 2012.

105. Martinez, L.; Andrade, R.; Birgin, E.; Martinez, J., PACKMOL: A Package for Building Initial Configurations for Molecular Dynamics Simulations. *J. Comput. Chem.* **2009,** *30* (13), 2157-2164.

106. Frisch, M. J.; Trucks, G. W.; Schlegel, H. B.; Scuseria, G. E.; Robb, M. A.; Cheeseman, J. R.; Scalmani, G.; Barone, V.; Mennucci, B.; Petersson, G. A.; et al., *Gaussian 09*. 2009.

107. Plath, K. L.; Takahashi, K.; Skodje, R. T.; Vaida, V., Fundamental and Overtone Vibrational Spectra of Gas-Phase Pyruvic Acid. *J. Phys. Chem. A* **2009,** *113* (26), 7294-7303.

108. Hollenstein, H.; Akermann, F.; Gunthard, H. H., Vibrational analysis of pyruvic acid and D−, ^{13}C− and ^{18}O-labelled species: Matrix spectra, assignments, valence force field and normal coordinate analysis. *Spectrochim. Acta A* **1978,** *34* (11), 1041-1063.

109. Reva, I. D.; Stepanian, S. G.; Adamowicz, L.; Fausto, R., Combined FTIR matrix isolation and ab initio studies of pyruvic acid: Proof for existence of the second conformer. *J. Phys. Chem. A* **2001,** *105* (19), 4773-4780.

110. Reva, I.; Nunes, C. M.; Biczysko, M.; Fausto, R., Conformational Switching in Pyruvic Acid Isolated in Ar and N_2 Matrixes: Spectroscopic Analysis, Anharmonic Simulation, and Tunneling. *J. Phys. Chem. A* **2015,** *119* (11), 2614-2627.

111. Tsilomelekis, G.; Josephson, T. R.; Nikolakis, V.; Caratzoulas, S., Origin of 5-Hydroxymethylfurfural Stability in Water/Dimethyl Sulfoxide Mixtures. *ChemSusChem* **2014,** *7* (1), 117-126.

112. Khemalapure, S. S.; Katti, V. S.; Hiremath, C. S.; Hiremath, S. M.; Basanagouda, M.; Radder, S. B., Spectroscopic (FT-IR, FT-Raman, NMR and UV-Vis), ELF, LOL, NBO, and Fukui Function Investigations on (5-bromo-benzofuran-3-yl)-Acetic Acid Hydrazide (5BBAH): Experimental and Theoretical Approach. *J. Mol. Struct.* **2019,** *1196*, 280-290.

113. Vimalraj, V.; Vijayalakshmi, S.; Umayaparvathi, S.; Krishnan, A. R., Vibrational, NMR spectral studies of 2-furoic hydrazide by DFT and ab initio HF methods. *Spectrochim. Acta A* **2011,** *78* (2), 670-675.

114. Luňák, S.; Frumarová, B.; Vyňuchal, J.; Hrdina, R., Geometry and Raman Spectra of P.R. 255 and its Furo-Furanone Analogue. *Chem. Phys.* **2009,** *359* (1), 45-52.

115. Glushonok, G. K.; Glushonok, T. G.; Maslovskaya, L. A.; Shadyro, O. I., A ^{1}H and ^{13}C NMR and UV Study of the State of Hydroxyacetone in Aqueous Solutions. *Russ. J. Gen. Chem.* **2003,** *73* (7), 1027-1031.

116. Murto, J.; Raaska, T.; Kunttu, H.; Rasanen, M., Conformers and Vibrational Spectra of Pyruvic Acid: An Ab Initio Study. *J. Mol. Struct.-Theochem.* **1989,** *59*, 93-101.

117. Raczynska, E. D.; Duczmal, K.; Darowska, M., Experimental (FT-IR) and Theoretical (DFT-IR) Studies of Keto-Enol Tautomerism in Pyruvic Acid. *Vib. Spectrosc.* **2005,** *39* (1), 37-45.

118. Kakkar, R.; Pathak, M.; Radhika, N. P., A DFT Study of the Structures of Pyruvic Acid Isomers and Their Decarboxylation. *Org. Biomol. Chem.* **2006,** *4* (5), 886-895.

119. Barone, V.; Biczysko, M.; Bloino, J.; Cimino, P.; Penocchio, E.; Puzzarini, C., CC/DFT Route toward Accurate Structures and Spectroscopic Features for Observed and Elusive Conformers of Flexible Molecules: Pyruvic Acid as a Case Study. *J. Chem. Theory Comput.* **2015,** *11* (9), 4342-4363.

CHAPTER VIII: MG-NaCl

1. Ervens, B.; Volkamer, R., Glyoxal Processing by Aerosol Multiphase Chemistry: Towards a Kinetic Modeling Framework of Secondary Organic Aerosol Formation in Aqueous Particles. *Atmos. Chem. Phys.* **2010,** *10* (17), 8219-8244.

2. Ervens, B.; Turpin, B. J.; Weber, R. J., Secondary Organic Aerosol Formation in Cloud Droplets and Aqueous Particles (AqSOA): A Review of Laboratory, Field and Model Studies. *Atmos. Chem. Phys.* **2011,** *11* (21), 11069-11102.

3. Sareen, N.; Schwier, A. N.; Shapiro, E. L.; Mitroo, D.; McNeill, V. F., Secondary Organic Material Formed by Methylglyoxal in Aqueous Aerosol Mimics. *Atmos. Chem. Phys.* **2010,** *10*, 997.

4. Noziere, B.; Dziedzic, P.; Cordova, A., Inorganic Ammonium Salts and Carbonate Salts Are Efficient Catalysts for Aldol Condensation in Atmospheric Aerosols. *Phys. Chem. Chem. Phys.* **2010,** *12*, 3864.

5. De Haan, D. O.; Hawkins, L. N.; Kononenko, J. A.; Turley, J. J.; Corrigan, A. L.; Tolbert, M. A.; Jimenez, J. L., Formation of Nitrogen-Containing Oligomers by Methylglyoxal and Amines in Simulated Evaporating Cloud Droplets. *Environ. Sci. Technol.* **2011,** *45* (3), 984-991.

6. Sareen, N.; Schwier, A. N.; Lathem, T. L.; Nenes, A.; McNeill, V. F., Surfactants from the Gas Phase May Promote Cloud Droplet Formation. *Proc. Natl. Acad. Sci. U. S. A.* **2013,** *110* (8), 2723-2728.

7. Gopalakrishnan, S.; Jungwirth, P.; Tobias, D. J.; Allen, H. C., Air−Liquid Interfaces of Aqueous Solutions Containing Ammonium and Sulfate: Spectroscopic and Molecular Dynamics Studies. *The Journal of Physical Chemistry B* **2005,** *109* (18), 8861-8872.

8. Jungwirth, P.; Tobias, D. J., Specific Ion Effects at the Air/Water Interface. *Chemical Reviews* **2006,** *106* (4), 1259-1281.

9. Nemet, I.; Vikic-Topic, D.; Varga-Defterdarovic, L., Spectroscopic Studies of Methylglyoxal in Water and Dimethylsulfoxide. *Bioorg. Chem.* **2004,** *32* (6), 560-570.

10. Wren, S. N.; Valley, N. A.; Gordon, B. P.; McWilliams, L. E.; Richmond, G. L., Hydration, Orientation, and Conformation of Methylglyoxal at the Air-Water Interface. *J. Phys. Chem. A* **2015,** *119* (24), 6391-6403.

11. Loeffler, K. W.; Koehler, C. A.; Paul, N. M.; De Haan, D. O., Oligomer Formation in Evaporating Aqueous Glyoxal and Methyl Glyoxal Solutions. *Environ. Sci. Technol.* **2006,** *40* (20), 6318-6323.

12. De Haan, D. O.; Corrigan, A. L.; Tolbert, M. A.; Jimenez, J. L.; Wood, S. E.; Turley, J. J., Secondary Organic Aerosol Formation by Self-Reactions of Methylglyoxal and Glyoxal in Evaporating Droplets. *Environ. Sci. Technol.* **2009,** *43* (21), 8184-8190.

13. Tan, Y.; Carlton, A. G.; Seitzinger, S. P.; Turpin, B. J., SOA From Methylglyoxal in Clouds and Wet Aerosols: Measurement and Prediction of Key Products. *Atmos. Environ.* **2010,** *44* (39), 5218-5226.

14. Yasmeen, F.; Sauret, N.; Gal, J. F.; Maria, P. C.; Massi, L.; Maenhaut, W.; Claeys, M., Characterization of Oligomers from Methylglyoxal Under Dark Conditions: A Pathway to Produce Secondary Organic Aerosol Through Cloud Processing During Nighttime. *Atmos. Chem. Phys.* **2010,** *10* (8), 3803-3812.

15. Krizner, H. E.; De Haan, D. O.; Kua, J., Thermodynamics and Kinetics of Methylglyoxal Dimer Formation: A Computational Study. *J. Phys. Chem. A* **2009,** *113* (25), 6994-7001.

16. Gordon, B. P.; Moore, F. G.; Scatena, L. F.; Richmond, G. L., On the Rise: Experimental and Computational Vibrational Sum Frequency Spectroscopy Studies of Pyruvic Acid and Its Surface-Active Oligomer Species at the Air–Water Interface. *J. Phys. Chem. A* **2019**, *123* (49), 10609-10619.

17. Schwier, A. N.; Sareen, N.; Mitroo, D.; Shapiro, E. L.; McNeill, V. F., Glyoxal-Methylglyoxal Cross-Reactions in Secondary Organic Aerosol Formation. *Environ. Sci. Technol.* **2010,** *44* (16), 6174-6182.

18. Waxman, E. M.; Elm, J.; Kurtén, T.; Mikkelsen, K. V.; Ziemann, P. J.; Volkamer, R., Glyoxal and Methylglyoxal Setschenow Salting Constants in Sulfate, Nitrate, and Chloride Solutions: Measurements and Gibbs Energies. *Environmental Science & Technology* **2015,** *49* (19), 11500-11508.

19. Rapf, R. J.; Dooley, M. R.; Kappes, K.; Perkins, R. J.; Vaida, V., pH Dependence of the Aqueous Photochemistry of α-Keto Acids. *J. Phys. Chem. A* **2017,** *121* (44), 8368-8379.

20. McNeill, V. F., Aqueous Organic Chemistry in the Atmosphere: Sources and Chemical Processing of Organic Aerosols. *Environ. Sci. Technol.* **2015,** *49* (3), 1237-1244.

21. Waxman, E. M.; Dzepina, K.; Ervens, B.; Lee-Taylor, J.; Aumont, B.; Jimenez, J. L.; Madronich, S.; Volkamer, R., Secondary Organic Aerosol Formation from Semi- and Intermediate-Volatility Organic Compounds and Glyoxal: Relevance of O/C as a Tracer for Aqueous Multiphase Chemistry. *Geophys. Res. Lett.* **2013,** *40* (5), 978-982.

22. Kampf, C. J.; Jakob, R.; Hoffmann, T., Identification and Characterization of Aging Products in the Glyoxal/Ammonium Sulfate System - Implications for Light-Absorbing Material in Atmospheric Aerosols. *Atmos. Chem. Phys.* **2012,** *12*, 6323.

23. Li, S. Y.; Du, L.; Wei, Z. M.; Wang, W. X., Aqueous-Phase Aerosols on the Air-Water Interface: Response of Fatty Acid Langmuir Monolayers to Atmospheric Inorganic Ions. *Sci. Total. Environ.* **2017,** *580*, 1155-1161.

24. Bain, C. D.; Davies, P. B.; Ong, T. H.; Ward, R. N.; Brown, M. A., Quantitative Analysis of Monolayer Composition by Sum-Frequency Vibrational Spectroscopy. *Langmuir* **1991,** *7* (8), 1563-1566.

25. Eisenthal, K. B., Liquid Interfaces Probed by Second-Harmonic and Sum-Frequency Spectroscopy. *Chem. Rev.* **1996,** *96* (4), 1343-1360.

26. Lambert, A. G.; Davies, P. B.; Neivandt, D. J., Implementing the Theory of Sum Frequency Generation Vibrational Spectroscopy: A Tutorial Review. *Appl. Spectrosc. Rev.* **2005,** *40* (2), 103-145.

27. Shen, Y. R., Basic Theory of Surface Sum-Frequency Generation. *J. Phys. Chem. C* **2012,** *116* (29), 15505-15509.

28. Scatena, L. F.; Brown, M. G.; Richmond, G. L., Water at Hydrophobic Surfaces: Weak Hydrogen Bonding and Strong Orientation Effects. *Science* **2001,** *292* (5518), 908-912.

29. Moore, F. G.; Becraft, K. A.; Richmond, G. L., Challenges in interpreting vibrational sum frequency spectra: Deconvoluting spectral features as demonstrated in the calcium fluoride-water-sodium dodecylsulfate system. *Appl. Spectrosc.* **2002,** *56* (12), 1575-1578.

30. Richmond, G. L., Molecular Bonding and Interactions at Aqueous Surfaces as Probed by Vibrational Sum Frequency Spectroscopy. *Chem. Rev.* **2002,** *102* (8), 2693-2724.

31. Blower, P. G.; Ota, S. T.; Valley, N. A.; Wood, S. R.; Richmond, G. L., Sink or Surf: Atmospheric Implications for Succinic Acid at Aqueous Surfaces. *J. Phys. Chem. A* **2013,** *117* (33), 7887-7903.

32. Valley, N. A.; Robertson, E. J.; Richmond, G. L., Twist and Turn: Effect of Stereoconfiguration on the Interfacial Assembly of Polyelectrolytes. *Langmuir* **2014,** *30* (47), 14226-14233.

33. Valley, N. V.; Blower, P. G.; Wood, S. R.; Plath, K. L.; McWilliams, L. E.; Richmond, G. L., Doubling Down: Delving into the Details of Diacid Adsorption at Aqueous Surfaces. *J. Phys. Chem. A* **2014,** *118* (26), 4778-4789.

34. McWilliams, L. E.; Valley, N. A.; Wren, S. N.; Richmond, G. L., A Means to an Interface: Investigating Monoethanolamine Behavior at an Aqueous Surface. *Phys. Chem. Chem. Phys.* **2015,** *17*, 21458-21469.

35. Valley, N. A.; Richmond, G. L., Solvation Station: Microsolvation for Modeling Vibrational Sum-Frequency Spectra of Acids at Aqueous Interfaces. *J. Chem. Theory Comput.* **2015,** *11* (10), 4780-4790.

36. Valley, N. A.; Richmond, G. L., Computational Vibrational Sum Frequency Spectra of Formaldehyde and Hydroxymethanesulfonate at Aqueous Interfaces. *J. Phys. Chem. C* **2016,** *120* (26), 14122-14129.

37. McWilliams, L. E.; Valley, N. A.; Vincent, N. M.; Richmond, G. L., Interfacial Insights into a Carbon Capture System: CO2 Uptake to an Aqueous Monoethanolamine Surface. *J. Phys. Chem. A* **2017,** *121* (41), 7956-7967.

38. Gordon, B. P.; Moore, F. G.; Scatena, L. F.; Valley, N. A.; Wren, S. N.; Richmond, G. L., Model Behavior: Characterization of Hydroxyacetone at the Air–Water Interface Using Experimental and Computational Vibrational Sum Frequency Spectroscopy. *J. Phys. Chem. A* **2018,** *122* (15), 3837-3849.

39. Schabes, B. K.; Altman, R. M.; Richmond, G. L., Come Together: Molecular Details into the Synergistic Effects of Polymer–Surfactant Adsorption at the Oil/Water Interface. *J. Phys. Chem. B* **2018,** *122* (36), 8582-8590.

40. Schabes, B. K.; Hopkins, E. J.; Richmond, G. L., Molecular Interactions Leading to the Coadsorption of Surfactant Dodecyltrimethylammonium Bromide and Poly(styrenesulfonate) at the Oil/Water Interface. *Langmuir* **2019,** *35* (22), 7268-7276.

41. Du, Q.; Superfine, R.; Freysz, E.; Shen, Y. R., Vibrational Spectroscopy of Water at the Vapor/Water Interface. *Phys. Rev. Lett.* **1993,** *70* (15), 2313-1316.

42. Morita, A.; Hynes, J. T., A theoretical analysis of the sum frequency generation spectrum of the water surface. *Chem. Phys.* **2000,** *258* (2-3), 371-390.

43. Raymond, E. A.; Tarbuck, T. L.; Brown, M. G.; Richmond, G. L., Hydrogen-Bonding Interactions at the Vapor/Water Interface Investigated by Vibrational Sum-Frequency Spectroscopy of HOD/H2O/D2O Mixtures and Molecular Dynamics Simulations. *J. Phys. Chem. B* **2003,** *107* (2), 546-556.

44. Lu, R.; Gan, W.; Wu, B.-h.; Chen, H.; Wang, H.-f., Vibrational Polarization Spectroscopy of CH Stretching Modes of the Methylene Group at the Vapor/Liquid Interfaces with Sum Frequency Generation. *J. Phys. Chem. B* **2004,** *108* (22), 7297-7306.

45. Shen, Y. R.; Ostroverkhov, V., Sum-Frequency Vibrational Spectroscopy on Water Interfaces: Polar Orientation of Water Molecules at Interfaces. *Chem. Rev.* **2006,** *106* (4), 1140-1154.

46. Tian, C. S.; Shen, Y. R., Sum-Frequency Vibrational Spectroscopic Studies of Water/Vapor Interfaces. *Chem. Phys. Lett.* **2009,** *470* (1-3), 1-6.

47. Feng, R. r.; Guo, Y.; Lü, R.; Velarde, L.; Wang, H. f., Consistency in the Sum Frequency Generation Intensity and Phase Vibrational Spectra of the Air/Neat Water Interface. *J. Phys. Chem. A* **2011,** *115* (23), 6015-6027.

48. Verreault, D.; Hua, W.; Allen, H. C., From Conventional to Phase-Sensitive Vibrational Sum Frequency Generation Spectroscopy: Probing Water Organization at Aqueous Interfaces. *J. Phys. Chem. Lett.* **2012,** *3* (20), 3012-3028.

49. Vinaykin, M.; Benderskii, A. V., Vibrational Sum-Frequency Spectrum of the Water Bend at the Air/Water Interface. *J. Phys. Chem. Lett.* **2012,** *3* (22), 3348-3352.

50. Nagata, Y.; Hsieh, C.-S.; Hasegawa, T.; Voll, J.; Backus, E. H. G.; Bonn, M., Water Bending Mode at the Water–Vapor Interface Probed by Sum-Frequency Generation Spectroscopy: A Combined Molecular Dynamics Simulation and Experimental Study. *J. Phys. Chem. Lett.* **2013,** *4* (11), 1872-1877.

51. Ni, Y.; Skinner, J. L., IR and SFG Vibrational Spectroscopy of the Water Bend in the Bulk Liquid and at the Liquid-Vapor Interface, Respectively. *J. Chem. Phys.* **2015,** *143* (1), 014502.

52. Medders, G. R.; Paesani, F., Dissecting the Molecular Structure of the Air/Water Interface from Quantum Simulations of the Sum-Frequency Generation Spectrum. *J. Am. Chem. Soc.* **2016,** *138* (11), 3912-3919.

53. Kundu, A.; Tanaka, S.; Ishiyama, T.; Ahmed, M.; Inoue, K.-i.; Nihonyanagi, S.; Sawai, H.; Yamaguchi, S.; Morita, A.; Tahara, T., Bend Vibration of Surface Water Investigated by Heterodyne-Detected Sum Frequency Generation and Theoretical Study: Dominant Role of Quadrupole. *J. Phys. Chem. Lett.* **2016,** *7* (13), 2597-2601.

54. Perakis, F.; Marco, L. D.; Shalit, A.; Tang, F.; Kann, Z. R.; Kühne, T. D.; Torre, R.; Bonn, M.; Nagata, Y., Vibrational Spectroscopy and Dynamics of Water. *Chem. Rev.* **2016,** *116* (13), 7590-7607.

55. Khatib, R.; Hasegawa, T.; Sulpizi, M.; Backus, E. H. G.; Bonn, M.; Nagata, Y., Molecular Dynamics Simulations of SFG Librational Modes Spectra of Water at the Water–Air Interface. *J. Phys. Chem. C* **2016,** *120* (33), 18665-18673.

56. Dutta, C.; Benderskii, A. V., On the Assignment of the Vibrational Spectrum of the Water Bend at the Air/Water Interface. *J. Phys. Chem. Lett.* **2017,** *8* (4), 801-804.

57. Pezzotti, S.; Galimberti, D. R.; Gaigeot, M.-P., 2D H-Bond Network as the Topmost Skin to the Air–Water Interface. *J. Phys. Chem. Lett.* **2017,** *8* (13), 3133-3141.

58. Suzuki, Y.; Nojima, Y.; Yamaguchi, S., Vibrational Coupling at the Topmost Surface of Water Revealed by Heterodyne-Detected Sum Frequency Generation Spectroscopy. *J. Phys. Chem. Lett.* **2017,** *8* (7), 1396-1401.

59. Tang, F.; Ohto, T.; Hasegawa, T.; Xie, W. J.; Xu, L.; Bonn, M.; Nagata, Y., Definition of Free O–H Groups of Water at the Air–Water Interface. *J. Chem. Theory Comput.* **2018,** *14* (1), 357-364.

60. Woutersen, S.; Emmerichs, U.; Bakker, H. J., Femtosecond mid-IR pump-probe spectroscopy of liquid water: Evidence for a two-component structure. *Science* **1997,** *278* (5338), 658-660.

61. Monson, P. R.; Patumtev, S.; Kaufmann, K. J.; Robinson, G. W., Dominance of Methyl-Groups in Picosecond Vibrational-Relaxation in Hydrocarbons. *Chem. Phys. Lett.* **1974,** *28* (3), 312-315.

62. Chieffo, L.; Shattuck, J.; Amsden, J. J.; Erramilli, S.; Ziegler, L. D., Ultrafast Vibrational Relaxation of Liquid H2O Following Librational Combination Band Excitation. *Chem. Phys.* **2007,** *341* (3), 71-80.

63. Knop, S.; Lindner, J.; Vöhringer, P., OH and NH Stretching Vibrational Relaxation of Liquid Ethanolamine. *Z. Phys. Chem.* **2011,** *225* (9-10), 913-926.

64. Case, D. A.; Darden, T. A.; T.E. Cheatham, I.; Simmerling, C. L.; Wang, J.; Duke, R. E.; Luo, R.; Walker, R. C.; Zhang, W.; Merz, K. M., *AMBER 12; University of California: San Francisco*. 2012.

65. Martinez, L.; Andrade, R.; Birgin, E.; Martinez, J., PACKMOL: A Package for Building Initial Configurations for Molecular Dynamics Simulations. *J. Comput. Chem.* **2009,** *30* (13), 2157-2164.

66. Frisch, M. J.; Trucks, G. W.; Schlegel, H. B.; Scuseria, G. E.; Robb, M. A.; Cheeseman, J. R.; Scalmani, G.; Barone, V.; Mennucci, B.; Petersson, G. A.; Nakatsuji, H.; Caricato, M.; Li, X.; Hratchian, H. P.; Izmaylov, A. F.; Bloino, J.; Zheng, G.; Sonnenberg, J. L.; Hada, M.; Ehara, M.; Toyota, K.; Fukuda, R.; Hasegawa, J.; Ishida, M.; Nakajima, T.; Honda, Y.; Kitao, O.; Nakai, H.; Vreven, T.; Montgomery, J. A.; Peralta, J. E.; Ogliaro, F.; Bearpark, M.; Heyd, J. J.; Brothers, E.; Kudin, K. N.; Staroverov, V. N.; Kobayashi, R.; Normand, J.; Raghavachari, K.; Rendell, A.; Burant, J. C.; Iyengar, S. S.; Tomasi, J.; Cossi, M.; Rega, N.; Millam, J. M.; Klene, M.; Knox, J. E.; Cross, J. B.; Bakken, V.; Adamo, C.; Jaramillo, J.; Gomperts, R.; Stratmann, R. E.; Yazyev, O.; Austin, A. J.; Cammi, R.; Pomelli, C.; Ochterski, J. W.; Martin, R. L.; Morokuma, K.; Zakrzewski, V. G.; Voth, G. A.; Salvador, P.; Dannenberg, J. J.; Dapprich, S.; Daniels, A. D.; Farkas, O.; Foresman, J. B.; Ortiz, J. V.; Cioslowski, J.; Fox, D. J., *Gaussian 09*. 2009.

67. Maron, M. K.; Takahashi, K.; Shoemaker, R. K.; Vaida, V., Hydration of Pyruvic Acid to Its Geminal-Diol, 2,2-Dihydroxypropanoic Acid, in a Water-Restricted Environment. *Chem. Phys. Lett.* **2011,** *513* (4-6), 184-190.

68. Larsen, M. C.; Vaida, V., Near Infrared Photochemistry of Pyruvic Acid in Aqueous Solution. *J. Phys. Chem. A* **2012,** *116* (24), 5840-5846.

69. Griffith, E. C.; Carpenter, B. K.; Shoemaker, R. K.; Vaida, V., Photochemistry of Aqueous Pyruvic Acid. *Proc. Natl. Acad. Sci. U. S. A.* **2013,** *110* (29), 11714-11719.

70. Reed Harris, A. E.; Ervens, B.; Shoemaker, R. K.; Kroll, J. A.; Rapf, R. J.; Griffith, E. C.; Monod, A.; Vaida, V., Photochemical Kinetics of Pyruvic Acid in Aqueous Solution. *J. Phys. Chem. A* **2014,** *118* (37), 8505-8516.

71. Perkins, R. J.; Shoemaker, R. K.; Carpenter, B. K.; Vaida, V., Chemical Equilibria and Kinetics in Aqueous Solutions of Zymonic Acid. *J. Phys. Chem. A* **2016,** *120* (51), 10096-10107.

72. Reed Harris, A. E.; Doussin, J. F.; Carpenter, B. K.; Vaida, V., Gas-Phase Photolysis of Pyruvic Acid: The Effect of Pressure on Reaction Rates and Products. *J. Phys. Chem. A* **2016,** *120* (51), 10123-10133.

73. Reed Harris, A. E.; Pajunoja, A.; Cazaunau, M.; Gratien, A.; Pangui, E.; Monod, A.; Griffith, E. C.; Virtanen, A.; Doussin, J. F.; Vaida, V., Multiphase Photochemistry of Pyruvic Acid under Atmospheric Conditions. *J. Phys. Chem. A* **2017,** *121* (18), 3327-3339.

74. Rapf, R. J.; Perkins, R. J.; Carpenter, B. K.; Vaida, V., Mechanistic Description of Photochemical Oligomer Formation from Aqueous Pyruvic Acid. *J. Phys. Chem. A* **2017,** *121* (22), 4272-4282.

75. Rapf, R. J.; Perkins, R. J.; Yang, H. S.; Miyake, G.; Carpenter, B. K.; Vaida, V., Photochemical Synthesis of Oligomeric Amphiphiles from Alkyl Oxoacids in Aqueous Environments. *J. Am. Chem. Soc.* **2017,** *139* (20), 6946-6959.

76. Reed Harris, A. E.; Cazaunau, M.; Gratien, A.; Pangui, E.; Doussin, J. F.; Vaida, V., Atmospheric Simulation Chamber Studies of the Gas-Phase Photolysis of Pyruvic Acid. *J. Phys. Chem. A* **2017,** *121* (44), 8348-8358.

77. Rapf, R. J.; Perkins, R. J.; Dooley, M. R.; Kroll, J. A.; Carpenter, B. K.; Vaida, V., Environmental Processing of Lipids Driven by Aqueous Photochemistry of α-Keto Acids. *Acs Central Science* **2018,** *4* (5), 624-630.

78. Fang, Y.; Lesnicki, D.; Wall, K. J.; Gaigeot, M. P.; Sulpizi, M.; Vaida, V.; Grassian, V. H., Heterogeneous Interactions between Gas-Phase Pyruvic Acid and Hydroxylated Silica Surfaces: A Combined Experimental and Theoretical Study. *J. Phys. Chem. A* **2019,** *123* (5), 983-991.

79. Alves, M. R.; Fang, Y.; Wall, K. J.; Vaida, V.; Grassian, V. H., Chemistry and Photochemistry of Pyruvic Acid Adsorbed on Oxide Surfaces. *J. Phys. Chem. A* **2019,** *123* (35), 7661-7671.

80. Glushonok, G. K.; Glushonok, T. G.; Maslovskaya, L. A.; Shadyro, O. I., A 1H and 13C NMR and UV Study of the State of Hydroxyacetone in Aqueous Solutions. *Russ. J. Gen. Chem.* **2003,** *73* (7), 1027-1031.

CHAPTER VIII: GL

1. Loeffler, K. W.; Koehler, C. A.; Paul, N. M.; De Haan, D. O., Oligomer Formation in Evaporating Aqueous Glyoxal and Methyl Glyoxal Solutions. *Environ. Sci. Technol.* **2006,** *40* (20), 6318-6323.

2. De Haan, D. O.; Corrigan, A. L.; Tolbert, M. A.; Jimenez, J. L.; Wood, S. E.; Turley, J. J., Secondary Organic Aerosol Formation by Self-Reactions of Methylglyoxal and Glyoxal in Evaporating Droplets. *Environ. Sci. Technol.* **2009,** *43* (21), 8184-8190.

3. Gordon, B. P.; Moore, F. G.; Scatena, L. F.; Valley, N. A.; Wren, S. N.; Richmond, G. L., Model Behavior: Characterization of Hydroxyacetone at the Air–Water Interface Using Experimental and Computational Vibrational Sum Frequency Spectroscopy. *J. Phys. Chem. A* **2018,** *122* (15), 3837-3849.

4. Wren, S. N.; Valley, N. A.; Gordon, B. P.; McWilliams, L. E.; Richmond, G. L., Hydration, Orientation, and Conformation of Methylglyoxal at the Air-Water Interface. *J. Phys. Chem. A* **2015,** *119* (24), 6391-6403.

5. Gordon, B. P.; Moore, F. G.; Scatena, L. F.; Richmond, G. L., On the Rise: Experimental and Computational Vibrational Sum Frequency Spectroscopy Studies of Pyruvic Acid and Its Surface-Active Oligomer Species at the Air–Water Interface. *J. Phys. Chem. A* **2019**, *123* (49), 10609-10619.

6. Valley, N. V.; Blower, P. G.; Wood, S. R.; Plath, K. L.; McWilliams, L. E.; Richmond, G. L., Doubling Down: Delving into the Details of Diacid Adsorption at Aqueous Surfaces. *J. Phys. Chem. A* **2014,** *118* (26), 4778-4789.

CHAPTER IX: Computational Improvements

1. Nemet, I.; Vikic-Topic, D.; Varga-Defterdarovic, L., Spectroscopic Studies of Methylglyoxal in Water and Dimethylsulfoxide. *Bioorg. Chem.* **2004,** *32*, (6) 560-570.

2. Wren, S. N.; Gordon, B. P.; Valley, N. A.; McWilliams, L. E.; Richmond, G. L., Hydration, Orientation, and Conformation of Methylglyoxal at the Air-Water Interface. *J. Phys. Chem. A.* **2015**, *119*, 6391-6403.

3. Glushonok, G. K.; Glushonok, T. G.; Maslovskaya, L. A.; Shadyro, O. I., ^{1}H- and ^{13}C-NMR and UV Study of the State of Hydroxyacetone in Aqueous Solutions. *Russ. J. Gen. Chem.* **2001,** *73*, No. 7, 1027-1031.

4. Smiechowski, M.; Sun, J.; Forbert, H.; and Marx., Solvation shell resolved THz spectra of simple aqua ions – distinct distance- and frequency- dependent contributions of solvation shells. *Phys.Chem.Chem.Phys*., **2015**, *17*, 8323-8329.

5. Calwell, J. W.; Kollman, P. A., Structure and Properties of Neat Liquids Using Nonadditive Molecular Dynamics: Water, Methanol, and *N*-Methylacetamide. *J. Phys. Chem.* **1995,** *99*, 6208-6219.

6. Jorgensen, W. L.; Chandrasekhar, J.; Madura, J. D.; Impey, R. W.; Klein, W., Comparison of simple potential functions for simulating liquid water. *J. Chem. Phys*, **1983**, *79*, 926–935.

7. Berendsen, H. J. C.; Grigera, J. R.; Straatsma, T. P., The missing term in effective pair potentials. *J. Phys. Chem*, **1987**, *91*, 6269–6271.

8. Horn, H.; Swope, W. C.; Pitera, J. W.; Madura, J. D.; Dick, T. J.; Hura, G. L.; Head-Gordon, T., Development of an improved four-site water model for biomolecular simulations: TIP4P-Ew. *J. Chem. Phys.*, **2004**, *120*, 9665-9678.

9. Vega, C.; Abascal, J. L. F., Simulating Water With Rigid Non-Polarizable Model: A General Perspective. *Phys. Chem. Chem. Phys.* **2011,** *13*, 19663-19688.

10. Zadi, S.; Building Water Models: A Different Approach". *J. Phys.Chem. Lett*., **2014**, *21*, 3863–3871.

11. Howard, J. C..; Enyard, J. D.; Tschumpe, G. S., Assessing the accuracy of some popular DFT methods for computing harmonic vibrational frequencies of water clusters. *J. Chem. Phys.* **2015**,*143*, 214103.

12. Gordon, B. P.; Moore, F. G.; Scatena, L. F.; Valley, N. A.; Wren, S. N.; Richmond, G. L., Model Behavior: Characterization of Hydroxyacetone at the Air–Water Interface Using Experimental and Computational Vibrational Sum Frequency Spectroscopy. *J. Phys. Chem. A* **2018,** *122* (15), 3837-3849.

13. Kawamura, K.; Okuzawa, K.; Aggarwal, S. G.; Irie, H.; Kanaya. Y.; Wang, Z.; Determination of Gaseous and Particulate Carbonyls (Glycoaldehyde, hydroxyacetone, glyoxal, methylglyoxal, nonal and decanal) in the atmosphere at Mt. Tai. *Atmos. Chem. Phys.* **2013,** *13*, 5369-5380.

14. Hornak, V.; Abel, R.; Okur, A.; Strockbine, B.; Roitberg, A.; Simmerling, C.; Comparison of multiple Amber force fields and development of improved protein backbone parameters. Proteins, **2006**, *65*, 712-725.

15. Habartova, A.; Valsaraj, K. T.; Roeselova, M., Molecular Dynamics Simulations of Small Halogenated Organics at the Air-Water Interface: Implications in Water Treatment and Atmospheric Chemistry. *J. Phys. Chem. A.* **2013,** *117*, 9205-9215.

APPENDIX B: Neat-MG

1. Gan, W.; Wu, D.; Zhang, Z.; Feng, R. R.; Wang, H. F., Polarization and Experimental Configuration Analyses of Sum Frequency Generation Vibrational Spectra, Structure, and Orientational Motion of the Air/Water Interface. *J. Chem. Phys.* **2006,** *124*, No. 114705.

2. Blower, P. G.; Ota, S. T.; Valley, N. A.; Wood, S. R.; Richmond, G. L., Sink or Surf: Atmospheric Implications for Succinic Acid at Aqueous Surfaces. *J. Phys. Chem. A* **2013,** *117*, 7887-7903.

3. Blower, P. G.; Shamay, E. S.; Kringle, L.; Ota, S. T.; Richmond, G. L., Surface Behavior of Malonic Acid Adsorption at the Air/Water Interface. *J. Phys. Chem. A* **2013,** *117*, 2529-2542.

4. Valley, N. V.; Blower, P. G.; Wood, S. R.; Plath, K. L.; McWilliams, L. E.; Richmond, G. L., Doubling Down: Delving into the Details of Diacid Adsorption at Aqueous Surfaces. *J. Phys. Chem. A* **2014,** *118*, 4778-4789.

5. Rosen, M. J., *Surfactants and Interfacial Phenomena*. 3rd ed.; John Wiley & Sons, Inc.: New York, 2004.

6. Gopalakrishnan, S.; Liu, D.; Allen, H. C.; Kuo, M.; Shultz, M. J., Vibrational Spectroscopic Studies of Aqueous Interfaces: Salts, Acids, Bases, and Nanodrops. *Chem. Rev.* **2006,** *106*, 1155-1175.

7. Jang, M.; Czoschke, N. M.; Lee, S.; Kamens, R. M., Heterogeneous Atmospheric Aerosol Production by Acid-Catalyzed Particle-Phase Reactions. *Science* **2002,** *298*, 814-817.

8. Hazra, M. K.; Francisco, J. S.; Sinha, A., Hydrolysis of Glyoxal in Water-Restricted Environments: Formation of Organic Aerosol Precursors Through Formic Acid Catalysis. *J. Phys. Chem. A* **2014,** *118*, 4095-4105.

APPENDIX C: HA SI

1. Du, Q.; Superfine, R.; Freysz, E.; Shen, Y. R. Vibrational Spectroscopy of Water at the Vapor/Water Interface. *Phys. Rev. Lett.* **1993,** *70*, 2313-2316.

2. Ishiyama, T.; Imamura, T.; Morita, A. Theoretical Studies of Structures and Vibrational Sum Frequency Generation Spectra at Aqueous Interfaces. *Chem. Rev.* **2014,** *114*, 8447-8470.

3. Medders, G. R.; Paesani, F. Dissecting the Molecular Structure of the Air/Water Interface from Quantum Simulations of the Sum-Frequency Generation Spectrum. *J. Am.Chem. Soc.* **2016,** *138*, 3912-3919.

4. Perakis, F.; Marco, L. D.; Shalit, A.; Tang, F.; Kann, Z. R.; Kühne, T. D.; Torre, R.; Bonn, M.; Nagata, Y. Vibrational Spectroscopy and Dynamics of Water. *Chem. Rev.* **2016,** *116*, 7590-7607.

5. Raymond, E. A.; Tarbuck, T. L.; Brown, M. G.; Richmond, G. L. Hydrogen-Bonding Interactions at the Vapor/Water Interface Investigated by Vibrational Sum-Frequency Spectroscopy of HOD/H_2O/D_2O Mixtures and Molecular Dynamics Simulations. *J. Phys. Chem. B* **2003,** *107*, 546-556.

6. Raymond, E. A.; Tarbuck, T. L.; Richmond, G. L. Isotopic Dilution Studies of the Vapor/Water Interface as Investigated by Vibrational Sum-Frequency Spectroscopy. *J. Phys. Chem. B* **2002,** *106*, 2817-2820.

7. Richmond, G. L. Molecular Bonding and Interactions at Aqueous Surfaces as Probed by Vibrational Sum Frequency Spectroscopy. *Chem. Rev.* **2002,** *102*, 2693-2724.

8. Tang, F.; Ohto, T.; Hasegawa, T.; Xie, W. J.; Xu, L.; Bonn, M.; Nagata, Y. Definition of Free O–H Groups of Water at the Air–Water Interface. *J. Chem. Theory Comput.* **2018,** *14*, 357-364.

9. Shen, Y. R.; Ostroverkhov, V. Sum-Frequency Vibrational Spectroscopy on Water Interfaces: Polar Orientation of Water Molecules at Interfaces. *Chem. Rev.* **2006,** *106*, 1140-1154.

10. Pezzotti, S.; Galimberti, D. R.; Gaigeot, M.P. 2D H-Bond Network as the Topmost Skin to the Air–Water Interface. *J. Phys. Chem. Lett* **2017,** *8*, 3133-3141.

11. Schaefer, J.; Backus, E. H. G.; Nagata, Y.; Bonn, M. Both Inter- and Intramolecular Coupling of O–H Groups Determine the Vibrational Response of the Water/Air Interface. *J. Phys. Chem. Lett.* **2016,** *7*, 4591-4595.

12. Suzuki, Y.; Nojima, Y.; Yamaguchi, S. Vibrational Coupling at the Topmost Surface of Water Revealed by Heterodyne-Detected Sum Frequency Generation Spectroscopy. *J. Phys. Chem. Lett.* **2017,** *8*, 1396-1401.

13. Nagata, Y.; Hsieh, C.S.; Hasegawa, T.; Voll, J.; Backus, E. H. G.; Bonn, M. Water Bending Mode at the Water–Vapor Interface Probed by Sum-Frequency Generation Spectroscopy: A Combined Molecular Dynamics Simulation and Experimental Study. *J. Phys. Chem. Lett.* **2013,** *4*, 1872-1877.

14. Ni, Y.; Skinner, J. L. IR and SFG vibrational spectroscopy of the water bend in the bulk liquid and at the liquid-vapor interface, respectively. *J. Chem. Phys.* **2015,** *143* (1), 014502.

15. Vinaykin, M.; Benderskii, A. V. Vibrational Sum-Frequency Spectrum of the Water Bend at the Air/Water Interface. *J. Phys. Chem. Lett.* **2012,** *3*, 3348-3352.

16. Dutta, C.; Benderskii, A. V. On the Assignment of the Vibrational Spectrum of the Water Bend at the Air/Water Interface. *J. Phys. Chem. Lett.* **2017,** *8*, 801-804.

17. Kundu, A.; Tanaka, S.; Ishiyama, T.; Ahmed, M.; Inoue, K.I.; Nihonyanagi, S.; Sawai, H.; Yamaguchi, S.; Morita, A.; Tahara, T. Bend Vibration of Surface Water Investigated by Heterodyne-Detected Sum Frequency Generation and Theoretical Study: Dominant Role of Quadrupole. *J. Phys. Chem. Lett.* **2016,** *7*, 2597-2601.

18. Khatib, R.; Hasegawa, T.; Sulpizi, M.; Backus, E. H. G.; Bonn, M.; Nagata, Y. Molecular Dynamics Simulations of SFG Librational Modes Spectra of Water at the Water–Air Interface. *J. Phys. Chem. C* **2016,** *120*, 18665-18673.

19. Rosen, M. J., In *Surfactants and Interfacial Phenomena 3rd ed.*, John Wiley & Sons, Inc.: New York, 2004.

APPENDIX E: PA SI

1. Du, Q.; Superfine, R.; Freysz, E.; Shen, Y. R. Vibrational Spectroscopy of Water at the Vapor/Water Interface. *Phys. Rev. Lett.* **1993,** *70*, 2313-2316.

2. Ishiyama, T.; Imamura, T.; Morita, A. Theoretical Studies of Structures and Vibrational Sum Frequency Generation Spectra at Aqueous Interfaces. *Chem. Rev.* **2014,** *114*, 8447-8470.

3. Medders, G. R.; Paesani, F. Dissecting the Molecular Structure of the Air/Water Interface from Quantum Simulations of the Sum-Frequency Generation Spectrum. *J. Am.Chem. Soc.* **2016,** *138*, 3912-3919.

4. Perakis, F.; Marco, L. D.; Shalit, A.; Tang, F.; Kann, Z. R.; Kühne, T. D.; Torre, R.; Bonn, M.; Nagata, Y. Vibrational Spectroscopy and Dynamics of Water. *Chem. Rev.* **2016,** *116*, 7590-7607.

5. Raymond, E. A.; Tarbuck, T. L.; Brown, M. G.; Richmond, G. L. Hydrogen-Bonding Interactions at the Vapor/Water Interface Investigated by Vibrational Sum-Frequency Spectroscopy of HOD/H_2O/D_2O Mixtures and Molecular Dynamics Simulations. *J. Phys. Chem. B* **2003,** *107*, 546-556.

6. Raymond, E. A.; Tarbuck, T. L.; Richmond, G. L. Isotopic Dilution Studies of the Vapor/Water Interface as Investigated by Vibrational Sum-Frequency Spectroscopy. *J. Phys. Chem. B* **2002,** *106*, 2817-2820.

7. Richmond, G. L. Molecular Bonding and Interactions at Aqueous Surfaces as Probed by Vibrational Sum Frequency Spectroscopy. *Chem. Rev.* **2002,** *102*, 2693-2724.

8. Tang, F.; Ohto, T.; Hasegawa, T.; Xie, W. J.; Xu, L.; Bonn, M.; Nagata, Y. Definition of Free O–H Groups of Water at the Air–Water Interface. *J. Chem. Theory Comput.* **2018,** *14*, 357-364.

9. Shen, Y. R.; Ostroverkhov, V. Sum-Frequency Vibrational Spectroscopy on Water Interfaces: Polar Orientation of Water Molecules at Interfaces. *Chem. Rev.* **2006,** *106*, 1140-1154.

10. Pezzotti, S.; Galimberti, D. R.; Gaigeot, M.P. 2D H-Bond Network as the Topmost Skin to the Air–Water Interface. *J. Phys. Chem. Lett* **2017,** *8*, 3133-3141.

11. Schaefer, J.; Backus, E. H. G.; Nagata, Y.; Bonn, M. Both Inter- and Intramolecular Coupling of O–H Groups Determine the Vibrational Response of the Water/Air Interface. *J. Phys. Chem. Lett.* **2016,** *7*, 4591-4595.

12. Suzuki, Y.; Nojima, Y.; Yamaguchi, S. Vibrational Coupling at the Topmost Surface of Water Revealed by Heterodyne-Detected Sum Frequency Generation Spectroscopy. *J. Phys. Chem. Lett.* **2017,** *8*, 1396-1401.

13. Nagata, Y.; Hsieh, C.S.; Hasegawa, T.; Voll, J.; Backus, E. H. G.; Bonn, M. Water Bending Mode at the Water–Vapor Interface Probed by Sum-Frequency Generation Spectroscopy: A Combined Molecular Dynamics Simulation and Experimental Study. *J. Phys. Chem. Lett.* **2013,** *4*, 1872-1877.

14. Ni, Y.; Skinner, J. L. IR and SFG vibrational spectroscopy of the water bend in the bulk liquid and at the liquid-vapor interface, respectively. *J. Chem. Phys.* **2015,** *143* (1), 014502.

15. Vinaykin, M.; Benderskii, A. V. Vibrational Sum-Frequency Spectrum of the Water Bend at the Air/Water Interface. *J. Phys. Chem. Lett.* **2012,** *3*, 3348-3352.

16. Dutta, C.; Benderskii, A. V. On the Assignment of the Vibrational Spectrum of the Water Bend at the Air/Water Interface. *J. Phys. Chem. Lett.* **2017,** *8*, 801-804.

17. Kundu, A.; Tanaka, S.; Ishiyama, T.; Ahmed, M.; Inoue, K.I.; Nihonyanagi, S.; Sawai, H.; Yamaguchi, S.; Morita, A.; Tahara, T. Bend Vibration of Surface Water Investigated by Heterodyne-Detected Sum Frequency Generation and Theoretical Study: Dominant Role of Quadrupole. *J. Phys. Chem. Lett.* **2016,** *7*, 2597-2601.

18. Khatib, R.; Hasegawa, T.; Sulpizi, M.; Backus, E. H. G.; Bonn, M.; Nagata, Y. Molecular Dynamics Simulations of SFG Librational Modes Spectra of Water at the Water–Air Interface. *J. Phys. Chem. C* **2016,** *120*, 18665-18673.

19. Rosen, M. J., In *Surfactants and Interfacial Phenomena 3rd ed.*, John Wiley & Sons, Inc.: New York, 2004.